University of California
Santa Barbara

Photophysics of Thermally Activated Delayed Fluorescence in Small Molecules and Lewis Acid Interactions with Semiconducting Polymers

A dissertation submitted in partial satisfaction
of the requirements for the degree

Doctor of Philosophy
in
Materials Chemistry

by

Brett Alexander Yurash

Committee in charge:

Professor Thuc-Quyen Nguyen, Chair
Professor Guillermo C. Bazan
Professor Steven K. Buratto
Professor Michael J. Gordon

December 2019

The Dissertation of Brett Alexander Yurash is approved.

Professor Guillermo C. Bazan

Professor Steven K. Buratto

Professor Michael J. Gordon

Professor Thuc-Quyen Nguyen, Committee Chair

October 2019

Photophysics of Thermally Activated Delayed Fluorescence in Small Molecules and Lewis Acid Interactions with Semiconducting Polymers

by

Brett Alexander Yurash

This dissertation is dedicated to the heroes who helped me throughout my PhD: Socrates, for stimulating my pursuit of truth and ethically guiding me in times of doubt; Theodore Roosevelt, for encouraging me to push my limits and to fulfill my potential as a duty owed to humanity; Ayn Rand, for teaching me to take pride in my actions and to be confident in my abilities.

Acknowledgements

I am humbled by the support I received on my path to a PhD. It was a long, difficult road and I am grateful to the friends and family who supported me in my endeavor, and who put up with my excessive complaining when times were especially hard. My long-time friend and current housemate, Daniel Zewdu, showed exceptional patience for listening to my incessant problems. For these kind individuals, I am forever grateful. I am especially grateful for the scientific collaborators I had the pleasure of working with during my time at UCSB, who I acknowledge at relevant sections in this thesis. Of course, I am very grateful for my advisor, Quyen, who supported me throughout the duration of my PhD and allowed me to be creative in my research. I was fortunate enough to be given a mentorship opportunity in the laboratory, which turned out to be very fruitful for both myself and my mentee, Carolina Espinoza. I am thankful for all of the hard work she contributed to my research, and I wish her success in her future endeavors. I would also like to acknowledge those who I feel were particularly instrumental in my development as a young, inquisitive scientist: Oleksandr Mikhnenko, Alexander Mikhailovsky, Niva Ran, Hung Phan, Ben Luginbuhl, Martin Seifrid, and Alexander Moreland.

This dissertation was supported by the Department of the Navy, Office of Naval Research (Award No. N000141410580), the Department of Energy under Award No. DE-SC0017659, and the Broida-Hirschfelder Graduate Fellowship Award. Many of the measurements carried out in this work were accomplished in the MRL Shared Experimental Facilities, a MRSEC Program of the NSF under Award No. DMR 1720256. For quantum chemical calculations I acknowledge the use of the Center for Scientific Computing, a part of CNSI (Award No. NSF CNS-1725797).

Curriculum Vitæ

Brett Alexander Yurash

Education

2019 Ph.D. in Materials Chemistry, University of California, Santa Barbara.

2014 B.S. in Chemistry, *magna cum laude*, Santa Clara University.

Publications

2019 **Yurash, B.**; Cao, D. X., Brus, V. V.; Leifert, D., Wang, M.; Dixon, A.; Seifrid, M.; Mansour, A. E.; Lungwitz, D.; Liu, T.; Santiago, P. J.; Graham, K. R.; Koch, N.; Bazan, G. C.; Nguyen, T.-Q. *Nat. Mater.* 2019 In press. Towards understanding the doping mechanism of organic semiconductors by Lewis acids.

2019 **Yurash, B.**; Leifert, D.; Reddy, G. N. M.; Cao, D. X.; Biberger, S.; Brus, V. V.; Seifrid, M.; Santiago, P. J.; Khler, A.; Chmelka, B. F.; Bazan, G. C.; Nguyen, T.-Q. *Chem. Mater.* 2019, 31, 17, 6715-6725 Atomic-level insight into the postsynthesis band gap engineering of a Lewis base polymer using Lewis acid tris(pentafluorophenyl)borane.

2019 **Yurash, B.**; Nakanotani, H.; Olivier, Y.; Beljonne, D.; Adachi, C.; Nguyen, T.-Q. *Adv. Mater.* 2019, 31, 21, 1804490 Photoluminescence quenching probes spin conversion and exciton dynamics in thermally activated delayed fluorescence materials.

2019 Hughes, M. P.; Rosenthal, K. D.; Dasari, R. R.; Luginbuhl, B. R.; **Yurash, B.**; Marder, S. R.; Nguyen, T.-Q. *Adv. Funct. Mater.* 2019, 29, 29, 1901269 Charge Recombination Dynamics in Organic Photovoltaic Systems with Enhanced Dielectric Constant.

2018 Ogawa, T.; Hosoyamada, M.; **Yurash, B.**; Nguyen, T.-Q.; Yanai, N.; Kimizuka, N. *J. Am. Chem. Soc.* 2018, 140, 8788 Donor-Acceptor-Collector Ternary Crystalline Films for Efficient Solid-State Photon Upconversion.

2017 Olivier, Y.; **Yurash, B.**; Muccioli, L.; DAvino, G.; Mikhnenko, O.; Sancho-Garcia, J.; Adachi, C.; Nguyen, T.-Q.; Beljonne, D. *Phys. Rev. Mater.* 2017, 1, 075602. Nature of the singlet and triplet excitations mediating thermally activated delayed fluorescence.

2013 Fuller, A. A.; **Yurash, B. A.**; Schaumann, E. N.; Seidl, F. J. *Org. Lett.* 2013, 15, 5118. Self-Association of Water-Soluble Peptoids Comprising (S)-N-1-(Naphthylethyl)glycine Residues.

Presentations

2015 - 2019	Annual research presentation to members of the Center for Polymers and Organic Solids, UCSB, (oral)
2018	Exciton Dynamics in TADF Materials, Hybrid Electronic and Photonic Materials and Phenomena, Gordon Research Conference, Hong Kong (oral and poster)
2017	Exciton Dynamics in TADF Materials, Materials Research Society Fall Conference, Boston, Massachusetts (oral)
2017	TADF Project Proposal, presentation to Christopher Savoie, CEO of Kyulux, Inc., UCSB, California (oral)
2017	Exciton Dynamics in TADF Materials, SCUT-UCSB Collaborative Workshop, UCSB, California (oral)
2014	Structural Studies of Water-Soluble Peptoids Incorporating N-(S)-1-Naphthylethyl Side Chains, ACS National Meeting Dallas, Texas (poster)
2013	Structural Studies of Water-Soluble Peptoids Incorporating N-(S)-1-Naphthylethyl Side Chains, ACS Western Regional Meeting, Santa Clara, California (poster)
2012	Structural Studies of Water-Soluble Peptoids Incorporating N-(S)-1-Naphthylethyl Side Chains, 8th Peptoid Summit, Lawrence Berkeley National Laboratory, Berkeley, California (poster)
2011	Peptoid Chemistry, Summer Research Department Symposium, Santa Clara University (oral)

Honors and Awards

2019	Dixon-Levy Graduate Student Association Service Award
2018	Mananya Tantiwiwat Fellowship Award
2018	Broida-Hirschfelder Graduate Fellowship Award
2017	Outstanding Service to the Department Award
2016	Outstanding Service to the Department Award
2015	Phi Lambda Upsilon Award
2014	The American Institute of Chemists Student Award
2013	American Chemical Society Award in Analytical Chemistry
2012	Gerald & Sally DeNardo Science Scholar Award
2008	National Latin Exam Gold Medal
2007	National Mythology Exam Gold Medal

Research Experience

2014 - 2019	Study of optoelectronic processes in organic semiconductors; advised by Prof. Thuc-Quyen Nguyen
2010 - 2014	Synthesis and characterization of peptidomimetics; advised by Prof. Amelia Fuller
2019	Summer internship at HRL Laboratories, LLC.; research in the quantum optics laboratory

Teaching Experience

2018	Guest lecturer for Instrumental Methods in Materials Chemistry (CHEM 282C)
2016 - 2018	Teaching assistant for Advanced Analytical Chemistry (CHEM 153)
2017 - 2018	Teaching assistant for Biophysical Chemistry (CHEM 112A, 112B)
2016 - 2017	Teaching assistant for Physical Chemistry (CHEM 113A, 113B)
2014 - 2016	Teaching assistant for General Chemistry Laboratory sections (CHEM 1AL, 1BL, 1CL)

Abstract

Photophysics of Thermally Activated Delayed Fluorescence in Small Molecules and Lewis Acid Interactions with Semiconducting Polymers

by

Brett Alexander Yurash

In part one of this thesis, I develop a novel analytical model that can be used to measure specific properties of materials that exhibit thermally activated delayed fluorescence (TADF). TADF materials are promising candidates for use in organic light-emitting diodes, because they are able to harness the energy of triplet excitons without the use of expensive heavy metal atoms, such as Pt and Ir. Key to their success is the phenomenon of reverse intersystem crossing, a property that is challenging to experimentally measure. Besides being able to determine this photophysical rate, my analytical model is also able to determine the singlet-triplet splitting energy and diffusion coefficients of singlet and triplet excitons. After applying the model to a small library of molecules in order to elucidate structure-property relationships, a particular brominated derivative is found to be able to interconvert between the singlet and triplet excited state approximately 36 times during one lifetime, and whose exciton diffusion length exceeds 40 nm, both highly unique properties.

In part two of this thesis, I investigate how the addition of particular Lewis acids to Lewis basic semiconducting polymers affects their optical and electrical properties. In some cases, Lewis acids have been shown to modify the optical properties of organic semiconductors, making them a useful tool for post-synthesis tuning of a materials optical bandgap. In other cases, Lewis acids have been shown to act as efficient p-type dopants, dramatically increasing a materials conductivity. However, a unified theory that accounts

for both of these behaviors has been missing, and neither process has been well understood in general. Using a variety of spectroscopic techniques on a range of Lewis acids and Lewis basic semiconducting polymers, I propose a unified theory in which both phenomena are accounted for. In particular, I propose that p-type doping is mediated by trace amounts of water, which ultimately protonate the polymer backbone and, subsequently, lead to electron transfer events. For polymers with strongly Lewis basic atoms, the Lewis acids tend to form adducts with the polymer, leading to a reduction of the polymer bandgap and precluding the doping process.

Contents

Chapter 1

Introduction

Inorganic semiconductors are essential to the vast majority of modern electronics and the metal-oxide semiconductor field-effect transistor (MOSFET) is the most widely manufactured object on the planet. Although inorganic semiconductors work well in an astronomical number of applications (solar cells, light-emitting diodes, transistors, etc.), they do have some limitations. The limitations of inorganic semiconductors will be briefly highlighted here, with an emphasis on silicon since it is by far the most widely used inorganic semiconductor. First off, inorganic semiconductors are relatively dense materials, which can be a nuisance for certain applications where excessive weight is either very expensive or not an option at all. Satellites typically have solar panels, which must obviously be sent on a rocket into orbit, a task which becomes increasingly expensive with increasing weight. Generating power in remote locations via solar cells is only feasible if you can get the solar panels to your location. If travelling by foot, you probably can't carry many solar panels. Second, the production of crystalline silicon and other inorganic semiconductors are very energy intensive, since they are usually made at temperatures above 1000 degrees Celsius. Third, silicon has an indirect bandgap, which means it is not so great at collecting sunlight, and also means it does not efficiently emit light. This is

easily overcome by the use of other inorganic semiconductors, but these are more expensive to produce than silicon. Fourth, the emission of light from inorganic semiconductor crystals are heavily directionally dependent. This is great for certain applications, e.g. lasers, but not so great for other applications, such as television displays and overhead lighting, where a wide emission angle is obviously preferable. Fifth, inorganic semiconductors tend to be stiff, brittle solids. If you want your device to be flexible or conform to the shape of an arbitrary object, inorganic semiconductors are not a good option. Of course you could connect a bunch of semiconductors together with flexible joints, but this is not very practical. Sixth, inorganic semiconductors are not very biocompatible, i.e. living organisms typically have adverse reactions to the presence of inorganic semiconductors. One could easily coat a device with a material that is biocompatible so the inorganic semiconductor can exist inside of living tissue, but this makes interfacing between the semiconductor and the tissue rather challenging.

Thus, it is apparent that inorganic semiconductors have room for improvement. Organic (i.e. carbon-based) semiconductors are a promising class of materials which may be able to overcome many of the limitations of inorganic semicondcutors highlighted above. However, given the massive, mature infrastructure already in existence for the production of silicon, it is unlikely that organic semiconductors could truly rival its the market share. But there do exist certain applications where the use of organic semiconductors is so much more advantageous than the use of inorganic semiconductors, that it is cost-effective and/or practical to use them. For example, organic semiconductors are already in mass use across the globe by smart phone users in the form of organic light-emitting diodes (OLEDs). Organic semiconductors are used for many smart phone (and some television) displays, because they are able to efficiently convert electricity into light of desirable wavelengths and then emit that light at a wide distribution of angles for good user viewing. In addition, bulk organic semiconductors have some inher-

ent degree of physical flexibility, making their incorporation into curved and/or flexible screens very simple. More generally, organic semiconductors are much lighter than their inorganic counterparts, can be produced at far lower temperatures (less energy intensive production and assembly), can be designed to absorb or emit light very efficiently, and can potentially be bio-compatible. Although the commercial applications of technologies that use organic semiconductors are rather limited today, hopefully I have convinced the reader that they hold enough promise to be worthy of considerable research and design efforts.

Although a significant amount of research has already taken place in the field of organic semiconductors since the discovery of conducting polymers in the 1970s by Alan J. Heeger, Alan MacDiarmid, and Hideki Shirakawa, the field still has a lot of room to grow. A major challenge to overcome are the poor electrical properties typical of most organic semiconductors. This stems primarily from two issues: (i) organic semiconductors do not exhibit band-like transport (except for the case of single crystals, which have very limited applicability to practical devices) and (ii) the way in which individual molecules assemble into a bulk material can have a profound effect on electrical properties. The first issue cannot be overcome and is an inherent limitation of organic semiconductors, but is not so huge of a limitation. In theory and in practice, the electrical properties of organic semiconductors have much room to improve. Improving the electrical characteristics of organic semiconductors will improve device performance and make commercial viability that much more realistic. Although their electrical characteristics will never get very close to those of silicon and other inorganic semiconductors, the other advantages that organic semiconductors have to offer, as highlighted above, will outweigh their relatively poor electrical performance. For example, the power conversion efficiency (PCE) of organic solar cells could be significantly improved if an organic semiconductor with better electrical properties is discovered. The second issue mentioned is more problematic in

practice, because it is extremely difficult to make an organic semiconductor that has good electrical properties on the device scale. There is a massive chemical space available for sythetic chemists to choose from when designing a new organic semiconductor, but it is difficult to predict *a priori* if a certain chemical structure will have good electrical properties. Furthermore, it is nearly impossible to know *a priori* how that molecule will organize itself to form a bulk solid-state material, and the way in which the molecules are organized can dramatically impact their electrical performance. As a result, most attempts to make a superior organic semiconductor are a shot in the dark, so to speak, guided loosely by chemical intuition and recognizing patterns of previous successes and failures in the literature. Thus, it is extremely important for scientists in this field to make new molecules and carefully assess their properties, so that a growing body of accessible knowledge is maintained and incremental improvements can be had by building on the success of particular strategies. If lucky, every once-in-a-while a shot in the dark will yield a massively improved molecule, and the field will have improved enormously, seemingly overnight.

The intent of this doctoral thesis is to add knowledge to the field of organic semiconductors by very carefully studying a few select materials, drawing insight from how subtle variations in chemical structure affect their bulk properties. In addition, I investigated how adding particular chemicals, i.e. Lewis acids, can change the electrical and optical properties of organic semiconductors. While in pursuit of this basic thesis, I inadvertently developed a novel experimental method for determining particular photophysical parameters which are traditionally very difficult (if not impossible) to measure, and discovered the previously unknown mechanism of p-type doping by Lewis acids.

In this Chapter and Chapter 2 citations are limited, because the information contained within is generally accepted to be true and can be found in numerous textbooks on related subject matter. The sources from which I drew upon most heavily in these two chapters

are [1, 2, 3, 4]. For any graduate student whose research concerns organic semiconductors, I cannot recommend highly enough [1]. I even had the pleasure of meeting with Prof. Anna Köhler and Heinz Bässler, and shamelessly asked them to sign my copy of their textbook, which they were happy to do. For any graduate student concerned with the optical properties of organic molecules, I highly recommend [3]. The level of detail in that textbook is truly astounding.

1.1 Organic Semiconductors: Theory

Before I try to define what an organic semiconductor is, it is perhaps beneficial to first define what an inorganic semiconductor is, at least in general terms. In most General Chemistry courses we are taught that metals are unique in that they form a crystalline lattice held together by 'a sea of electrons'. Because all of the atoms of the crystal are covalently bound together, their atomic orbitals mix to form a large number of bonding and anti-bonding molecular orbitals. Due to the rules of quantum mechanics, the energy of each molecular orbital must not be degenerate with the other orbitals deriving from the same atomic orbitals. In a large crystal, this results in a large number of molecular orbitals that electrons can fill with only very small deviations in energy, effectively forming a continuum of energy levels, i.e. a band with some minimum and maximum energy. In a filled band, the motion of electrons is severely restricted. In an empty band, electrons can move much more freely. For metals, there is little to no energy separation between the highest energy occupied band (valence band) and the lowest energy unoccupied band (conduction band). Thus, electrons can easily move from the valence band to the conduction band, where they are then able to move around much more freely. Hence, metals easily conduct electricity. In addition, with such a continuum of energy states available for electrons, a photon of nearly any energy can be

absorbed and re-emitted, a phenomenon which accounts for the luster of many metals. In semiconductors, however, there is a finite energy gap between the valence and conduction bands. This gap dramatically reduces the ease with which electrons can move from the valence to conduction band, limiting their conductivity. However, when a multitude of charge carriers are promoted into the valence or conduction band by some extrinsic means, e.g. chemical doping or absorption of a photon, then the material can become reasonably conductive. Hence, the term *semi*conductor.

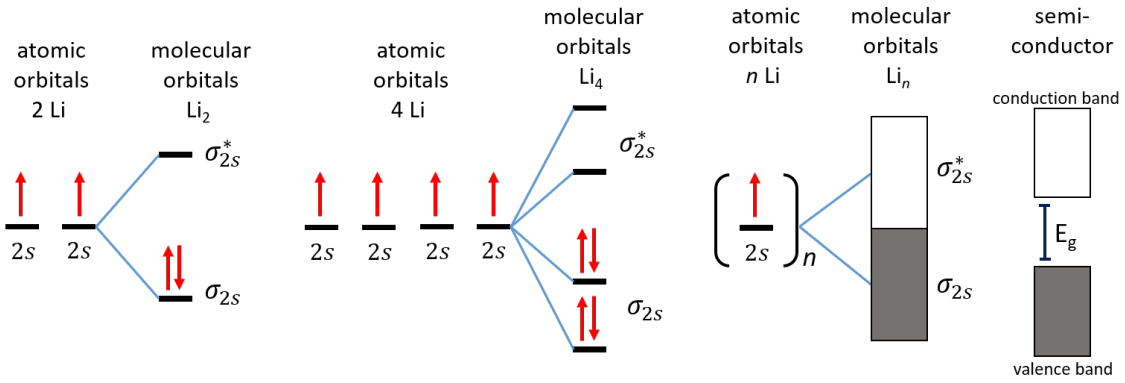

Figure 1.1: Generalized theory accounting for the band structure of metals and semiconductors.

Carbon has 4 valence electrons and, therefore, is able to make up to 4 bonds with adjacent atoms of suitable compatibility. For this example, let's just consider carbon atoms. In order to achieve the lowest energy bonding conformation, the atomic orbitals of carbon hybridize and share electrons through σ bonds. These σ bonds are sp^3 hybridized, meaning they have 25% s character, and 75% p character. Specifically, the s and p atomic orbitals hybridize in a manner that minimizes electron repulsion, giving the carbon atom a tetrahedral geometry with respect to the bonds it forms with the 4 adjacent carbon atoms. Each hybrid orbital contains some s-character and some p-character from each of the 3 orthogonal p orbitals (p_x, p_y, p_z). However, carbon can form stable bonds with just 3 adjacent atoms, instead of 4. In this case, the atomic orbitals of carbon will become

sp^2 hybridized, such that 3 of its molecular orbitals each contain 33% s-character and 66% p-character. These three hybrid orbitals (which form σ bonds) will adopt a trigonal planar geometry in order to minimize electron repulsion. However, in this hybridization scheme, one of the atomic p-orbitals does not mix with the s orbitals. This p-orbital is commonly denoted as the p_z orbital, and it is oriented perpendicular to the plane of bonding. Each carbon atom will donate 1 of its 4 valence electrons into each σ bond that it has, which is 3. The remaining electron goes into the p_z orbital, and it will form a π bond with the electron in an adjacent p_z orbital. If a series of sp^2 hybridized carbons are bonded together in a chain, they will each have a p_z orbital with a single electron in it. These electrons in p_z orbitals form π bonds and are able to delocalize along the backbone of the carbon atom chain, as shown in Figure 1.2. The area over which the electrons are delocalized are known as conjugated segments, and these are the basic building blocks of organic semiconductors. Because not all atoms in the condensed phase of an organic semiconductor are covalently bound to each other, i.e. there are discrete molecules, they do not form 'bands' in the material the way that an inorganic lattice allows.

If we were to remove an electron from a conjugated segment, which could be a section of a polymer or perhaps a single molecule, we would remove an electron that was residing in the highest occupied molecular orbital, or HOMO. The two electrons in this filled orbital have the least amount of energy of all the electrons in the conjugated segment, which makes them easiest to remove. Removing an electron from the HOMO will leave behind a positively charged 'hole' which is delocalized over the conjugated segment. Now consider that an identical conjugated segment is in close proximity to the segment that contains a hole. There is a reasonable probability that an electron from the HOMO of the neutral conjugated segment will 'hop' over to the conjugated segment that has a positively charge hole. If we apply an electric field in just the right direction, we can greatly improve the odds of this charge transfer process. Conversely, if we add an electron to a neutral

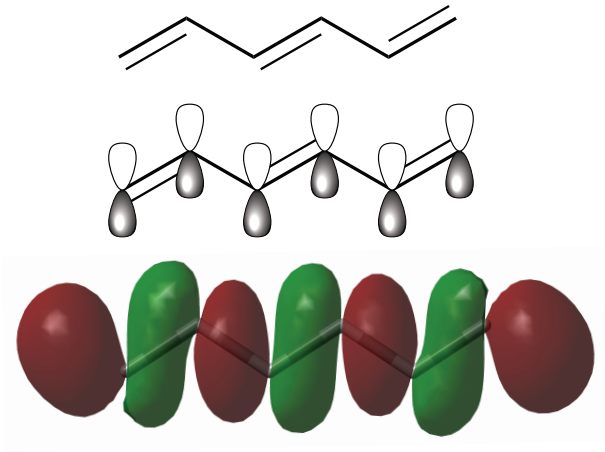

Figure 1.2: The chemical structure of (E)-hexa-1,3,5-triene shown as a chemist would normally draw the structure (top), showing each carbon atom's p_z orbital (middle), and showing the highest occupied molecular orbital (HOMO) wavefunction as calculated by DFT methods (bottom). Clearly, an electron in the HOMO is delocalized along the conjugated backbone. Note the presence of an anti-node at each carbon atom. Hydrogen atoms not shown.

conjugated segment, we will form a radical anion where the additional electron will sit in the lowest unoccupied molecular orbital, or LUMO. Again, there is a probability that this electron will hop to a neighboring conjugated segment, completing a charge transfer process. This is essentially what forms the basis of organic semiconductors. One hop at a time, holes in the HOMO or electrons in the LUMO move from conjugated segment to conjugated segment, creating electrical current, as depicted in Figure 1.3. Importantly, organic semiconductors do not exhibit band-like transport. A material that is better at transporting holes (electrons) than electrons (holes) is called p-type (n-type). A material with an excess of holes (electrons) is said to be p-doped (n-doped). Doping is the process by which excess charges are introduced in a semiconductor, and is discussed in more detail in the following sections.

So far I have basically just considered carbon atoms, but carbon atoms are really just the foundation of organic semiconductors. In reality, organic semicondcutors can incorporate a wide variety of atoms into their structure. Many organic semiconductors

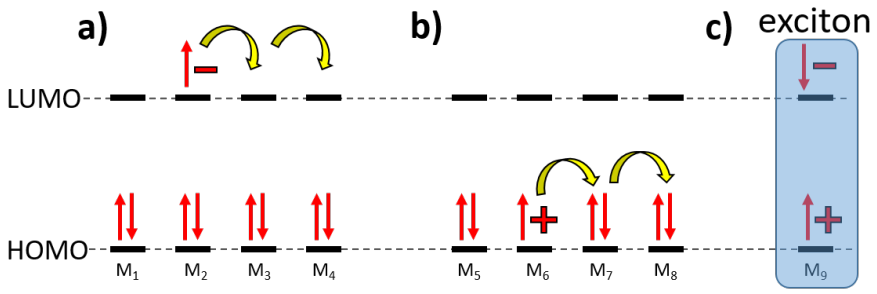

Figure 1.3: Simplified digram of how electrons hop from one molecule to another through the LUMO (a) and holes through the HOMO (b). In (c) an exciton is portrayed as a Coulombically-bound electron-hole pair.

incorporate heteroatoms (nitrogen, sulfur, oxygen, fluorine etc.) into their structure, which greatly impacts the electronic structure of the conjugated segment, i.e. the nature of the HOMO and LUMO wavefunctions. Thus, a change in chemical structure will change how efficiently charge is transferred between conjugated segments. When an ensemble of conjugated segments come together in the condensed phase, a variety of effects are important to consider, of which I will briefly describe two. One consideration is the orientation of one conjugated segment with respect to another, which can have a dramatic impact on their ability to transport charges between themselves. A favorable alignment will increase their wavefunction overlap and facilitate charge hopping. Thus, the way in which molecules orient themselves in the solid-state can have a dramatic impact on the material's electrical properties. The other consideration is that when a charge is introduced on a conjugated segment, the equilibrium geometry of that segment, and sometimes neighboring segments, too, will shift in order to better stabilize the presence of charge. This is called a polaron. A polaron describes the presence of charge and concomitant geometric relaxation that occurs around it. When a positive or negative polaron hops from one site to the next, one must take into consideration the reorganization energies of both sites, each of which experiences a change in its charge state. A rigorous mathematical approach to the problem of charge transport begins by studying

the Marcus Theory of electron transfer, which is beyond the scope of this thesis.

A very useful framework that helps describe the probability of charge hopping events is the density of states (DOS) picture. If we had 100 organic semiconductor molecules in vacuum at zero Kelvin that were infinitely far apart, each of them would have exactly identical HOMO and LUMO energies. However, in the condensed phase at finite temperatures, each molecule will find itself in a slightly different environment due the effects of orientation (except for the case of molecular crystals). In these slightly different environments, the HOMO and LUMO energies will depend on the surrounding environment's polarity, which can vary not only in space, due to orientation, but also in time, due to vibrational motion. HOMO and LUMO energies are also impacted by the relative degree of electronic coupling between adjacent molecules, which can vary in space and time. Thus, due to statistical averaging, HOMO and LUMO energies in the condensed phase can be described by a Gaussian distribution. The density of states (DOS) describes not only the mean HOMO or LUMO energy, but also the variation in energy of each molecule or site. For a material that has a large variation in site energy, i.e. a large degree of disorder, it has a broad DOS. Meanwhile, a narrow DOS implies relatively little disorder and energy levels that are closely spaced together. Charges will be more likely to hop to a neighboring site in a narrow DOS, compared to a broad DOS, because on average the charge in a narrow DOS can find a neighboring site to hop to that doesn't have a prohibitively high energy barrier. In a broad DOS, a charge might not have any nearby sites to hop to with suitable energy, which confines the charge to its original position. Obviously, it is desirable to have a high degree of disorder so that the movement of charges is not impeded by the lack of available sites to hop to.

In reality, one must consider more than just the conjugated segments themselves. Although molecular crystals do exist, which are essentially organic semiconductors that consist only of perfectly repeating conjugated segments, these crystals are difficult to

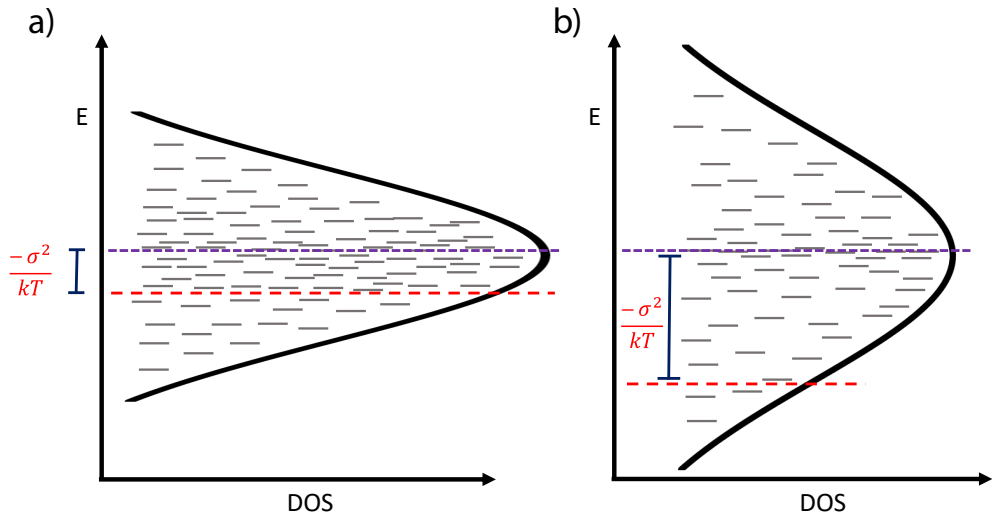

Figure 1.4: Schematic of a narrow DOS (a) and a broad DOS (b). The center energy is denoted by the purple dashed line. The red dashed line indicates thermal equilibrium, i.e. the energy at which a particle in the DOS is most likely to end up at.

fabricate, very fragile, and insoluble. Handling them is very problematic. Thus, making molecular crystals is not a practical way to make an organic semiconductor device. Adding a solubilizing component, such as simple alkyl chains, enables conjugated segments, or conjugated molecules, to be handled very easily in common solvents. This type of molecular architecture usually consists of a planar conjugated backbone with long, floppy sidechains. This strategy enables us to deposit thin films of conjugated material from solution through processing techniques such as drop-casting or spin-casting. However, these solubilizing side chains often disrupt the meso and nano-scale organization of the conjugated segments, which can significantly affect the material's ability to transport charges, as mentioned above.

Up to this point I have described how organic semiconductors are able to transport charge, but I haven't really described what makes them *semi*conductors. Electrical current in a device is the sum of drift and diffusion currents, which are promoted by electric fields and concentration gradients, respectively. Apply an electric field, and, on average, charges will tend to hop either against the direction of the field, or in the same direction

of the field, depending on polarity of the charge. Put a lot of charges in one area of your material, and they will tend to diffuse away from the area of high concentration to areas of lower concentration, in a series of hopping motions. Conductivity, which is the reciprocal of resistivity, describes how well a material can conduct electricity through it. Conductivity is proportional to mobility and the number of free charge carriers. Mobility, μ, is a parameter that describes the velocity of charge carriers in a given electric field strength. Electronic wavefunction overlap between conjugated segments is proportional, then, to mobility. Better wavefunction overlap will make charge hopping between conjugated segments easier, which would manifest itself as a larger mobility. The number of free charge carriers (n for electrons and p for holes) are the charges that are free to move about the material through the HOMO or LUMO, hopping from site to site (conjugated segment to conjugated segment). I specify 'free' here, because there are a handful of reasons that charges might exist in the material but which are unable to move freely. Charges that aren't free are often considered to be 'trapped'. This could be the result of defects in the chemical structure or morphology, which create sites in the material that are so low in energy that a charge can't overcome the energy barrier and hop to a neighboring site. Perhaps the material has a very broad DOS, in which case charges that end up at very low energy sites become unable to hop any further because all of the surrounding sites have too large of an energy. Another reason a charge might not be 'free', is due to the relatively low dielectric of most organic materials. Because of their low dielectric constant, the Coulombic attraction and repulsion of charges are not well screened. Thus, if an electron in the HOMO of a conjugated segment is promoted to the LUMO of the same conjugated segment, the electron in the LUMO will feel a very strong attraction to the hole in the HOMO, limiting the probability that either of the charges migrate to a neighboring segment. At any rate, an organic semiconductor at 0 K has two electrons in its HOMO and no electrons in its LUMO - zero free charge carriers.

The energy gap between HOMO and LUMO prevents the spontaneous creation of free charge carriers. However, at elevated temperatures, thermal energy can assist in moving some electrons from the HOMO into the LUMO, though even at room temperature, the number of free charge carriers generated in this way is very small for typical organic semiconductors (which have an energy gap of more than 1.0 eV between HOMO and LUMO).

As just mentioned, organic semiconductors tend to have a low dielectric constant (typically around 3-4), whereas inorganic semiconductors can have much larger dielectric constants (11.7 for Silicion and much higher for certain other inorganic materials). A large dielectric constant leads to the efficient Coulombic screening of charges, which means that when when an electron gets promoted from the ground state into the excited state, for instance, by absorption of a photon, the excited state electron does not feel a strong Coulombic attraction to the hole it left behind. The electron immediately becomes a free charge and is not strongly attracted to any holes that it might pass by. For organic semiconductors, however, their low dielectric constant leads to a strong Coulombic attraction between opposite charges, leading to the formation of excitons. Excitons refer to the excited state of a molecule which has significant electron-hole attraction. Despite having this strong Coulombic attraction, excitons are neutral species, i.e. they have zero net charge, as shown in Figure 1.3. When an electron is promoted from the ground state into the excited state, the excited state electron will feel a strong attraction to the hole which is left behind, resulting in a large exciton binding energy. For organic semiconductors exciton binding energies typically range from hundreds of millielectron volts up to 1.0 volts. Many inorganic semiconductors have an exciton binding energy below 20 meV (Silicon's exciton binding energy is about 15 meV), which is far enough below ambient thermal energy at room temperature (25-26 meV) that excitons don't really form at all. For an exciton in an organic semiconductor, however, it will need some

type of additional energy in order to overcome the exciton binding energy and create a free electron and hole. Just like charges, excitons are able to diffuse through a material and hop from site-to-site. Although, since they are electrically neutral, excitons do not experience drift in an electric field, the way that free electrons and free holes do. A more detailed description of exciton diffusion is given in Chapter 2.

Technically, when we speak about the HOMO and LUMO of a material we are limiting our description to a one-electron description of molecular orbitals. In other words, we choose to ignore electron-electron interactions, such as Coulombic repulsion and spin. This is done in order to massively simplify the Schrödinger equation, for which an analytical solution to the energy of electron-electron interactions is not possible. Thus, the wavefunction of a single electron in some orbital is determined by replacing its interaction energy with of all of the other electrons by some mean field. Modern calculation methods will often do a good job of approximating electron-electron interactions, resulting in HOMO and LUMO wavefunctions that are reasonably accurate. Still, when we speak of HOMO and LUMO we do not consider the spin of electrons. Moreover, the HOMO (LUMO) wavefunction for a material will change when an electron is removed (added) to create a hole (electron) in that orbital, since the energies and wavefunctions of all the other electrons in the molecule will be affected by the absence (presence) of charge. If we wish to speak of how electrons are arranged in the various molecular orbitals, including their spin, then we must refer to state diagrams. State diagrams are used to describe how electrons are arranged in molecular orbitals, which is particularly useful in the description of excited states (singlet, triplet, etc.), whose energies and properties are greatly affected by electron-electron interactions, such as spin. Furthermore, since the absorption and emission of photons in molecules cannot be accurately described without considering electron-electron interactions, it is best not to use the terms HOMO and LUMO in those contexts. The subtly of when it is proper to refer to molecular orbitals or state diagrams

is often overlooked, which is why I have chosen to mention it here. Electron-electron interactions are less important to consider for inorganic semiconductors (because of their high dielectric constant), which is why the terms 'conduction band' and 'valence band' can be used pretty indiscriminately. 'HOMO' and 'LUMO' have become the de facto replacement for 'valence' and 'conduction' band, respectively, despite the inaccuracy. In this thesis I will try to use the appropriate terms accordingly, but I cannot guarantee my fidelity to that task. A detailed description of singlet and triplet states in organic semiconductors can be found in Chapter 2.

Organic semiconductors aren't very good at transporting charges, and it is rather difficult to create free charges in them, in the first place. The charges are localized to conjugated segments and need a fair amount of coercing to get their move on, so-to-speak. Furthermore, because of poor Coulombic screening, opposite charges are prone to forming excitons and recombining, making it difficult to separate charges so that they are free to move throughout the material. Since they do not have a high concentration of free charge carriers under ambient conditions, and their mobilities are generally low, organic semiconductors are not inherently conductive. Inorganic semiconductors are typically much more conductive under ambient conditions because their charges are delocalized over the entire crystal lattice (not just one little conjugated segment), and they have a higher dielectric constant, meaning that the majority of charges that are present in the material are truly 'free'. Although organic semiconductors are not inherently so conductive, if we can manage to create some free charge carriers in the material, then the conductivity can become quite reasonable, allowing us to make practical devices out of the material such as solar cells, field-effect transistors, and light-emitting diodes. The following sections will describe general methods for managing charges and excitons in organic semiconductors, in the context of some applications.

1.2 Organic Field-Effect Transistors

Organic Field-Effect Transistors (OFETs) have a similar operating principle as inorganic FETs: they are three-electrode devices in which a gate electrode is separated from the active (semiconducting) layer by an insulating dielectric layer. Two other electrodes, called the source and drain, are placed on opposite sides of the active layer, both on the opposite side of the dielectric layer from the gate electrode. See Figure 1.5 for a schematic of this device. The area of the active layer that is located between the source and drain is called the channel, and it is here that current will flow. If a voltage bias is applied between the source and drain, creating an electric field in the channel, only a small amount of current will flow between the two electrodes due to the intrinsically low conductivitity of the semiconducting material. In order to enhance that conductivity by several orders of magnitude, a voltage bias is applied between the gate electrode and the source and drain. With no bias between the source and drain electrodes, the gate bias does not directly produce any current. However, the electric field will promote charges from the source and drain to flow out from the metal into the active layer (with the type of charge, positive or negative, determined by the electric field direction and type of semiconductor). These charges are do not directly create current between the source/drain and gate, because the dielectric layer prevents charges from travelling across it into the gate electrode. The accumulation of charges in the channel effectively dopes the active layer, leading to a dramatic increase in conductivity by increasing the number of free charge carriers. This effect is amplified by an increase in mobility, since the accumulation of free charge carriers in the semiconductor enables the filling of low-energy sites in the DOS (which have poor mobilities) and leads to the filling of higher-energy states in the DOS, where the density of sites is much greater and energy separation between sites much lower, and, thus, charges at these energies in the DOS have much higher mobilities.

Now the application of an electric field between the source and drain will result in a large amount of current flow. The gate voltage is used to modulate the carrier density in the channel, which in turn affects the relative amount of current flowing between source and drain. For inorganic semiconductors, whose conductivities are typically already somewhat high, FETs are operated in depletion mode. A heavily doped active layer (achieved through chemical means) is highly conductive with no gate voltage applied. Upon applying the correct gate voltage, charge carriers are swept out of the active layer, and the channel becomes much less conductive. Here still, the amount of current flowing through the channel is modulated by means of the gate voltage. For optimal performance, a small change in the gate voltage should create a large change in the source/drain current, a parameter which is characterized by the on-off ratio. In addition to a large on-off ratio, FETs should have a fast switching frequency: the time it takes to turn the device on and off should be as short as possible.

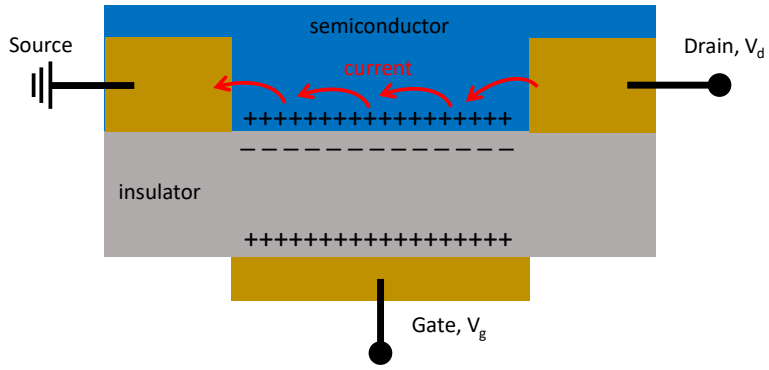

Figure 1.5: Schematic of OFET operation.

The main advantages of organic FETS over inorganic FETs are the relative cost, method of manufacturing, and mechanical properties of the device. In particular, inkjet printing and roll-to-roll coating of organic semiconductor solutions offer a low-cost, scalable alternative to the production of batch-quantities of inorganic semicondcutors in high temperature furnaces. The mechanical flexibilty of OFETs, compared to their stiff and

brittle inorganic counterparts, offers the potential for devices which are inherently flexible. Because of the possibility of introducing specific chemical functionalities in organic semiconductors, OFETs also show promise as chemical sensors, whereby the binding of an analyte to a specific functional group on the organic semiconductor results in the modulation of the amount of current in the channel. Today there exist commercial applications of OFETs, particularly in active and passive matrix displays. Even so, the performance of OFETs is still well below the performance of inorganic FETs. Thus, while OFETs are advantageous in specific applications, their widespread adoption is limited by their relatively low mobilities (copared to inorganic semicondcutors), which manifests in poor on-off ratios and slow switching frequencies.

1.3 P-Type Doping

In contrast to the previous section, where an excess of charge was introduced in the semiconductor by electrical means, an excess of charge can also be introduced by chemical means. For inorganic semiconductors with atoms covalently bonded in a crystal lattice, doping is achieved by the intentional introduction of lattice defects. Specifically, some other type of atom is introduced in small quantities (either during crystal growth of the semiconductor or diffused as a gas into the crystal), such that the dopant atoms replace some of the lattice sites where there otherwise would have been the host crystal's atom(s). For silicon these dopant atoms are typically boron, for p-type doping, or phosphorus, for n-type doping. Bear in mind that silicon has four valence electrons and has a face-centered cubic crystal structure (akin to diamond), in which each silicon atom is bonded to four neighboring silicon atoms. In the case of boron in a silicon lattice, its covalent interactions with the silicon host atoms creates an empty energy state that lies just above the valence band edge - meaning that electrons from the valence band have a

probablility to occupy that defect site, leaving behind a mobile hole in the valence band. Chemically, this is a result of the fact that boron only has three valence electrons, and, therefore, can only make bonds with three of its four neighboring silicon atoms. The boron-silicon site which has only one electron available between them (a valence electron from silicon), would prefer to have an additional electron so that a stable bond can be made. Thus, a free electron wandering around the material is likely to become trapped at this site, creating a negatively charged, stationary boron atom, but leaving behind a mobile hole elsewhere in the valence band of silicon. In the case of n-type doping, the covalent interaction of the dopant with the crystal lattice creates an occupied energy state just below the conduction band - meaning that the electrons in these defect sites have a probability of leaving the dopant atom and entering the conduction band. For example, a phosphorus atom which replaces silicon at some site has five valence electrons, four of which will make covalent bonds with neighboring silicon atoms. The unpaired fifth electron is only very weakly bound to the phosphorus atom, so it is very likely to leave, thereby becoming a free electron in the conduction band of silicon, while also leaving behing a positive charge on the stationary phosphorus atom. Chemical doping is a highly desirable phenomenon because it enables the precise control of free charge carrier concentration and type, which in turn allows scientists and engineers to control the conductivity of semiconductors and make useful devices. With such a tool for tuning conductivity, the development of specific semiconductor applications becomes a practical reality. Unfortunately, controllable doping of organic semiconductors remains a challenge in many respects, limiting their commercial viability.

Doping must be achieved by other means for organic semiconductors, since they do not have a covalently-bonded crystal lattice which can accept atom substitution defects. Substituting atoms in an organic semiconductor will simply change its chemical structure, which would make it a wholly different organic semiconductor - not just the same

underlying one with more electrons or holes, like for the inorganic case. In order to add (n-dope) or remove (p-dope) electrons from organic semiconductors, we must to powerful oxidizing and reducing agents. N-type doping of organic semiconductors remains especially challenging, because these dopants are themselves susceptible to reduction by oxygen and water. P-type dopants for organic semiconductors are intrinsically more stable in this respect. Because p-type dopants are typically more stable and easier to handle than n-type dopants, far more research has been carried out on p-type dopants for organic semiconductors, compared to n-type. Keeping with this trend, I will focus almost exclusively on p-type doping.

P-type doping was first realized through the use of strongly oxidizing gases, such as I_2 and AsF_5. By exposing organic semiconductors to the vapors of these gases, electron transfer would occur from the organic semiconductor to the oxidizing gas. This integer charge transfer (ICT) results in the creation of holes in the organic semiconductor, greatly enhancing its conductivity. A necessary by-product of this reaction, however, is the formation of a counterion - a negatively charged dopant molecule. In order for the newly created hole to become a free charge carrier, it will have to overcome the Coulombic attraction of the dopant anion. Thus, even if every dopant molecule results in the creation of a hole in the organic semiconductor, not all of those holes are necessarily free charge carriers. Doping efficiency, therefore, is usually denoted by the number of free charge carriers generated per addition of dopant molecule. The stability of dopant anions has been a grand challenge for chemists in this field - although the strongly oxidizing gases were able to dope films of organic semiconductors to high conductivities, the dopant anions had a tendency to diffuse through the material, leading to instability of electrical properties. In many cases the negatively charged dopant molecules were also reactive to oxygen. Recall that in the case of inorganic semiconductor doping, the dopant atom is stabilized in the crystal lattice by covalent interactions. For dopant anions in organic

semiconductors, they are stabilized only by van der Waals interactions and Coulomb forces.

The development of stable p-type dopants was revolutionized through the pioneering work of Karl Leo and coworkers. They developed conjugated small molecules with very large ionization potentials and electron affinities, such as 2,3,5,6-tetrafluoro-7,7,8,8-tetracyanoquinodimethane (F_4TCNQ). In this scheme, which is analagous for other methods of p-type doping which generate ICT, the electron affinity (EA) of the dopant molecule is energetically very close, or below, the energy of the organic semiconductor's ionization potential (IP). For example, the IP of a typical organic semiconductor is 5.0 ± 1.0 eV, and the electron affinity of F_4TCNQ is about 5.2 eV. Thus, it can be energetically favorable for an electron in the HOMO of the organic semiconductor (which is approximately equal to the IP) to be transferred into the LUMO (which is approximately equal to the EA) of the dopant molecule. This mechanism, ICT, is by far the most commonly encountered process by which p-type doping occurs, and is depicted in Figure 1.6.

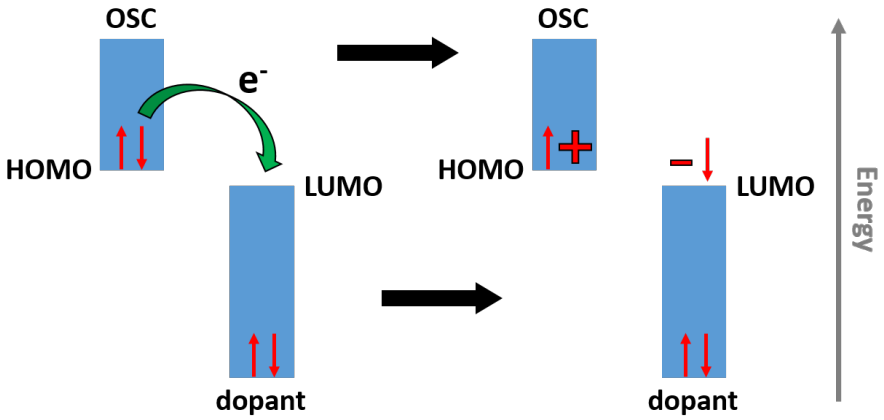

Figure 1.6: Simplified schematic showing how integer charge transfer occurs with molecular dopants and organic semiconductors (OSCs) with suitable energy levels. In this scheme I have ignored the energy level shifts in frontier molecular orbitals that occur upon the transfer of charge.

A less frequently encountered mechanism of p-type doping, dubbed charge-transfer complexation (CTX), occurs when the frontier molecular orbitals of the organic semiconductor hybridize with the frontier molecular orbitals of the dopant molecule, resulting in new energy states just below and above the HOMO energy of the organic semiconductor. Although the lower energy state will tend to be fully occupied by two electrons, the higher energy state will present the opportunity for an electron in the HOMO of some other organic semiconductor molecule to jump to this state, leaving behind a hole. This mechanism is generally not desirable, because it tends to have low doping efficiencies, and the lower energy states that result from hybridization tend to act as hole traps. It has been shown that the orientation between the organic semiconductor and dopant has a strong impact on the viability of CTX. Thus, CTX can be avoided through the use of specially designed dopants which inhibit frontier molecular orbital hybridization with organic semiconductors. This is typically achieved through the incorporation of side chains on the dopant which prevent its aromatic core from becoming spatially proximate to the conjugated backbone of the organic semiconductor.

ICT can also occur from certain organic salts, such as trityl tetrakis(pentafluorophenyl)-borate, TrTPFB. In this mechanism, electron transfer occurs from the HOMO of the organic semiconductor to the cation of the salt - resulting in a neutral, radical species for one component of the organic salt. Meanwhile, the anion of the salt is somewhat of a spectator, although it is the counterion of the newly created hole in the organic semiconductor. ICT from organic salts presents an interesting comparison to ICT from neutral molecular dopants, because in one case, electron transfer from the organic semiconductor results in a radical anion, and in the other case results in a neutral radical. In the former case, the radical anion must be spatially proximate to the organic semiconductor in order for electron transfer to occur. However, this means that there will be a strong Coulombic attraction between the hole and counterion. In the case of electron transfer to the

organic salt, the negatively charged anion does not need to be spatially proximate to the organic semiconductor, such that holes may not feel such a strong Coulombic attraction. Although organic salts continue to be used as p-type dopants, a fundamental study of the mechanism and comparison of the by-products with those of ICT from neutral molecular doping remains to be seen. How these by-products affect trapping of mobile holes would make for an excellent study, in my opinion.

P-type doping of organic semiconductors can also be achieved through the use of strong acids, such as HCl and trifluoroacetic acid (TFA). Although strong acids such as H_2SO_4 can also p-dope organic semiconductors, they are also strongly oxidizing, which convolutes the precise mechanism of action. Thus, non-oxiding acids are more straightforward to categorize. Protonic acid doping was realized quite early on in the development of conductive polymers, around the mid 1980s. However, a complete description of the underlying mechanism with substantial evidence for key intermediates is significantly lacking in the literature. Up until very recently, most theories put forward involved the double protonation of one semiconductor molecule, followed by electron transfer from a nearby, neutral conjugated segment (could be inter- or intra-molecular) to the doubly-protonated segment. The resulting species were said to be two polarons, one of which looked like a typical hole, but the other having two protons attached to the conjugated backbone, along with the overall +1 charge of that segment. The difficulty in identifying the intermediates and by-products of protonic acid doping lies in the presence of radical species. Radical species greatly interfere with nuclear magnetic resonance (NMR) experiments, which are typically sought after for chemical identification of products, to the point where NMR spectra of doped species rarely, if ever, contain meaningful information. Electron paramagnetic resonance (EPR) would also be a suitable technique for studying the products of protonic acid doping, but the disorder inherent in most organic semiconductors is enough to eliminate most distinguishing features. Thus, the precise

mechanism of protonic acid doping has remained elusive for quite some time. Here again, like for the case of ICT from organic salts, it would be interesting to compare the by-products of the different doping mechanisms and try to understand how those differences impact doping efficiency and the trapping of free holes.

Lastly, p-type doping of organic semiconductors can be realized through the use of certain Lewis acids, such as BF_3 and tris(pentafluorophenyl)borane (BCF). Doping by Lewis acids is a recently discovered phenomenon, first reported in 2014. Until recently, the mechanism of doping was unknown, but, at any rate, Lewis acid doping had been shown to be quite efficient compared to other means of doping. Thus, there became quite a bit of interest surrounding the mystery of how Lewis acids can p-dope organic semiconductors, an interest which did not pass over myself. A significant portion of this thesis (Chapters 5, 6, and 7) will cover my attempt to understand this mechanism, and, in that process, I also spent considerable effort understanding other mechanisms of doping, specifically ICT from molecular dopants and protonic acid doping. Because of the potential importance of controllable doping in organic semiconductors, and considering much is still left to be understood about the various doping mechanisms, fundamental studies on organic semiconductor doping are of high scientific relevance.

1.4 Organic Photovoltaics

Photovoltaics enable the conversion of light into electricity, a phenomenon which has been expertly developed in silicon to great commercial success. In general, solar energy is a green energy alternative to fossil fuels, and although it may not be feasible for solar energy to completely replace all of the energy we currently generate from fossil fuels, it could certainly offset much of it. Typical inorganic solar cells are realized through p-n junctions, e.g. a piece of silicon that has p-doped on one side and n-doped on the

other. This results in an excess of holes on the p-doped side, an excess of electrons on the n-doped side, and a depletion region in the middle which doesn't have an excess of free charge carriers of either type, a result of recombination from the doped layers. In the absence of an applied voltage, incident photons can generate free holes and free electrons primarily in the depletion region, which are then swept to the p-doped and n-doped layers, respectively, on account of the internal electric field. The amount of current generated in this way is referred to as the short-circuit current (J_{SC}). Applying a forward bias to the device generates current that flows in the opposite direction of the current generated from the internal electric field, and when these currents become equal in the device, no current is produced. The voltage at which this occurs is called the open-circuit voltage (V_{OC}). Power being the product of current and voltage, a forward bias with magnitude in between the short-circuit and open-circuit condition will generate power. In order to assess how efficient a particular solar cell is at generating power, we define a parameter called the fill factor, FF. It is given by the ratio of maximum power produced by the device to the maximum possible power that could be theoretically generated in the device ($P_{max} = J_{SC} \times V_{OC}$). For a variety of reasons, in particular, recombination of charges, fill factors are never 100%, although some materials have much higher fill factors than others. Thus, solar cells are not just a physics problem, but a materials problem. Besides fill factor, the short-circuit current and open-circuit voltage vary from material to material. Thus, a more practical way of comparing solar cells of various types is by measuring the power conversion efficiency (PCE). The PCE of a solar cell is determined by:

$$PCE = \frac{V_{OC} \times I_{SC} \times FF}{P_{in}} \tag{1.1}$$

where V_{OC} is the open-circuit voltage, I_{SC} is the short-circuit current, FF is the fill factor, and P_{in} is the incident power (for sunlight this is about 100 mW/cm^2) . These

parameters can be easily understood graphically from a plot of a solar cell's current-voltage characteristics, as shown in Figure 1.7.

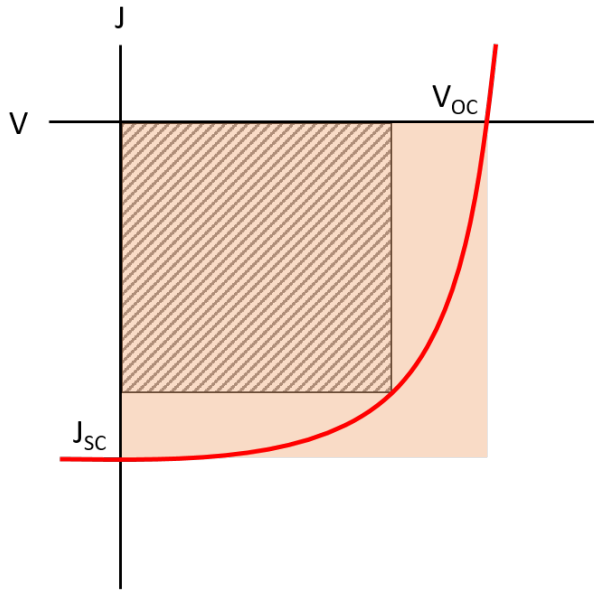

Figure 1.7: Portrayal of a typical current-voltage (J-V) curve for a solar cell. The fill factor is the ratio between the area of the large orange square and the shaded region. The point where the shaded region touches the 'experimental' curve is the voltage at which the solar cell produces the most power.

Although silicon photovoltaic technology has achieved high power-conversion efficiencies ($> 20\%$) and great market success in the recent decades, organic photovoltaics (OPVs) have been plagued by low power conversion efficiencies. Despite their low efficiencies, OPVs are an active area of research due to the potential advantages they offer over their inorganic counterparts. In particular, the possibility of low-cost, scalable manufacturing methods are an attractive quality of OPVs. A skeptic might point out that silicon solar cells have become so cheap that even a reasonable relative offset in production cost of OPVs will not be strong enough of a factor to compete with the already well-established infrastructure developed for silicon technology. Besides, the PCE of OPVs are below that of silicon. Fair enough. However, there are certainly niches where the use of OPVs are market-relevant. One of these niches is related to the relative

weight of OPVs. OPVs are strong light absorbers, where just a 100-200 nm thick layer can absorb all of the sun's incident light (except for the radiation that lies outside of the bandgap, obviously). Silicon has an indirect bandgap, and requires much thicker layers (hundreds of microns) to absorb all of the relevant incident sunlight. Consider also that the density of silicon is about 2.3 g/cm^3 whereas the density of most organic semiconductors is around 1.3 g/cm^3. Thus, silicon solar cells are significantly heavier than OPVs. While this isn't a problem if you want to build solar cells on the ground, it can become a real problem when you want to put solar cells on the roof of a building. Thus, OPVs may be a viable alternative to silicon solar cells for existing buildings whose roofs were not built to support the weight of heavy solar cells. Another niche area for OPVs concerns transparent solar cells. Inorganic solar cells are band absorbers, meaning that any photon above the bandgap of the material can be absorbed. However, organic semiconductors are excitonic absorbers, meaning that photons with energy higher than the main optical transition might not be absorbed at all. The absorption spectrum of an organic semiconductor can be tailored through chemical modification to absorb strongly in the near infrared (NIR) and ultraviolet (UV) regions of the solar spectrum, but be nearly transparent to the visible region. Thus, organic semicondcutors are prime targets for the development of transparent solar cells, which could be utilized in place of any glass screen to generate some electricity from the sun, while still acting like a transparent window for humans to look out of or plants to grow from. While these niches for OPVs are gaining some momentum in the marketplace, more widespread adoption would be rapidly facilitated by enhanced PCEs.

In order to understand how the PCE of OPVs may be improved, it is insightful to first understand how they work, which is significantly different from the operating mechanism of inorganic solar cells. As mentioned before, the large exciton binding energy found in organic semicondcutors means that free charges are typically not generated upon

the absorption of a photon. In order to separate the exciton into free charges more efficiently, another organic semiconductor with different HOMO and LUMO energies must be incorporated into the device. Thus, the active layer of most OPVs contains 2 different compounds: a donor material and an acceptor material. The acceptor material is chosen such that its LUMO energy is larger than the LUMO energy of the donor. Because of this energy difference, a high-energy excited electron from the donor can hop to the LUMO of a nearby, neutral acceptor molecule, in a process called photo-induced electron transfer (PET). This process converts a donor exciton into a donor hole and acceptor electron, and can be a very efficient method of charge separation. Similarly, the HOMO energy of the donor should be smaller than the HOMO energy of the acceptor, so that when an exciton forms on an acceptor molecule, a hole can be transferred from the acceptor HOMO to the donor HOMO, in a process called photo-induced hole transfer (PHT). The mechanisms of PET and PHT are portrayed in Figure 1.8. Once light has been absorbed and the exciton split into charges, the charges move throughout the material under an applied electric field towards their respective electrodes (holes to the anode, electrons to the cathode) where they generate electrical current with the potential to do work. The basic processes underlying OPV operation are shown schematically in Figure 1.9.

In a planar heterojunction device, the donor and acceptor materials comprise two separate layers sandwiched on top of each other, creating a single interfacial plane between the two materials. This is somewhat analagous to the p-n junctions utilized for inorganic cells. When an exciton forms at the interface, it can be separated into free charges, and those charges will travel through their respective domains to the electrodes with little chance of recombination on the way. However, light that is absorbed away from the interface will not be converted into free charges unless the exciton can diffuse to the interface. Because exciton diffusion lengths in organic semiconductors are typi-

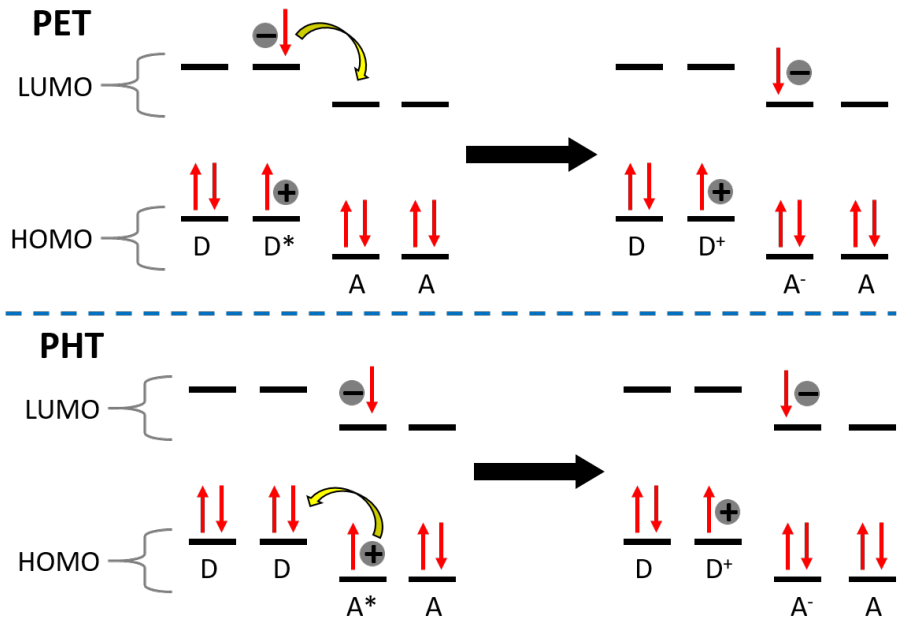

Figure 1.8: Schematic representation of photo-induced electron transfer (PET), above, and photo-induced hole transfer (PHT), below. D = Donor ; A = Acceptor; * = excited state.

cally 10-20 nm, the planar heterojunction is not an efficient structure for generating free charges. Organic semiconductors typically need 100-200 nm thick layers to absorb the maximum possible amount of sunlight. A far more successful device structure is the bulk heterojunction, wherein the donor and acceptor materials are blended together in the active layer. This creates a three-dimensional network of intercalating donor and acceptor regions throughout the active layer. Intense research into the morphology of bulk heterojunctions has actually revealed that in optimized blends there are three different types regions: pure donor domains, pure acceptor domains, and mixed regions. Those investigations have also revealed that the domain sizes of each region is of critical importance in the efficient operation of the device. If the domains are small, then excitons will not have to diffuse far to find an interface where they can become separated into free charges, but if the domains are too small then there may not be an efficient, contiguous

pathway of the domain to the proper electrode for charges to find their way out of the active layer. In that case, charges will become trapped in their domains or be too close to the opposite domain, either case leading to enhanced recombination. If the domains are large, then holes (electrons) will travel unencumbered through the donor (acceptor) domains to the anode (cathode), but if the domains are too large, then excitons that are formed near the middle of those domains will not be able to diffuse to a donor-acceptor interface, precluding the possibility of generating free charges. Thus, the morphology of bulk heterojunction active layers play a critical role in device performance.

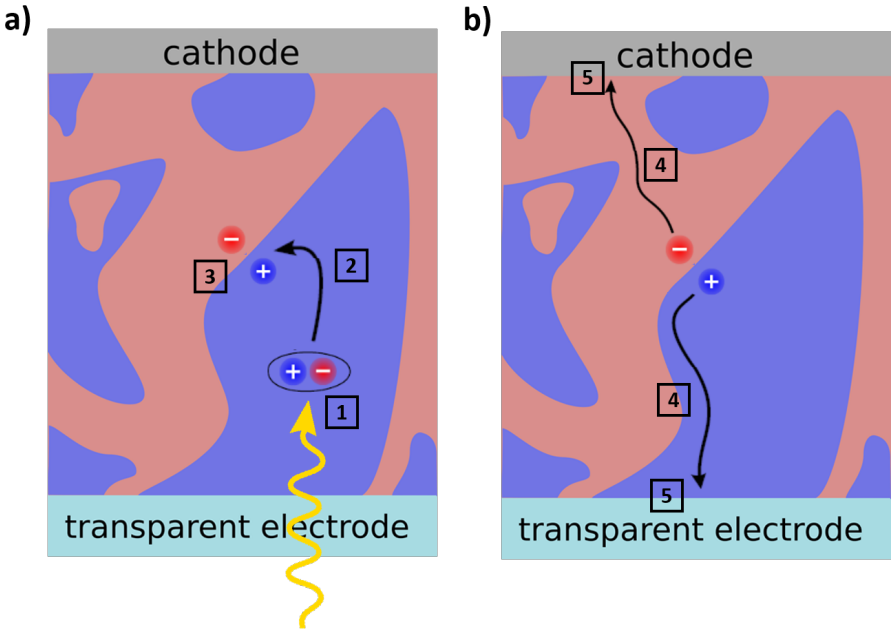

Figure 1.9: Simplified schematic of the operating principles of a bulk heterojunction OPV, where blue regions are donor domains and red regions are acceptor domains. Step 1 is the absorption of light, creating an exciton. In step 2, the exciton diffuses to a donor-acceptor interface. In step 3, the exciton splits into free charges. In step 4 the charges move toward their respective collecting electrodes. In step 5, the free charges are extracted at the electrodes, generating current.

There are numerous factors that affect bulk heterojunction solar cell performance besides morphology, including, but not limited to, material purity, energy level alignment of donor and acceptor, energy level alignment with the electrodes, recombination rate,

absorption spectrum, mobility, trap concentration, etc. Many of these factors are also interrelated, making device performance of OPVs a truly complex subject. At any rate, exciton diffusion is often overlooked in the characterization of OPV materials despite its great importance. In Chapter 2 I investigate exciton diffusion in a semiconducting polymer and explore how different fullerene acceptors impact the efficiency of photo-induced electron transfer. I also characterize relative efficiencies of photo-induced electron and hole transfer in blends containing nonfullerene acceptors.

1.5 Organic Light-Emitting Diodes

At their most simple, an organic light-emitting diode (OLED) is a device that converts electricity into light. When a luminescent material is sandwiched between the appropriate electrodes and a voltage bias is applied, there is the opportunity for holes to be injected into the HOMO of the luminescent material, and electrons into its LUMO. The charges could hop through the device to the electrode on the opposite side, producing some current, or, far more desirably, the electron and hole may meet on a single molecule (or nearby ones), forming an exciton, which can then radiatively decay to the ground state, emitting light. Inorganic LEDs are able to transform electrical current into light, similar to the way OLEDs can, but OLEDs offer a few key advantages which makes them an active area of research and development. In particular, OLEDs have a wide emission angle, because the emitter molecules are randomly oriented in the device. Compare this to LEDs, which tend to emit uni-directionally (anisotropic emission). OLEDs have a relatively large bandwidth, i.e. their output covers a broad range of wavelengths. LEDs have a very narrow bandwidth, which makes it more difficult to achieve true white light and some specific colors. Because of their intrinsically low charge-carrier densities, OLEDs can achieve better contrast (true blackness) than LEDs. Lastly, OLEDs are intrinsically

lightweight, flexible, and do not require thick films for high brightness, qualitites which are desirable for many types of displays. OLEDs are the largest commercial market for organic semiconductors, and that market is growing quickly, fueled by advances in material design and consumer demand for lightweight, portable displays.

Here I will briefly outline the evolution of the OLED, which will contextualize the architecture of today's state-of-the-art OLEDs. This evolution was driven largely by the pursuit of maximizing the external quantum efficiency (EQE), i.e. the number of ouput photons per input of charge. It should be noted that the EQE of a device with a planar emitting surface is limited to about 30% due to the phenomenon of total internal reflection. Thus, it is often convenient to describe the performance of an OLED by its internal quantum efficiency (IQE), which is the number of radiatively decayed excitons per input of charge.

Perhaps the most simple way to improve your device efficiency is to increase the probability of radiative decay. Thus, the first OLEDs used fluorescent dye molecules, which have a fluorescence quantum yield of near 100%. Still, device efficiencies were poor. It turns out that for most organic semiconductors, charge transport is not symmetric, i.e. electrons travel faster (or slower) than holes. Electrons and holes weren't recombining in the center of the device, but instead near one of the electrodes. This is problematic, because metallic contacts are known to efficiently quench excitons. This problem was ameliorated by using charge transport layers. Balanced electron and hole currents travel through the transport layers to the center of the device where the emitter material is located. In addition, scientists could separate the problem of charge transport from the optical properties of the emitter, leading to less restrictive criteria for each. Now that excitons aren't quenched by the electrodes, what else might be limiting the performance? The next obvious step is to increase the probability that electrons and holes recombine, instead of just passing by each other. This can be achieved through the use of hole

and electron-blocking layers, effectively confining charges to the emitter layer. Another strategy to improve recombination is to place the emitter material in a host matrix - a wider bandgap material with slightly higher LUMO and lower HOMO. Thus, electrons and holes will find that going from the host matrix material to the emitter is energetically favorable. With the right doping concentration of the emitter in the host, the emitters are sufficiently far apart as to suppress charge and exciton transport. This is essentially the state-of-the-art OLED architecture, as shown in Figure 1.10. In fact, many modern OLEDs comprise even more layers.

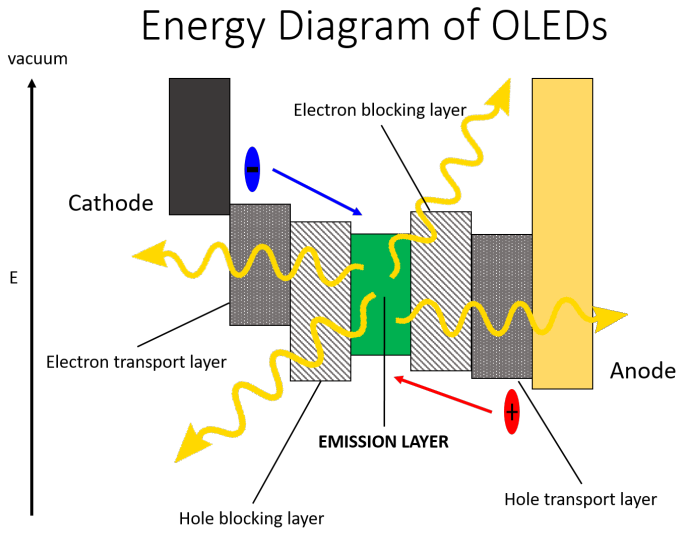

Figure 1.10: Simplified schematic of some of the layers that can be found in OLED devices.

However, the IQE of OLEDs using fluorescent dye emitters were still disappointingly low (around 25%). This was improved to 100% upon the discovery and implementation of heavy atom phosophorescent emitters, such as $Ir(ppy)_3$. The reason is due to the spin statistics of injected charges and their recombination. Opposing charges having a randomly oriented spin upon injection in the device, upon recombination there is a roughly 75% probablity that the newly formed exciton is a triplet. In most fluorescent dyes, triplets are not emissive. The efficient phosphorescence of particular materials is

enabled partly by the heavy atom effect, which confers very large spin-orbit coupling to the molecule, dramatically enhancing the rate of intersystem crossing. If a singlet exciton is formed in one of these materials, it will convert to the triplet state with almost unity efficiency. Using some rational design strategies, triplet emitters were synthesized with very low levels of non-radiative decay, enabling a photoluminescence efficiency of near 100%. However, going from fluorescent-based devices to phosphorescent ones didn't come without problems. Because spin-flip transitions are clasically forbidden, triplet lifetimes are rather long, on the order of microseconds, whereas singlet lifetimes are typically on the order of nanoseconds. At high current densities, long-lived excitons are problematic because they increase the probability of undergoing unwanted bimolecular reactions, such as exciton-charge annihilation and triplet-triplet annihilation. Besides long lifetimes, increased diffusivity of excitons will contribute to these undesirable phenomena. Not only do these processes reduce the IQE, but, in particular, exciton-charge annihilation can result in the formation of highly reactive species, which then undergo unwanted chemical interactions, slowly degrading the device over time. Additionally, these phosphorescent emitters typically have a singlet-triplet splitting energy of about 0.5 - 1.0 eV. The high energy singlet can increase the amount of driving voltage required to operate the device, and can also be a rather reactive species. Despite these drawbacks, phosphorescent OLEDs can perform very well and are commercially available, the most common example being their use in smartphone displays. However, these phosphorescent emitters typically require heavy atoms such as Pt and Ir, since it is through these atoms of high atomic number that high magnitudes of spin-orbit coupling are achieved. Because OLEDs are becoming an increasingly popular choice for display technology, such as for smartphone screens and flat-panel televisions, it is imperative that OLEDs are produced and operated as efficiently as possible so that the carbon footprint of the expanding market is minimized to the greatest extent possible. According to The Insight Partners the global OLED

market is projected to increase from 12.5 billion dollars in 2015 to 39 billion dollars by 2025. Furthermore, platinum group elements are a finite resource which are becoming increasingly difficult to mine, and yet demand for these elements continues to steadily increase due to their use in electronics, catalytic converters, and jewelry.

Now, a new type of emitter has emerged that rivals the efficiency of phosphorescent emitters, but is much cheaper to synthesize and doesn't require heavy atoms such as Pt and Ir. This new type of material exhibits thermally activated delayed fluorescence (TADF) which can be successfully harnessed to make very efficient OLEDs. Thermally activated delayed fluorescence occurs in materials which have a very small energy gap between the singlet and triplet excited state. The gap is small enough (on the order of room temperature energy, i.e. 26 meV) that *reverse* intersystem crossing becomes feasible, and even quite significant for some materials. Thus, triplet excitons are able to convert into singlet excitons where they can emit from the singlet state as fluorescence. Most TADF materials are not phosphorescent, although a few are. Regardless, many TADF materials are able to convert 100% of molecular excitations into radiative singlet excitons.

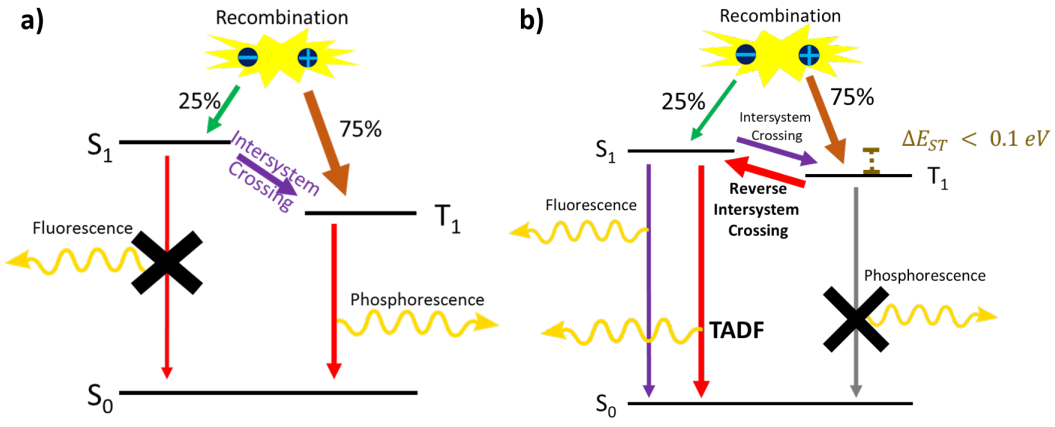

Figure 1.11: Schematic representation of the operating principles of (a) Phosphorescent OLEDs and (b) TADF-OLEDs.

TADF was first exploited for use in an OLED by Chihaya Adachi in 2009. Since then, the field has grown rapidly with numerous publications reporting highly efficient TADF-OLEDs of various colors. Outdoing himself once again, in 2014 Chihaya Adachi pioneered another new type of OLED which exploited a phenomenon dubbed 'Hyperfluorescence'. In this device architecture, a TADF material is used in the emission zone as a recombination center which subsequently shuttles its excited-state energy to a fluorescent dye through Förster resonant energy transfer. Thus, the TADF material converts all molecular excitations (singlet and triplet) into singlet excitons, which are then efficiently channeled to highly emissive fluorescent dyes as radiative singlet excitons, subsequently emitting light. This strategy reduces the triplet lifetime of excitons in the emitting layer, providing the opportunity for bright, efficient, long-lasting OLED devices. On October 7th, 2019 the first OLED display based on Hyperfluorescence became commercially available, courtesy of Kyulux and WiseChip. (I had the pleasure of presenting some of my research on TADF materials to the former and current CEOs of Kyulux.) Although a wealth of reported TADF materials and their device characteristics exist in the literature, a fundamental understanding of the factors that influence this phenomenon is still just beginning to materialize. Continuing on in true OLED fashion, the practical development of TADF in OLEDs precedes its scientific understanding. In this thesis (Chapter 3) I investigate the structure-property relationships of a handful of TADF materials. After carefully examining other methods used in the literature for characterizing the fundamental photophysical properties of TADF materials, I develop my own method for doing so, which I show to be more accurate and reliable than existing methods. Just as for solar cells, exciton diffusion is often overlooked during the characterization of OLED materials. In particular, very few scientists have investigated exciton diffusion in TADF materials. As part of my investigation into TADF materials, I also characterized their exciton diffusion lengths - for both singlet and triplet excitons.

Chapter 2

Exciton Diffusion in Organic Semiconductors

The contents of this chapter are unpublished.

Organic semiconductors have relatively low dielectric constants and weak intermolecular forces, which confine Coulombically-bound electron-hole pairs (excitons) to a single molecule, or perhaps several neighboring molecules. Although spatially confined, the energy contained in these excitons can be transferred to other nearby molecules via exciton diffusion, which follow a 'random walk' motion. In OPVs an exciton is formed by the absorption of solar irradiation. In order to separate into free charges, however, that exciton must find an interface where there is an energetic driving force for charge separation. If the exciton does not find a suitable interface during its excited-state lifetime, it will decay radiatively or non-radiatively, processes which do not contribute to the solar cell's photocurrent. On the other hand, in OLEDs excitons are formed when charges injected from opposite electrodes come into close contact. For optimal device performance an exciton should immediately emit a photon (radiative decay) or immediately transfer its

energy to its target (c.f. Hyperfluorescence). If it does not, then the exciton has a chance to diffuse throughout the active layer and potentially undergo unwanted bimolecular processes, such as exciton-charge annihilation and triplet-triplet annihilation. Thus, exciton diffusion is a critical factor in the performance of optoelectronic devices.

The relevant intramolecular optical transitions of an exciton are indicated in Figure 2.1. Because the ground state of typical organic semiconductors is a singlet (S_0), absorption of a photon will result in the promotion of an electron to a higher-lying singlet excited state (S_n). This process only takes a few femtoseconds to occur. Then, in a process called internal conversion, the excited state electron will quickly (picosecond time scale, sometimes faster) relax to the lowest energy singlet excited state (S_1). Similarly, the excited electron will also quickly relax to its lowest energy vibrational state (assuming moderate temperatures). From the S_1 state, the electron can decay radiatively (fluorescence) or non-radiatively, processes which typically occur on the nanosecond timescale. A singlet exciton could also undergo intersystem crossing to the triplet state (T_n), which requires a spin-flip. Because a spin-flip is classically forbidden, this process is typically very slow, on the order of microseconds. However, spin-orbit coupling can be utilized to enhance intersystem crossing, potentially making it orders of magnitude faster. From a T_n state the electron will rapidly undergo internal conversion and vibrational relaxation to the lowest energy T_1 state. From the T_1 state the triplet exciton can undergo radiative (phosphorescence) or non-radiative decay to S_0. Because these transitions are also classically forbidden and require a spin-flip, they tend to occur on the microsecond to millisecond timescale. These processes, like intersystem crossing, can become much faster through spin-orbit coupling. The lifetime of a singlet or triplet exciton is a measure of how much time it spends in that state before decaying to another state.

In the condensed phase of a pure material, however, singlet and triplet excitons can also experience intermolecular processes, namely, exciton diffusion. Excitons diffuse in

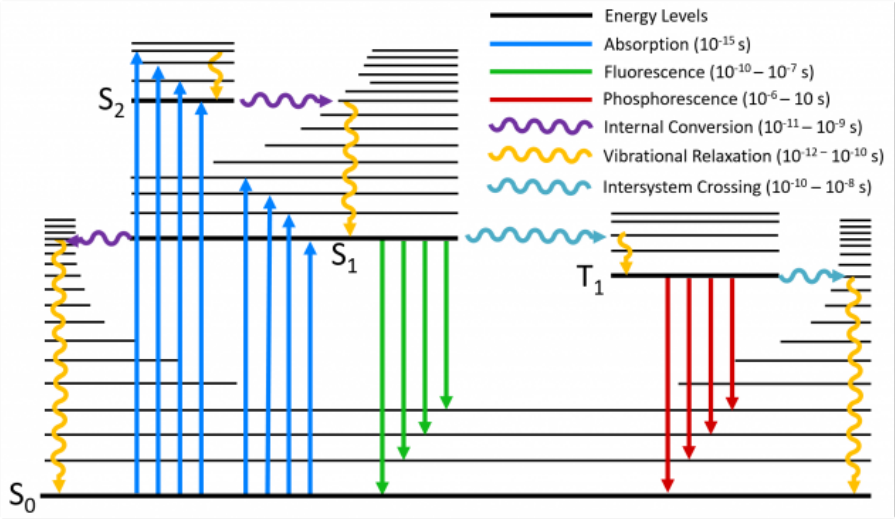

Figure 2.1: Typical Jablonski diagram with indicated rates. Reproduced from www.edinst.com/blog/jablonski-diagram.

a material via one of two methods: Dexter energy transfer and/or Förster resonant energy transfer (FRET). As shown in Figure 2.2, Dexter energy transfer can be thought of as a concerted electron exhange between two molecules. The initially excited donor molecule transfers its excited state electron to the excited state of the acceptor, while simultaneously an electron in the ground state of the acceptor is transferred to the ground state of the donor. Because Dexter energy transfer requires the physical exchange of electrons, a necessary requirement for this process is wavefunction overlap of the donor and acceptor excited states, as well as wavefunction overlap of the donor and acceptor ground states. Because electron density decays exponentially with distance, so too does the rate of Dexter energy transfer. Because of the wavefunction overlap requirement, Dexter energy transfer is said to be a 'through-bond' interaction. Dexter energy transfer is spin-conserving but can occur for both singlets and triplets. Dexter energy transfer is the dominant mechanism of triplet exciton diffusion and is usually insignificant for singlet exciton diffusion. Singlets diffuse primarily via FRET, which is a 'through-space' dipole-mediated interaction. A critical requirement for this process to occur is the spectral

overlap of the donor's emission spectrum and acceptor's absorption spectrum. Because triplets are typically not emissive or absorptive, they do not experience FRET. Since this phenomenon is a dipole-dipole mediated interaction, the rate of FRET decays with distance (r) as $\frac{1}{r^{-6}}$. As such, FRET can transfer the excitation energy of a donor molecule to an acceptor molecule that is several nanometers away, sometimes even past 10 nm. Note that electrons are not exchanged in this process, nor is this simply emission of a photon from the donor and reabsorption by an acceptor. For Dexter energy transfer to occur, donor and acceptor must not be more than 1 or 2 nm apart. For singlet states in typical organic semiconductors, the rate of FRET is much faster than the rate of Dexter energy transfer. A more detailed and quantitative explanation of these processes are given in Chapter 3.

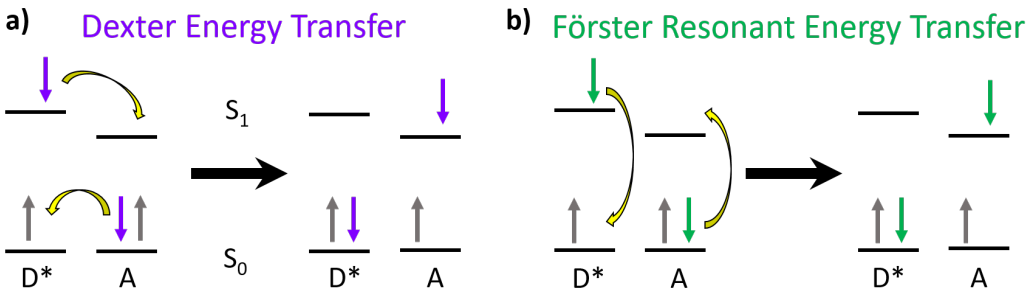

Figure 2.2: Schematic representation of Dexter energy transfer (a) and FRET (b) from an excited donor molecule (D*) to an acceptor molecule (A). Only singlet states are portrayed.

Excitons diffuse in a random-walk motion during their lifetime, meaning that they undergo a series of hops to neighboring molecules (or conjugated segments) in no preferred direction. Although these hops will preferentially go to lower energy sites, in a disordered material (which is the case for the molecules and polymers considered in this thesis), those sites are randomly distributed. In order to know how far an exciton will diffuse during its lifetime, we only need to know the diffusion coefficient of the exciton (D) and its excited state lifetime (τ). Specifically, for 3-dimensional motion, the diffusion length (L_d) is given

by $L_d = \sqrt{6D\tau}$.

Besides exciton diffusion, singlet and triplet excitons in the condensed phase can also experience other intermolecular interactions, such as photo-induced electron transfer (PET) and photo-induced hole transfer (PHT), shown schematically in Figure 1.8. While these processes are of fundamental importance for the generation of charges in OPVs, these processes can also be exploited to gain insight into the exciton diffusion coefficient of an organic semiconductor. Specifically, if a suitable quencher (i.e. energy levels conducive to PET and/or PHT from the host, donor material) is introduced into a host material so that the quencher molecules are dispersed in the host with a separation distance similar to the diffusion length of excitons in the host, then there is a reasonable probability that the host excitons will encounter a quencher during its lifetime. After undergoing PHT or PET, the separated charges will quickly recombine, since the quencher molecules are sufficiently dispersed as to preclude charge migration. Thus, the extrinsic quenchers create an additional decay pathway for host excitons, thereby reducing their lifetime. As more quenchers are introduced into the host, the probability of encountering a quencher will increase in proportion to its exciton diffusion coefficient. Based on this premise, the exciton diffusion coefficient can be measured through a series of fluorescence lifetime measurements with increasing concentrations of a quencher. In Figure 2.3, the fluorescence lifetime of a polymer, PCDTBT, is shown with various concentrations of the exciton quencher, PCBM. Lifetimes were acquired by a time-correlated single-photon counting (TCSPC) technique, which is described in later chapters of this thesis.

2.1 Analytical Measurement

In order to determine the exciton diffusion from the proposed method, we must understand the theory of collisional quenching. Below, I derive the Stern-Volmer equation and

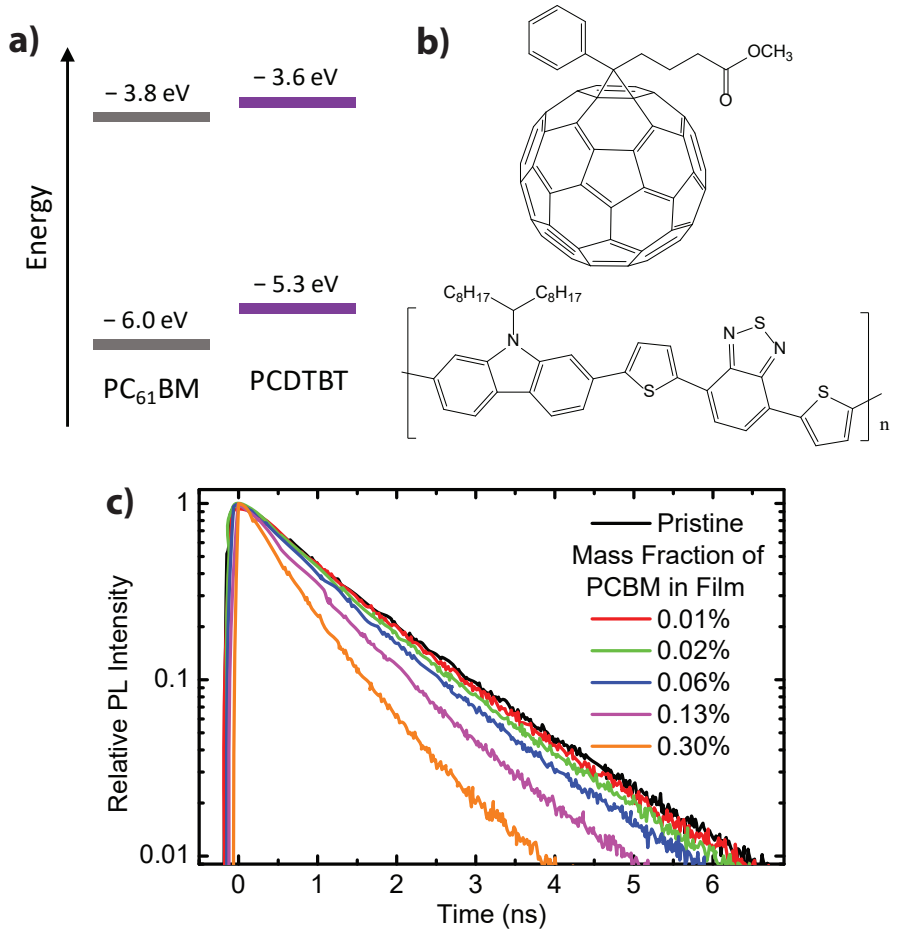

Figure 2.3: a) Energy levels of frontier molecular orbitals for PCDTBT and PCBM. b) Chemical structures of the polymer PCDTBT and the exciton quencher PCBM. c) Fluorescence decay of PCDTBT with increasing amounts of PCBM.

include an interpretation of the bimolecular quenching constant introduced by Marian Smoluchowski.

The fluorescence intensity for a molecule, F, is proportional to its excited-state concentration, $[F*]$. Under constant illumination, this concentration reaches a steady-state given by

$$\frac{d[F*]}{dt} = f(t) - \gamma[F*]_0 = 0 \tag{2.1}$$

where $f(t)$ is the rate at which the excited state is populated, γ is the rate of decay from the excited state, and $[F*]_0$ is the excited-state concentration in the absence of quencher.

When some concentration of quencher, $[Q]$, is introduced to the system, the steady-state equation becomes

$$\frac{d[F*]}{dt} = f(t) - (\gamma + k_q[Q])\,[F*] = 0 \tag{2.2}$$

where k_q is the bimolecular quenching constant and $[F*]$ is the excited-state concentration in the presence of quencher. The bimolecular quenching constant is a measure of the quenching probability - a factor that is influenced by steric accessibility, diffusion rates, the quenching mechanism, etc. Division of Equation 2.2 by Equation 2.1, followed by just a bit of algebra, yields the Stern-Volmer equation:

$$\frac{F_0}{F} = \frac{\gamma + k_q[Q]}{\gamma} = 1 + k_q\tau_0[Q] \tag{2.3}$$

Now, consider that the inverse of γ is the molecule's lifetime in the absence of quencher, i.e.

$$\tau_0 = \frac{1}{\gamma} \tag{2.4}$$

The lifetime in the presence of quencher, then, is given by

$$\tau = \frac{1}{\gamma + k_q[Q]} \tag{2.5}$$

since collisional quenching can be thought of as merely adding another decay process to the excited-state molecule. After dividing Equation 2.4 by Equation 2.5 and doing some algebra, we arrive at the following equation:

$$\frac{\tau_0}{\tau} = \frac{\gamma + k_q[Q]}{\gamma} = 1 + k_q\tau_0[Q] \tag{2.6}$$

which is identical to Equation 2.3. Thus, for the case of collisional quenching, the reduction of a molecule's lifetime due to the presence of a quencher is equivalent to the

reduction in its fluorescence intensity. The amount of steady-state fluorescence from a material is dependent on its concentration, which, in the solid-state, is proportional to volume. When preparing thin films of organic semiconductors, it is extremely challenging to produce films of the exact same thickness, especially if some extrinsic molecule (i.e. a quencher at various concentrations) is mixed in. Thus, the time-dependent Stern-Volmer equation is far more useful in terms of practical considerations. Dividing Equation 2.6 by τ_0, we arrive at the following equation:

$$\frac{1}{\tau} = \frac{1}{\tau_0} + k_q[Q] \tag{2.7}$$

From this equation, one can see that in a plot of a material's lifetime versus concentration of quencher the slope will be equal to k_q, as shown in Figure 2.4.

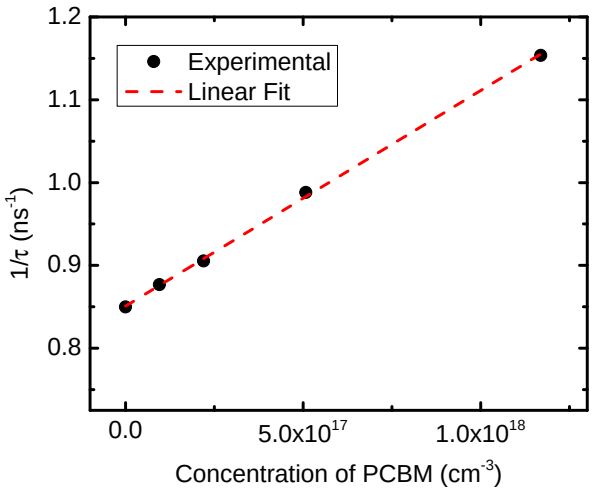

Figure 2.4: Time-dependent Stern-Volmer plot of PCDTBT with PCBM.

In order to understand how this parameter is related to the exciton diffusion coefficient, we must turn to Smoluchowski. Consider that the collisional frequency of fluo-

rophore and quencher (Z) is given by

$$Z = k_0[Q] \tag{2.8}$$

where k_0 is the diffusion-limited bimolecular rate constant. According to Smoluchowski, this parameter is given by

$$k_0 = 4 \times \pi \times (r_F + r_Q) \times (D_F + D_Q) \tag{2.9}$$

This parameter can be understood as the diffusive flux of molecules with combined diffusion coefficients (D) and spherical volumes of r. The bimolecular quenching constant is then simply a product of the probability of quenching (P_Q) upon any given encounter and the diffusion-limited bimolecular rate constant, i.e.

$$k_q = P_Q \times k_0 \tag{2.10}$$

Substituting these equations back into the Stern-Volmer equation, we arrive at the following:

$$\frac{1}{\tau} = \frac{1}{\tau_0} + 4 \times \pi \times P_Q \times (r_F + r_Q) \times (D_F) \tag{2.11}$$

where D_Q was eliminated, because in the condensed phase the quenchers are static. For PCBM, $P_Q \approx 1.0$ and $r_Q \approx 0.5$ nm. According to the literature, a reasonable exciton size is also $r_F \approx 0.5$ nm. Thus, from the slope of Figure 2.4 and the assumptions just stated, we can determine the diffusion coefficient for singlet excitons in PCDTBT, which I found to be 2.07×10^{-4} cm^2/s, corresponding to a diffusion length of 12.1 nm. Unfortunately, this analytical method is only suitable for materials that exhibit a monoexponential PL decay. Fortunately, the same data can be used in conjunction with Monte Carlo

simulation to determine the exciton diffusion coefficient, irrespective of whether the PL decays are monoexponential or multiexponential.

2.2 Monte Carlo Simulation

This section describes the use of a Monte Carlo simulation developed by Dr. Oleksandr Mikhnenko, who I was fortunate to work with for the first few months of graduate school, before he moved on. [5, 6, 7] The input parameters for this simulation are the fitting parameters for the PL decay of a pristine film of the material in question, the concentration of PCBM, and the experimental quenching efficiency, $Q(c)$, determined at that particular concentration of PCBM. The quenching efficiency is given by

$$Q(c) = 1 - \frac{\int PL(c)dt}{\int PL_0 dt} \tag{2.12}$$

where $PL(c)$ is the integrated PL decay of a material with some concentration of quencher and PL_0 is the integrated PL decay of the pristine film. It is important that the intensity of the PL decays of all measurements are normalized to unity.

The simulation approximates quenchers as spheres, so PCBM is an excellent choice of quencher. The quencher radius can be adjusted if so desired. The simulation assumes an exciton radius of 0.5 nm, but this, too, can be adjusted. The simulation creates a 3-dimensional grid of randomly placed spheres (quencher molecules), with an average intermolecular spacing determined by the concentration of quencher. A certain number of 'excitons' (also just spheres) are then randomly distributed on the grid. When the simulation starts, the excitons execute a series of hops in random directions. The hopsize is given by

$$hopsize = \frac{\delta s}{\sqrt{dt}} \tag{2.13}$$

and is related to a diffusion coefficient by

$$D = \frac{\delta s^2}{6dt} = \frac{hopsize^2}{6} \tag{2.14}$$

In the simulation the time (dt) and space (δs) discretization are variable parameters. From simulation to simulation, however, the time discretization should remain constant. In order to simulate different diffusion coefficients, only the space discretization is varied. Starting from an initial guess of the diffusion coefficient, the simulation lets the excitons undergo random walk and the population will decay according to the exponential decay parameters given on input. In addition, if an exciton encounters a quencher, it is also counted as decayed. Thus, when the simulation stops, it merely counts the remaining excitons and compares it to the initial number of generated excitons. From that ratio, the simulation determines a quenching efficiency, and compares it to the experimental quenching efficiency that the user supplied for the given concentration. Depending on whether the simulation was above or below the experimental efficiency, the hopsize is adjusted accordingly, and the simulation repeated. This goes on until the simulated quenching efficiency agrees with the experimental value, at which point the exciton diffusion coefficient is known. More details on the simulation can be found in the relevant publications. In order to enhance the accuracy of this method, the simulation is usually performed for several different concentrations of quencher and then compared back to the experimental data, as shown in Figure 2.5. From this method a singlet exciton diffusion length of 12.0 nm was determined, in excellent agreement with the analytical method.

It is important to consider that both the Monte Carlo and analytical methods for determining exciton diffusion are agnostic to the quenching mechanism. Different mechanisms of quenching are likely to manifest as changes in the quenching probability (P_Q) and quencher radius (r_Q). In the Monte Carlo simulation, the quenching probability

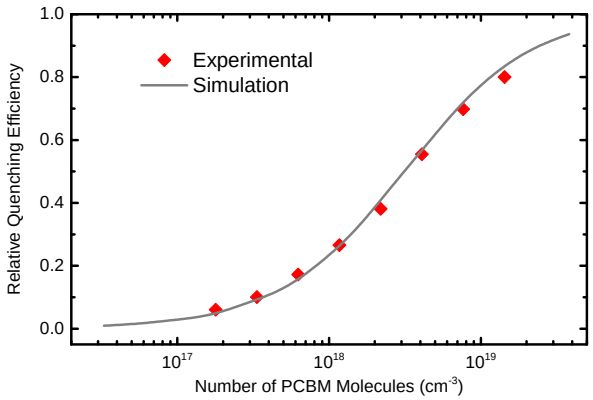

Figure 2.5: Results of the Monte Carlo simulation. The simulation was run for each quencher concentration, determining a diffusion coefficient for each concentration. The average of the diffusion coefficients was taken, and then the simulation used to determine the quenching efficiency for the given concentrations and average diffusion coefficient.

is assumed to be unity. In light of these considerations, the quencher radius is not a measure of physical size, but, rather, a measure of its interaction radius.

2.3 Quenching Probability of Various Fullerene Derivatives

TCSPC measurements were performed on films of PCDTBT with various amounts of selected fullerene derivatives, plus the nonfullerene acceptor PDI (perylene diimide). From these lifetime measurements, Stern-Volmer plots were constructed, as shown in Figure 2.7a. Looking back to Equation 2.11, we can see that the different slopes are proportional to the quenching probability P_Q, plus the radius of the quencher. The values of P_Q in Figure 2.7b were calculated assuming the radius of each quencher was identical to that of PC[60]BM's, i.e. 0.5 nm. (In this section I refer to PCBM explicity as PC[60]BM in order to properly differentiate it from other fullerenes. Elsewhere I do not make the distinction.) Values for electron affinity (EA) were taken from available

literature data, as measured by inverse photoemission spectroscopy. The electron affinity of PCDTBT is approximately 3.6 eV. Thus, these measurements suggest that 100% quenching can be achieved when the acceptor has an EA approximately $0.1 - 0.2$ eV greater than that of the donor material. The relative quenching probability of PDI was determined to be 51.7%.

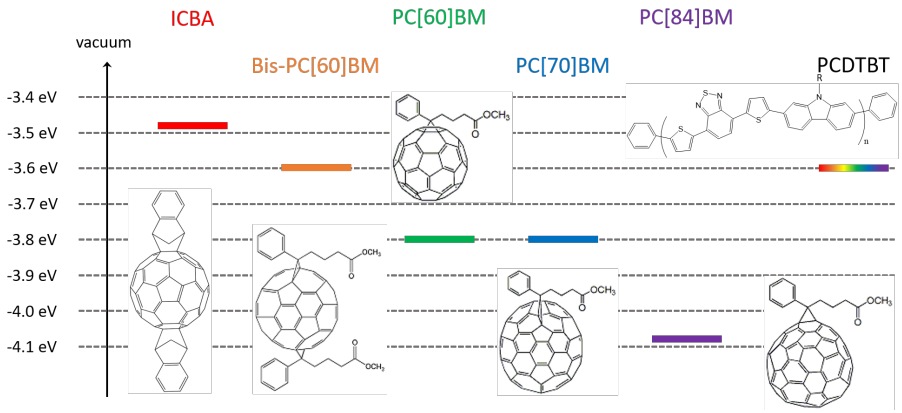

Figure 2.6: Energy diagram of LUMO energies for selected materials. LUMO energies indicated by colored bars. Chemical structures also shown.

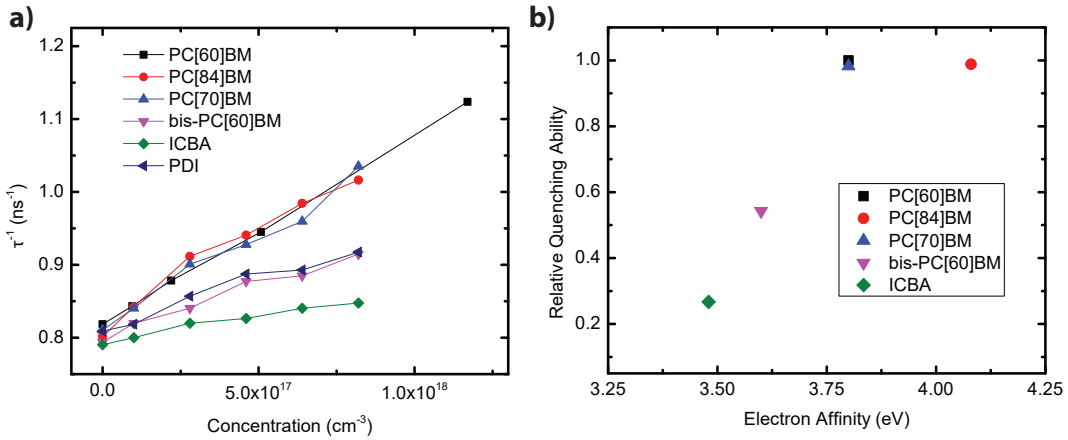

Figure 2.7: a) Stern-Volmer plot of PCDTBT with various fullerene acceptors, and the nonfullerene acceptor PDI. b) Plot of the relative quenching ability of the fullerene derivatives with respect to their electron affinity (EA).

2.4 Trap Density in PCDTBT

According to [8], the trap concentration for a material can be estimated by comparing the lifetime in the pristine solid-state to the lifetime in an inert host matrix. Let's consider a polymer, like PCDTBT. The rate at which the excited state decays is dependent on both intramolecular effects and intermolecular effects. If a polymer strand were isolated in the gas phase it would probably have a lifetime of several nanoseconds, or perhaps longer. But, in the solid-state, new decay pathways are introduced, making the lifetime of a polymer strand shorter. In particular, excitons can diffuse throughout the material and find low-energy defect sites, i.e. traps. Thus, we can use Equation 2.11 to estimate the concentration of traps. In order to obtain a reasonable estimation of trap density, the polymer should have confined excitons which are in a host environment not unlike their own condensed phase. A comparison to the gas phase would neglect non-radiative decay pathways that are the result of vibronic coupling to adjacent molecules, which most wouldn't consider to be 'trapping'. Thus, measuring the lifetime of a polymer in an inert host matrix of similar chemical composition, like polystyrene, and then comparing the lifetime to the neat polymer film, is a reasonable way to estimate exciton trap density. The PL decay of PCDTBT in several molecular environments is shown in Figure 2.8. The relevant equation for trap concentration (c_0) is:

$$c_0 = \frac{1}{4\pi r D}\left(\frac{1}{\tau(neat)} - \frac{1}{\tau(confined)}\right) \tag{2.15}$$

where r is the sum of exciton and trap radii and D is the diffusion coefficient of excitons. The lifetime of neat PCDTBT is 1.19 ns, in chloroform 3.16 ns, and in polystyrene 1.69 ns. Thus, the trap concentration (compared to the polystyrene confinement) is 9.02×10^{17} cm^{-3}. Calculated from the lifetime in chloroform, $c_0 = 1.96 \times 10^{18}$ cm^{-3}, but this should

be thought of as an extreme upper bound.

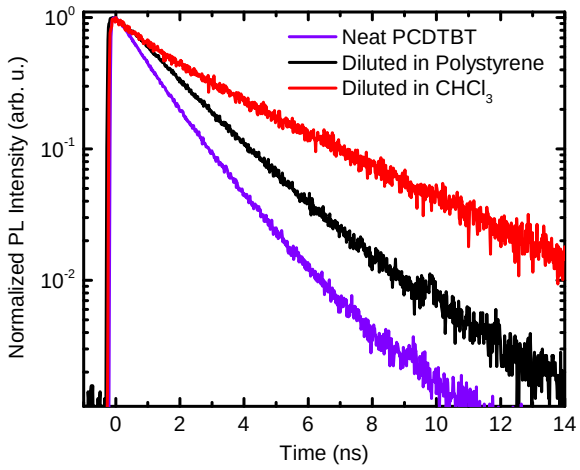

Figure 2.8: Fluorescence decay of PCDTBT in various molecular environments. The concentration in chloroform was 10 μM. A polystyrene:PCDTBT film was made by mixing 1% by weight PCDTBT with polystyrene, then spin-casting a thin film.

2.5 Impact of Dopants on Exciton Diffusion Length

The impact of various dopants on exciton diffusion was investigated by two sets of experiments. In the first, a dopant was added to PCDTBT in a series of increasing concentrations, and the PL decay of each film was measured. Then, the radius of the dopant was estimated via DFT. Finally, a Stern-Volmer plot was used in order to determine the quenching probability of the dopant. In the second type of experiment, a fixed amount of dopant was added to PCDTBT and then a series of films were made with increasing concentration of PCBM. Then, the Monte Carlo simulation was used to determine the diffusion coefficient of PCDTBT excitons. This procedure effectively treats PCDTBT plus the fixed amount of dopant as a single homogenous material, not a heterogeneous blend of two different materials. The dopants I chose to study included F_4TCNQ, TCNQ (tetracyanoquinodimethane), BCF (tris(pentafluorophenyl)borane), TrTPFB (trityl tetrakis

(pentafluorophenyl) borate), and TBABr (tetrabutylammonium bromide). In the literature, F_4TCNQ is claimed to be able to dope PCDTBT, but from UV-Vis-NIR absorption experiments, I could find no evidence. TCNQ has a similar chemical structure to F_4TCNQ, but its electron affinity is smaller. Thus, TCNQ is far less likely to dope PCDTBT. TrTPFB, however, does dope PCDTBT as confirmed by the appearance of NIR absorption upon addition of the salt to PCDTBT, which is attributable to PCDTBT polaron absorption. Being an organic salt, I thus also chose TBABr, since it is also an organic salt but does not dope PCDTBT. Finally, I included the Lewis acid BCF, which, by UV-Vis-NIR, apparently did nothing to PCDTBT. I will refer to all of these as dopants here, but a better name for them would be 'additives' so as to not confuse between chemicals that increase free charge carrier concentration and those that do something else.

The results of the first experiment type are shown in Figure 2.9 and Table 2.5. The results of the second experiment type are shown in Figure 2.10. For the diffusion measurements, the concentration of dopant was fixed at 0.43 molar equivalents with respect to the repeat unit of the PCDTBT polymer.

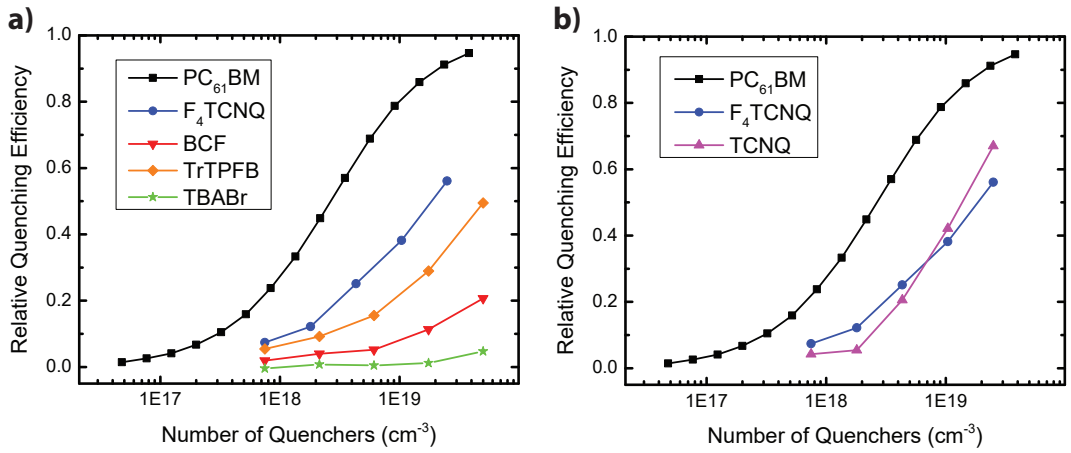

Figure 2.9: Quenching efficiency of dopants (additives) versus their concentration in films of PCDTBT.

Table 2.1: Parameters determined from Stern-Volmer plots, where each dopant was added in various concentrations to PCDTBT.

Dopant	Radius (nm)	Quenching Probability
F_4TCNQ	0.28	31%
TCNQ	0.28	23%
BCF	0.41	3%
TrTPFB	0.53	26%
TBABr	0.26	0.4%

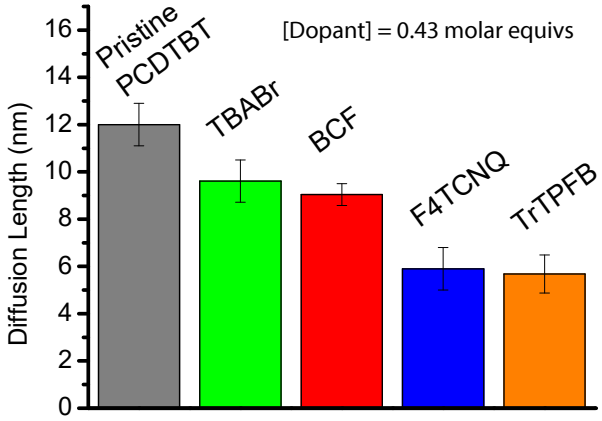

Figure 2.10: Exciton diffusion length of PCDTBT with 0.43 molar equivalents of various dopants. The average intermolecular spacing of the dopants was calculated to be 5.85 nm.

Unfortunately, this project was cut short when my laptop was stolen from out of my office on campus and much of my data analysis was lost. Rather than re-analyzing all of my raw data, I ended up devoting my time to a newer project and never had a chance to revisit this work. Without any additional experimental evidence, it is difficult to draw any meaningful conclusions from this data.

2.6 Photo-Induced Hole Transfer in Nonfullerene Acceptors

At one point in time our lab was very interested in studying nonfullerene acceptors (NFAs) in solar cells, and Guillermo Bazan's research group happened to be synthesizing them. A certain postdoctoral scholar in our group was generally using two different donor materials, PCE10 and PM2, and he was trying to optimize their solar cell performance using one of three different NFAs: IOTIC-2F, COTIC-4F, and SiOTIC-4F. Their chemical structures are irrelevant to the following analysis and is, therefore, left to the eager reader who is fond of solving mysteries to determine. At any rate, the NFAs had relatively similar characteristics, and the postdoctoral scholar spent numerous hours trying to optimize the different binary combinations of donor and NFA for maximum PCE. Some combinations performed quite well, and believing that most of the combinations should also be able to perform similarly, grew very frustrated when certain combinations just didn't achieve a high PCE as he hoped. I found this to be a very interesting problem, and wondered if there was some particular parameter(s) that could explain why some combinations worked and others didn't. Given my affinity to optical properties, I endeavored to determine whether PET and PHT were favorable in each of the blend combinations. If either wasn't, then the solar cell devices would not efficiently generate free charges from excitons, limiting their performance.

The Gibbs energy of PET and PHT is given by

$$\Delta G = IP(D) - EA(A) - \Delta G_{00} - \frac{e^2}{\epsilon_0 \epsilon d} \tag{2.16}$$

where $IP(D)$ is the ionization potential of the donor, $EA(A)$ is the electron affinity of the acceptor, ΔG_{00} is the optical bandgap, e is the charge of an electron, ϵ is the relative

dielectric constant, ϵ_0 is the permittivity of free space, and d is the separation distance between donor and acceptor. If the donor bandgap is used for ΔG_{00}, then Equation 2.16 determines the Gibbs energy for PET. If the acceptor bandgap is used for ΔG_{00}, then Equation 2.16 determines the Gibbs energy for PHT. Assuming that when free charges are generated their effective separation distance is infinity, the Coulomb term in this equation was ignored. In Table 2.6 the relevant parameters are given for the materials in question. The values for optical bandgaps, IP, and EA were not obtained by me. The data was kindly provided to me after I asked. From the data in the table, ΔG was determined for both PET and PHT, as shown in Figure 2.11.

Table 2.2: Parameters used for calculating Gibbs energy of PET and PHT.

Molecule	ΔG_{00} (eV)	IP (eV)	EA (eV)
PCE10	1.59	4.87	N/A
PM2	1.42	5.08	N/A
IOTIC-2F	1.31	N/A	4.06
COTIC-4F	1.10	N/A	4.17
SiOTIC-4F	1.17	N/A	4.12

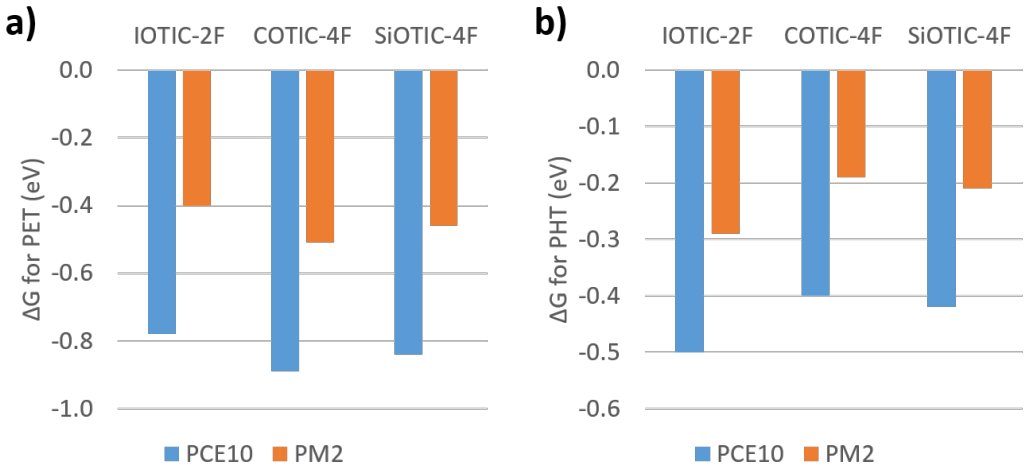

Figure 2.11: Gibbs energy of PET (a) and PHT (b).

After comparing these data to the optimized PCE of the blends, I noticed an inter-

esting correlation with the Gibbs energy of PHT, shown in Figure 2.12. Although some problems require brute force, which often happens when optimizing something with many dependent variables, such as PCE; other times, there exists a more elegant solution to the problem.

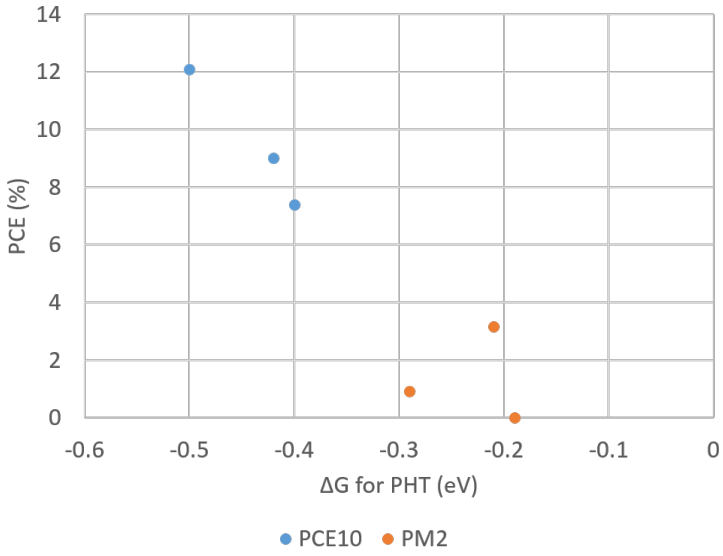

Figure 2.12: Power conversion efficiency (PCE) versus Gibbs energy for photo-induced hole transfer (ΔG for PHT).

Chapter 3

Photophysics of Thermally Activated Delayed Flourescence

The contents of this chapter appear in [9].

Fluorescent materials that efficiently convert triplet excitons into singlets through reverse intersystem crossing (RISC) rival the efficiencies of phosphorescent state-of-the-art organic light-emitting diodes (OLEDs). This upconversion process, a phenomenon known as thermally activated delayed fluorescence (TADF), is dictated by the rate of RISC, a material-dependent property that is challenging to determine experimentally. In this work, a new analytical model is developed which unambiguously determines the magnitude of RISC, as well as several other important photophysical parameters such as exciton diffusion coefficients and lengths, all from straight-forward time-resolved photoluminescence measurements. From a detailed investigation of 5 TADF materials, we derive important structure-property relationships and identify a brominated derivative of 4CzIPN that has an exciton diffusion length of over 40 nm and whose excitons interconvert between the singlet and triplet state approximately 36 times during one lifetime.

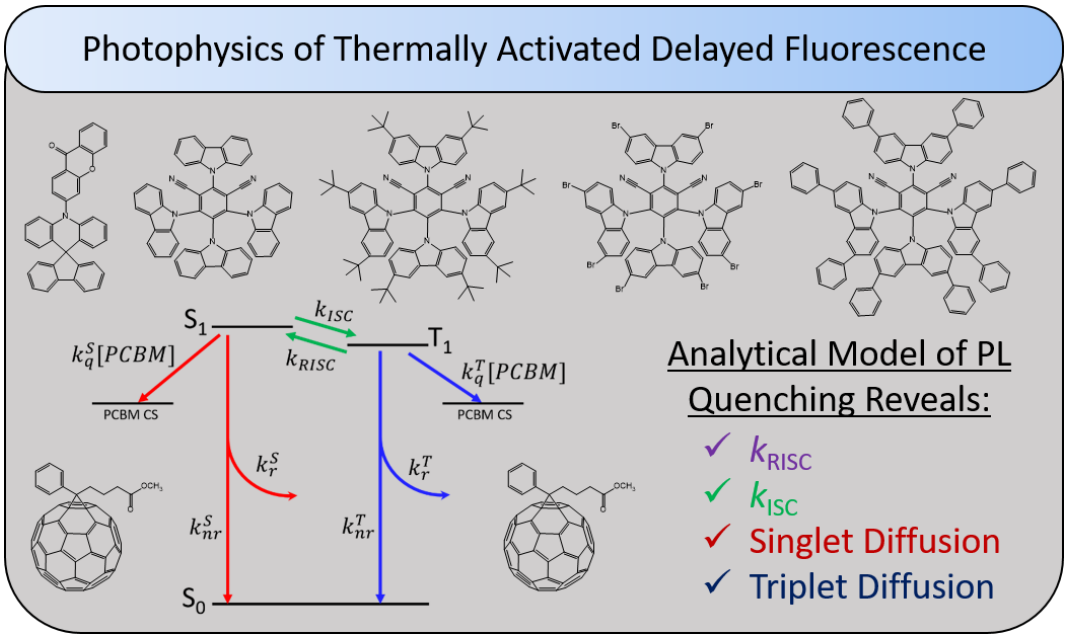

Figure 3.1: Summary of this chapter's contents.

I would like to especially thank Alexander Moreland for his help in synthesizing 4CzIPN-Br. Without his guidance, that synthesis would have been excruciatingly difficult. I managed to synthesize that molecule over a winter break when the Chemistry building was nearly empty except for Alex and I. It was a challenging and lonely winter break, but well worth the struggle. Alex was excellent company to have in lab, besides being an amazing chemist. On the day my reaction was successful, I had been in lab standing on my feet for a continuous 26 hours (besides the occassional break for food). I would also like to thank Dr. Alexander Mikhailovsky for his help with TCSPC, and for offering me valuable scientific insight throughout my PhD. He was an immense resource of knowledge and practical lab advice for the duration of my PhD. Of course, I am indebted to Chihaya Adachi, from whose lab I received several materials to study. I was also fortunate to meet him at a conference in Hong Kong, where we chatted at length about my research. His humility was notable, and his curiosity tangible.

3.1 Background

In organic light-emitting diodes (OLEDs), due to the spin statistics of injected charges, roughly 75% of all molecular excitations in the emissive layer have triplet character with the remaining 25% being singlet. Thus, in order to achieve the ultimate device efficiency, emitter molecules must be able to transform both singlet excitons and triplet excitons into emitted photons. In 2009, OLEDs based on a new class of materials were demonstrated to be capable of efficiently harvesting triplet excitons via reverse intersystem crossing (RISC), which is enabled in molecules with small singlet-triplet splitting energy (ΔE_{ST}).[10] The photoemission observed when a triplet exciton upconverts into a singlet exciton and then emits from the singlet state is known as thermally activated delayed fluorescence (TADF). Whereas commercially available OLEDs which currently rely on phosphorescence (PhOLEDs) require expensive heavy metals with a limited global supply, OLEDs based on TADF (TADF-OLEDs) are amenable to facile, scalable, and inexpensive synthetic routes.[11, 12, 13] Already some TADF-OLEDs have been shown to have an external quantum efficiency of over 20%, which is comparable to the best PhOLEDs and implies an internal quantum efficiency (IQE) of nearly 100%.[14, 15]

The efficiency with which triplet excitons are upconverted into radiative singlet excitons is dictated primarily by the rate of RISC in a material, and, therefore, this property is a critical factor in how well a material will perform in the emissive layer of an OLED. From a basic level of understanding one would expect that the magnitude of the energy barrier, ΔE_{ST}, that must be overcome for RISC to occur will strongly influence the rate of RISC itself. Thus, synthetic efforts have been primarily concerned with minimizing ΔE_{ST}, which is typically achieved through the spatial separation of a molecule's HOMO and LUMO, for example, by employing a twisted donor-acceptor molecular architecture. Through this spatial separation electron correlation effects are greatly reduced, which in

turn decreases the electron exchange integral - the primary factor that determines the energy difference of different spin states. For example, in Figure 3.2, one can plainly see that the LUMO wavefunction of 4CzIPN (a frequently-studied TADF material) is localized on the dicyanobenzene core, whereas the HOMO wavefunction is localized on the peripheral carbazole moieties. Interestingly, TADF has been observed in some materials with $\Delta E_{ST} \approx 0.2$ eV (nearly an order of magnitude above thermal energy at room temperature) while in other examples different molecules with the same ΔE_{ST} do not show TADF. Furthermore, TADF has been observed in molecules that do not have a donor-acceptor twisted architecture nor even significant spatial separation of the HOMO and LUMO orbitals (e.g. C_70, protoporphyrin IX, gold nanoparticles, erythrosin B, eosin Y, and fluorescein).[16, 17, 18, 19] Clearly, ΔE_{ST} is not the only factor that determines the relative magnitude of RISC. A better mechanistic understanding of RISC will, therefore, contribute to our fundamental understanding of TADF as well as elucidate strategies for maximizing the efficiency of TADF-OLEDs.

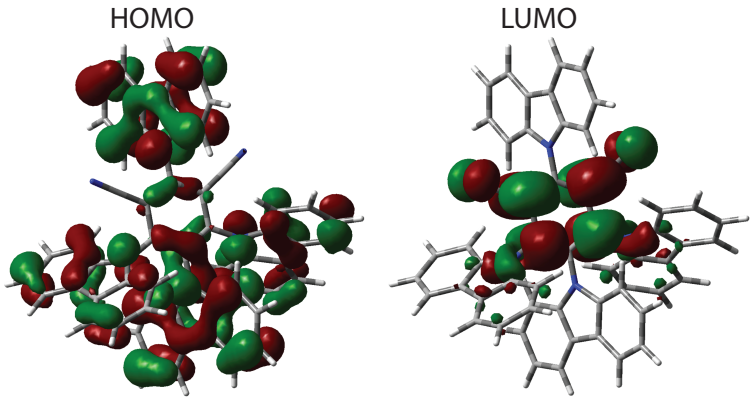

Figure 3.2: HOMO and LUMO wavefunctions of 4CzIPN calculated by DFT (*in vacuo*). The B3LYP functional and 6-31G(d,p) basis set were used.

Although there has been a significant theoretical and computational effort addressing the mechanistic aspects of RISC, the experimental determination of RISC has not been thoroughly revisited since the pioneering work of Berberan-Santos and co-workers.[20,

21, 22, 23] The Berberan-Santos (B.-S.) method, which is the most frequently drawn upon model in the TADF literature, relies on two key assumptions: (i) that the rate of intersystem crossing (k_{ISC}) is significantly larger than the rate of RISC (k_{RISC}) and (ii) that the material of interest exhibits 'strong' delayed fluorescence. However, not all TADF materials meet these criteria. Furthermore, this method depends heavily on the accurate determination of k_{ISC}, which is not trivial. One of the commonly used methods to determine k_{ISC}, which involves triplet exciton quenching via oxygen, depends on criterion (ii), mentioned above.[24] Another commonly used method is predicated on the assumption that non-radiative decay from the singlet state is negligible, which is certainly not the case for all TADF materials, as will be shown in this work.[25, 3] Although this condition is commonly satisfied at cryogenic temperatures, the subsequent value of k_{ISC} that is determined at these low temperatures will only apply to room temperature conditions if k_{ISC} and the rate of radiative decay from the singlet state are independent of temperature, which is found not to be true at least for the series of compounds investigated herein.

In light of all of these considerations, a more robust and widely applicable method of determining k_{RISC} in TADF materials is highly desirable. In this work, I develop an analytical model that describes the time-dependent photoluminescence (PL) decay of TADF materials in the presence of an exciton quencher, i.e. [6,6]-phenyl C_{61} butyric acid methyl ester (PCBM). From just time-resolved data my analytical model is able to accurately determine not only the rate of RISC in TADF materials, but also the rate of ISC, ΔE_{ST} and the diffusivity of both singlet and triplet excitons. With this new analytical approach (combined with complementary quantum-chemical calculations performed by collaborators), I have managed to unravel the complex photophysical properties of 5 TADF molecules in pristine films and in solution.

3.2 Experimental Methods and Materials

Pristine films of the TADF materials were produced by dissolving the material in chloroform (approximately 10 mg/mL) and spin-casting onto a clean glass substrate. In order to produce blend films with a specific concentration of PCBM, small quantities of PCBM dissolved in chloroform (1 mg/mL) were added to a solution of the TADF material (10 mg/mL), also in chloroform, in the desired ratio and then spin-casted onto a clean glass substrate. All films prepared were approximately 100 nm thick as determined by a profilometer (Ambios) and X-Ray Reflectivity (Rigaku Smarlab). Samples were prepared in an inert nitrogen atmosphere and promptly encapsulated using epoxy and another glass substrate to avoid exposure to oxygen during subsequent optical measurements. Temperature dependent measurements were taken by mounting samples in a closed-cycle nitrogen cryostat, pumping to vacuum (approximately 10^{-5} Torr), and modulating the temperature with a LakeShore autotuning temperature controller (model 321). For our solution-phase studies all samples were prepared in an inert glovebox environment and transferred to air-tight quartz cuvettes before being removed for optical measurements, thus excluding oxygen entirely.

Photoluminescence (PL) decay measurements were carried out using a Time-Correlated Single Photon Counting (TCSPC) technique. Samples were excited with a Ti:Sapphire laser (Coherent Mira 900) that has an approximately 200 fs pulse width. An excitation wavelength of 400 nm was obtained by using a commercial optical harmonic generator (Inrad) that doubled the fundamental frequency of the Ti:Sapphire laser. The repetition rate of the laser was reduced by a home-made acousto-optical pulse picker in order to prevent saturation of the chromophore. The detector used was a single photon avalanche diode manufactured by Micro Photon Devices. The detection wavelength was determined by the wavelength of maximum emission intensity. The PL decay was found to not change

significantly at different detection wavelengths. For all measurements, the intensity of the laser was attenuated such that each pulse produced fewer than 3×10^{11} excitons cm^{-2} (corresponding to an energy density of 500 pj cm^{-2}). Steady-state PL spectra were obtained by using an Acton Research SPC-500 monochromator and a charge-coupled device camera (Princeton Instruments PIXIS: 400). For the steady-state temperature-dependent photoluminescence measurements a 400 nm continuous wave diode laser with constant power output was employed.

Density Functional Theory calculations were performed by Dr. Yoann Olivier and Prof. David Beljonne at the University of Mons, Belgium. All of the ground state optimization has been carried out at the DFT level with Gaussian 09 using the PBE0 functional and the 6-31G(d,p) basis considering toluene as solvent (ϵ=2.3741) within the integral equation formalism model polarizable continuum model (IEFPCM).[26] Excited state calculations have been performed at Time-Dependent DFT (TD-DFT) within the Tamm-Dancoff approximation (TDA) using the same functional, basis set and solvent model as for ground state geometry optimization.[27] The Φ_S values have been calculated using the NANCY_EX software based on the hole and electron densities as computed in the attachment/detachment formalism.[21, 28] The spin-orbit coupling calculations have been performed using the PBE0 functional and the Double Zeta Polarized basis set (DZP) within the scalar approximation to Zero Order Regular Approximation (ZORA) to the Full Breit-Dirac relativistic equation as implemented in ADF 2016.101.[29, 30, 31, 32, 33] Please refer to the relevant publication to view the computed excited state electon and hole wavefunctions (they are in the SI).

The following TADF materials were studied in this work: 3-(10*H*-spiro[acridine-9,9'-fluoren]-10-yl)-9*H*-xanthen-9-one (FSA-XT), 2,4,5,6-tetrakis(carbazol-9-yl)isophthalonitrile (4CzIPN), 2,4,5,6-tetrakis(3,6-di-tert-butylcarbazol-9-yl)isophthalonitrile (4CzIPN-tBu), 2,4,5,6-tetrakis(3,6-dibromocarbazol-9-yl)isophthalonitrile (4CzIPN-Br), and 2,4,5,6-tetrakis(3,6-

diphenylcarbazol-9-yl)isophthalonitrile (4CzIPN-ph). See Figure 3.3 for chemical structures. They were kindly provided courtesy of the lab of Prof. Chihaya Adachi (except for 4CzIPN-Br, which I synthesized myself, to great personal satisfaction). [6,6]-Phenyl C_{61} butyric acid methyl ester (PCBM) was purchased from Solenne in 99.9% purity and used as received. Pyrene (which was also used as an exciton quencher) was purchased from Sigma-Aldrich in 98% purity and used as received.

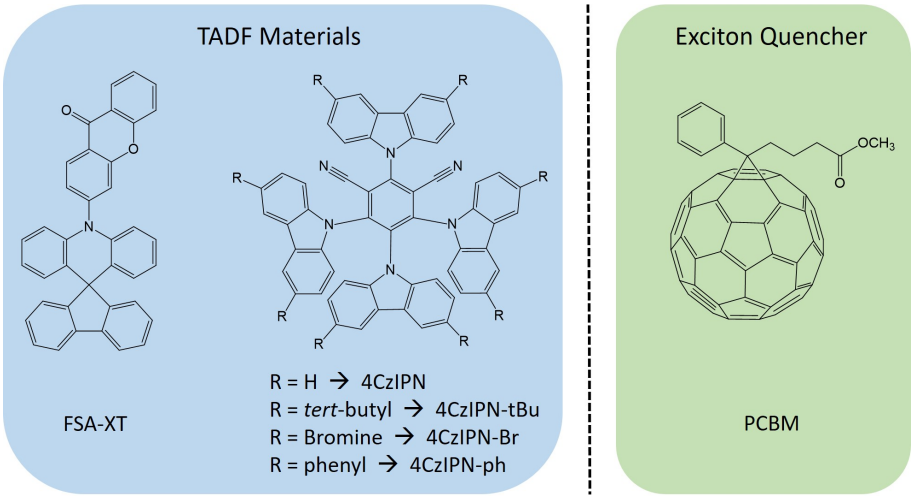

Figure 3.3: Chemical structure and names of the TADF materials studied herein and the exciton quencher, PCBM.

The molar absorptivity and photoluminescence of thin films of these materials are shown in Figure 3.4. The molar absorptivity(ϵ) of thin films was calculated according to:

$$\epsilon = \frac{A \times ln(10)}{d \times c} \tag{3.1}$$

where A is the absorption, d is the fim thickness, and c is the concentration in molarity. The concentration was determined by:

$$c = \frac{\rho}{M_W} \tag{3.2}$$

where ρ is the density of the film (determined by X-Ray Reflectivity) and M_W is the

molecular weight of the material. Conveniently, ρ and M_W also allow one to determine the Wigner-Seitz radius, r, for each material:

$$r = \frac{1}{\sqrt[3]{\frac{4\pi N}{3V}}} \tag{3.3}$$

where N/V is the molecular density of the material. The molecular density was calculated by:

$$\frac{N}{V} = \frac{\rho N_A}{M_W} \tag{3.4}$$

where N_A is Avogadro's number.

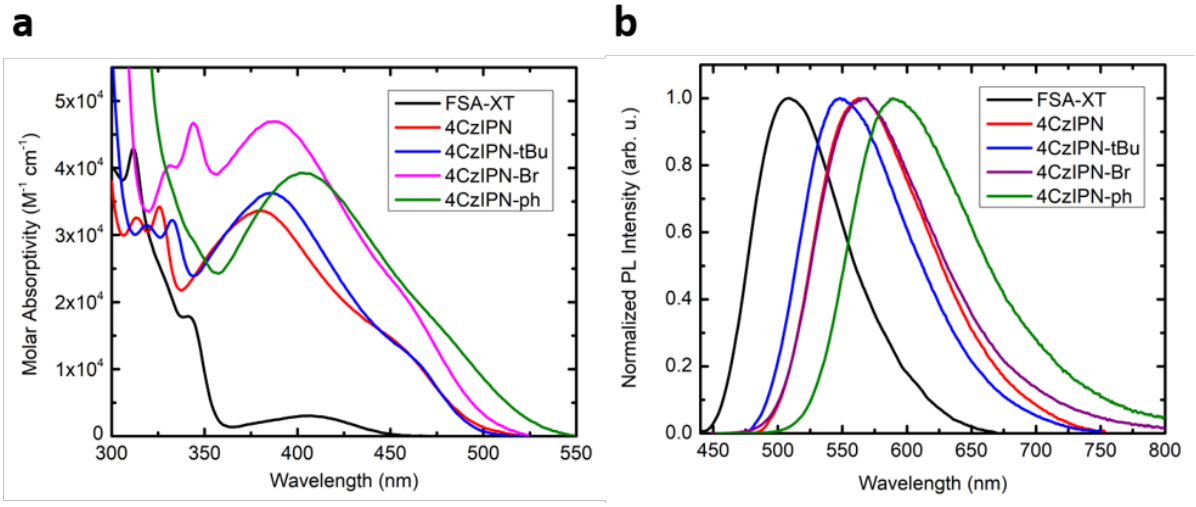

Figure 3.4: Molar absorptivity (a) and photoluminescence (b) of pristine thin films of the TADF materials.

The 4CzIPN-related molecules are characterized by moderate molar absorptivities in the 400 nm region, which is attributed to a donor-acceptor (carbazole-dicyanobenzene) $\pi \rightarrow \pi^*$ transition. The extremely weak molar absorptivity around 400nm for FSA-XT is a direct consequence of the high degree of charge-transfer character in this optical transition. Density Functional Theory (DFT) calculations suggest this optical transition is the result of a donor-acceptor (acridine-xanthenone) $\pi \rightarrow \pi^*$ transition with very little

wavefunction overlap between the electron and hole. The overlaps between electron and hole densities computed in the attachment/detachment formalism, Φ_S, are listed in Table 1.[28] The calculated equilibrium geometries (gas-phase) of the materials corroborate these differences in molar absorptivity: the donor-acceptor dihedral angle in FSA-XT is approximately 90°, whereas for the 4CzIPN-related molecules it resides closer to 80°.

3.3 Analytical Model for Determining k_{ISC} and k_{RISC}

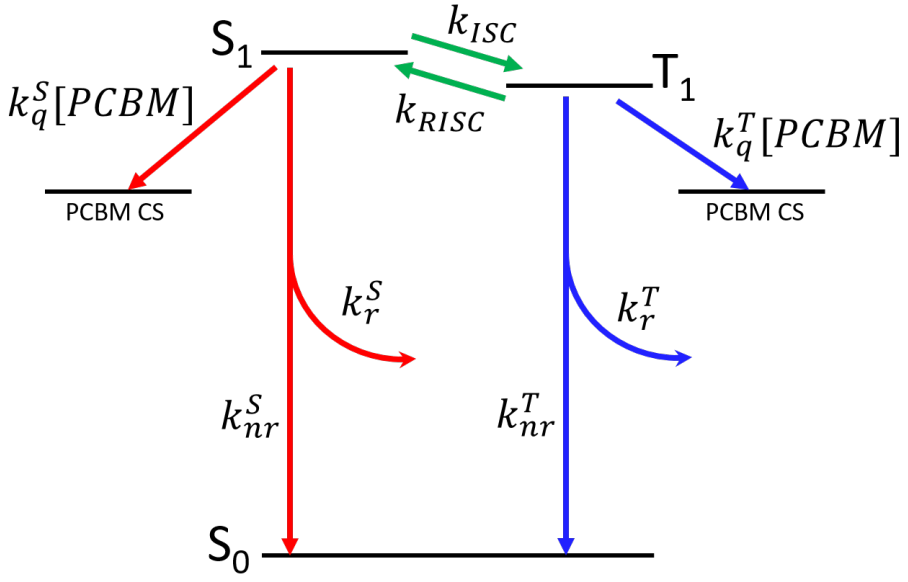

Figure 3.5: Simplified Jablonski diagram showing the relevant excited-state transitions for a TADF material in the presence of an exciton quencher, i.e. PCBM.

All of the possible excited-state transitions that can occur in a thin-film of a TADF material while in the presence of a small amount of exciton quencher (PCBM) are shown in the simplified energy diagram of Figure 3.5. S_1 and T_1 represent the lowest energy singlet and triplet excited states, respectively. The Charge Separated (CS) state to PCBM is included to reflect the possibility of singlet and triplet exciton quenching via photo-induced electron transfer, which is expected to be favorable due to PCBM's strong elec-

tron affinity. k_q^S and k_q^T are the bimolecular quenching constants for singlets and triplets, respectively, and are related to diffusion coefficients via the Smoluchowski equation.[4] k_{nr}^S and k_{nr}^T are the non-radiative rates of decay for singlets and triplets, respectively. k_r^S and k_r^T are the radiative rates of decay for singlets and triplets, respectively. k_{ISC} and k_{RISC} are the rates of intersystem crossing and reverse intersystem crossing, respectively. As shown in Figure 3.6, the incorporation of small amounts of the exciton quencher, PCBM, into thin films results in a faster rate of decay for both the prompt (k_p) and delayed (k_d) components of the fluorescence decay of 4CzIPN (and similarly for the other TADF materials). In this section, a novel analytical model is developed which describes k_p and k_d as a function of exciton quencher. As will be shown, numerical values obtained from fitting the PL decays of pristine (no quencher present) and blend (small amount of quencher) films can be fit to this model, resulting in the determination of k_{ISC}.

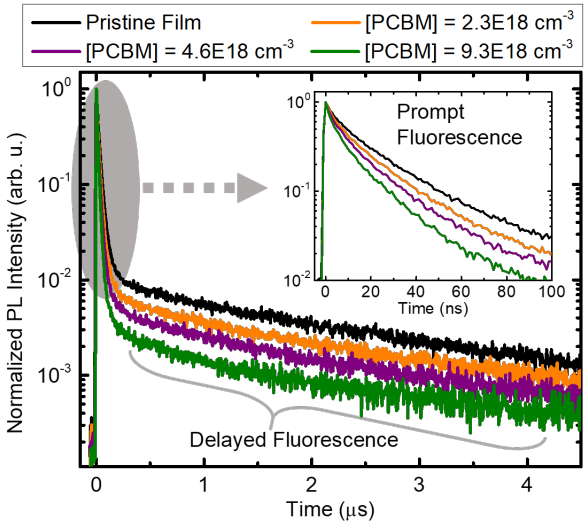

Figure 3.6: PL decay of 4CzIPN in the presence of various amounts of PCBM.

The sum of the rates for decay pathways that originate in the singlet state is given by:

$$X = k_{nr}^S + k_r^S + k_{ISC} + k_q^S[PCBM] \tag{3.5}$$

where k_{nr}^S is the rate of non-radiative decay via internal conversion, k_r^S is the radiative rate of decay (fluorescence), k_{ISC} is the rate of intersystem crossing, and k_q^S is the bimolecular quenching constant for singlet excitons. Likewise, the sum of the rates for the decay of the triplet state is given by:

$$Y = k_{nr}^T + k_r^T + k_{RISC} + k_q^T[PCBM] \tag{3.6}$$

where k_{nr}^T is the rate of non-radiative decay via internal conversion, k_r^T is the radiative rate of decay (phosphorescence), k_{RISC} is the rate of reverse intersystem crossing, and k_q^T is the bimolecular quenching constant for triplet excitons. The bimolecular quenching constants, k_q^S and k_q^T, are determined by the Smoluchowski equation:

$$k_q^{S,T} = 4 \times \pi \times (R_e + R_q) \times D_{singlet,triplet} \tag{3.7}$$

where R_e is the radius of the exciton (which we take to be 0.5 nm), R_q is the radius of the exciton-quenching species (known to be 0.5 nm for PCBM and estimated to be 0.2 nm for pyrene), and $D_{singlet,triplet}$ is the diffusion coefficient of singlet or triplet excitons, respectively.[4, 34] The differential rate laws for the decay of singlets (S_1) and triplets (T_1) are given by:

$$\frac{-d[S_1]}{dt} = X[S_1] - k_{RISC}[T_1] \tag{3.8}$$

$$\frac{-d[T_1]}{dt} = Y[T_1] - k_{ISC}[S_1] \tag{3.9}$$

From the initial boundary condition that only singlets are directly excited, i.e. $[S_1] = [S_1]_0$ and $[T_1] = 0$ when $t = 0$, we find a solution for the decay of singlets given by:

$$[S_1] = A_p exp(-k_p t) + A_d exp(-k_d t) \tag{3.10}$$

where A_p and A_d are the relative amplitudes of the prompt and delayed decay components, respectively, k_p is the rate of prompt fluorescence, and k_d is the rate of delayed fluorescence. Thus, a simple biexponential fit to a TADF material's PL decay will determine the values for A_p, A_d, k_p, and k_d. Figure 3.7 shows the pristine PL decays for the 5 TADF materials, which are obviously biexponential.

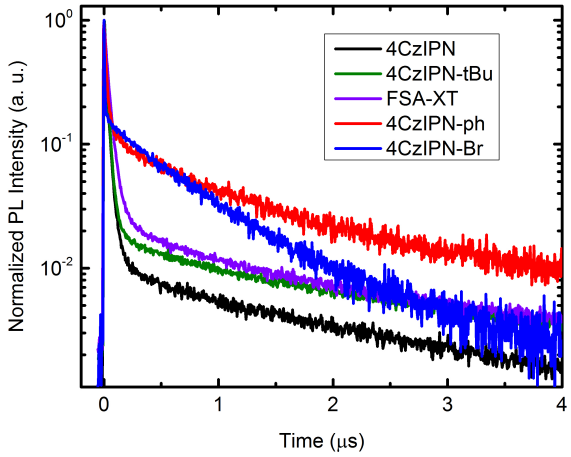

Figure 3.7: PL decay of pristine films measured by TCSPC.

A solution for the population of triplet excitons is given by:

$$[T_1] = \frac{[S_1]_0 k_{ISC}}{k_p - k_d}\Big(exp(-k_d t) - exp(-k_p t)\Big) \tag{3.11}$$

In the above solutions, the rates of prompt (k_p) and delayed (k_d) fluorescence are given specifically by:

$$k_p = \frac{1}{2}\left\{(X+Y) + \sqrt{(Y-X)^2 + 4k_{ISC}k_{RISC}}\right\} \tag{3.12}$$

$$k_d = \frac{1}{2}\left\{(X+Y) - \sqrt{(Y-X)^2 + 4k_{ISC}k_{RISC}}\right\} \tag{3.13}$$

The bimolecular quenching constant for singlet excitons can be determined from our

analytical model by first considering the very different lifetimes of singlets and triplets. At short timescales (i.e. tens of nanoseconds) the dominating term in Equation 3.8 is $X[S_1]$, because $k_{RISC} \ll X$ and $[T_1] < [S_1]$. The former assumption is clearly satisfied for any TADF material given that k_{RISC} is a classically forbidden transition (resulting in comparatively small rates), whereas X is dominated by classically allowed transitions. Thus, the differential rate law describing singlet decay at short timescales is given by:

$$\frac{-d[S_1]}{dt} \cong X[S_1] \tag{3.14}$$

from which it follows that the integrated rate law is:

$$[S_1] = A_p exp(-k_p t) \tag{3.15}$$

where $k_p = X$. We can now rewrite Equation 3.12 as:

$$k_p = k_{p0} + k_q^S[PCBM] = X \tag{3.16}$$

where k_{p0} is the rate of prompt fluorescence in the absence of PCBM. As shown in Figure 3.8, values of k_q^S are determined from the slope of a linear fit to the rate of prompt fluorescence as a function of PCBM concentration, from which $D_{singlet}$ is calculated via Equation 3.7.

Next, we address the delayed component of fluorescence described by our analytical model. Considering that TADF materials in general have a triplet lifetime that is only limited by k_{RISC}, we take k_{nr}^T and k_r^T in Equation 3.6 to be negligible, resulting in $Y \cong k_{RISC}$ (in the absence of PCBM).[25, 24, 35] This is further justified by (i) the near-unity internal quantum efficiency of TADF-OLEDs using 4CzIPN [14] and FSA-XT [7][36], (ii) the lack of observable phosphorescence from room temperature to below

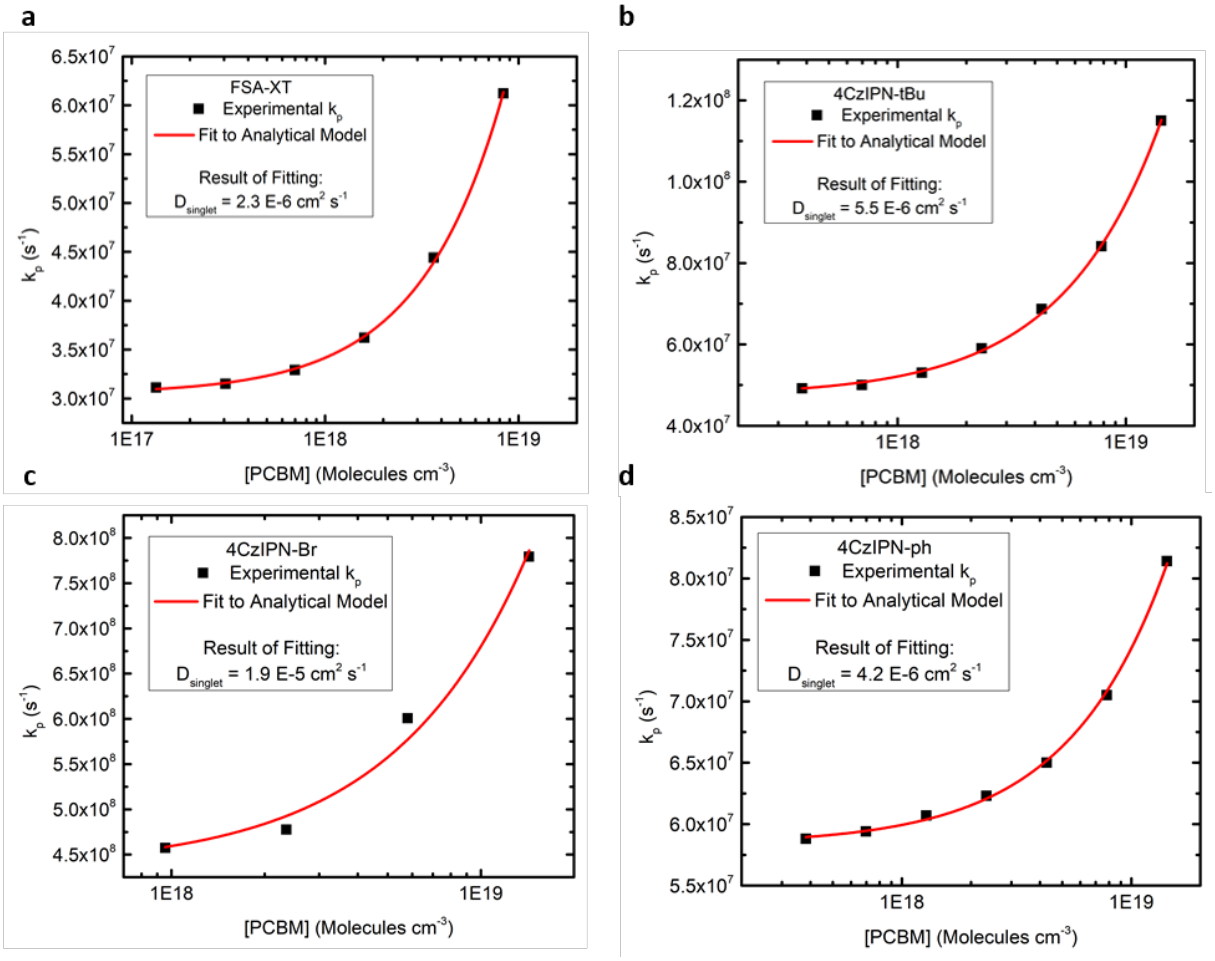

Figure 3.8: Fits of the rate of prompt fluorescence, k_p, to the analytical model resulting in the singlet exciton diffusion coefficient. (a) FSA-XT, (b) 4CzIPN-tBu, (c) 4CzIPN-Br, and (d) 4CzIPN-ph.

150K (Figure 3.9), and (iii) the relatively large energy gap between T_1 and S_0 (which is expected to suppress non-radiative decay according to the energy gap law).

Upon substitution of $k_{p0} = X$ and $k_{RISC} = Y$ into Equation 3.13 we obtain:

$$k_{d0} = \frac{1}{2}\left\{(k_{p0} + k_{RISC}) - \sqrt{(k_{RISC} - k_{p0})^2 + 4k_{ISC}k_{RISC}}\right\} \tag{3.17}$$

where k_{d0} and k_{p0} are the rates of delayed and prompt fluorescence, respectively, in the

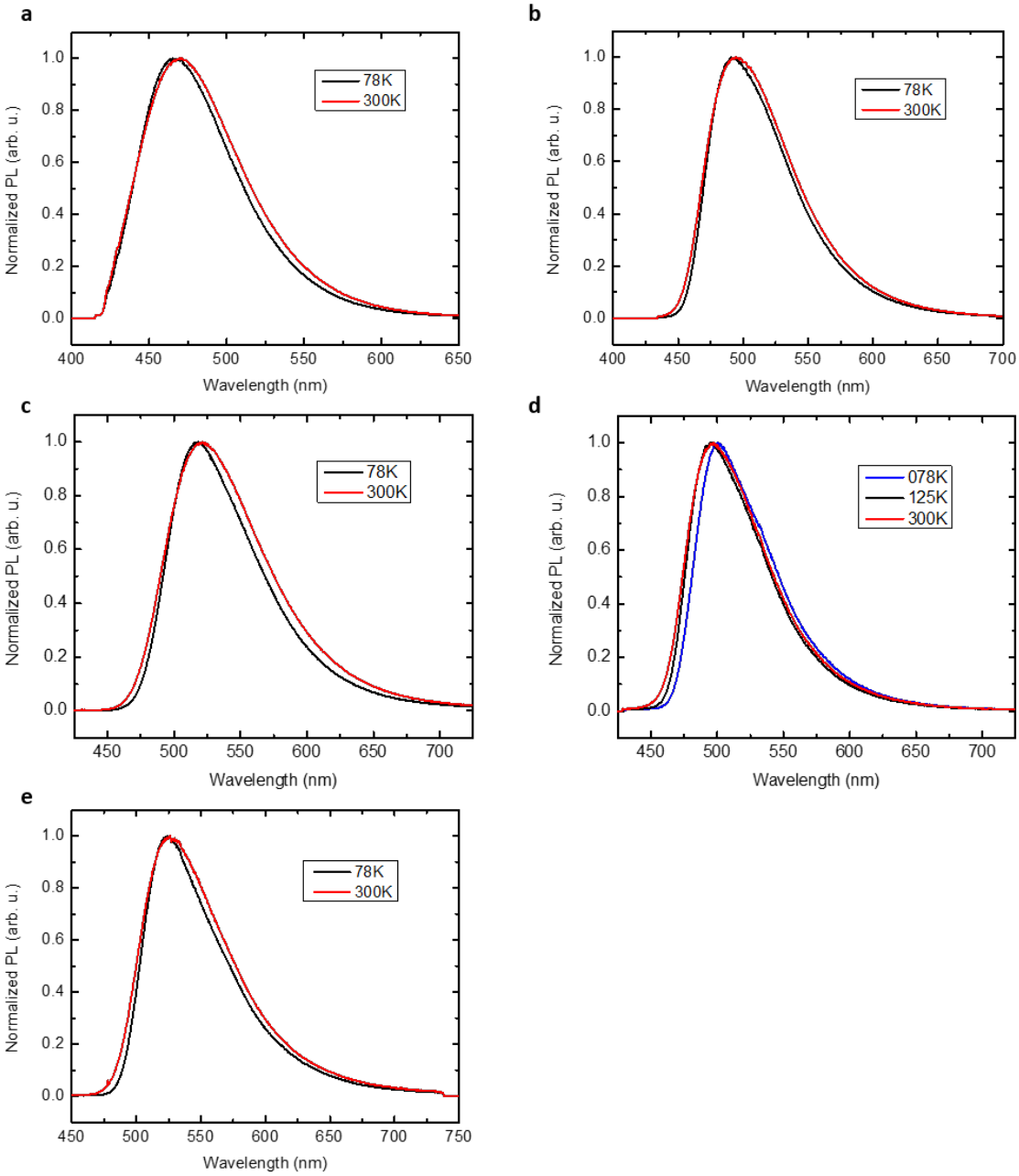

Figure 3.9: Temperature dependent steady-state photoluminescence spectra for films that are < 2 mol % in polystyrene in order to confine excitons (i.e. eliminate the possibility of exciton diffusion) for (a) FSA-XT, (b) 4CzIPN, (c) 4CzIPN-tBu, (d) 4CzIPN-Br, and (e) 4CzIPN-ph. The lack of a discernable redshift at lower temperatures indicates a negligible contribution from phosphorescence. It seems as though 4CzIPN-Br begins exhibiting some phosphorescence below 125K.

absence of PCBM. Upon solving for k_{RISC} we obtain:

$$k_{RISC} = \frac{k_{d0}^2 - k_{p0}k_{d0}}{k_{ISC} + k_{d0} - k_{p0}} \tag{3.18}$$

In order to determine the value of k_{ISC} for each material, the effect of quenching by PCBM on the rate of delayed fluorescence must be considered. Starting from Equation 3.13, we use the value of X given by Equation 3.16 and the value of k_{RISC} given by Equation 3.18, resulting in the rate of delayed fluorescence, k_d, as a function of PCBM concentration where the only unknown variables are k_{ISC} and k_q^T:

$$k_d = \frac{1}{2}\Big(k_{p0} + k_q^S[PCBM] + \frac{k_{d0}^2 - k_{p0}k_{d0}}{k_{ISC} + k_{d0} - k_{p0}} + k_q^T[PCBM]\Big)$$
$$-\frac{1}{2}\sqrt{\left[\frac{k_{d0}^2 - k_{p0}k_{d0}}{k_{ISC} + k_{d0} - k_{p0}} + k_q^T[PCBM] - k_{p0} - k_q^S[PCBM]\right]^2 + 4k_{ISC}\frac{k_{d0}^2 - k_{p0}k_{d0}}{k_{ISC} + k_{d0} - k_{p0}}} \tag{3.19}$$

The results of fitting Equation 3.19 to the PL decay data is shown in Figure 3.10.

When pyrene was used as an exciton quencher, instead of PCBM, nearly identical values were obtained (Figure 3.11), demonstrating the versatility of this analytical model. The S_1 and T_1 energy levels for 4CzIPN, PCBM, and pyrene are shown in Figure 3.12. These energy levels indicate the feasibility of Förster and Dexter energy transfer, which are viable quenching mechanisms of the PL of 4CzIPN (except for Förster energy transfer from 4CzIPN S_1 to pyrene S_1). The energy levels only approximate the feasibility of photo-induced electron transfer from 4CzIPN to the quenchers - a more accurate estimation would require knowing the IPs and EAs of the molecules.

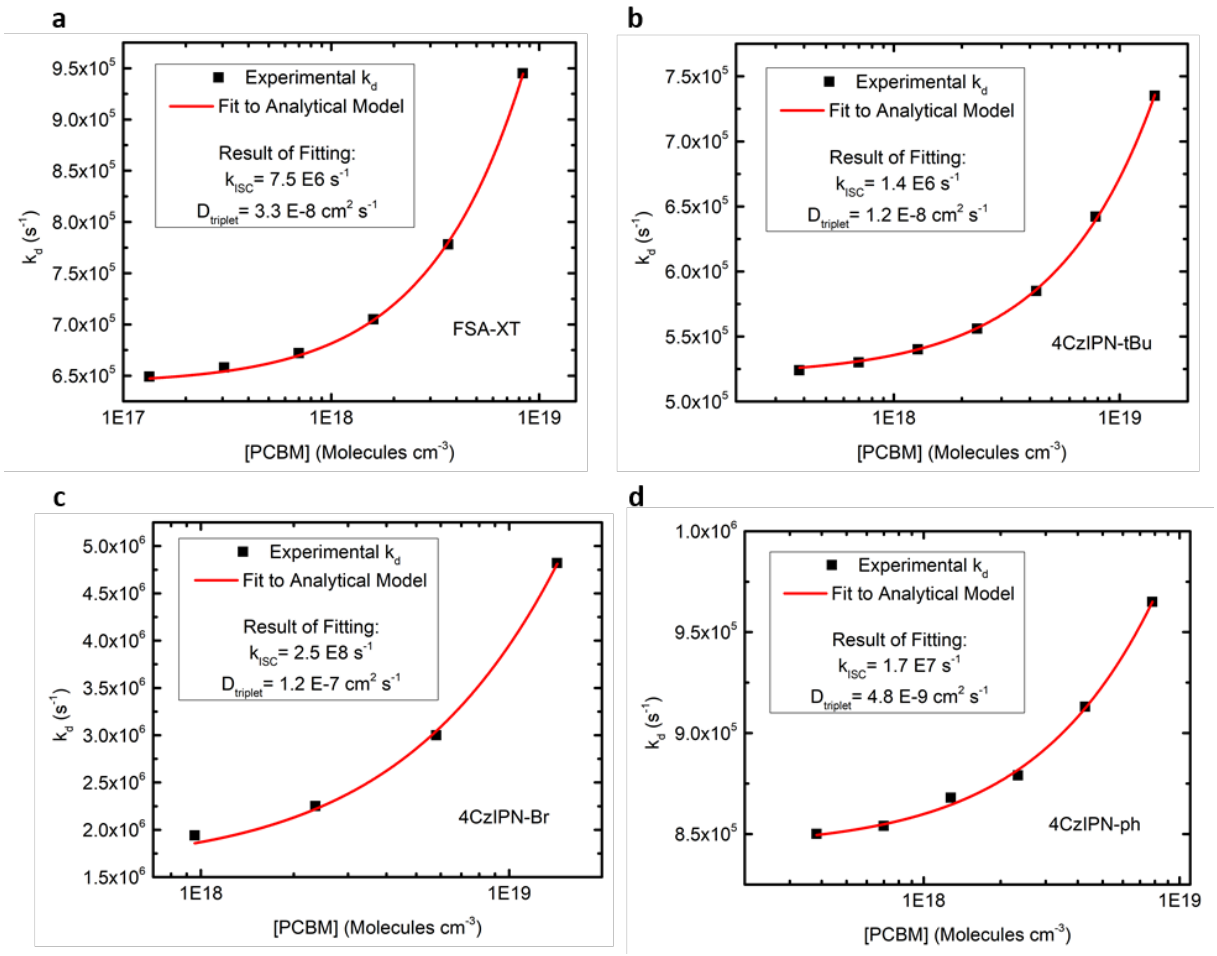

Figure 3.10: Fits of the rate of delayed fluorescence, k_d, to the analytical model resulting in the rate of ISC and the triplet exciton diffusion coefficient. (a) FSA-XT, (b) 4CzIPN-tBu, (c) 4CzIPN-Br, and (d) 4CzIPN-ph.

3.4 Other Methods in the Literature for Determining k_{ISC} and k_{RISC}

In this section I introduce some other relevant experimental methods used for characterizing certain properties of TADF materials. Berberan-Santos and coworkers developed the theory behind many of the equations often used in the relevant literature [23]; however, below, I show ways in which their method for determining k_{RISC} is significantly flawed. In addition I outline the theory behind the experimental determination of some

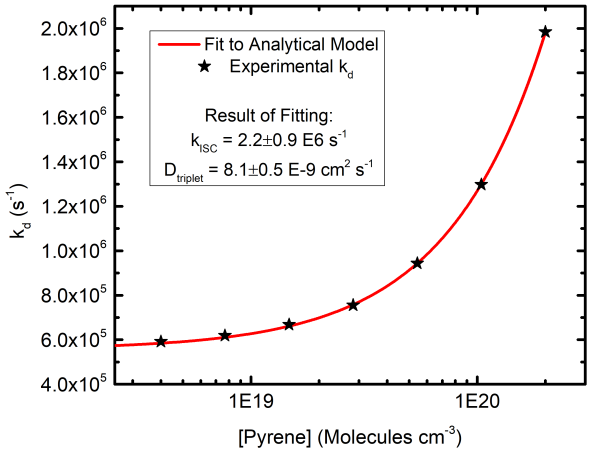

Figure 3.11: Results of the analytical model for 4CzIPN in the solid-state at room temperature when pyrene is used as the exciton-quenching species.

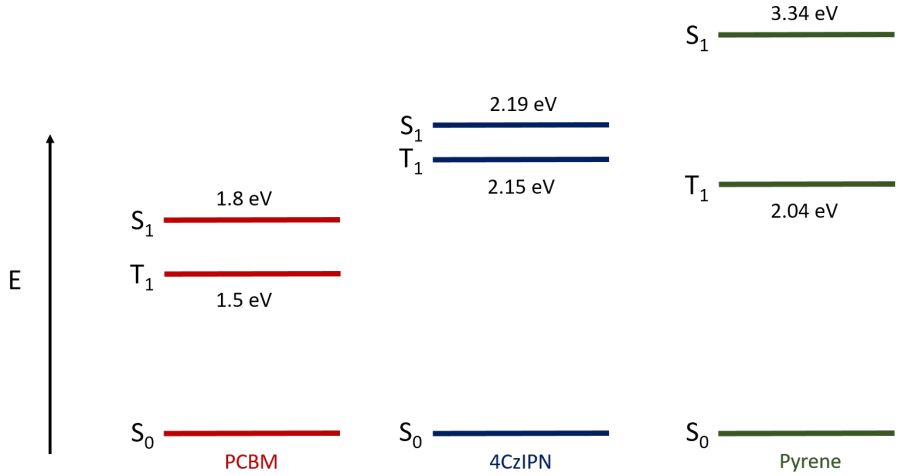

Figure 3.12: Lowest energy excited states for 4CzIPN and the two quenchers used in this study, PCBM and pyrene. Horizontal lines indicating energy levels are not to scale. The indicated energies are accurate, and the relative positioning of the horizontal lines is accurate.

other relevant parameters (e.g. prompt, delayed quantum yield), which I believe to be significantly accurate and robust methods.

3.4.1 Berberan-Santos (B. S.) Method for determining k_{RISC}

Assuming that $k_{ISC} \gg k_{RISC}$ and that the material in question exhibits strong delayed fluorescence, i.e. $\Phi_d \geq 4 \times \Phi_p$, then the following equation for k_{RISC} should be accurate:

$$k_{RISC}(T) = \frac{k_p(T)k_d(T)}{k_{ISC}} \times \frac{\Phi_d(T)}{\Phi_p(T)} \tag{3.20}$$

where the rate of intersystem crossing is assumed to be temperature independent, Φ_d is the quantum yield of delayed fluorescence, and Φ_d is the quantum yield of prompt fluorescence. The total photoluminescence quantum yield, Φ, of each material at room temperature is easily obtained through the use of an integrating sphere according to a previously developed technique.[37] Φ is given by the sum of the prompt and delayed quantum yields:

$$\Phi = \Phi_p + \Phi_d \tag{3.21}$$

The prompt and delayed quantum yields can be simply understood by looking at the PL decay of a TADF material, as shown in Figure 3.13. The total area underneath the PL decay curve represents the total amount of fluorescence. The area underneath the prompt component of the PL decay is the relative amount of the total fluorescence that decays via the prompt channel, and likewise for the delayed component. The equations below quantify this precisely.

The steady-state PL spectrum was measured (with constant excitation power) at various temperatures and then integrated in order to estimate the temperature dependence of the total quantum yield. The quantum yields of the prompt (Φ_p) and delayed (Φ_d) components were determined from the PL decay of pristine films at various temperatures according to:

$$\Phi_p = \Phi \times \frac{A_p\tau_p}{A_p\tau_p + A_d\tau_d} \tag{3.22}$$

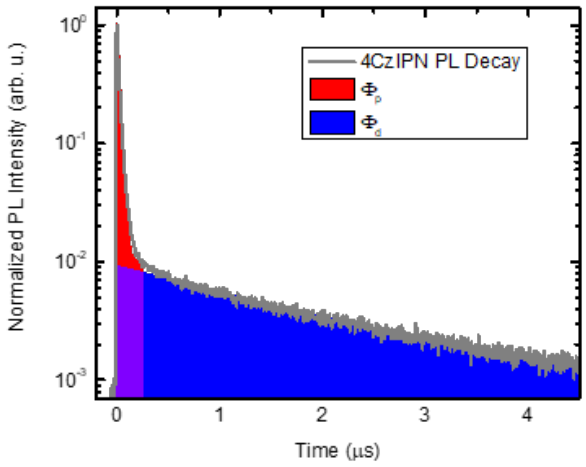

Figure 3.13: Experimental PL decay of 4CzIPN where the regions contributing to prompt and delayed fluorescence quantum yields have been highlighted red and blue, respectively. In this schematic, it is assumed that the total area underneath the PL decay curve is normalized to the experimental value of the total photoluminescence quantum yield.

$$\Phi_d = \Phi \times \frac{A_d \tau_d}{A_p \tau_p + A_d \tau_d} \tag{3.23}$$

where τ_p and τ_d are equivalent to the reciprocal of k_p and k_d, respectively. The average number, $\overline{n}$, of $S_1 \rightarrow T_1 \rightarrow S_1$ cycles can be simply calculated from the ratio of the delayed quantum yield to the prompt quantum yield:

$$\overline{n} = \frac{\Phi_d}{\Phi_p} \tag{3.24}$$

In terms of this spin-cycling parameter, $\overline{n}$, 'strong' delayed fluorescence is observed when $\overline{n} \geq 4$. Finally, ΔE_{ST} is determined by the slope of an Arrhenius plot according to the relationship:

$$k_{RISC}(T) \propto exp\left(\frac{-\Delta E_{ST}}{k_B T}\right) \tag{3.25}$$

where T is the temperature and k_B is the Boltzmann constant.

Although for most molecules k_{ISC} is expected to be significantly larger than k_{RISC},

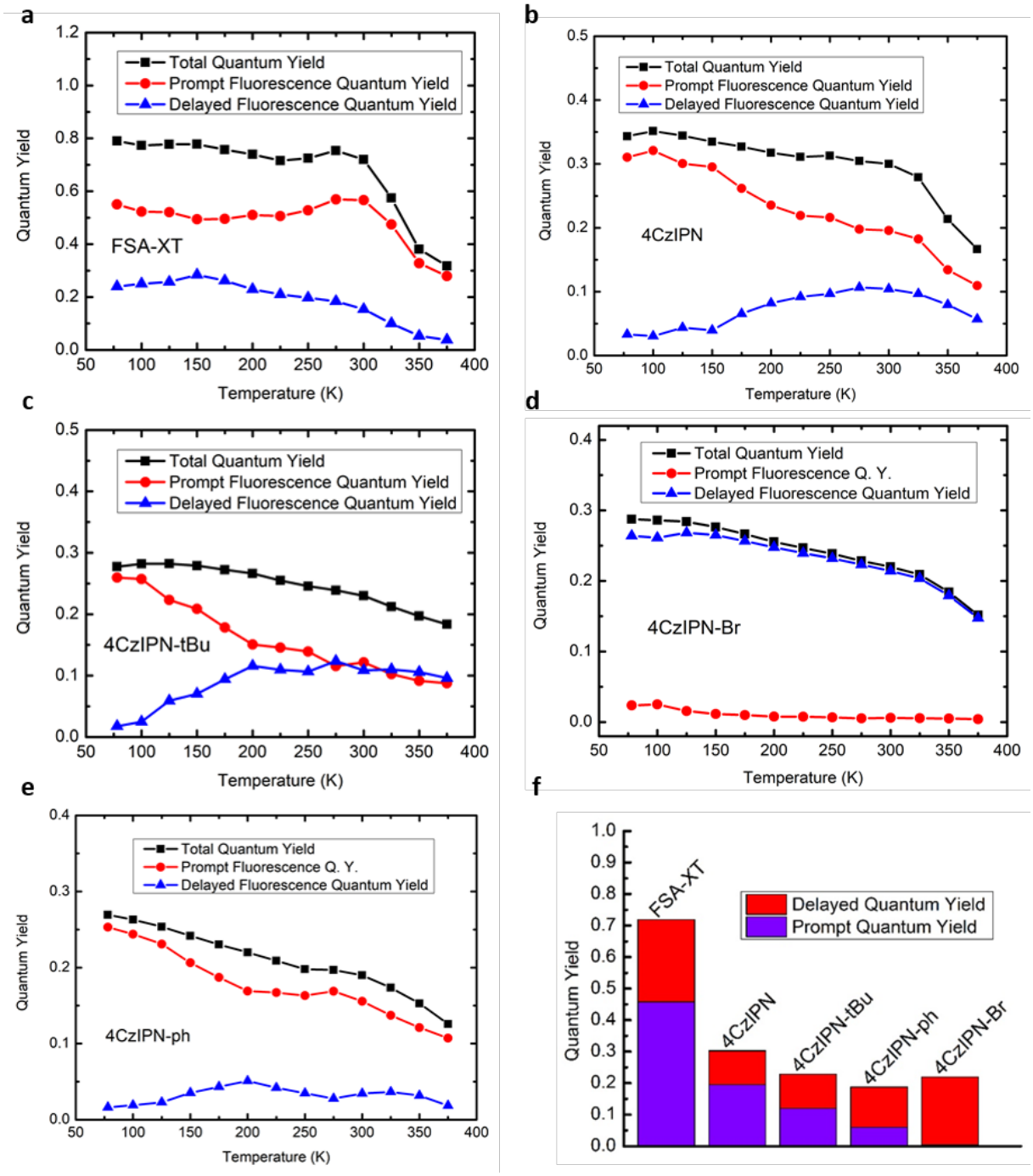

Figure 3.14: Temperature dependence of the solid-state photoluminescence quantum yields for (a) FSA-XT, (b) 4CzIPN, (c) 4CzIPN-tBu, (d) 4CzIPN-Br, and (e) 4CzIP-N-ph. (f) Total, prompt, and delayed PL quantum yields at room temperature.

this does not have to be the case. As shown in my work, these values are within one order of magnitude of each other in the case of 4CzIPN and 4CzIPN-tBu. While plenty of TADF materials have been shown to exhibit strong delayed fluorescence (as defined above), there are other TADF materials, such as 4CzIPN, which do not exhibit strong delayed fluorescence (see Table 3.6 for values of $\overline{n}$) and yet show very good performance in OLEDs. Thus, the performance of a TADF material in an OLED is not determined by whether or not it exhibits strong delayed fluorescence.

Because ISC is assumed to be temperature-independent in the Berberan-Santos method, any real temperature variations of k_{ISC} will result in the inaccurate determination of ΔE_{ST} from the Arrhenius plot. In my work, I find that k_{ISC} is, in fact, mildly temperature-dependent for most of the TADF materials studied. Indeed, in Equation 3.20 k_{ISC} is a variable parameter which necessitates it being accurately measured in the first place if an accurate value of k_{RISC} is desired. Examination of Figure 3.15 exemplifies the necessity of accurately determining k_{ISC}. In the following sections I review common methods for determining k_{ISC} and highlight their shortcomings.

3.4.2 Determination of k_{ISC}

Typically, k_{ISC} is calculated after experimentally determining the quantum efficiency of ISC, Φ_{ISC}, according to $k_{ISC} = k_p \times \Phi_{ISC}$. In the case of materials which exhibit strong delayed fluorescence, Φ_{ISC} can be accurately calculated from either just the fluorescence decay of the material or from steady-state measurements of the PL in the presence, and absence, of oxygen. [24] Again, because the accuracy of these techniques depend on a material exhibiting strong delayed fluorescence, their application is limited.

Another method that is sometimes used to determine Φ_{ISC} relies on first measuring the prompt fluorescence quantum yield via Equation 3.22 and then calculating Φ_{ISC}

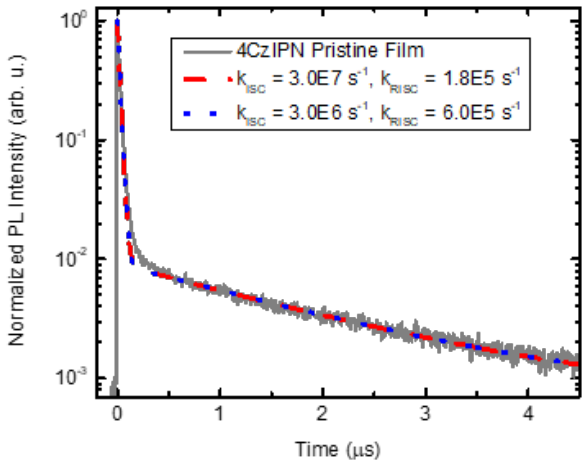

Figure 3.15: Experimental PL decay of 4CzIPN with simulated PL decays (dashed lines) using the specified values of k_{ISC} and k_{RISC}. PL decays were simulated by using the analytical model described in Section 3.3. Values for k_r^S, k_{nr}^S, k_p, k_d, A_p, and A_d were fixed to be those determined experimentally for 4CzIPN, thus only leaving k_{ISC} and k_{RISC} as variable parameters.

according to $\Phi_{ISC} = 1 - \Phi_p$ where it is assumed that $k_{nr}^S \ll k_r^S + k_{ISC}$. [25, 3] According to this assumption, every singlet exciton that does not emit a photon will undergo ISC. This assumption is reasonable for many aromatic molecules at cryogenic temperatures, but if there is any temperature-dependence of k_r^S or k_{ISC} then this approach will be inaccurate. This approach will also be inaccurate if k_{nr}^S is not negligible at cryogenic temperatures. From our temperature-dependent analysis of these rates (Figures 3.24 and 3.25) we find that these criteria are not adequately met for the materials investigated.

3.4.3 Derivation of $\overline{n}$, the extent of spin cycling

This parameter (specifically, Equation 3.24) was originally derived by Berberan-Santos and his colleagues, but I did not find their proof convincing. During the review of my manuscript which contained the TADF work, a referee asked about $\overline{n}$. Confused about the meaning of the parameter itself, he asked for the derivation of Equation 3.24. After struggling to understand the original derivation myself, I got out some pencil and

paper and set out to derive the equation myself. The full derivation is provided below. Some of the definitions used here are slightly different than those used above. Do not use them interchangeably.

First, we define two quantities, the quantum yield of singlet formation from the triplet state, Φ_S, and the quantum yield of triplet formation from the singlet state, Φ_T, as follows:

$$\Phi_S = \frac{k_{RISC}}{k_{RISC} + k_{nr}^T + k_r^T} \tag{3.26}$$

$$\Phi_T = \frac{k_{ISC}}{k_{ISC} + k_{nr}^S + k_r^S} \tag{3.27}$$

Then, we consider how singlet emission, over multiple spin cycles, contributes to the overall fluorescence quantum yield, Φ_F. This can be represented as the following geometric power series:

$$\Phi_F = \Phi_p \left[1 + \Phi_T\Phi_S + (\Phi_T\Phi_S)^2 + \cdots\right] = \frac{\Phi_p}{1 - \Phi_T\Phi_S} \tag{3.28}$$

where Φ_p is the quantum yield of prompt fluorescence. In this equation, the first term corresponds to prompt fluorescence (the zeroth cycle), the second term corresponds to the first cycle of delayed fluorescence, and so on. A geometric probability distribution can be used to describe the probability of fluorescence after n $S_1 \rightarrow T_1 \rightarrow S_1$ cycles (p_n):

$$p_n = (1 - \Phi_T\Phi_S)(\Phi_T\Phi_S)^n \tag{3.29}$$

Then, the average number of spin cycles, $\overline{n}$, is determined by:

$$\begin{aligned}\overline{n} = \sum_{n=0}^{\infty} np_n = \sum_{n=0}^{\infty} n(1 - \Phi_T\Phi_S)(\Phi_T\Phi_S)^n \\ = (1 - \Phi_T\Phi_S)\sum_{n=0}^{\infty} n(\Phi_T\Phi_S)^n = \frac{\Phi_T\Phi_S}{1 - \Phi_T\Phi_S}\end{aligned} \tag{3.30}$$

The above algebra is enabled by the known relation:

$$\sum_{n=0}^{\infty} nx^n = \frac{x}{(1-x)^2} \tag{3.31}$$

Now, let us also consider that the total fluorescence quantum yield is equal to the sum of prompt and delayed fluorescence quantum yields:

$$\Phi_F = \Phi_p + \Phi_d = \frac{\Phi_p}{1 - \Phi_T \Phi_S} \tag{3.32}$$

where Equation 3.28 was used. Solving Equation 3.32 for Φ_d yields:

$$\Phi_d = \frac{\Phi_p}{1 - \Phi_T \Phi_S} - \Phi_p = \Phi_p \left(\frac{1}{1 - \Phi_T \Phi_S} - 1 \right) = \Phi_p \left(\frac{\Phi_T \Phi_S}{1 - \Phi_T \Phi_S} \right) \tag{3.33}$$

This time, the above algebra was enabled by use of the known relation:

$$\frac{1}{1-x} - 1 = \frac{x}{1-x} \tag{3.34}$$

One can see from Equation 3.33 that taking the ratio $\frac{\Phi_d}{\Phi_p}$ will yield the same result as Equation 3.30, thus completing the proof:

$$\frac{\Phi_d}{\Phi_p} = \frac{\Phi_T \Phi_S}{1 - \Phi_T \Phi_S} = \overline{n} \tag{3.35}$$

3.5 Exciton Diffusion

Because singlet and triplet exciton diffusion appear as fitting parameters of the analytical model, I independently evaluated these parameters using a Monte Carlo simulation of exciton diffusion. I was also motivated to study exciton diffusion, because very little

is known about exciton diffusion in TADF materials. To the best of my knowledge, there has been only one other report concerning the measurement of exciton diffusion in a TADF material.[38] For more details on the Monte Carlo simulation of exciton diffusion, please refer to Section 2.2. Simulating singlet exciton diffusion in typical fluorescent molecules (i.e. ones that do not display TADF) is straightforward. It is less apparent how the previously described simulation can be used to calculate both singlet and triplet exciton diffusion. Below, I outline just how this was accomplished. The quenching efficiency (Q) of PCBM (or any other exciton quencher) at a particular concentration, c, can be calculated by:

$$Q(c) = 1 - \frac{\int_0^\infty PL_{blend}(c)dt}{\int_0^\infty PL_{pristine}dt} \tag{3.36}$$

where $PL_{pristine}$ and PL_{blend} represent the exponential decay resulting from a fit of Equation 3.10 to the pristine and blend films, respectively. In order to differentiate between the quenching efficiency of singlets and triplets, the prompt and delayed components of fluorescence were analyzed independently. The quenching efficiency of singlets (Q^S) was calculated by:

$$\begin{aligned} Q^S(c) &= 1 - \frac{\int_0^\infty A_p(c)exp(-k_p(c)t)dt}{\int_0^\infty A_p(pristine)exp(-k_p(pristine)t)dt} \\ &= 1 - \frac{A_p(c)k_p(pristine)}{A_p(pristine)k_p(c)} \\ &= 1 - \frac{k_p(pristine)}{k_p(c)} \end{aligned} \tag{3.37}$$

The final transformation above is a result of normalizing the PL decays, i.e. $A_p(pristine) = A_p(c) = 1.0$. When considering the quenching efficiency of triplets, however, we can expect that the quenching of the prompt fluorescence will result in the reduction of the relative amplitude of the delayed component, A_d, due to the change in the relative concentration of singlets and triplets (c.f. Figure 3.6). In other words, $A_d(pristine) \neq A_d(c)$.

Regardless, we chose to calculate the quenching efficiency of triplet excitons (Q^T) by only considering the relative change in the rate of delayed fluorescence (which is effectively normalizing the delayed component of fluorescence):

$$\begin{aligned} Q^T(c) &= 1 - \frac{\int_0^\infty A_d(c) exp(-k_d(c)t)dt}{\int_0^\infty A_d(pristine) exp(-k_d(pristine)t)dt} \\ &= 1 - \frac{A_d(c)k_d(pristine)}{A_d(pristine)k_d(c)} \\ &= 1 - \frac{k_d(pristine)}{k_d(c)} \end{aligned} \tag{3.38}$$

From the calculated quenching efficiencies, the volume fraction of PCBM, and the PL decay fitting parameters for a pristine film, the Monte Carlo simulation is used to model the reduction of the prompt and delayed fluorescence decay components, resulting in the exciton diffusion coefficient as the only fitting parameter. [5, 6] The results of the Monte Carlo simulations are shown in Figure 3.16.

Once the diffusion coefficient has been extracted, it is then insightful to consider the exciton diffusion length, i.e. the root mean square displacement of the excitons. The diffusion length (L_D) of a singlet or triplet exciton during once occurrence of the singlet or triplet spin state, respectively, is given by:

$$L_D = \sqrt{6D\tau} \tag{3.39}$$

where τ is the singlet or triplet exciton lifetime (the inverse of k_p and k_{RISC}, respectively) in a pristine film, D is the exciton diffusion coefficient of singlets or triplets, and the factor of 6 is a proportionality constant for diffusion in three dimensions. [1] The average cumulative amount of time, $\overline{\tau}$, that an exciton spends in the excited state is given by:

$$\overline{\tau} = (\overline{n} + 1)\tau_{singlet} + \overline{n}\tau_{triplet} \tag{3.40}$$

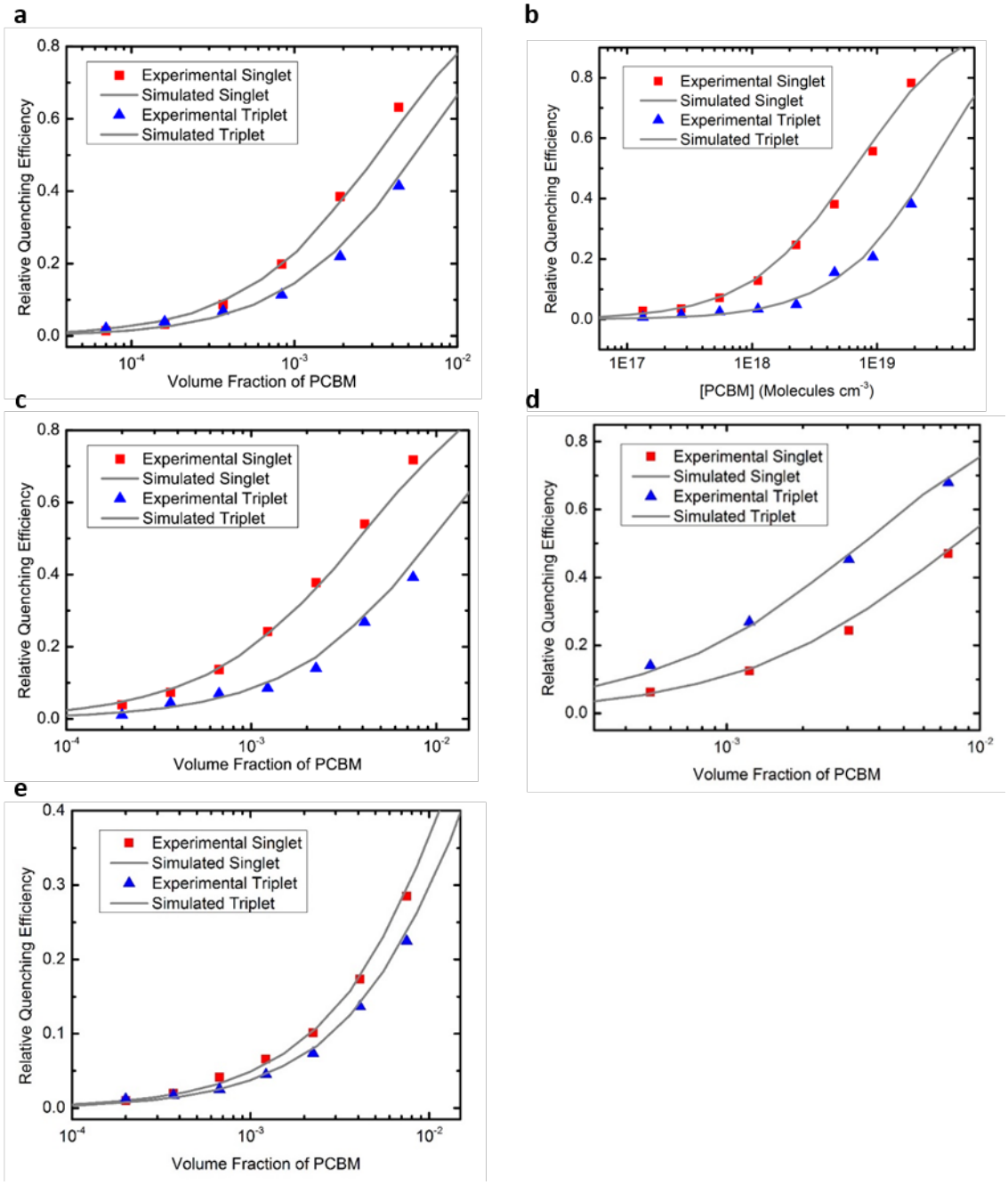

Figure 3.16: Quenching efficiency plots (room temperature) with experimental data (red squares and blue triangles) and data resulting from the Monte Carlo simulation (smooth lines). (a) FSA-XT, (b) 4CzIPN (c) 4CzIPN-tBu, (d) 4CzIPN-Br, and (e) 4CzIPN-ph.

where $\overline{n}+1$ is the number of times that an exciton encounters the singlet state and $\overline{n}$ is the number of times that an exciton encounters the triplet state. [23] Thus, the total distance that an exciton travels during its lifetime as a singlet, L_D^S, is given by:

$$L_D^S = \sqrt{6D_{singlet}(\overline{n}+1)\tau_{singlet}} \tag{3.41}$$

where $\tau_{singlet}$ is the inverse of k_p. The total distance that an exciton travels during its lifetime as a triplet, L_D^T, is given by:

$$L_D^T = \sqrt{6D_{triplet}\overline{n}\tau_{triplet}} \tag{3.42}$$

where $\tau_{triplet}$ is the inverse of k_{RISC}. Thus, the total distance an exciton travels on average during its lifetime, including the effects of spin cycling, is given by:

$$L_D^{cumulative} = L_D^S + L_D^T = \sqrt{6D_{singlet}(\overline{n}+1)\tau_{singlet}} + \sqrt{6D_{triplet}\overline{n}\tau_{triplet}} \tag{3.43}$$

which we refer to as the cumulative exciton diffusion length.

3.6 Results

Figure 3.17a shows the results of the analytical model for 4CzIPN. In order to obtain these results, a pristine film and several films with increasing concentration of PCBM (the exciton quencher) were fabricated via spin-coating. The PL decay of each film was measured, and then fitted to Equation 3.10. The extracted parameters of k_p were then used in Equation 3.16 to determine the value of k_q^S (fit shown in Figure 3.17a, red line). Next, the extracted parameters of k_p, k_d, and k_q^S are used in Equation 3.19 in order to determine the values of k_{ISC} and k_q^T (fit shown in Figure 3.17a, blue line). Finally,

Table 3.1: Summary of the photophysical parameters of the TADF materials.

	FSA-XT	4CzIPN	4CzIPN-tBu	4CzIPN-Br	4CzIPN-ph
k_{p0} [s^{-1}]	3.2×10^7	4.5×10^7	5.1×10^7	4.2×10^8	6.7×10^7
k_{ISC} [s^{-1}]	7.5×10^6	2.6×10^6	1.4×10^6	2.5×10^8	1.7×10^7
k_{RISC} [s^{-1}]	1.4×10^6	5.9×10^5	6.5×10^5	4.4×10^6	1.1×10^6
k_{d0} [s^{-1}]	1.0×10^6	5.7×10^5	6.3×10^5	1.7×10^6	8.3×10^5
Experimental ΔE_{ST} [meV]	21	43	57	18	39
Theoretical ΔE_{ST} [meV]	12	80	79	53	21
V_{SOC} ISC/RISC [meV]	0.004/0.004	0.016/0.024	0.015/0.020	0.089/0.142	0.003/0.006
$\Phi_S(S_1)$ / $\Phi_S(T_1)$	0.16/0.18	0.40/0.46	0.35/0.41	0.33/0.39	0.33/0.43
$D_{singlet}$ [$cm^2\ s^{-1}$]	2.3×10^{-6}	3.9×10^{-6}	5.5×10^{-6}	1.9×10^{-5}	4.2×10^{-6}
$D_{triplet}$ [$cm^2\ s^{-1}$]	3.3×10^{-8}	7.3×10^{-9}	1.2×10^{-8}	1.2×10^{-7}	4.8×10^{-9}
E_a, Singlet Diffusion [meV]	34	32	52	8	37
E_a, Triplet Diffusion [meV]	144	92	117	128	134
Solid-State PLQY	0.72	0.30	0.23	0.22	0.19
Wigner-Seitz radius, r [nm]	0.52	0.65	0.75	0.73	0.78
$\overline{n}$	0.27	0.53	0.89	36.12	0.22

Equation 3.18 is used to determine k_{RISC}. Good agreement between the analytical model and experimental data cannot be achieved for other values of k_{ISC} as shown in Figure 3.17b.

After implementing this technique for each of the 5 TADF materials, it becomes quite clear that there is a positive correlation between the rate of ISC and the rate of RISC (Figure 3.18). This makes sense, because ISC and RISC likely proceed through the same mechanism, such that the main difference is simply the direction of the process and whether that means the initial state is higher or lower in energy than the final state. Thus, RISC is expected to be slower than ISC and a chemical modification that

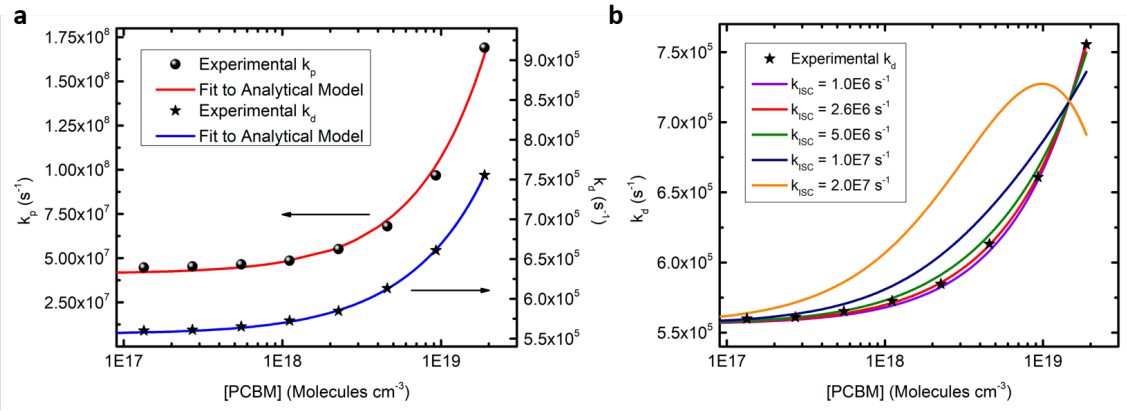

Figure 3.17: a) Dependence of k_p and k_d on [PCBM] for 4CzIPN with fitting to the analytical model described in the text. b) Dependence of k_d on [PCBM] for 4CzIPN where arbitrary input values of k_{ISC} are fixed, resulting in k_q^T as the only fitting parameter.

is designed to increase either of them will most likely end up increasing both. Although slow ISC may be incommensurable with fast RISC (a combination which would be ideal for TADF-OLEDs), the efficiency of ISC can be reduced if k_r^S is comparatively high. The design strategy for an ideal TADF material that emerges from this picture is to obtain a high k_{RISC} and high k_r^S. In terms of structure-property relationships, it is apparent that the inclusion of the heavy bromine atoms results in a large increase of both k_{ISC} and k_{RISC}. This is clearly associated with the much larger $S_1 - T_1$ spin-orbit coupling (V_{SOC}) calculated for 4CzIPN-Br in comparison to the other compounds, an obvious result of the heavy atom effect (see Table 3.6). The addition of t-butyl groups to the 4CzIPN structure had a minimal impact on the rates of ISC and RISC, but phenyl substituents resulted in significantly increased spin conversion rates. It was found that FSA-XT, most likely on account of its very small ΔE_{ST}, undergoes faster spin conversion than 4CzIPN.

Another interesting trend that was observed is that k_{d0} is roughly proportional to k_{ISC} and k_{RISC}, as shown in Figure 3.19. If one wanted to quickly estimate the relative rates of spin interconversion of some new TADF materials they synthesized, this trend would be immensely useful. Besides, making the films with the exciton quencher, measuring all

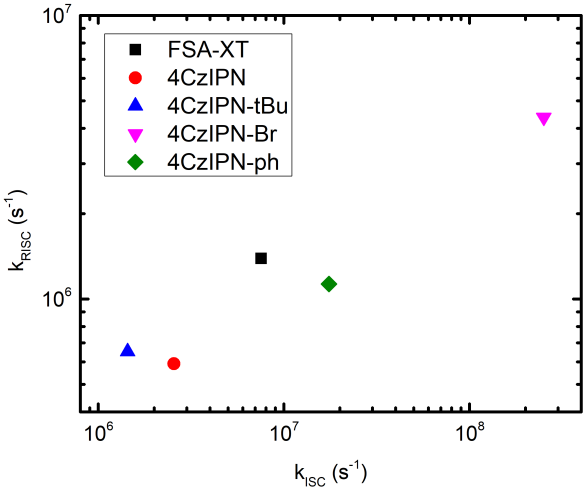

Figure 3.18: Plot of k_{ISC} versus k_{RISC} for the 5 TADF materials.

the PL decays, and utilizing the analytical model may be too tedious for some.

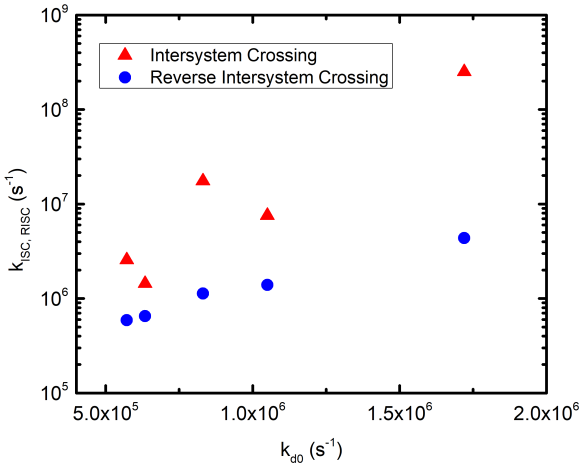

Figure 3.19: Plot of k_{d0} (rate of delayed fluorescence in the absence of quencher) versus k_{RISC} for the 5 TADF materials.

The dynamics of spin interconversion can be calculated directly from the analytical model. This analysis is surprisingly absent from the literature. The ratio of the triplet concentration relative to the singlet concentration is determined by dividing Equation

3.11 by Equation 3.10, where $[S_1]_0 = 1.0$ (since the PL decays are normalized):

$$\frac{[T_1]}{[S_1]} = \frac{\frac{[S_1]_0 k_{ISC}}{k_p - k_d}\Big(exp(-k_d t) - exp(-k_p t)\Big)}{A_p exp(-k_p t) + A_d exp(-k_d t)} \tag{3.44}$$

This ratio is shown as a function of time for all 5 TADF materials in Figure 3.20. The time at which the rapid onset of triplet formation occurs is determined primarily by the rate of ISC, after which a quasi-equilibrium between the concentration of singlets and triplets is reached. A clear picture of why certain materials maintain a larger relative concentration of triplets at quasi-equilibrium cannot be determined due to the convoluted nature of the equations mentioned above, which are dependent on all of the rate constants for a particular material and not just one or two easily comprehensible parameters. Nevertheless, this ratio should be taken into consideration when performing pump-probe experiments on TADF materials, because the concentration of singlets after prompt fluorescence may not be negligible, which is certainly the case for several of the materials studied herein.

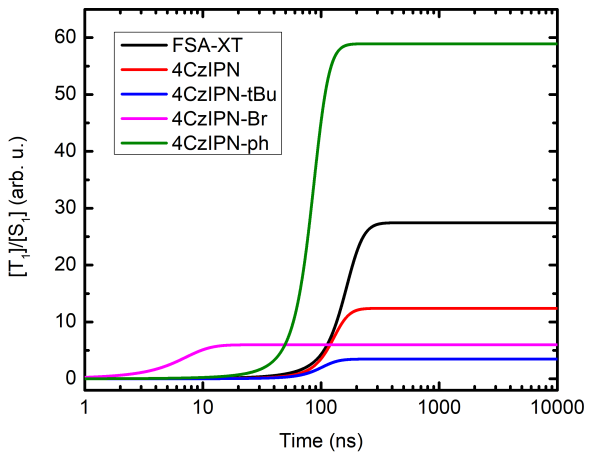

Figure 3.20: Dynamics of triplet and singlet exciton populations after pulsed photo-excitation.

In order to determine ΔE_{ST} via the analytical model, it was necessary to perform

the PL quenching experiments (and data analysis) at various temperatures. From the temperature dependence of k_{RISC}, which ought to exhibit Arrhenius-like behavior, one can extract ΔE_{ST}. In this interpretation I assume that the activation energy for RISC is equivalent to ΔE_{ST}, which may not necessarily be the case. If RISC proceeds from the triplet manifold into a vibrationally excited S_1 state, then the true ΔE_{ST} is actually slightly smaller than the measured activation energy for RISC. Regardless of this nuance, it is the activation energy required for RISC which is of paramount importance in TADF materials, because it is this energy barrier which will influence the relative rate of RISC. The orange squares in Figure 3.21 show the data obtained for 4CzIPN after using our analytical model, where the slope of the solid gray line is proportional to the activation energy for RISC (ΔE_{ST}) in 4CzIPN. Note how at low temperatures k_{RISC} becomes much less temperature dependent, indicating a transition to a regime dominated by quantum mechanical tunneling.[39]

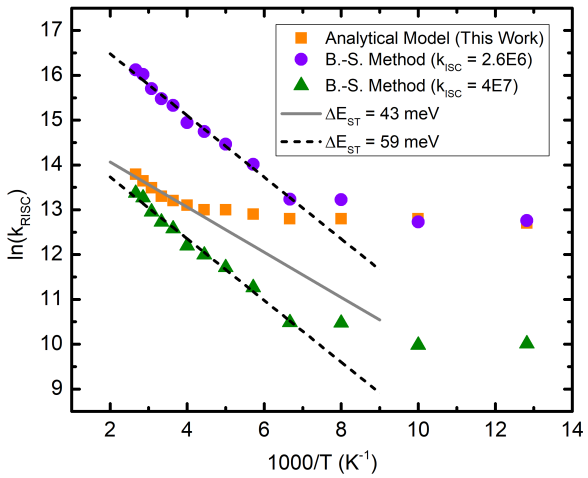

Figure 3.21: Arrhenius plot of reverse intersystem crossing in 4CzIPN.

Figure 3.21 also shows the results for 4CzIPN when the Berberan-Santos method is used.[23] In that method, the magnitude of k_{RISC} is inversely proportional to the magnitude of k_{ISC}, and, therefore, an accurate determination of k_{RISC} is predicated on the

accurate determination of k_{ISC}. Additionally, it is assumed that k_{ISC} is independent of temperature. As shown later, k_{ISC} is found to be mildly temperature dependent. It is also worth mentioning that the Berberan-Santos method is only valid for materials that exhibit strong delayed fluorescence ($\overline{n} \geq 4$) and that 4CzIPN does not meet this requirement ($\overline{n} = 0.53$). Two vastly different values of k_{ISC} were chosen for the Berberan-Santos method of analysis: 2.6×10^6 s^{-1} (purple circles) which is the value determined in this work at room temperature, and 4.0×10^7 s^{-1} (green triangles) which is the value reported elsewhere in the literature for 4CzIPN.[14, 40] In the first case, one finds that k_{RISC} at room temperature (5.3×10^6 s^{-1}) is larger than k_{ISC}, which is thermodynamically unreasonable. In the second case, the calculated value of k_{RISC} at room temperature (3.4×10^5 s^{-1}) is within reasonable agreement to our value (5.9×10^5 s^{-1}), but the ratio k_{ISC}/k_{RISC} is far off from what is obtained with my refined model (and also supported by recent computational efforts).[22] In the aforementioned reference, we discovered that our calculated (DFT) values of k_{ISC} and k_{RISC} were close to the experimentally determined values only after taking into consideration the polarizability of the surrounding environment. Nevertheless, good agreement between theoretical results and my analytical model was achieved for 4CzIPN. My work highlights how the Berberan-Santos method can be less accurate for some TADF materials in regard to the magnitudes of k_{ISC} and k_{RISC}.

For several of the materials we encountered difficulties extracting ΔE_{ST} using the Berberan-Santos method (e.g. non-linear Arrhenius plots around room temperature), but never had issues using our model (Figure 3.22). As one can see from Figure 3.22, assigning a slope to the proper data range for determining ΔE_{ST} is unambiguous when considering the values determined by my analytical model (blue lines). However, when considering the Berberan-Santos method it is not as clear where the data should be fit to extract ΔE_{ST}. The transition between the two regimes of RISC (thermal activation at high temperatures versus quantum tunneling at low temperatures) is much less clear in

the Berberan-Santos method. Using the Berberan-Santos method for FSA-XT resulted in a positive slope at high temperatures, which doesn't make physical sense. Also note that when the analytical model is used for 4CzIPN-Br the transition temperature seems to lie outside the measured temperature range. This could be simply due to its very small ΔE_{ST} (compare to the transition temperature of FSA-XT), but may also be a result of the degree to which spin-orbit coupling participates in RISC. Since the bromine atoms of 4CzIPN-Br contribute a significant amount of spin-orbit coupling and spin-orbit coupling is expected to be roughly independent of temperature, perhaps this is why a transition temperature for 4CzIPN-Br is not observed.

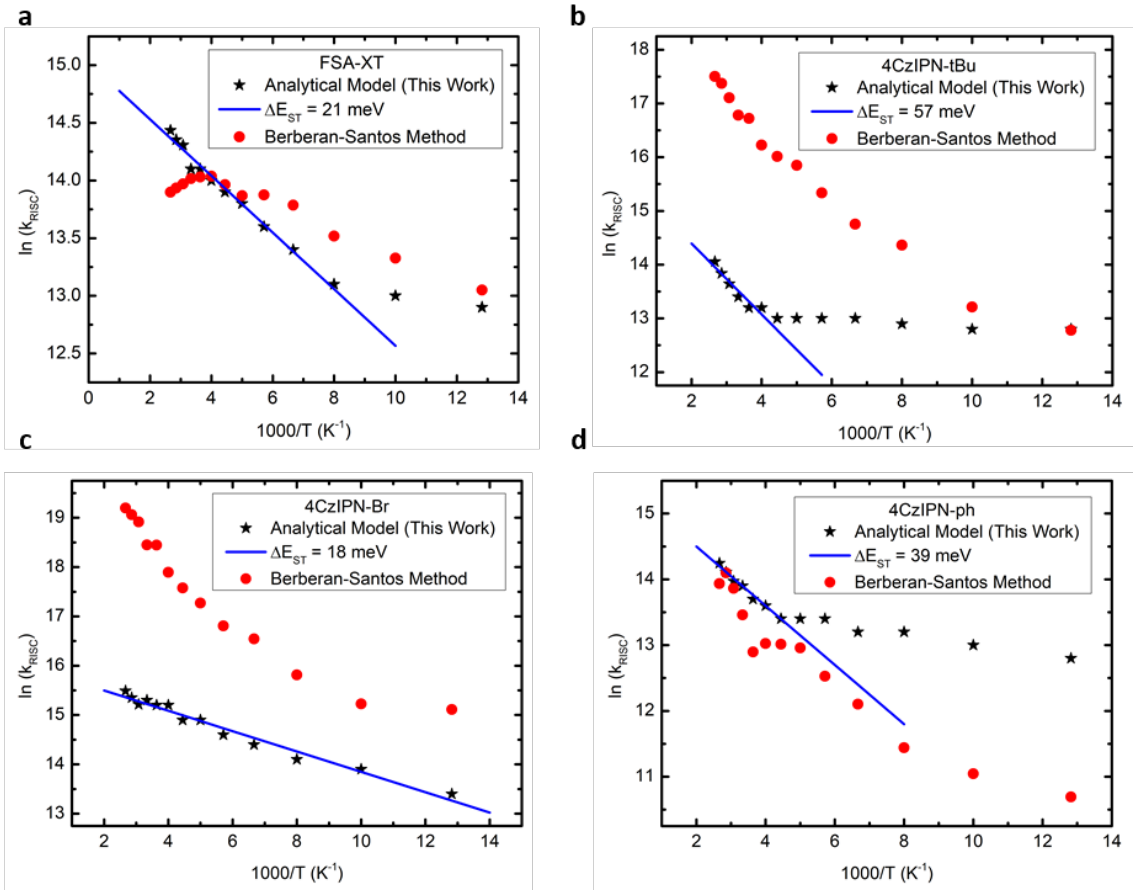

Figure 3.22: Arrhenius plots of k_{RISC} showing results from our analytical model (black stars), as well as the results from the Berberan-Santos method (red circles). (a) FSA-XT, (b) 4CzIPN-tBu, (c) 4CzIPN-Br, and (d) 4CzIPN-ph.

In Table 3.6, k_{ISC} is determined from the results of the analytical model. The second row of data is the value of k_{RISC} based on the value of k_{ISC} in row 1 and Equation 3.18 (my analytical model). The third row of data is the value of k_{RISC} based on the Berberan-Santos method (Equation 3.20) where the value for k_{ISC} is that determined by my analytical model (first row of data). For 4CzIPN, 4CzIPN-tBu, and 4CzIPN-Br the Berberan-Santos method significantly overestimates k_{RISC}. Good agreement between both methods is achieved for FSA-XT. For 4CzIPN-ph the Berberan-Santos method slightly underestimates k_{RISC}.

Table 3.2: Comparison of results (at room temperature) from my analytical model versus the Berberan-Santos method.

	FSA-XT	4CzIPN	4CzIPN-tBu	4CzIPN-Br	4CzIPN-ph
k_{ISC} (s^{-1}) Analytical Model	7.5 E6	2.6 E6	1.4 E6	2.5 E8	1.7 E7
k_{RISC} (s^{-1}) Analytical Model	1.4 E6	5.9 E5	6.5 E5	4.4 E6	1.1 E6
k_{RISC} (s^{-1}) Berberan-Santos Method	1.2 E6	1.6 E7	1.9 E7	1.0 E8	7.0 E5

As shown in Figure 3.23, we find that the rate of RISC is inversely proportional to ΔE_{ST}, just as expected. Indeed, reasonable agreement is found between measured and calculated singlet-triplet exchange energies. Both experiment and theory yield the largest ΔE_{ST} values for 4CzIPN and 4CzIPN-tBu, in line with the largest Φ_S in their T_1 and S_1 excited-state wavefunctions suggesting an increased admixture of localized excitations in comparison to the other compounds. For 4CzIPN-Br, the decrease in ΔE_{ST} compared to 4CzIPN is induced by the presence of the electro-active bromine groups at the periphery of the carbazole units, which further separate away the hole from the electron density resulting in a more pronounced charge-transfer character. As expected, FSA-XT exhibits the lowest computed ΔE_{ST} due to the $\approx 90°$ dihedral angle between donor and acceptor

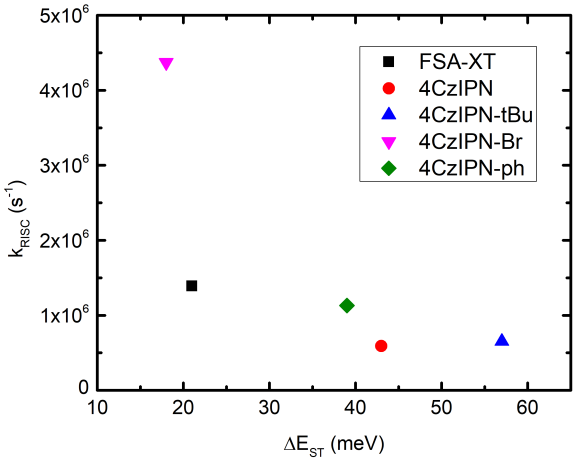

Figure 3.23: Plotted values of k_{RISC} (at room temperature) and ΔE_{ST} for each of the 5 TADF materials as determined by temperature-dependent PL quenching experiments.

moieties, which also confers a high degree of CT character (small Φ_S). In contrast to experiments, however, our calculations predict a surprisingly low ΔE_{ST} value for 4CzIPN-Ph. Close inspection of the wavefunctions shows a partial delocalization of the hole electronic density into the outer phenyl rings, which enhances its CT character and thus reduces ΔE_{ST}. The fact that comparable values are, instead, measured for 4CzIPN and 4CzIPN-Ph suggests that, likely because of steric conformational effects in the solid state, the phenyl rings are relatively decoupled from the core of the molecule in 4CzIPN-Ph.

By appling the analytical model to temperature-dependent PL quenching experiments I was able to determine the temperature dependence of k_{ISC}, as shown in Figure 3.24. These data show that k_{ISC} is not independent of temperature, which is an assumption of the Berberan-Santos method. In order to understand the nature of each material's temperature dependence, one would have to consider how temperature influences the solid-state packing of these materials and in turn how that effects the vibrational and rotational dynamics of the system, which is beyond the scope of my PhD.

The temperature dependence of the radiative and non-radiative rates of decay from

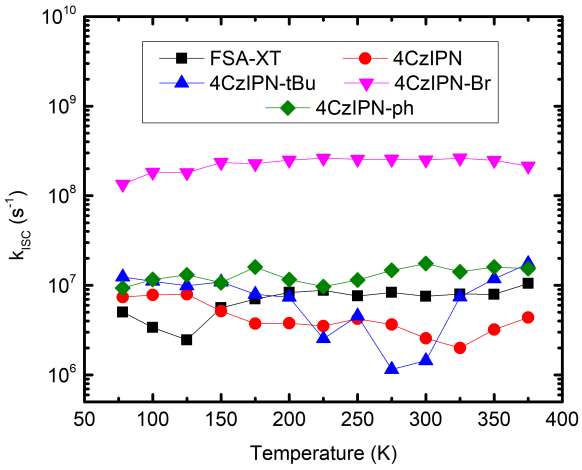

Figure 3.24: Temperature dependence of ISC as determined by the analytical model. Note the logarithmic axis, which underemphasizes the fluctuations in each material's k_{ISC}.

the singlet state were also investigated, as shown in Figure 3.25. The rate of radiative decay from the singlet state (k_r^S) was determined by:

$$\Phi_p = \frac{k_r^S}{k_p} \tag{3.45}$$

The rate of non-radiative decay from the singlet state (k_{nr}^S) was then determined by:

$$k_{nr}^S = k_p - k_r^S - k_{ISC} \tag{3.46}$$

The temperature dependence of k_r^S was found to be mild for most of the materials investigated, with the exception of 4CzIPN-Br, which showed a marked decrease in the rate of radiative decay with increasing temperature. FSA-XT was the only material which showed a slight increase of k_r^S with increasing temperature. As expected, the rate of non-radiative decay was found to increase with increasing temperature for all 5 materials. The magnitudes of decay channels from the singlet state are plotted for each material in Figure 3.26.

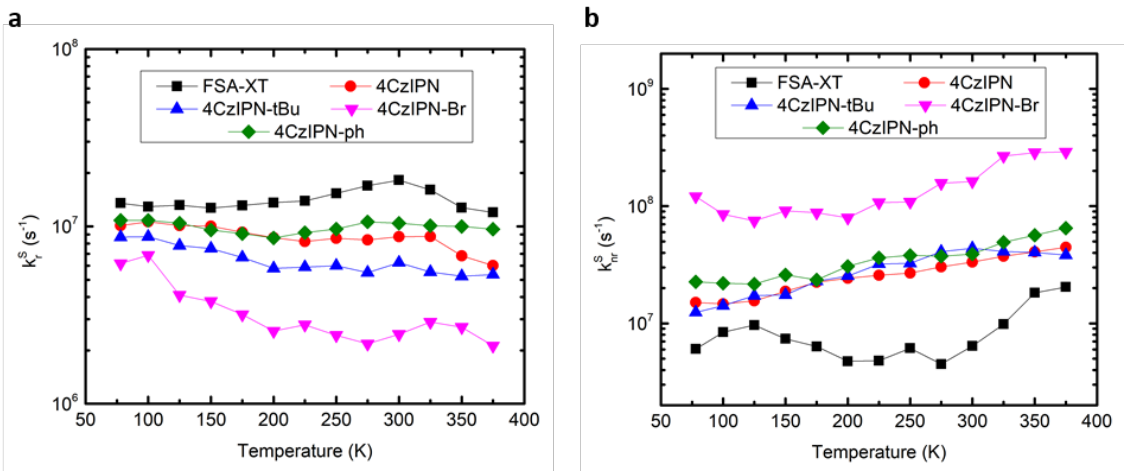

Figure 3.25: (a) Temperature dependence of the rate of radiative decay from the singlet state, k_r^S. (b) Temperature dependence of the rate of non-radiative decay from the singlet state, k_{nr}^S.

Interestingly, k_r^S is not proportional to ΔE_{ST} (with the exception of 4CzIPN-Br), as shown in Figure 3.26. This is noteworthy because an exciton's extent of electron and hole wavefunction overlap is expected to be directly proportional to not only ΔE_{ST}, but also to the oscillator strength of optical transitions, i.e. k_r^S. Furthermore, since both the Einstein coefficient of spontaneous emission and the Einstein coefficient of absorption are proportional to oscillator strength, we would expect that the absorptivity of a material should be proportional to its rate of radiative decay. We found this general principle to not hold true for the majority of the TADF materials investigated. In particular, note how 4CzIPN-Br has the highest molar absorptivity and FSA-XT has the lowest molar absorptivity (Figure 3.4), but k_r^S is highest in FSA-XT and lowest in 4CzIPN-Br.

Interestingly, it was found that the total solid-state PLQY is inversely proportional to the size of the molecule and its Wigner-Seitz radius, r, a parameter that is commonly used to estimate average intermolecular distances. This trend is shown in Figure 3.27. Therefore, when designing new TADF materials it may be worthwhile to keep the size of the molecule as small as possible while also enabling them to pack densely in the solid

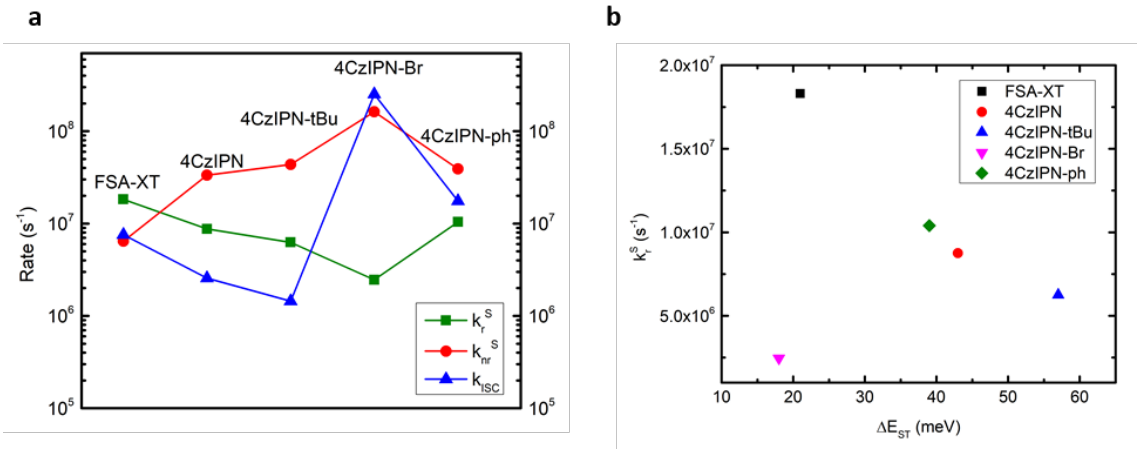

Figure 3.26: (a) Rate constants for decay pathways from the singlet state. Each material has its three parameters located directly below it. (b) k_r^S is plotted against ΔE_{ST}, demonstrating that it can be reduced without necessarily reducing k_r^S.

state. Although a low molar absorptivity is often associated with a low PLQY (since poor absorbers are often poor emitters), through our subsequent analysis of rate constants, we found that the high PLQY of FSA-XT can be mostly attributed to its small rate of non-radiative decay from the singlet state. Thus, increasing the rate of radiative decay is not the only design strategy for enhancing PLQY.

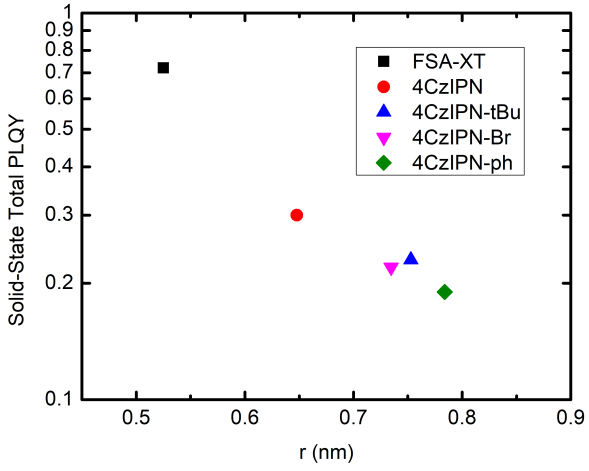

Figure 3.27: Plot of the solid-state total photoluminescence quantum yield versus the Wigner-Seitz radius, r.

My esteemed Belgian collaborators estimated the impact of molecular architecture

and substitution on the spin-orbit coupling, V_{SOC}, mediating spin conversion; these calculations were performed on the basis of the S_1 and T_1 geometries, relevant for ISC and RISC, respectively (Table 3.6). In line with our previous findings, V_{SOC} is larger for compounds with greater differences between their S_1 and T_1 Φ_S values.[22] However, the calculated V_{SOC} values alone are not enough to understand the experimentally determined trend in spin interconversion magnitudes, which leads us to believe that there may be a significant dynamic component (rotations, vibrations, torsions, etc.) that contributes to k_{ISC} and k_{RISC}. Besides, our previous collaboration efforts showed, from molecular dynamics simulations, that 4CzIPN experiences torsions on a timescale commensurate with rates of spin interconversion. Thus, I suspected that putting TADF materials in a different environment, i.e. one that afforded more or less flexibility in regard to molecular vibrations, would result in a change in the rates of ISC and RISC.

To test this hypothesis, we employed our analytical model to 50 μM solutions of each TADF material in benzene at room temperature using pyrene as an exciton-quencher (results shown in Table 3.6). See also Appendix C. Benzene was chosen as the solvent because it showed good solubility, has a dielectric constant of 2.3 (which is similar to the dielectric constant of the TADF materials), and is non-chlorinated (chlorinated solvents should be avoided when using pulsed, high-power lasers). The exciton-quenching species chosen was pyrene, because PCBM absorbs significantly at 400 nm, whereas pyrene does not. The concentration of PCBM required to induce significant quenching of singlet and triplet excitons resulted in a noticeable inner filter effect which distorted the PL spectrum of the TADF emitter. As can be seen from Figure 3.28, pyrene is able to effectively quench triplet excitons but not singlet excitons. Thus, for these solution studies a value of zero was used for k_q^S. This is probably due to a combination of pyrene's relatively small electron affinity as well as the short lifetime of singlet excitons in the TADF material, resulting in a smaller probability of collisional quenching. Because

of the relatively large separation distances between the TADF molecules in solution, the bimolecular quenching constant for triplet excitons used in the fitting procedure is now a descriptor of the translational motion of the molecules and not of exciton diffusion which stems from energy transfer.

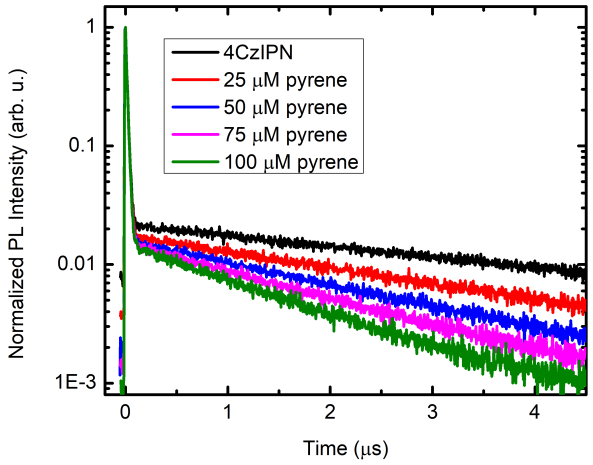

Figure 3.28: 4CzIPN PL decay in benzene with increasing concentration of pyrene.

For these solution studies a fixed value of k_q^T had to be used in order to have fits of Equation 3.19 converge. Values of k_q^T were obtained by the Stern-Volmer method, as shown in Figure 3.29, and are consistent with the diffusion of small molecules in solution.

Figure 3.30 shows that k_{ISC} and k_{RISC} were significantly higher in solution than in the solid-state for the 4CzIPN derivatives. This is most likely attributable to the extent of donor-acceptor rotational freedom available to the molecules. Whereas in the solid-state these rotations may have prohibitively high energy barriers, in solution these rotations are expected to happen quickly and efficiently. Previous work has shown that these rotations allow a molecule to explore its configurational space until a geometry is reached which favors (R)ISC.[21, 22, 35] We suspect that the additional rotations afforded by the phenyl groups of 4CzIPN-ph are responsible for its relative increase in spin conversion rates compared to 4CzIPN. For FSA-XT in solution k_{ISC} was marginally

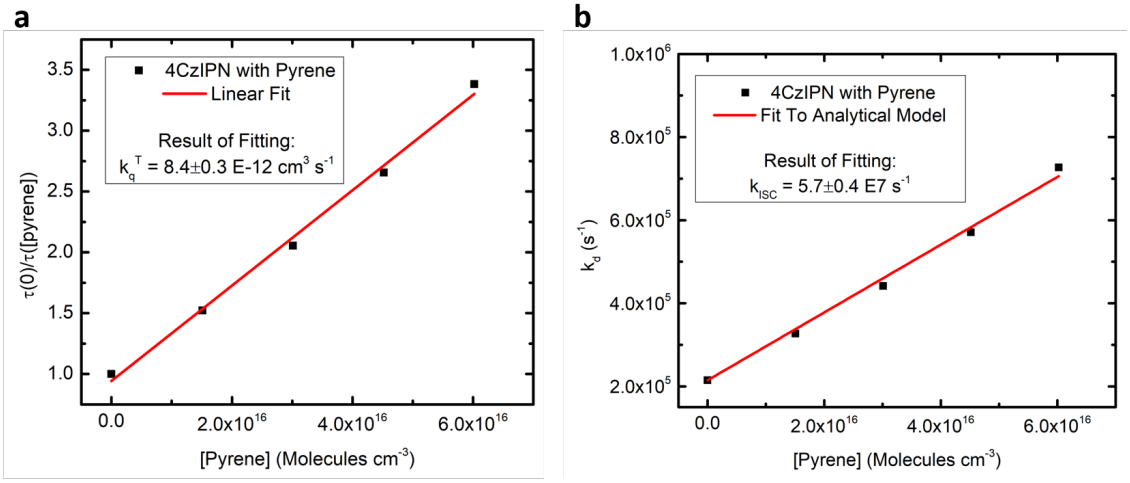

Figure 3.29: Stern-Volmer plot used to determine k_q^T of 4CzIPN and pyrene. (c) Fit to analytical model resulting in a value for k_{ISC} (4CzIPN).

higher than in the solid-state and k_{RISC} was actually found to be smaller. We believe that this is a consequence of FSA-XT's molecular geometry, such that (R)ISC would not benefit from additional rotational freedom and, in fact, suffers most probably due to the change in dielectric constant of the surrounding medium.[41]

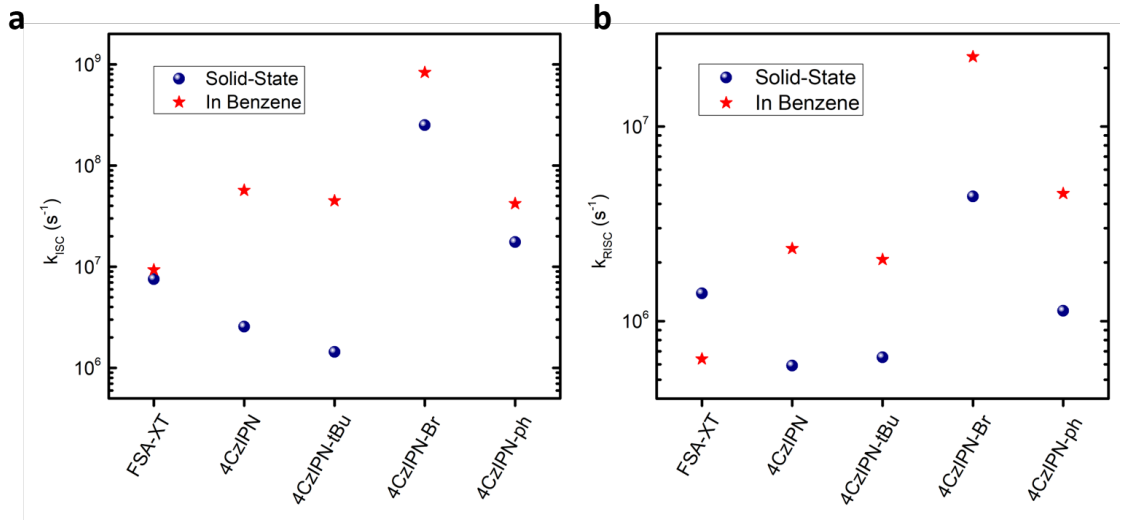

Figure 3.30: Comparison of (a) the rate of intersystem crossing and (b) the rate of reverse intersystem crossing for the solid-state (pristine films) and solution (50 μM in benzene).

The enhancement of spin interconversion rates in solution and suppression of non-radiative decay pathways leads to a large increase in the average number of spin cycles, $\overline{n}$, each molecule experiences in the excited state, as shown in Figure 3.30. Recall that $\overline{n} = 1$ is defined as a $S_1 \rightarrow T_1 \rightarrow S_1$ cycle. A value of $\overline{n} < 1$ means that most of the generated excitons emit directly from the singlet state after absorption of light without ever undergoing ISC. For 4CzIPN-Br, we calculated $\overline{n}$ to be 275 in benzene solution and 36 in the solid-state. To the best of our knowledge these are the largest values of $\overline{n}$ reported in the literature for any TADF material (the highest values of $\overline{n}$ that we could find ranged between 10 and 15).[23, 24, 40]

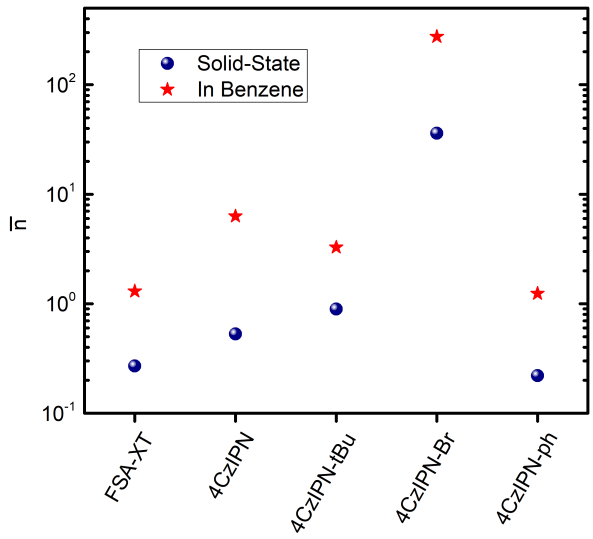

Figure 3.31: Comparison of the spin cycling parameter, $\overline{n}$, for the solid-state (pristine films) and solution (50 μM in benzene).

3.7 Exciton Diffusion Results

Very good agreement is found between the Monte Carlo simulation and results from the analytical model - within 17% for 4CzIPN. However, it appears as though for materials with larger spin interconversion rates there is a larger deviation of the simulated

Table 3.3: Summary of photophysical parameters of the TADF materials in benzene.

	FSA-XT	4CzIPN	4CzIPN-tBu	4CzIPN-Br	4CzIPN-ph
k_{p0} (s^{-1})	2.52 E7	6.28 E7	5.41 E7	8.52 E8	4.90 E7
k_{d0} (s^{-1})	3.99 E5	2.15 E5	3.48 E5	5.22 E5	5.89 E5
k_q^T (cm^3 s^{-1})	8.25 E-12	8.43 E-12	4.56 E-12	9.81 E-12	6.07 E-12
k_{ISC} (s^{-1})	9.31 E6	5.69 E7	4.48 E7	8.32 E8	4.21 E7
k_{RISC} (s^{-1})	6.39 E5	2.36 E6	2.07 E6	2.28 E7	4.52 E6
$\overline{n}$	1.3	6.3	3.3	274.6	1.2

exciton diffusion results from the analytical results. This is reasonable, because as spin interconversion rates increase, treating prompt and delayed components of the PL decay independently becomes increasingly inaccurate. The results from the analytical model and Monte Carlo simulation are shown in Table 3.7.

Table 3.4: Comparison of exciton diffusion coefficients determined by the analytical model versus the Monte Carlo simulation.

	FSA-XT	4CzIPN	4CzIPN-tBu	4CzIPN-Br	4CzIPN-ph
$D_{singlet}$ Analytical Model [cm^2 s^{-1}]	2.3×10^{-6}	3.9×10^{-6}	5.5×10^{-6}	1.9×10^{-5}	4.2×10^{-6}
$D_{singlet}$ Monte Carlo [cm^2 s^{-1}]	2.9×10^{-6}	4.7×10^{-6}	3.7×10^{-6}	8.2×10^{-6}	6.6×10^{-7}
$D_{triplet}$ Analytical Model [cm^2 s^{-1}]	3.3×10^{-8}	7.3×10^{-9}	1.2×10^{-8}	1.2×10^{-7}	4.8×10^{-9}
$D_{triplet}$ Monte Carlo [cm^2 s^{-1}]	2.9×10^{-8}	7.8×10^{-9}	1.0×10^{-8}	1.5×10^{-7}	6.9×10^{-9}

Exciton diffusion coefficients, for both singlets and triplets, were found to be exceedingly low for organic semiconductors. The singlet exciton diffusion coefficient measured for the materials herein is on the order of 10^{-5} - 10^{-6} cm^2 s^{-1}, whereas typical organic semiconductors have a singlet exciton diffusion coefficient on the order of 10^{-4} cm^2 s^{-1}.[42] We found the triplet exciton diffusion coefficient for TADF materials to be on the order of 10^{-7} - 10^{-9} cm^2 s^{-1}. The triplet exciton diffusion coefficient for organic

semiconductors can vary widely, depending mostly on the relative crystallinity of the material in the solid-state. In highly crystalline materials, such as pyrene, the triplet diffusion coefficient can be as large as 10^{-4} cm^2 s^{-1}, but for more amorphous materials, such as Alq_3, the triplet diffusion coefficient is on the order of 10^{-7} cm^2 s^{-1}.[43, 44]

The small exciton diffusion coefficients measured in these materials suggests that they are amorphous and disordered in the solid state, a result of poor intermolecular electronic coupling. Indeed, the intramolecular twisting inherent in these materials makes π-π stacking over long length scales rather unlikely. We can infer from the quenching efficiency plots that PCBM makes an intimate, homogeneous blend with each material, because the experimental and simulated quenching efficiencies agree quite well over a large concentration range. Phase separation and PCBM aggregation would manifest themselves as a deviation of lower experimental quenching efficiencies, compared to the simulated curve, at higher concentrations of PCBM (owing to aggregation and subsequent reduction in the available quenching surface area).[5] Phase separation, even at very low loadings of PCBM, are not uncommon for semi-crystalline small molecule OPV materials with planar, extended π systems.[45] The triplet diffusion coefficient for each material is much lower than its singlet exciton diffusion coefficient, which is not surprising because triplet excitons can only diffuse via Dexter energy transfer, whereas singlets can diffuse via Dexter energy transfer and Förster Resonant Energy Transfer (which is more effective than Dexter at longer distances). With the exception of 4CzIPN-Br, triplet diffusion lengths are shorter than singlet diffusion lengths for the materials studied herein.

The three dimensional singlet and triplet exciton diffusion lengths obtained for the five molecules are shown in Figure 3.32. These values reflect how far a singlet or triplet exciton travels during its lifetime, excluding the possibility of RISC. Singlet exciton diffusion lengths seem to correlate inversely with molecular size, ranging from 7.9 nm (4CzIPN) to as short as 2.4 nm (4CzIPN-ph). Despite triplet excitons having a much longer lifetime

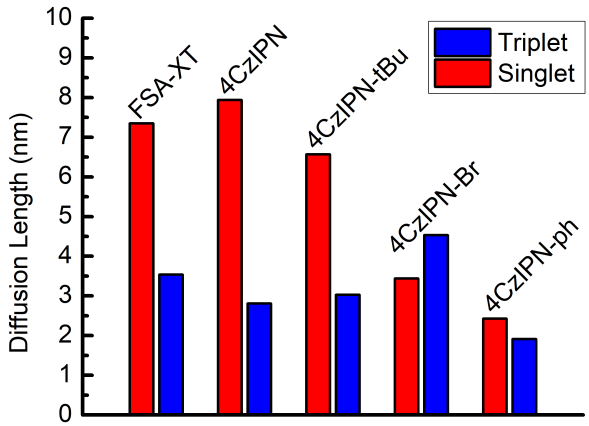

Figure 3.32: Singlet and triplet exciton diffusion lengths for one occurrence of the singlet or triplet excited state, respectively, at room temperature.

than singlet excitons, they tend to diffuse over smaller distances owing to their relatively small diffusion coefficients (around 2 orders of magnitude less than singlet exciton diffusion coefficients). This is not surprising, given that non-luminescent triplet excitons are limited to Dexter energy transfer, whereas singlet excitons are expected to diffuse primarily via a Förster resonant energy transfer mechanism. Aside from 4CzIPN-Br, the triplet exciton diffusion coefficients also scale inversely with the size of the molecule. A notable exception to the trend is 4CzIPN-Br, whose peripheral bromine atoms pulls the hole density toward the outer region of the molecule, likely improving intermolecular electronic interactions allowing for potential energy transfer via the Dexter (i.e. orbital overlap-driven) mechanism.

In order to grasp how far an exciton may diffuse during its entire lifetime (which we call the cumulative exciton diffusion length), the interconversion between the singlet and triplet states, i.e. spin cycling ($\overline{n}$), must be accounted for. Figure 3.33a shows how exciton diffusion is expected to change with increasing spin cycling. (The diffusion coefficients and lifetimes of 4CzIPN are used in Figure 3.33a for purely demonstrative purposes.) Spin cycling has a rather small effect on the cumulative exciton diffusion length for most of the

materials studied herein (Figure 3.33b) due to the low extent of spin cycling (Table 3.6). However, a notable exception is 4CzIPN-Br, whose high degree of spin cycling results in a dramatically increased cumulative exciton diffusion length (48.2 nm). This number appears to be exceptionally high in comparison to other materials exhibiting disordered thin film morphologies, such as certain π-conjugated polymers and small molecules, for which exciton diffusion lengths up to maximum 15 nm are usually reported.[46]

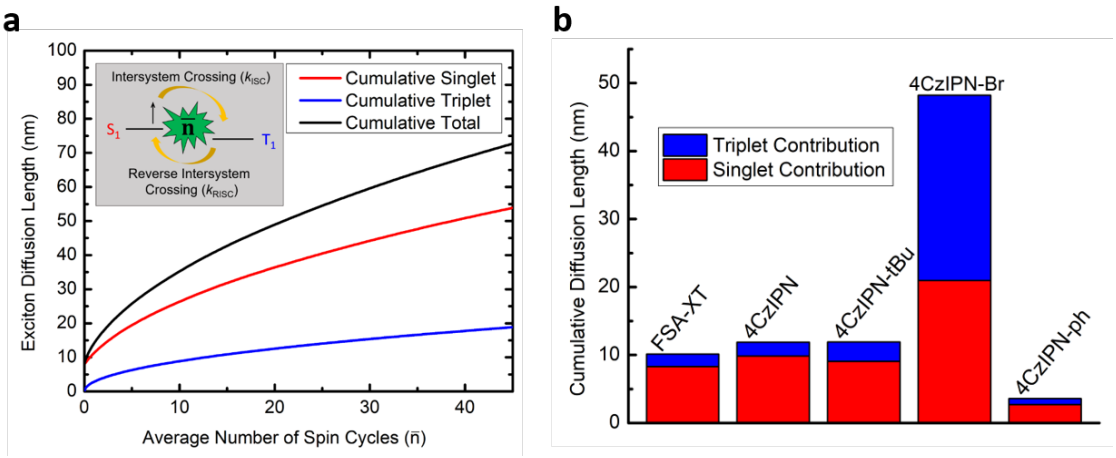

Figure 3.33: a) Theoretical demonstration of how the extent of spin cycling affects the cumulative exciton diffusion length. b) Cumulative exciton diffusion lengths at room temperature where the effect of spin cycling has been taken into account.

The activation energies for singlet and triplet exciton diffusion were determined by analyzing the temperature-dependence of the singlet and triplet exciton diffusion coefficients, respectively. For singlet diffusion (Figure 3.34), Arrhenius-like behavior was observed for temperatures above approximately 250 K, whereas for triplet exciton diffusion (Figure 3.35) Arrhenius-like behavior was observed for temperatures above approximately 225 K. Below these critical temperatures the diffusion coefficient becomes weakly temperature dependent, a clear indication of the transition from thermally-activated hopping to quantum mechanical tunneling. This transition temperature has been shown to be strongly influenced by the relative degree of energetic disorder, where more ordered sys-

tems require less thermal energy to achieve thermally activated hopping transport. Small molecule and polymer organic semiconductors typically have a transition temperature below 150 K.[47, 48, 42, 49] This would suggest that the TADF materials investigated in this work have a relatively large amount of disorder. Activation energies for singlet diffusion were found to be lower than the activation energies for triplet diffusion. Because singlets can diffuse via FRET, which is more effective than Dexter at long distances, singlet excitons have more available sites to hop to compared with triplet excitons, whose hops are limited to short distances. Thus, it is not surprising that singlet diffusion activation energies are significantly lower than those for triplets. For the 4CzIPN derivatives, the activation energy for triplet diffusion again scales approximately with molecular size.

The observed correlation between exciton diffusion properties and molecular size can be simply understood by considering that larger molecules require longer hop sizes for exciton diffusion to occur (from a center-of-mass perspective), and both Förster and Dexter energy transfer efficiencies rapidly decline with increasing hop distances.

In order to gain a deeper understanding of exciton diffusion in these materials, further analysis was undertaken through the lens of Förster and Dexter theory. The rate of Förster resonant energy transfer (FRET) is given by:

$$k_{FRET} = \frac{9 \times 10^{17} \times ln(10) \times \Phi_p \times \kappa^2 \times J}{128 \times N_A \times \tau_p \times l^6 \times n^4 \times \pi^5} \tag{3.47}$$

where Φ_p is the quantum yield of the prompt component of fluorescence, κ^2 is the dipole orientation factor (0.476 for randomly oriented, rigid dipoles), N_A is Avogadro's number, τ_p is the average lifetime of the prompt component of fluorescence in units of seconds, l is the average intermolecular separation in nm, n is the refractive index in the region of spectral overlap, and J is the spectral overlap integral in units of nm^4 M^{-1} cm^{-1}. The

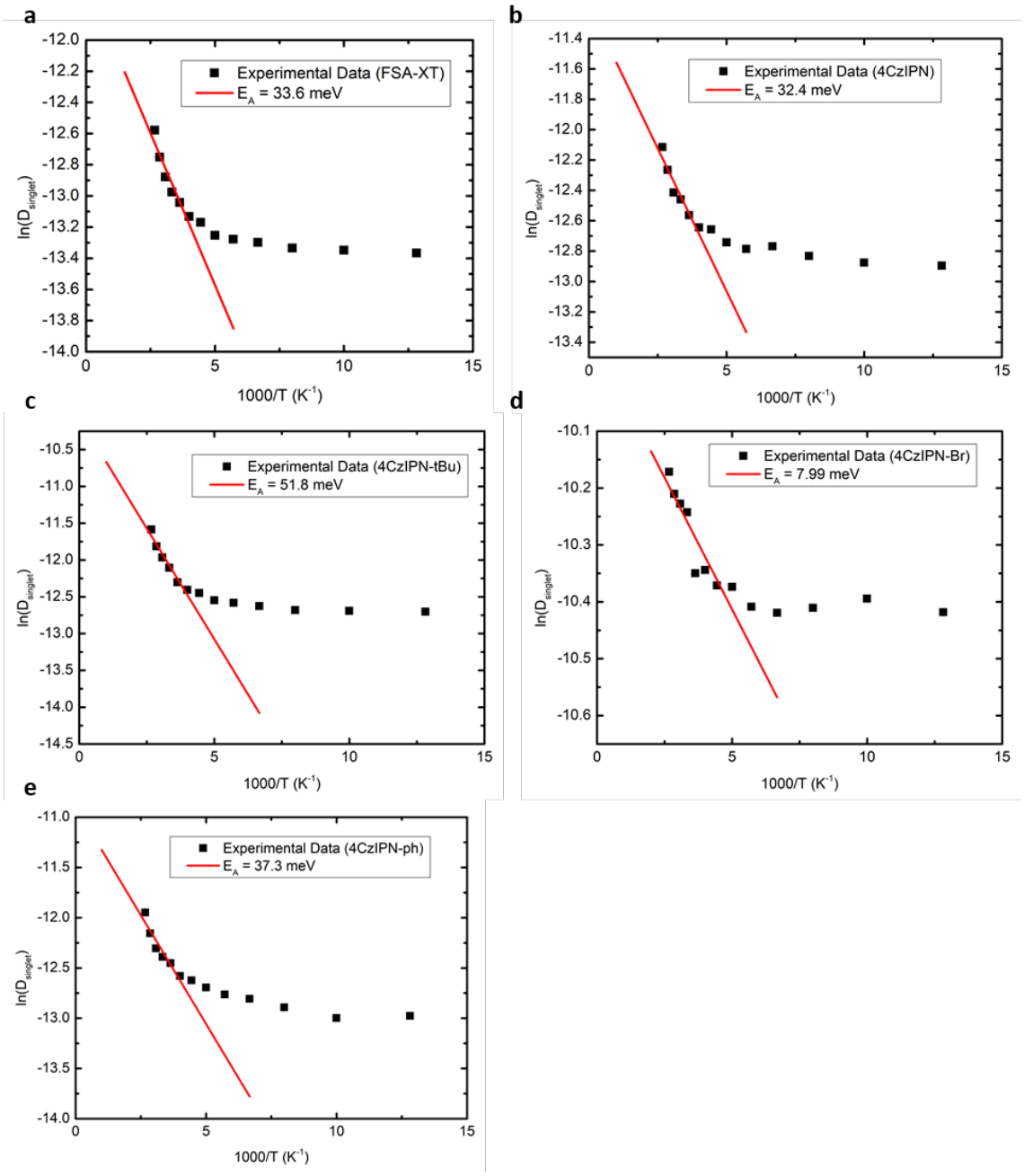

Figure 3.34: Arrhenius plots of singlet diffusion for (a) FSA-XT, (b) 4CzIPN (c) 4CzIPN-tBu, (d) 4CzIPN-Br, and (e) 4CzIPN-ph.

spectral overlap integral is given by:

$$J = \frac{\int_0^\infty F(\lambda)\epsilon(\lambda)\lambda^4 d\lambda}{\int_0^\infty F(\lambda)d\lambda} \tag{3.48}$$

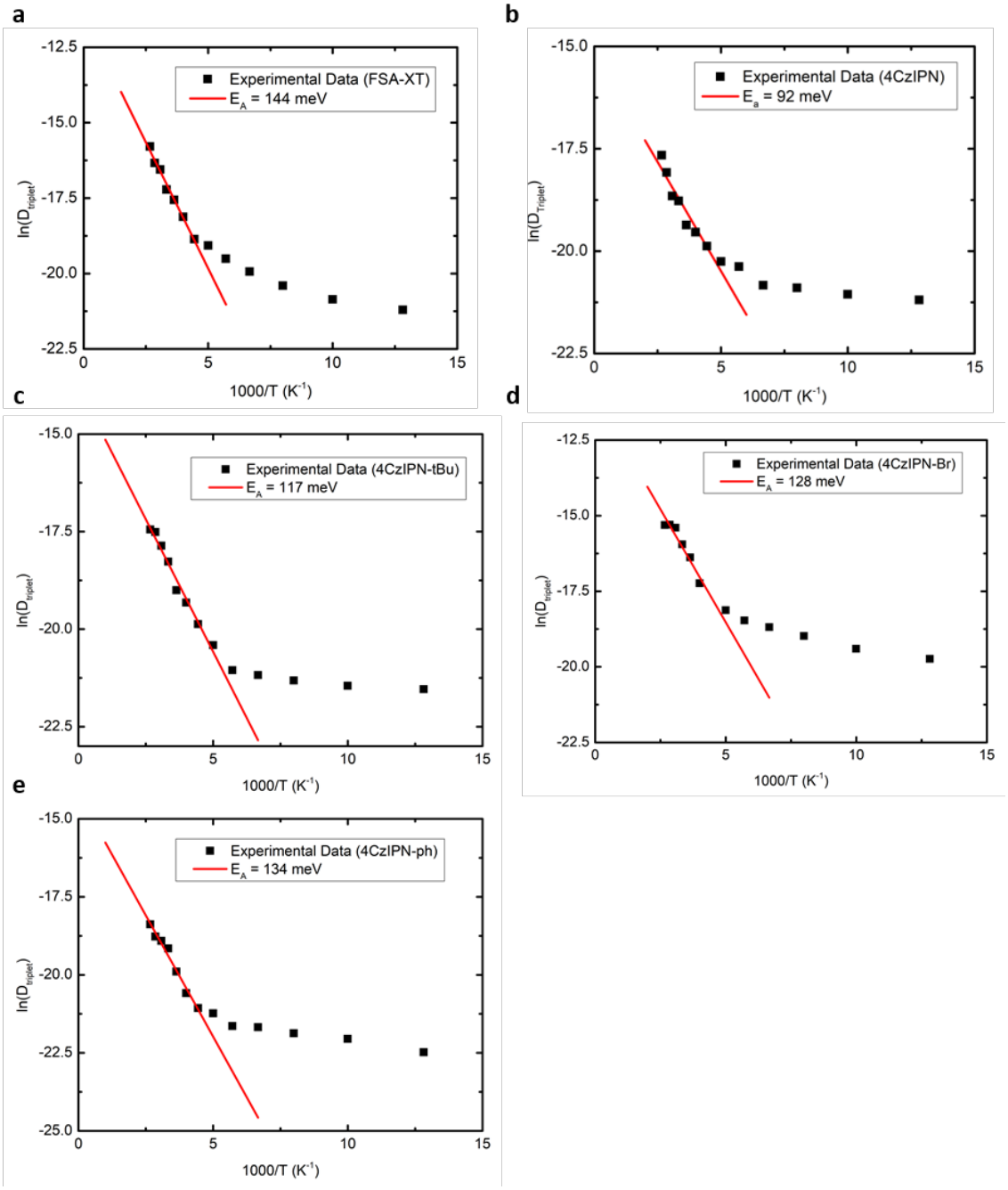

Figure 3.35: Arrhenius plots of triplet diffusion for (a) FSA-XT, (b) 4CzIPN (c) 4CzIPN-tBu, (d) 4CzIPN-Br, and (e) 4CzIPN-ph.

where $\epsilon(\lambda)$ is the molar absorptivity in units of M^{-1} cm^{-1}, $F(\lambda)$ is the photoluminescence spectrum in arbitrary units, and λ is the wavelength in nanometers. The factor of

10^{17} is included so that the units of k_{FRET} are in s^{-1}. For all three materials we use $n = 1.76$, which is the value measured for 4CzIPN in a previous study.[38] The average intermolecular separation for each material was determined by doubling its Wigner-Seitz radius.

From the diffusion coefficient, D, a rate of energy transfer can be calculated simply by:

$$k_{energy\,transfer} = \frac{6D}{l^2} \tag{3.49}$$

where l is the average intermolecular separation and 6 is the proportionality constant for diffusion in 3 dimensions. Because triplet excitons can only diffuse by Dexter transport, the rate of Dexter energy transfer can be calculated directly from the triplet exciton diffusion coefficient. The rate of singlet diffusion, $k_{singlet\,diffusion}$, can be determined from Equation 3.49 when values of singlet exciton diffusion are used. On the other hand, k_{FRET}, calculated from Equation 3.47, can be used in Equation 3.49 to determine the diffusion coefficient of singlet excitons, assuming their diffusion occurs primarily through FRET and not Dexter. The singlet exciton diffusion coefficients calculated in this latter manner are significantly lower than the measured singlet exciton diffusion coefficients. Although Förster theory tends to underestimate exciton diffusion in amorphous materials, the severity of these instances suggests that Dexter energy transfer has a significant contribution to singlet exciton diffusion in many TADF materials.[50]

The relative contribution of FRET to the overall diffusion of singlet excitons was determined by the ratio of k_{FRET} (Equation 3.47) to the rate of singlet diffusion, $k_{singlet\,diffusion}$ (Equation 3.49 where the singlet diffusion coefficient determined from PL quenching is used). When we compare this ratio to k_{Dexter} one can plainly see that materials with a fast rate of Dexter energy transfer have a smaller contribution from FRET to the overall rate of singlet diffusion (Figure 3.36). Although Dexter energy transfer for singlets should

Table 3.5: Relevant parameters of singlet and triplet exciton diffusion, especially in the context of Förster and Dexter theory.

	FSA-XT	4CzIPN	4CzIPN-tBu	4CzIPN-Br	4CzIPN-ph
l (nm)	1.05	1.30	1.51	1.47	1.57
J ($nm^4M^{-1}cm^{-1}$)	1.44E+11	1.99E+12	3.12E+12	6.17E+12	5.21E+12
τ_p (s)	3.10E-08	2.24E-08	1.94E-08	2.41E-09	1.49E-08
Φ_p	0.566	0.196	0.121	0.006	0.156
k_{FRET} (s^{-1})	8.57E+06	1.60E+07	7.28E+06	6.59E+06	1.59E+07
$D_{singlet}$ Förster theory (cm^2 s^{-1})	1.57E-08	4.48E-08	2.75E-08	2.37E-08	6.52E-08
$D_{singlet}$ Monte Carlo (cm^2 s^{-1})	2.90E-06	4.70E-06	3.70E-06	8.20E-06	6.60E-07
$D_{triplet}$ Monte Carlo (cm^2 s^{-1})	2.90E-08	7.80E-09	1.00E-08	1.50E-07	6.90E-09
k_{Dexter} (s^{-1})	1.81E+07	2.62E+06	3.07E+06	3.28E+07	1.17E+06
$k_{singlet\,diffusion}$ (s^{-1})	1.58E+09	1.68E+09	9.79E+08	2.28E+09	1.61E+08

be different from Dexter energy transfer for triplets due to their differing wavefunctions and reorganization energies, our results suggest that they are not so dissimilar. In other words, materials that have a fast rate of Dexter energy transfer for triplets will also have a high rate of Dexter energy transfer for singlets. As mentioned in the previous paragraph, it seems that for singlet excitons in TADF materials the Dexter mechanism of exciton diffusion is competitive with the Förster mechanism.

Dexter energy transfer is extremely sensitive to intermolecular distances and the spatial distribution of the hole and electron wavefunctions in a material, because the probability of Dexter energy transfer is dependent on the wavefunction overlap of adjacent molecules. Since the probability density of a wavefunction falls off exponentially with distance, chemical structure is a critical factor when determining the favorability of this type of exciton transport.[3] 4CzIPN-ph has the largest average intermolecular separation of the 5 materials studied, meaning that the probability of wavefunction overlap between adjacent molecules is small. Hence, 4CzIPN-ph has a very short triplet exciton diffusion

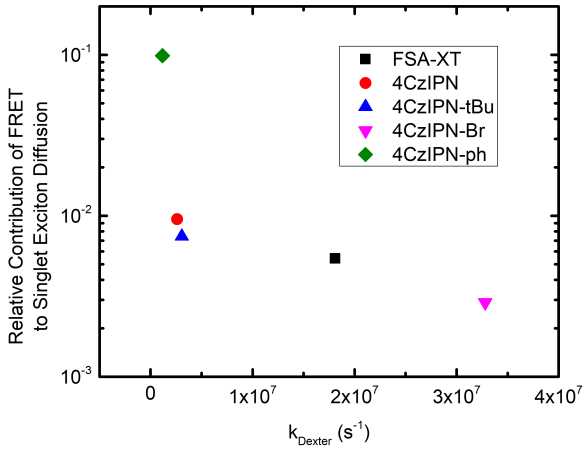

Figure 3.36: The relative contribution of FRET to singlet exciton diffusion plotted against the rate of Dexter energy transfer, k_{Dexter}.

length. To our surprise, the t-butyl groups of 4CzIPN-tBu increased the triplet exciton diffusion coefficient relative to 4CzIPN despite an increased average intermolecular separation. 4CzIPN-Br was found to have the largest triplet exciton diffusion coefficient of the materials studied. This may be a result of the hole wavefunction extending beyond the carbazole moieties onto the bromine atoms themselves, resulting in better wavefunction overlap, which would facilitate Dexter energy transfer. In other words, it seems as though the bromine substituents enhance intermolecular electronic coupling. Interestingly, for 4CzIPN-Br and FSA-XT the calculated rate of Dexter energy transfer is larger than the calculated rate of FRET. FSA-XT, which has a substantially longer triplet exciton diffusion length than 4CzIPN, has both a hole and electron wavefunctions that are relatively exposed to the surrounding environment, making wavefunction overlap between adjacent molecules relatively more favorable. Additionally, the average intermolecular separation of FSA-XT is significantly smaller than 4CzIPN.

3.8 Conclusion

In this work, I developed an analytical model based on photoluminescence quenching, which is capable of unambiguously determining many of the crucial excited-state rate constants in TADF materials, both in solution and solid films. The assumptions upon which this model rests are far less restrictive than other methods used in the community, representing significant progress toward the accurate determination of k_{ISC}, k_{RISC}, and ΔE_{ST}. Additionally, this experimental method enables the simultaneous measurement of the diffusion length for both singlet and triplet excitons, presenting a unique opportunity to investigate the different mechanisms of exciton diffusion without having to prepare separate samples or use more than one experimental technique. Using this method on 5 different TADF materials, we have gathered important insight on structure-function relationships. We have found that (i) heavy atoms (i.e. bromine) dramatically increase k_{ISC} and k_{RISC} while also reducing ΔE_{ST}, (ii) rotations about the donor and acceptor moieties heavily influence the dynamics of TADF, (iii) the extent of spin cycling, $\overline{n}$, substantially impacts exciton diffusion length, and (iv) molecular size is strongly correlated with exciton diffusion properties as well as solid-state PLQY. It is worth remarking on the exceptional properties of 4CzIPN-Br (fast k_{ISC} and k_{RISC}, small ΔE_{ST}, large $\overline{n}$, long exciton diffusion length, and reasonable oscillator strength), which, besides making it a really promising emitter for TADF OLEDs, also make it a potential candidate for (i) triplet sensitizing in triplet-triplet annihilation photon upconversion,[51, 52] (ii) the 3.5 generation/hyperfluorescent OLED devices where TADF materials act as assistant dopants from where singlet excitons upconverted from the triplet excited-state manifold follow a fast energy transfer towards narrow emission fluorescent dyes,[53, 54] and (iii) bilayer organic photovoltaics whose thicknesses (and consequently their ability to harvest photons) are typically limited by rather short exciton diffusion lengths.[49, 1]

As will be shown in the next chapter, 4CzIPN-Br was used as a triplet sensitizer in TTAUC applications with moderate success. Rumors from the lab of Prof. Chihaya Adachi suggest 4CzIPN-Br may not be very stable under operating conditions in OLED devices. As for 4CzIPN-Br's potential as a donor in bilayer solar cells, I fabricated bilayer solar cell devices with the structure ITO/PEDOT:PSS/4CzIPN-Br/C[60]/Al. Devices were also made using 4CzIPN. PEDOT:PSS and the TADF material were spin-coated, whereas C[60] was thermally evaporated. Unfortunately, none of these devices made good solar cells (efficiencies below 0.01%). However, considering the deep HOMO level of the TADF materials, there were very likely issues with charge injection/collection. Perhaps optimization of the electrode materials and charge transport layers could substantially improve the solar cell performance.

Chapter 4

Triplet-Triplet Annihilation Photon Upconversion

The contents of this chapter are unpublished.

Triplet-Triplet Annihilation Photon Upconversion (TTAUC) is a process whereby low energy, incoherent radiation is converted into photons of higher energy.[55] This technology enables the conversion of two, incoherent, low-energy photons into one high-energy photon, which has the potential to improve solar cells, of all types, by turning sub-bandgap photons which normally go unused, into above-gap photons which can contribute meaningfully to photocurrent. Although upconversion can be achieved by other mechanisms, such as two-photon absorption, these approaches require high-power, coherent light sources (i.e. not the sun). Some experts believe that solar energy is the only technology capable of meeting global energy demands in an environmentally friendly manner, and TTAUC could help meet this demand.[56] TTAUC could be a post-production add-on to solar cells that increases their efficiency, which has appeal on a global scale, household scale, and is even appealing for applications where space is limited and, there-

fore, efficiency is precious. Theoretically, TTAUC can boost solar cell efficiency by up to 15% on an absolute scale (so a solar cell with 28.2% efficiency can be boosted to an efficiency of 43.6% using TTAUC).[57] On the other side of the solar spectrum, this technology can be used to convert broadband solar radiation into high-energy UV light (most of which is absorbed by the atmosphere), offering an essentially free, limitless supply of light for photocatalytic reactions. For example, in the manufacture of vitamin D3, UV radiation is used to initiate the electrocyclic ring opening of 7-dehydrocholesterol. TTAUC also has applications in medicine and biology. Each specific application requires upconversion in a particular spectral region, which is determined by the type of donor and acceptor used. Because the magnitudes and efficiencies of upconversion are low across the board, in this project I try to develop general strategies for improvement of TTAUC. In particular, I investigate how upconversion can be maximized when using TADF materials as the triplet sensitizer.

For this chapter I would like to specifically thank Taku Ogawa, a visiting PhD student from Japan, who introduced me to the concept of TTAUC, and Carolina Espinoza, an undergraduate student at UCSB who carried out many of the experiments for this project under my guidance.

4.1 Background

The mechanism of TTAUC (shown in Figure 4.1) is very complex and many of the processes that contribute to this phenomenon not particularly well understood. The general process begins with the absorption of a photon on the donor molecule, creating a singlet excited state. Then, through intersystem crossing, a triplet exciton is formed on the donor molecule, followed by triplet energy transfer to an acceptor (host) material. If two triplet excitons (from separate acceptor molecules) encounter each other via triplet

exciton diffusion, they can undergo triplet-triplet annihilation (TTA), potentially resulting in the creation of a higher energy singlet exciton, which can then emit a high energy photon. TADF materials are well suited for donor materials in this application, because they have high rates of intersystem crossing and lose very little energy (< 0.1 eV) during this process. Typical donor molecules are based on expensive platinum-containing molecules and lose over 0.5 eV during intersystem crossing. Thus, TADF materials can result in larger energy upconversion and they are much cheaper to produce than phosphorescent triplet sensitizers.

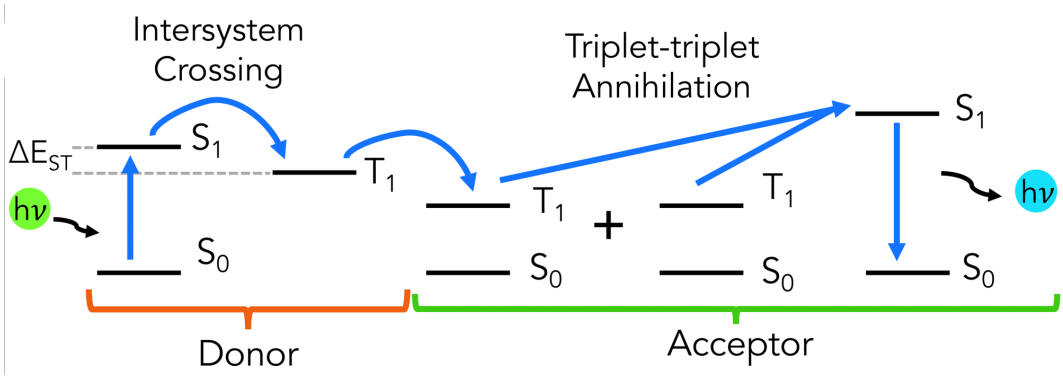

Figure 4.1: Simplified schematic of the TTAUC process.

The overall efficiency of the TTAUC process, Φ_{UC}, is a measure of how many upconverted, high-energy photons are emitted per absorbed photon of light. Therefore, the maximum efficiency that can be reached is 50%, since at the very least two photons of low energy are required to make a single photon of high energy. In the literature, Φ_{UC} is often taken as the number of upconverted photons emitter per 2 photons of absorbed light, such that the maximum achievable efficiency is 100%. I will clarify which definition is used when necessary. The efficiency of the TTAUC process is essentially a result of the quantum efficiency of each step required in the mechanism. Thus,

$$\Phi_{UC} = \Phi_{ISC} \times \Phi_{ET} \times \Phi_{TTA} \times f \times \Phi_{fl} \tag{4.1}$$

where Φ_{ISC} is the quantum yield of intersystem crossing of the donor sensitizer, Φ_{ET} is the quantum yield of triplet electron transfer from the donor to the acceptor, Φ_{TTA} is the quantum yield of triplet-triplet annihilation (i.e. the probability that two triplet acceptors encounter each and produce a singlet excited state), f is a spin-statistical factor, and Φ_{fl} is the quantum yield of fluorescence for the acceptor. The spin-statistical factor, f, and quantum yield of triplet-triplet annihilation, Φ_{TTA}, are somewhat related and require some explanation. At high pump fluences the concentration of triplet acceptors should be very high, and, therefore, the probability of two of them encountering each other is near unity. However, the process of triplet-triplet annihilation must obey spin statistics and the rules of quantum mechanics, which suggest that there are three spin states that can arise from TTA: a quintet, a triplet, or a singlet. These states are shown below, where A represents an acceptor molecule, superscripts denote spin multiplicity, subscripts denote the total spin of the species, and asterisks denote an excited state:

$$ {}^3A_1^* + {}^3A_1^* \rightleftharpoons {}^5(AA)_2^* \rightleftharpoons {}^5A_2^* + {}^1A_0 \tag{4.2} $$

$$ {}^3A_1^* + {}^3A_1^* \rightleftharpoons {}^3(AA)_1^* \rightleftharpoons {}^3A_1^* + {}^1A_0 \tag{4.3} $$

$$ {}^3A_1^* + {}^3A_1^* \rightleftharpoons {}^1(AA)_0^* \rightleftharpoons {}^1A_0^* + {}^1A_0 \tag{4.4} $$

Note how the intermediate states are two-molecule species, which then dissociate into separate states, one of which preserves the spin multiplicity, the other returning to the ground state. Taking into account the multiplicity of these states, the quintet has a degeneracy of 5, the triplet, 3, and the singlet, 1, with a total of 9 distinct spin states. Therefore, one would expect that there is only a 11% chance ($f = 0.11$) that TTA results

in the creation of a singlet excited state. However, experiments have shown and theories suggest that this value can actually be greater than 20%. [58]

Most research efforts have focused on solution-phase experiments utilizing phosphorescent triplet sensitizers, with maximum upconversion efficiencies of around 20% (on the 50% maximum scale). [55] Those done in the condensed phase or without the use of heavy metals typically have efficiencies below 10%. The anti-Stokes shift, defined here as the energy difference between the excitation wavelength and the first vibronic peak of the acceptor fluorescence spectrum, is typically below around 0.5 eV, although very recently a particular blend has achieved an anti-Stokes shift of 1.08 eV, the current world record. [59] That record blend, however, contains Pt. Several other novel strategies have been employed to increase anti-Stokes shifts in TTAUC, primarily focused on triplet sensitization routes. Some of these strategies, such as the use of inorganic nanocrystals for triplet sensitization, have resulted in anti-Stokes shift as large as 0.9 eV. Still, obtaining an anti-Stokes shift of over 1.0 eV is very challenging. A review of novel sensitization routes for TTAUC can be found in [60].

There are very few reports of TTAUC using TADF materials as the triplet sensitizer.[51, 52] The record for upconversion efficiency and anti-Stokes shift using a TADF sensitizer was achieved in the lab of Chihaya Adachi, for which a blend of 4CzIPN and p-terphenyl in benzene achieved an anti-Stokes shift of 0.83 eV and upconversion efficiency of 3% (50% maximum scale). This was the starting point for my own research. The first experiment I undertook was to measure the PL decay of 4CzIPN + p-terphenyl blends in benzene, in order to asses how efficient p-terphenyl was at quenching the triplet excitons of 4CzIPN. As shown in Figure 4.2, the addition of 25 mM p-terphenyl to 50 μM 4CzIPN in benzene has only a very small impact on the delayed fluorescence of 4CzIPN, implying that Φ_{ET} is low. Therefore, I wanted to explore different acceptors that might have more suitable energy levels, which could lead to a great increase in Φ_{ET}.

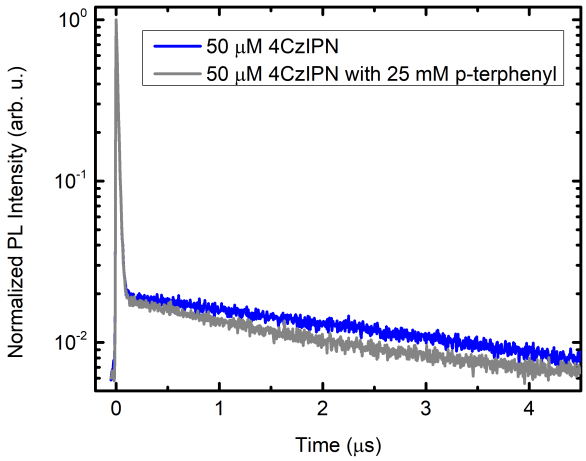

Figure 4.2: Photoluminescence decay of 4CzIPN with p-terphenyl in benzene, as determined by TCSPC.

4.2 Density Functional Theory

In order to assess the viability of different acceptor molecules, I pursued DFT calculations of the T_1 and S_1 energy levels for various small molecules. Calculations were performed in the gas phase using the B3LYP functional and 6-31G(d,p) basis set. The results are shown in Tables 4.2 and 4.2. Once the T_1 and S_1 energy levels had been determined, I calculated the ratio between them, in order to gain a sense of whether or not TTA could even result in upconversion (no upconversion for $S_1 > 2 \times T_1$). Ideally, for a maximized anti-Stokes shift, the S_1 energy should be just below twice the energy of T_1.

In order to determine which molecules would make the most promising acceptor candidates, I first threw out molecules with a S_1/T_1 ratio above 2.0. From the remaining molecules I downselected again by considering a maximum T_1 energy of 3.0 eV (approximately the value for p-terphenyl). I further downselected by throwing out molecules with a relatively low S_1 energy, and/or low S_1/T_1 ratio. In the last phase of selection, I got rid of molecules which are known to have a very low fluorescence quantum yield. An

Table 4.1: Singlet and triplet energy levels calculated via density functional theory.

Molecule	T_1 (eV)	S_1 (eV)	S_1/T_1 (eV)
naphthalene	2.73	4.46	1.63
1-methylnaphthalene	2.71	4.37	1.62
carbazole	3.19	4.15	1.30
fluorene	3.10	4.67	1.51
p-terphenyl	3.02	4.38	1.45
pyrene	2.12	3.72	1.75
2-methylnaphthalene	2.76	4.41	1.60
p-methyl anisole	3.72	5.30	1.43
1,4-dimethoxybenzene	3.74	5.28	1.41
9,10-dihydrophenanthrene	3.06	4.57	1.50
dibenzofuran	3.20	4.53	1.41
3-phenyl dibenzofuran	2.95	4.23	1.43
indole	3.25	4.88	1.50
2,5-diphenylfuran	2.35	3.76	1.60
2,5-diphenyloxazole	2.52	3.88	1.54
benzofuran	3.31	5.07	1.53
benzothiadiazole	2.23	3.86	1.73
isoindene	1.10	3.02	2.75
pentalene	0.55	1.63	2.95
fumaronitrile	2.70	5.36	1.99
1,3-cyclohexadiene	2.49	4.82	1.93

excellent source for finding the fluorescence quantum yield of various small molecules is [61]. This last criterion turned out to be not very essential, as will be shown later. From this analysis, it became clear that naphthalene and 1-methylnaphthalene would be great choices, with 2,5-diphenyloxazole (PPO), fumaronitrile, fluorene, carbazole, and 3-phenyl dibenzofuran as other potentially good acceptors.

4.3 Quenching Efficiency of Selected Acceptors

Using the chemicals available to me, I determined the quenching efficiency of selected acceptors at a concentration of 25 mM (with 50 μM 4CzIPN) in benzene by comparing

Table 4.2: Singlet and triplet energy levels calculated via density functional theory.

Molecule	T_1 (eV)	S_1 (eV)	S_1/T_1 (eV)
1,3,5-hexatriene [cis]	2.13	4.85	2.28
1,3,5-hexatriene [trans]	2.09	4.86	2.33
pyrrole	4.15	6.55	1.58
pyrazole	4.41	6.79	1.54
oxazole	4.04	6.40	1.58
thiazole	3.56	5.36	1.50
imidazole	4.33	6.58	1.52
furan	3.84	6.50	1.69
thiophene	3.48	5.92	1.70
thienothiophene	2.96	4.88	1.65
cyclopentadithiophene	2.31	4.01	1.74
benzodithiophene	2.64	3.99	1.51
1,4-cyclohexadiene	N/A	5.98	N/A
PPO-2	2.99	4.71	1.58
PPO-3	2.90	4.72	1.63
anthracene	1.80	3.28	1.82
9,10-dihydroanthracene	3.71	5.29	1.43
9,10-diphenylanthracene	1.74	3.17	1.82
tyrosine	3.69	5.05	1.37
acrylonitrile	3.33	6.10	1.83
tetracyanoethylene	1.94	4.33	2.23

4CzIPN's rate of delayed fluorescence (k_d) with and without the acceptor:

$$Q = 1 - \frac{k_d(pristine)}{k_d(blend)} \tag{4.5}$$

Pyrene was included not as a real acceptor candidate, but to assess what 100% quenching should look like, since its T_1 energy is very small. The results are shown in Figure 4.3. From these data, we can infer that the triplet energy of 4CzIPN is about 2.5 eV. Furthermore, these data rule out fluorene as being a potentially good acceptor. The quenching efficiency of carbazole was found to be oddly high for its relative triplet energy, so the data was not included in the figure. The fluorescence quantum yield of carbazole

is rather low, anyhow, so it wasn't further considered.

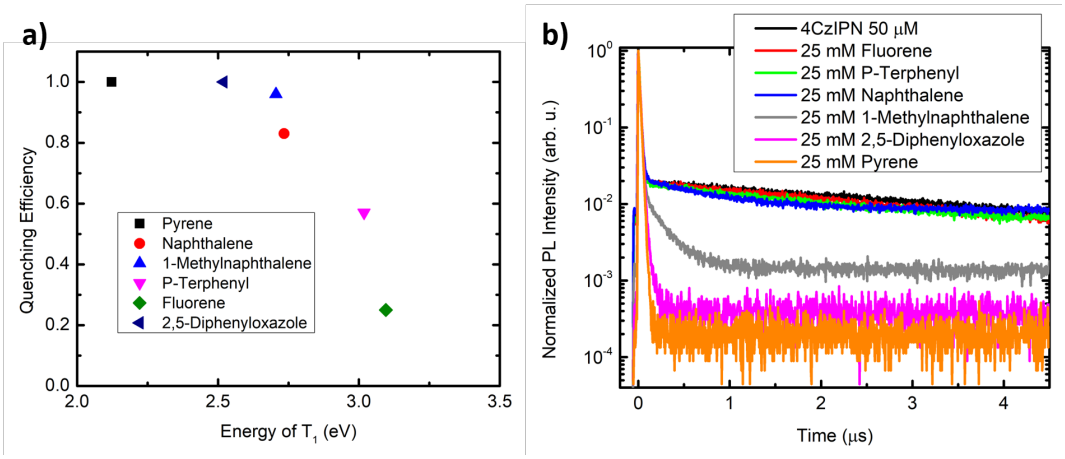

Figure 4.3: (a) Quenching efficiencies of acceptors plotted versus their T_1 energy level. (b) Photoluminescence decay of 4CzIPN with selected acceptors. Measurements were done using TCSPC.

Given that the calculated triplet energies of naphthalene and 1-methylnaphthalene are so similar, I was surprised to see such a difference in PL quenching experiments. I suspect that the energy of T_1 is not the only important factor of Φ_{ET}. Because triplet electron transfer is governed by the Dexter energy transfer mechanism, the donor and acceptor molecules must have suitable wavefunction overlap of their frontier molecular orbitals. Perhaps then, naphthalene and 1-methylnaphthalene differ significantly in this respect. I would also note that 1-methylnaphthalene has a lower degree of symmetry than naphthalene, which could be significant.

4.4 Upconversion Efficiency of Selected Blends

In the following upconversion measurements, the concentration of 4CzIPN was always 50 μM. A continuous-wave argon ion laser with 458 nm excitation wavelength was used for all upconversion measurements. The concentration of acceptor was kept constant at 25 mM because that is approaching the solubility limit of p-terphenyl and several of the

other acceptor molecules. It was also found that at very large concentrations (e.g. ≈ 5 M 1-methylnaphthalene), dimer formation dominated the fluorescence, which is severely detrimental for the anti-Stokes shift. As shown in Figure 4.4, a blend of 4CzIPN and 25 mM naphthalene results in an anti-Stokes shift of about 1.1 eV. Because of difficulties in measuring the absolute quantum yield of upconversion by comparison to standard dyes, we decided to simply compare relative upconversion efficiencies. This was achieved by comparing the integrated upconversion fluorescence spectra for different blends at the same pump power. Upconversion from naphthalene produced only about 40% as much upconversion compared to p-terphenyl at the same concentration. This is not surprising, however, considering that the Φ_{fl} of p-terphenyl is 95%, whereas the Φ_{fl} of naphthalene is about 23%.

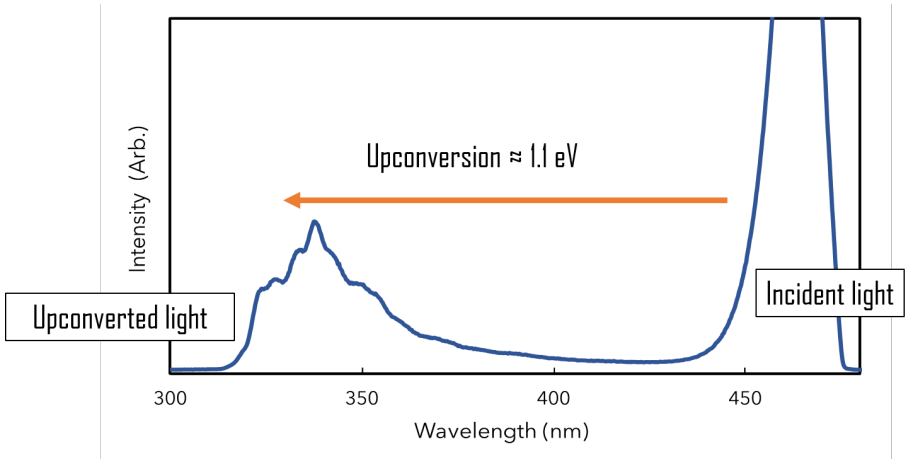

Figure 4.4: TTAUC in benzene with 50 μM 4CzIPN and 25 mM naphthalene. No filters were used to block residual fluorescence from 4CzIPN or scattered pump light.

In Figure 4.5, the relative amount of upconversion with three different acceptors is compared. Amazingly, using 1-methylnaphthalene as an acceptor with 4CzIPN results in an approximately 5-fold increase in upconversion compared to when p-terphenyl is used as an acceptor. If we take the upconversion efficiency measured in the literature [52] for 4CzIPN with p-terphenyl, 2.8% (on the 50% scale), this would imply that 4CzIPN with

1-methylnaphthalene has an upconversion efficiency of around 14%. This is extraordinary due to the large anti-Stokes shift, high upconversion efficiency, and lack of heavy atoms in this blend. These results were repeated multiple times and the difference in upconversion efficiency was consistent every time. What I have not been able to explain is how 1-methylnaphthalene is able to achieve such a higher efficiency compared to naphthalene, whose energy levels and quantum yield of fluorescence are nearly identical. Furthermore, I cannot explain how 1-methylnaphthalene is so much more efficient that p-terphenyl, despite p-terphenyl having a fluorescence quantum yield that is about four times higher than 1-methylnaphthalene. The quenching efficiency of 1-methylnaphthalene, meanwhile, is not even twice as large as the quenching efficiency of p-terphenyl. I strongly suspect that the symmetry of 1-methylnaphthalene may play a role, and that its symmetry may impact the energy and stability of the possible TTA products, in turn affecting f and Φ_{TTA}. Perhaps TTA in 1-methylnaphthalene strongly favors singlet formation, whereas in the other acceptors the triplet and quintet excited states are more competitive with the formation of the desired excited singlet state. If the triplet and quintet states can decay non-radiatively to the ground state, then one would expect their contribution to have a negative impact on the overally upconversion efficiency. I am optimistic that quantum chemical calculations could shed light on these experimental differences.

In the upconversion experiments using 4CzIPN as a triplet sensitizer, there was always a considerable amount of residual fluorescence from 4CzIPN. From the photophysical parameters measured in Chapter 3, the Φ_{ISC} of 4CzIPN in benzene is determined to be 0.91 and for 4CzIPN-Br 0.98. Therefore, I thought that the overall upconversion efficiency of blends could be improved by using 4CzIPN-Br instead of 4CzIPN. However, the quenching efficiency of 1-methylnaphthalene, naphthalene, and p-terphenyl were unexpectedly low for 4CzIPN-Br, despite the fact that its singlet and triplet energies are nearly identical to 4CzIPN. Clearly, the parameters that affect Φ_{ET} could benefit from further investi-

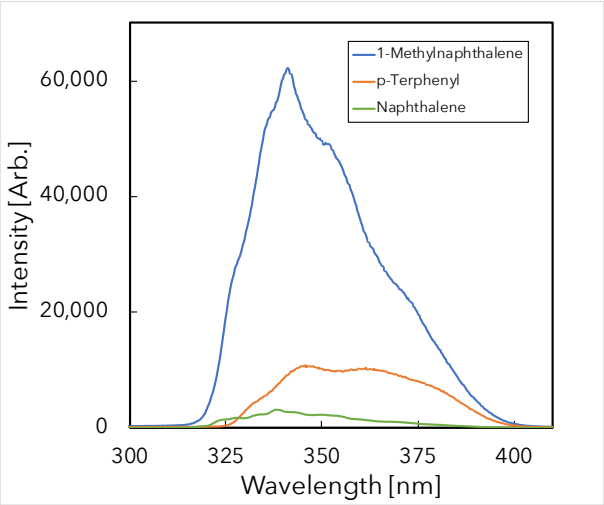

Figure 4.5: Upconversion spectra of 50 μM 4CzIPN with 25 mM of acceptor (identity indicated by the legend), using the same pump intensity and detector acquisition settings for each measurement so that the integrated spectra are directly proportional to Φ_{UC}.

gation. At any rate, the quenching efficiency of PPO toward 4CzIPN-Br was quite good (near 100%), and it was determined that using 4CzIPN-Br instead of 4CzIPN with PPO resulted in an approximately 2-fold increase in upconversion, as shown in Figure 4.6. It would seem as though the relative differences in ISC efficiency cannot alone explain such a large increase in upconversion. In order to better understand the difference, one would have to consider the effects of spin-cycling and include the differences in molar absorptivity for 4CzIPN and 4CzIPN-Br (even though the difference is quite small).

Inspired by the research that Taku Ogawa was working on (the visiting PhD researcher I worked with for a few months at UCSB), I thought it would be interesting to add a third component to the upconversion blends - an 'energy collector'.[62] Acceptor materials have strict singlet and triplet energy requirements, and few also have a high quantum yield of fluorescence emission. A third energy collector component can be used to transfer energy from the acceptor material, which has a poor fluorescence quantum yield, to the energy collector, which has a very good fluorescence quantum yield, through

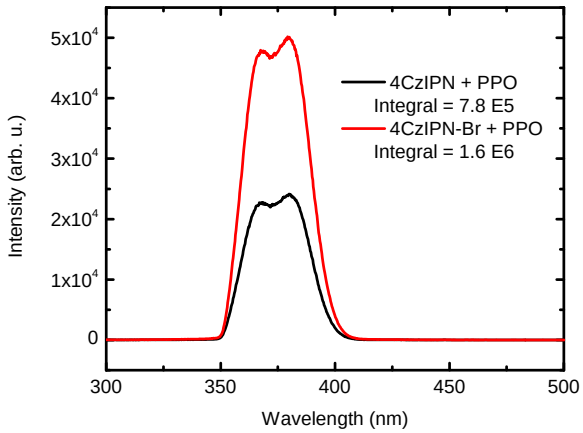

Figure 4.6: Upconversion spectra of 25 mM PPO with 4CzIPN and 4CzIPN-Br. The concentration of triplet sensitizer was 50 μM in both blends. A Thorlabs UG-11 filter was used to block scatterd pump light and residual fluorescence from the TADF materials.

efficient FRET. If the rate of FRET can outcompete the rate of singlet non-radiative decay from the acceptor, the poor fluorescence quantum yield of the acceptor will be completely circumvented by the energy collector's high fluorescence quantum yield. This also provides an opportunity for tuning the upconversion emission wavelength by simply selecting different energy collector materials to include in the blend. This is effectively the same strategy employed in Hyperfluorescence. The scheme for TTAUC with an energy collector is presented in Figure 4.7. Because 1-methylnaphthalene had the best quenching efficiently combined with a high singlet energy, it was the best choice for the intermediate acceptor. For the energy collector, we chose to use p-terphenyl. Although the spectral overlap integral was not expected to be high between 1-methylnaphthalene and p-terphenyl, I figured it would be good enough. Besides, I thought it would be very powerful to show that upconversion with 4CzIPN and p-terphenyl could be enhanced by simply adding another component to the blend. In choosing the right energy collector, it is very important that its T_1 energy is higher than the T_1 energy of the acceptor. In addition, the absorption spectrum of the energy collector should overlap considerably

with the fluorescence spectrum of the acceptor, in order to ensure fast FRET.

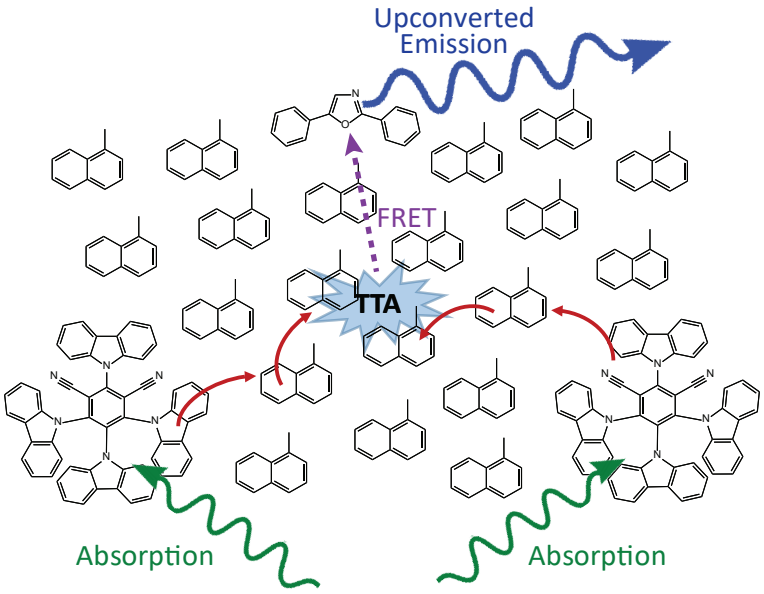

Figure 4.7: Schematic representation of an upconversion blend that utilizes a third component - an energy collector. In the scheme, 4CzIPN is used as the triplet sensitizer, 1-methylnaphthalene as the acceptor, and PPO as the energy collector. Solvent molecules are ignored.

Figure 4.8 shows the upconversion spectra with increasing concentration of the ternary energy collector p-terphenyl. All of the blends had 50 μM 4CzIPN and 25 mM 1-methylnaphthalene. Maximum upconversion was achieved when 18 mM p-terphenyl was added to the 4CzIPN and 1-methylnaphthalene blend, although, due to lack of data points at intermediate concentrations, upconversion may not be maximided at this concentration. The upconversion intensity was increased by a factor of ≈ 4.5, which implies a very high efficiency of FRET from 1-methylnaphthalene to p-terphenyl (the fluorescence quantum yield of 1-methylnaphthalene and p-terphenyl in benzene were determined to be 13% and 87%, respectively. If we take the relative upconversion efficiency of 4CzIPN and 1-methylnaphthalene to be 14%, as determined from Figure 4.5, then the upconversion efficiency of the ternary blend is 63%, which exceeds the 50% maximum theoretical efficiency. Thus, I suspect that the determination of the upconversion efficiency reported

by Chihaya Adachi et al. is inaccurate.

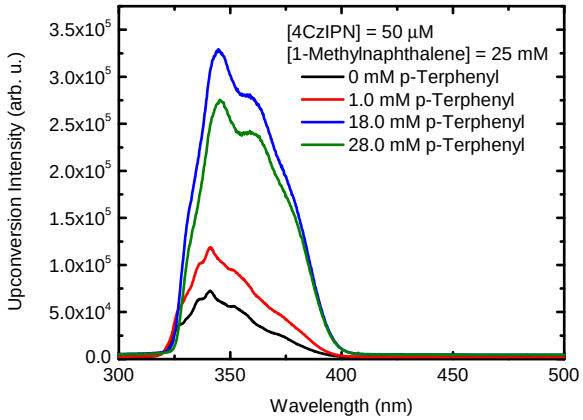

Figure 4.8: Upconversion spectra of ternary blends using identical pump power and acquisition settings.

Regardless, in these experiments I have demonstrated that careful selection of the acceptor molecule, combined with an appropriate energy collector, is able to enhance the upconversion yield by a factor of 22.5. With just careful selection of an acceptor, in this case 1-methylnaphthalene, the upconversion efficiency was improved over p-terphenyl by a factor of 5 and the anti-Stokes shift increased from 0.83 eV to 1.1 eV, a current world-best for anti-Stokes shifts in TTAUC.

Measuring the absolute quantum yield of upconversion is notoriously difficult, and could benefit from new experimental procedures. In particular, I believe it would be worthwhile to try measuring Φ_{UC} using air-tight, small-volume cuvettes in an integrating sphere, rather than by comparison to some standard dye solution, as is usually done. Further optimization of concentrations for binary and ternary blends could increase Φ_{UC} substantially. In addition, there may be other equally good, or better, acceptor candidates. Time permitting, I would have liked to have investigated the use of fumaronitrile and 3-phenyl dibenzofuran as acceptors. In addition, I would have liked to investigate TTAUC in solid-state thin films. 4CzIPN-Br, due to its long diffusion length, would be an ideal candidate for planar geometries (pure acceptor layer on top of a pure donor layer,

or, even better, two acceptor layers sandwiching a donor layer in the middle). Excimer and dimer formation would probably be a more serious problem in the solid-state, but hopefully not insurmountable.

Chapter 5

Adding Lewis Acids to Organic Semiconductors: A Primer

This brief chapter serves to prime the reader for the content of the next two chapters which concern adding Lewis acids to organic semiconductors. First, let us be clear about what a Lewis acid is and how it is different from a Brønsted acid. Lewis acids and bases can be broadly defined as electron acceptors and electron donors, respectively. A typical Lewis acid is boron trifluoride, BF_3, whose central boron atom is sp^2 hybridized. Thus, each fluorine atom makes a sigma bond with boron and the complex takes on a trigonal planar geometry. The central boron atom, however, also has an empty p_z orbital, which will be attracted to nearby electrons, should they happen to come into proximity. A typical Lewis base is ammonia, NH_3, a compound whose central nitrogen atom is sp^3 hybridized. With 5 valence electrons from nitrogen and one from each hydrogen atom, each hydrogen atom makes a sigma bond with nitrogen, leaving a fourth region of electron density surrounding nitrogen occupied by a lone pair of electrons. It is this lone pair that makes ammonia electron donating. Naturally, the electron-donating character of a Lewis base is reactive toward the electron-accepting character of a Lewis acid. When a Lewis

acid forms a bond with a Lewis base, it is called a Lewis acid-base adduct. This binding interaction results in a partial negative charge on the Lewis acid and a partial positive charge on the Lewis base. Lewis acid-base adducts have a very rich chemistry, and are often used as catalysts. For our purposes, however, we were interested just in the adduct itself, and not the reactivity of the adduct with other chemical species.

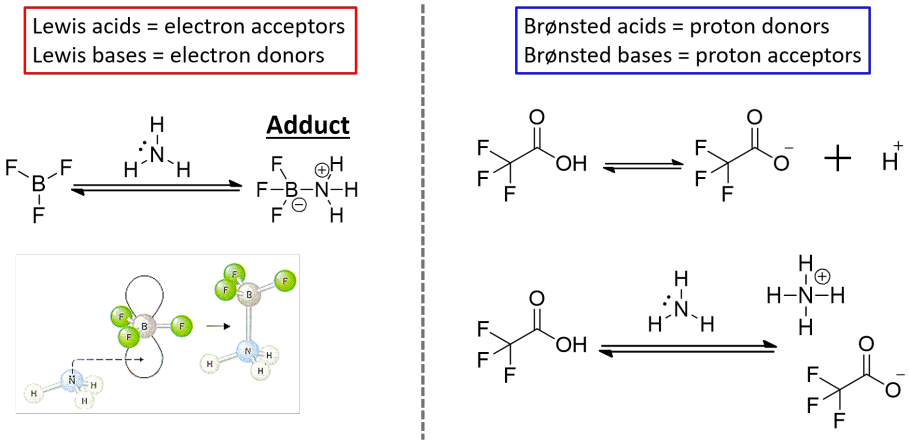

Figure 5.1: Comparison of Lewis acid/base and Brønsted acid/base definitions.

Brønsted acids and bases are not so dissimilar from the Lewis definition, except that Brønsted acids and bases are defined with respect to proton donating and accepting ability, rather than electron donating and accepting ability. Therefore, a Brønsted acid is a molecule who is capable of donating a proton to some other species, and a Brønsted acid is a molecule who is capable of accepting a proton from some other donor. Trifluoroacetic acid, TFA, is a typical strong acid, in that its single hydrogen atom is able to dissociate relatively easily from the rest of the complex, resulting in a positively charged proton and a negatively charged conjugate base. Because electron donors are typically capable of bonding to protons, the typical Lewis base NH_3 is also a Brønsted base. Similarly, a bare proton is essentially a Lewis acid. Although TFA is a Brønsted acid and, in some sense, a Lewis acid, BF_3 is definitively not a Brønsted acid, despite being a clear Lewis acid. These differences are summarized in Figure 5.1.

As I had just mentioned, Lewis acid-base adducts have been pretty extensively studied already. In particular, the Lewis acid 'BCF' has been studied a lot due to its relatively strong acidity and good stability in comparison to many other Lewis acids. This makes it reasonably reactive and relatively easy to handle, properties which have seen it used to accomplish a variety of chemical reactions which require the use of a Lewis acid. In particular, BCF is known to form stable adducts with many small molecules that contain Lewis basic functional groups, such as nitriles, amines, alcohols, and phosphines, to name a few. Because of their electron-donating properties, many Lewis basic aromatic heterocycles (thiophene, thiazole, pyridine, etc.) are incorporated into the backbone of organic semiconductors. Therefore, one might expect that adding a Lewis acid to an organic semiconductor with a sterically accessible Lewis basic site would result in adduct formation, although it isn't obvious what effect this will have on the organic semiconductor. In 2009 members of Guillermo Bazan's laboratory at UCSB had precisely this idea and found that adduct formation resulted in redshifting the organic semiconductor's absorbance, i.e. it decreased the optical gap, in proportion to the strength of the Lewis acid (Figure 5.2). Thus, they had discovered a strategy to modify the optical properties of organic semiconductors *post synthesis*. This could be immensely practical, because rather than synthesizing from scratch several different organic semiconductors with different optical properties tailored to particular applications, you could instead just make one organic semiconductor and then add the appropriate Lewis acid to get the desired optical property.

Several research groups around the world took advantage of this strategy, but a surprising discovery was made in 2014 by members of Thuc-Quyen Nguyen's laboratory, also at UCSB. They found that adding a small amount of the Lewis acid BCF to a particular organic semiconductor resulted in the symptoms of p-type doping, i.e. increased mobility and increased free charge carrier density. Soon thereafter, other research groups showed

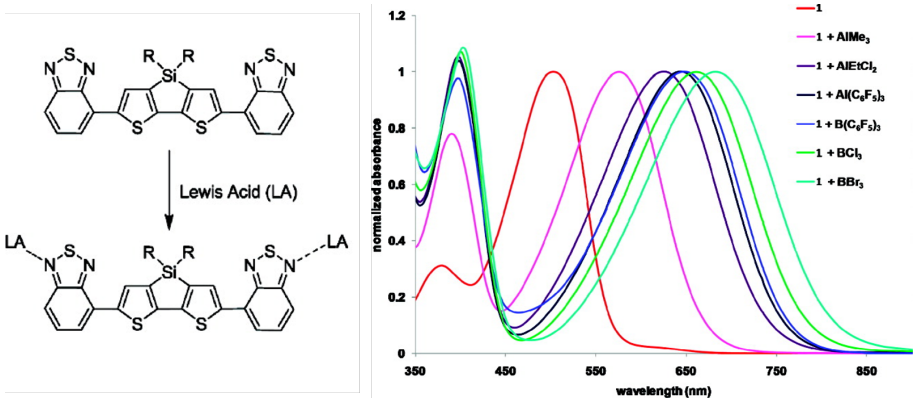

Figure 5.2: First demonstration of how Lewis acids can be used to tune the optical properties of an organic semiconductor oligomer.

evidence of p-type doping with BCF when added to other organic semiconductors. Some groups showed that it was a more efficient dopant than the archetypical p-type dopant of the time, F_4TCNQ, and others showed that it could dope materials which outright couldn't be doped by F_4TCNQ at all. With all of this buzz being generated, still nobody had shown how the Lewis acid BCF was capable of p-type doping. There was a bounty out for discovering the mechanism of doping behind adding BCF to organic semiconductors, and my research group was well positioned to solve this puzzle.

Members from Bazan's lab at UCSB (especially Dirk Leifert) synthesized a series of polymers specifically designed to probe this scientific problem. The three main polymers that we were to study included different combinations of four monomer units: fluorene, cyclopentadithiophene (CPDT), benzothiadiazole (BT), and pyridylthiadiazole (PT). Fluorene and CPDT are electron donating moieties, whereas BT and PT are electron deficient moieties. Thus, combining one of the electron donating moieties with one of the electron deficient moieties results in a donor-acceptor repeat unit that has been demonstrated to be a superb design strategy for synthesizing high-performance polymeric organic semiconductors. Fluorene is a weaker electron donor than CPDT, and BT is a weaker electron donor that PT. Critically, PT has a pyridyl nitrogen atom which is sig-

nificantly more Lewis basic and sterically accessible than the azole nitrogens of BT (PT also has azole nitrogens). The three polymers we studied are shown in Figure 5.3.

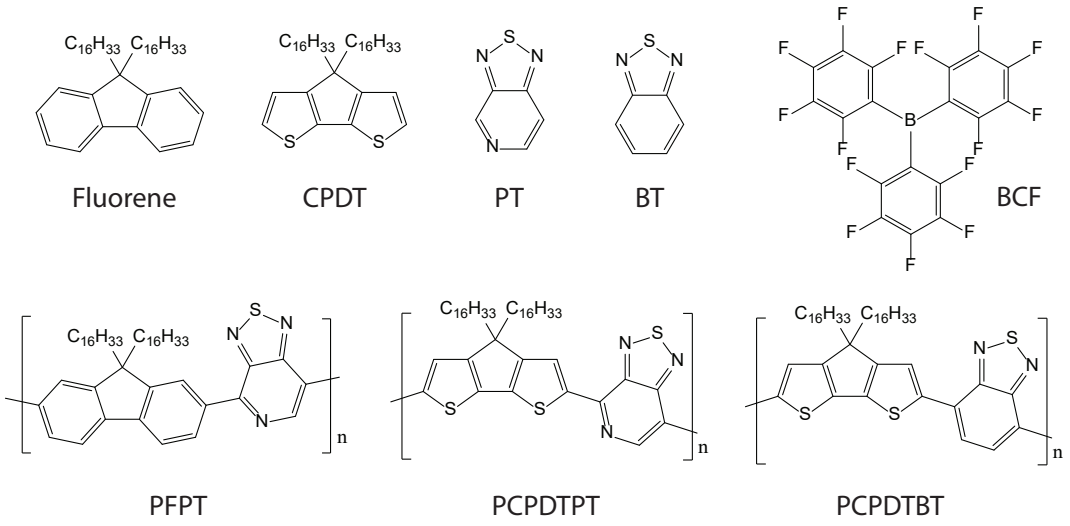

Figure 5.3: Chemical structures and abbreviations for the relevant monomers and polymers. The Lewis acid BCF is also shown.

We quickly determined that PFPT wasn't doped by BCF, but both PCPDTBT and PCPDTPT were. Therefore, we used the PFPT plus BCF system to do a thorough characterization of the adduct formation process, as described in Chapter 6, and used the two remaining polymers to investigate the doping mechanism, as described in Chapter 7. In the end, I was able to determine that doping by BCF occured through a completely unforeseen mechanism: BCF complexes with trace amounts of water, forming a strong Brønsted acid, which subsequently protonates the CPDT moiety of a suitable polymer. Then, a neutral conjugated segment donates an electron to the positively charged, protonated site, leaving behind a mobile hole. Thus, doping and adduct formation with the polymer are two separate phenomenon, as shown in Figure 5.4. Hopefully, this information will help the reader understand the context of the next two chapters.

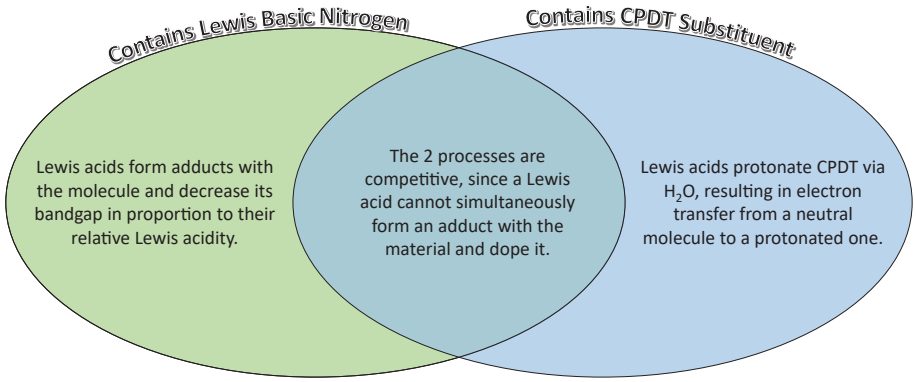

Figure 5.4: Venn diagram summarizing the effect of adding a Lewis acid to organic semiconductors.

Chapter 6

Optical Gap Engineering of Lewis Basic Polymers via Incorporation of Lewis Acids

The contents of this chapter appear in [63].

In this chapter, I investigate the binding properties of the Lewis acid tris(pentafluorophenyl)borane with a Lewis basic semiconducting polymer, PFPT, and the subsequent mechanism of bandgap reduction. Experiments and quantum chemical calculations confirm that the formation of a Lewis acid adduct is energetically favorable ($\Delta G^{\circ} < -0.2eV$), with preferential binding at the pyridyl nitrogen in the polymer backbone over other Lewis basic sites. Upon adduct formation, ultraviolet photoelectron spectroscopy indicates only a slight decrease in the HOMO energy, implying that a larger reduction in the LUMO energy is primarily responsible for the observed optical bandgap narrowing ($\Delta E_{opt} = 0.3eV$). Herein, we also provide the first spatially resolved picture of how Lewis acid adducts form in heterogeneous, disordered polymer:tris(pentafluorophenyl)borane

thin films via one- (1D) and two-dimensional (2D) solid-state nuclear magnetic resonance. Notably, solid-state 1D ^{11}B, ^{13}C{^{1}H} and ^{13}C{^{19}F} cross-polarization magic-angle spinning (CP-MAS) NMR and 2D ^{1}H{^{19}F} and ^{1}H{^{1}H} correlation NMR analyses establish that BCF molecules are intercalated between branched $C_{16}H_{33}$ sidechains with the boron atom facing towards the pyridyl nitrogen atoms of PFPT.

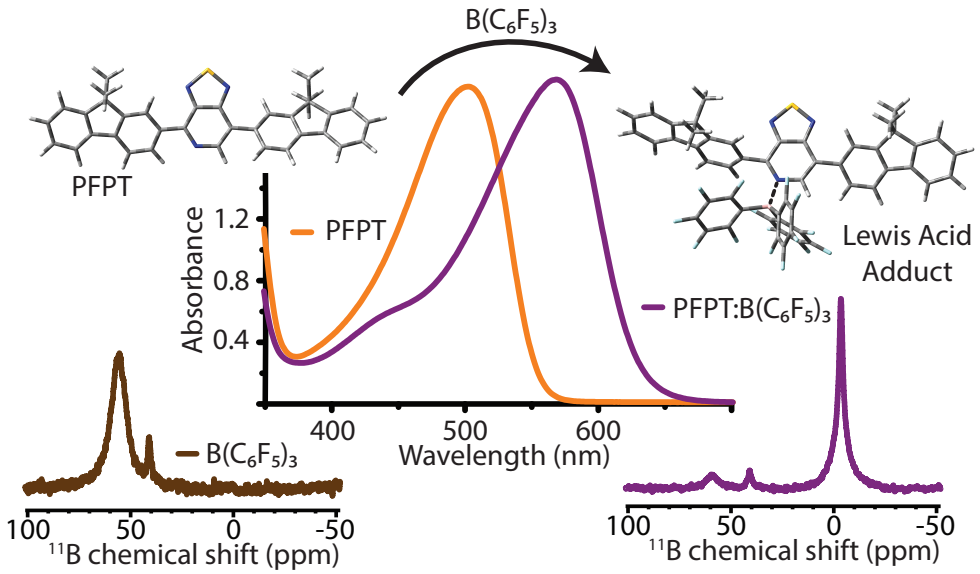

Figure 6.1: Summary of changes observed upon Lewis acid-base adduct formation using the Lewis acid BCF and Lewis basic semiconducting polymer PFPT.

This work was largely collaborative. I am indebted to Dr. G. N. Manjunatha Reddy for performing the solid-state NMR experiments, and was very grateful to receive some excellent practical advice from him concerning the preparation of figures. I wish I would have been shown how to prepare high quality figures at a much earlier stage in my PhD. Alas, better late than never. I am also grateful to Dirk Leifert, who synthesized PFPT and did some absorption measurements. I thank David Cao for performing XPS and UPS.

6.1 Background

A key advantage of organic semiconductors over inorganic counterparts is their ability to precisely tune the semiconductor's optical properties via synthetic modification.[64] Donor-acceptor (D-A) organic chromophores have become a particularly fruitful category of organic semiconductors with a wide variety of optical and electrical properties which has led to their incorporation in multiple technologies, such as organic photovoltaics (OPVs), organic field-effect transistors (OFETs), and organic light-emitting diodes (OLEDs).[65, 66, 67, 14, 68, 69, 70, 71] In these D-A molecular structures, there are alternating electron rich (D) and electron poor (A) moieties, resulting in excited states with significant intramolecular charge transfer (ICT) character. By tuning the relative strength of the donor and acceptor units, the optical bandgap (E_{opt}) can be tuned from the ultraviolet to the near-infrared. A post-synthesis strategy for tuning the optical properties of Lewis basic D-A type organic semiconductors via incorporation of Lewis acids was demonstrated by Welch et al. in 2009.[72] The resulting Lewis acid adducts showed red-shifted absorption, i.e. a reduction of the bandgap, to a degree consistent with the strength of the Lewis acid. Since then, this general strategy has been utilized by various research groups in order to adjust the optoelectronic properties of organic semiconductors with Lewis basic binding sites.[73, 74, 75, 76, 77] In particular, Lewis acids have been used to tune the emission of polymer light-emitting diodes (PLEDs) [78, 79] and enhance the charge transport properties (via p-type doping) of vertical diodes [80, 81], solar cells [82, 83], OFETs [84, 85], and organic thermoelectric devices [86].

$B(C_6F_5)_3$ has been the Lewis acid of choice due to its strong Lewis acidity, relative stability to air and to moisture, resistance to B-C bond cleavage, and high solubility in a variety of organic solvents.[87, 88, 89] While there has been considerable investigation into the changes in optical properties upon adduct formation in conjugated polymers, atomic-

level interactions that account for the binding mechanism, with concomitant electronic and thermodynamic descriptions, have remained poorly understood. X-ray diffraction studies of Lewis acid adduct single crystals have shed insight on the nature of bonding interactions between the Lewis acid and Lewis basic sites of small molecule organic chromophores, e.g. pyrroles and indoles, providing details such as boron-nitrogen bonding distances.[72, 90, 91, 92] However, for polymers exhibiting multiple different Lewis basic sites, achieving a complete description of structures and binding interactions using X-ray diffraction techniques is not feasible due to structural and compositional heterogeneities. Thus, alternative techniques are required to gain insight into the nature of binding interactions between Lewis acids and π-conjugated polymer systems.

Solid-state magic-angle spinning (MAS) nuclear magnetic resonance (NMR) spectroscopy, due to its sensitivity to molecular interactions, is well-suited to probe short-range structures in heterogeneous materials. The application of solid-state NMR spectroscopy for the study of conjugated polymers has largely been centered on techniques that provide key information of different local bonding environments around each atom.[93] Information obtained from chemical shifts and dipole-dipole couplings can be translated into a description of understanding how inter- and intramolecular interactions influence three-dimensional structures. To this end, powerful 2D solid-state NMR experiments in conjunction with modelling techniques have been employed to elucidate, for example, the inter- and intramolecular interactions in poly(3-hexylthiophene) [94], perylenediimide (PDI) [95], a bithiophene derivative (TT) [96], ribbon-like self-assembly of pyrimidine base [97], diketopyrrolo-pyrrole-dithienylthieno[3,2-b]thiophene (DPP-DTT) [98], and polymer:fullerence composites with different sidechain lengths and structures [99, 100, 101].

The main objective of this work is to elucidate the binding interactions of the Lewis acid tris(pentafluorophenyl)borane (BCF) with the organic semiconductor poly[2,7-(9,9-

bis(2-hexadecyl)-9*H*-fluorene)- *alt*-4,7-(9,9- dihexadecyl-9*H*- fluorene-2,7 diyl)bis[1,2,5]-thiadiazolo[3,4-*c*]pyridine)] (PFPT). This polymer was chosen due to (i) the lack of observable p-type doping upon adduct formation so that the effects of binding could be isolated from the effects of doping (Figure 6.2), and (ii) the incorporation of the [1,2,5]-thiadiazolo[3,4-c]pyridine (PT) acceptor moiety, which has been shown to strongly bind various Lewis acids, though it remains unclear which of the 4 Lewis basic sites participate in adduct formation (Figure 6.3).[74] With a more detailed investigation of the aforementioned binding interactions, the aim of this study is to achieve a fundamental understanding of how these interactions manifest themselves in the modification of optoelectronic properties.

In this chapter I study the novel PFPT polymer and its interaction with BCF in both solution and film by using a multitechnique approach that combines solution- and solid-state NMR spectroscopy, optical absorption spectroscopy, photoluminescence spectroscopy, X-ray photoelectron spectroscopy (XPS), ultraviolet photoelectron spectroscopy (UPS), and DFT calculations. Formation of the adduct is accompanied by a $\approx$ 0.3 eV red-shift of the main absorption peak. Further quantitative analysis of the absorbance changes in solution with various concentrations of BCF indicate that adduct formation follows the behavior of a 1:1 binding isotherm, with binding able to occur at up to 1 BCF molecule per repeat unit of PFPT. XPS, in addition to quantum chemical calculations, indicate that BCF preferentially binds to the pyridyl nitrogen of PT. We utilize multinuclear (^{1}H, ^{13}C, ^{11}B and ^{19}F) solid-state NMR to gain atomic-level insight into the intermolecular arrangements in PFPT:BCF adducts and find that BCF molecules are intercalated between the alkyl chains of fluorene moieties in PFPT such that the boron atom of BCF is directly adjacent to the pyridyl nitrogen of the PT moiety for efficient and energetically favorable binding. Finally, results from UPS show that the bandgap reduction observed when the PFPT:BCF complex forms is primarily attributable to a

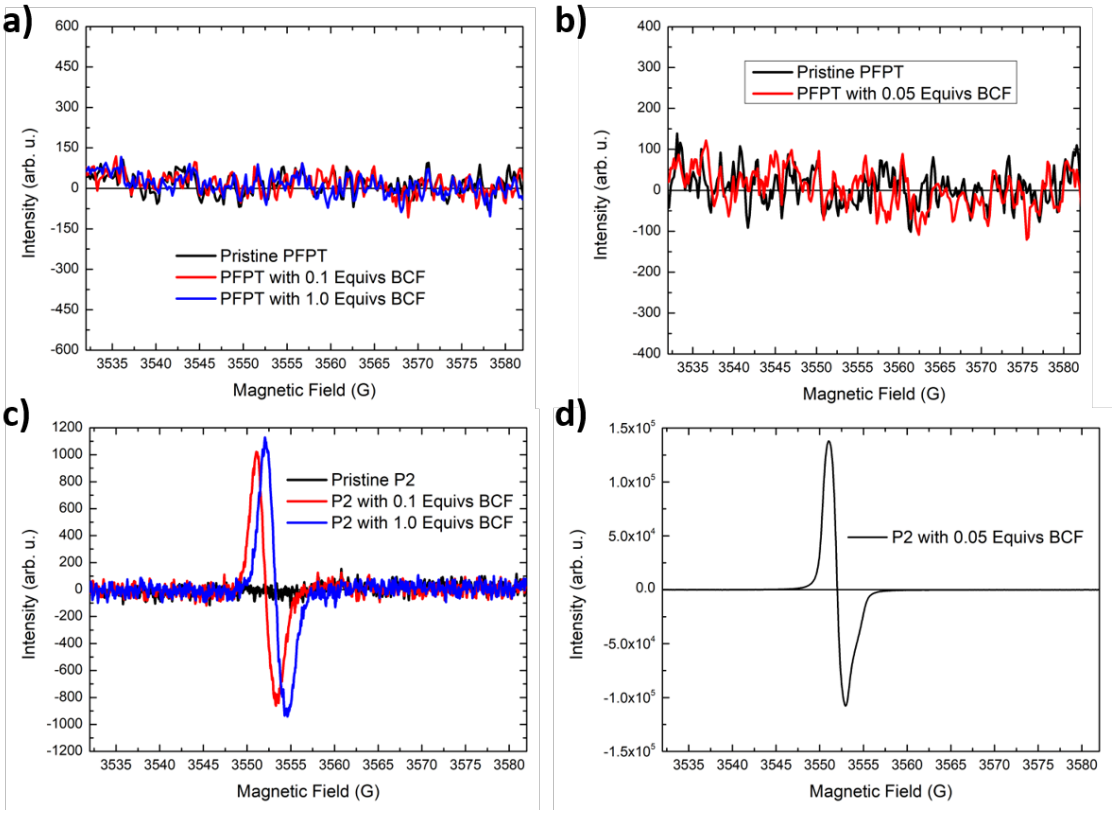

Figure 6.2: X-band EPR spectra of PFPT in solution (a) and solid state (b) with various amounts of BCF. Solutions for EPR were made at a polymer concentration of 0.125 mg/mL in chlorobenzene. No radicals were observed in solution or solid-state for PFPT. In (c) and (d) a different polymer, P2, is shown with BCF in solution (c) and solid state (d) to demonstrate what a doped polymer's EPR spectrum looks like.

reduction of the energy of the lowest unoccupied molecular orbital.

6.2 Experimental Methods and Materials

For the synthesis of the PFPT polymer, please refer to the appropriate publication.[63] The chemical structure of PFPT with proper regioregularity is shown in the same reference. BCF was purchased from Tokyo Chemical Industry in the purity greater than 98% and used as received. All solvents were purchased dry. Molecular sieve was added to these solvents before use. All measurements and sample preparation were carried out in

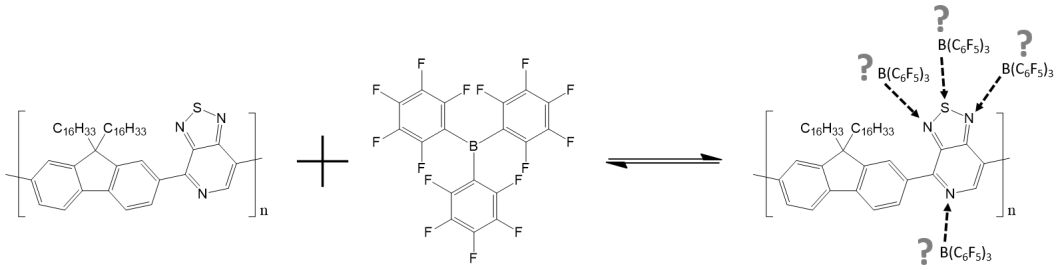

Figure 6.3: Schematic representation of Lewis acid adduct formation, which is an equilibrium process with multiple potential Lewis basic binding sites on the polymer PFPT.

oxygen-free environments. All solutions were allowed to equilibrate at room temperature overnight, or longer, before measurements were obtained or films prepared.

Thin films used for absorption and fluorescence spectroscopy were spun-coat (800 rpm) onto clean glass substrates from solutions in chloroform where the concentration of the polymer was approximately 20 mg/mL. They were then encapsulated using epoxy and another clean glass substrate to exclude the presence of oxygen, after which measurements were performed outside of the glovebox. For solution measurements samples were prepared inside a nitrogen atmosphere glovebox, loaded into a custom made cuvette with Teflon seal, sealed, and then brought out of the glovebox for measurements. Absorption measurements were performed on a Lambda 750 UV-Vis/NIR Spectrophotometer. The optical bandgaps (E_{opt}) were determined by the onset of absorption. A charge-coupled device camera (Princeton Instruments Pixis: 400) was used to obtain steady-state fluorescence spectra. A blackbody light source was used for spectral calibration of the detector. The photoluminescence quantum yields in solution ($\lambda_{exc} = 503$ nm) were determined in the usual way by reference to a standard dye, in this case, Rhodamine B.[4] The photoluminescence quantum yields in the solid state were determined using an integrating sphere and excitation wavelength of 458 nm.[37]

X-band Electron Paramagnetic Resonance measurements were performed on a Bruker

EMX spectrometer with a ER041MR microwave bridge using a dielectric cavity. The sample was placed in a 0.8 mm (inner diameter) round quartz capillary which was held in the cavity by a 4 mm quartz EPR tube. The microwave power was 60 mW, the modulation amplitude was 1 Gauss, and the modulation frequency was 100 kHz. A concentrated solution was drawn into the capillary in the glovebox, both ends were sealed with Critoseal, and then brought out of the glovebox for measurements. Solid state samples were prepared in a similar manner, except that the solvent was allowed to evaporate from the capillary before sealing with Critoseal in the glovebox.

For solution-state NMR, samples were measured using quartz NMR tubes with a custom-made Teflon screw-cap seal. Samples were loaded into the NMR tube inside the nitrogen atmosphere glovebox and sealed, then brought outside the glovebox for measuring. Deuterated chloroform was chosen due it being readily available, it being significantly cheaper than deuterated chlorobenzene, and improved solubility of the polymer in chloroform over chlorobenzene. Measurements were carried out on an Agilent Technologies 400 MHz, 400-MR DD2 Spectrometer. Proton chemical shifts are referenced to the proton peaks of residual chloroform in the bulk chloroform-d solvent. ^{11}B chemical shifts are reported relative to $\delta = 0.0$ for boron trifluoride diethyl etherate. In all solution NMR experiments the concentration of the polymer (with respect to the repeat unit) and/or BCF were 20 mM.

For solid-state NMR, samples were prepared by first creating a solution (where the concentration of the polymer was approximately 20 mg/mL in chloroform) in a clean 20 mL vial. Then, the solvent was allowed to evaporate in the nitrogen atmosphere glovebox. The material was scraped off the walls of the vial and the powder was transferred into an air-tight rotor for subsequent measurements in a glove box. PFPT:BCF complex was packed into a 2.5 mm (outer diameter) zirconia rotor fitted with a Vespel cap. The purity of the PFPT:BCF complex is reflected in the ^{1}H MAS NMR spectrum shown in

Figure 6.18, which is free from solvent ^{1}H signals. All solid-state MAS NMR spectra were acquired on a 9.4 T Bruker AVANCE-III NMR spectrometer equipped with 2.5 mm H-F-X probehead and Bruker variable temperature (VT) control unit. For more details on the ssNMR, please refer to the appropriate publication.

All ultraviolet photoelectron spectroscopy measurements were performed on a Kratos Axis Ultra DLD spectrometer under vacuum (10^{-7} Torr) using a He I ($h\nu$ = 21.2 eV) discharge lamp at a pass energy of 5 eV. The solutions were spun cast on top of solution cleaned indium tin oxide/glass substrates to give a film with a thickness of approximately 10 nm. The films were electrically grounded to the sample bar using nickel impregnated tape.

All X-ray photoelectron spectroscopy measurements were performed on a Kratos Axis Ultra DLD spectrometer under vacuum (10^{-8} Torr) using monochromated x-rays produced using an aluminum source running at a potential of 14 kV. A pass energy of 20 eV was used for all high-res element sweeps. The samples were spun-cast onto cleaned conductive indium tin oxide/glass substrates. The films were mounted onto a sample bar using double-sided tape, and electrically grounded to the sample bar using nickel impregnated tape. Peak fitting was performed using WINSPEC, and atomic sensitivity factors for each element were taken into account during peak integrations.

Calculated structures were optimized by DFT using the B3LYP functional and 6-31G(d,p) basis set.[26, 102] Solvent effects were considered by using the SMD solvation model (solvent = chlorobenzene). For orbital analysis (TD-DFT), single-point energy calculations were performed on the B3LYP optimized geometries using the ωB97XD functional and 6-31G(d,p) basis set.[103] The value of ω for each structure was determined after sampling a range of arbitrarily chosen values and selecting that which finally satisfied Koopman's theorem.[104] To be clear, the DFT calculations in this chapter were performed by me.

6.3 Optical Absorption and Photoluminescence

Upon addition of BCF to PFPT, a new, red-shifted absorption peak is observed (Figure 6.4, Table 6.3), accompanied by a change in its bright orange color to a dull purple color. Polymer concentrations are reported relative to the single donor-acceptor repeat unit, i.e. fluorene-PT. BCF induces a 0.3 eV (≈70 nm) red-shift in the maximum absorption of PFPT in both film and solution. In solution, adduct formation and concomitant change of the optical properties is fully reversible by the addition of a stronger Lewis base, e.g. pyridine. In solid state thin-films, the PFPT:BCF adduct was found to be relatively stable when exposed to air, despite BCF being known to be hygroscopic.[105] Specifically, over the course of 5 hours, the absorbance of the adduct peak (575 nm) decreased by only 2.8% (Figure 6.5a). After several days of exposure to air, large orange spots were visibly apparent on the otherwise purple film, indicating that BCF was no longer coordinated to a significant amount of the polymer (Figure 6.5b).

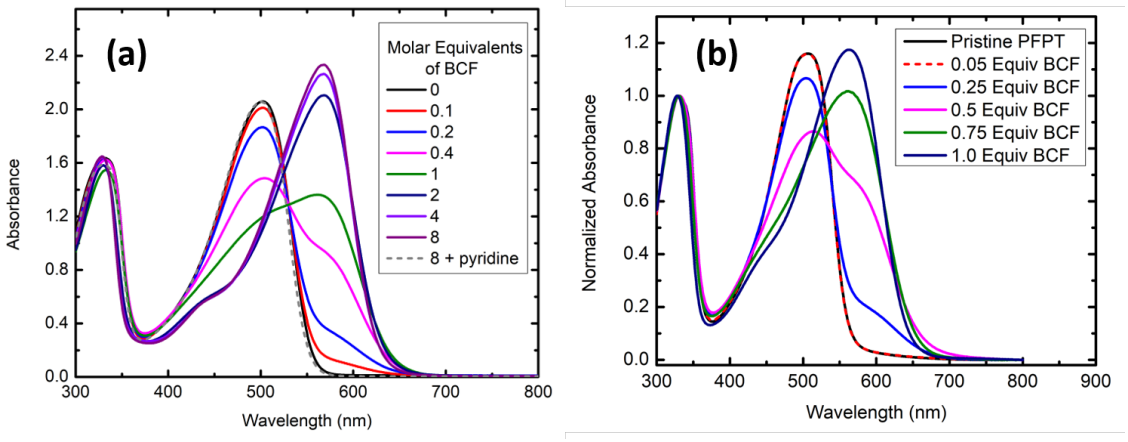

Figure 6.4: Absorption spectra of PFPT with various amounts of BCF in solution (a) and in the solid-state (b).

By analyzing how the concentration of BCF influences the absorbance of the new, red-shifted peak, we were able to determine that PFPT and BCF (in chlorobenzene solution) exhibit the behavior of a 1:1 binding isotherm. Specifically, the mole ratio plot, Figure

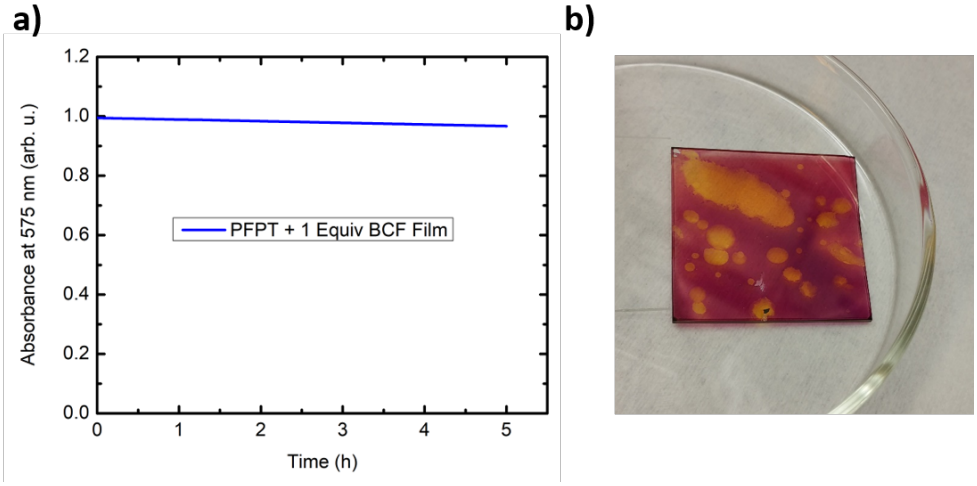

Figure 6.5: (a) Time-dependent absorption of a PFPT film with 1 equivalent of BCF exposed to air. After spin-coating in a nitrogen-filled glovebox, the sample was removed and the absorption measurement was immediately started. (b) Picture of film from (a) after 4 days left in the dark, but exposed to air. The orange spots correspond to pristine PFPT, whereas the dull purple areas correspond to the PFPT:BCF adduct.

6.6a, indicates a 1:1 binding stoichiometry.[106] Using a 1:1 stoichiometry, a Benesi-Hildebrand plot (Figure 6.6b) was constructed from the absorption data after applying a Taylor's series expansion in order to solve for the actual concentration of unbound BCF in solution.[107] The Benesi-Hildebrand equation for a 1:1 complex is given by:

$$\frac{b}{\Delta A} = \frac{1}{S_t K_{eq} \Delta\epsilon [L]} + \frac{1}{\Delta\epsilon S_t} \tag{6.1}$$

where b is the path length of the cuvette, S_t is the total substrate concentration, i.e. initial polymer repeat unit concentration, $[L]$ is the concentration of the unbound ligand at equilibrium, i.e. unbound BCF, ΔA is the change in absorbance at a defined wavelength for a particular ligand concentration (with respect to the free substrate), $\Delta\epsilon$ is the difference in molar absorptivity at the defined wavelength between the bound and unbound complex, and K_{eq} is the equilibrium constant for ligand binding. To use this equation, however, we must first determine $[L]$ at equilibrium after adding a given amount of the

Table 6.1: Summary of optical properties of PFPT and PFPT with 1.0 molar equivalents of BCF (indicated in the table as 'PFPT:BCF'). Errors in PLQY are the standard deviation from the mean for 3 separately prepared samples.

	PFPT, Solution	PFPT:BCF, Solution	PFPT, Film	PFPT:BCF, Film
Absorbance λ_{max} (nm/eV)	503/2.46	568/2.18	507/2.44	575/2.16
E_{opt} (eV)	2.2	1.9	2.2	1.9
PL λ_{max} (nm/eV)	570/2.18	743/1.67	581/2.13	726/1.71
PLQY (%)	75±3	5.4±0.3	11.1±0.6	6.6±0.2

ligand to solution. For a 1:1 binding isotherm model, mass balance of the ligand tells us that:

$$L_t = [L] + [SL] = [L] + \frac{S_t K_{eq}[L]}{1 + K_{eq}[L]} \tag{6.2}$$

where L_t is the total ligand concentration and $[SL]$ is the concentration of the bound complex at equilibrium. A Taylor's series expansion of L_t is:

$$L_t = g(L_t) + g'(L_t)([L] - L_t) + \frac{g''(L_t)}{2}([L] - L_t)^2 \cdots \tag{6.3}$$

where $g(L_t)$ is Equation 6.2, $g'(L_t)$ is $\frac{dL_t}{d[L]}$ and $g''(L_t)$ is $\frac{d^2L_t}{d[L]^2}$. Truncating at the linear term of Equation 6.3 and solving for $[L]$, we find a solution in the form of:

$$[L] = L_t - \frac{\left(\frac{K_{eq}S_tL_t}{1+K_{eq}L_t}\right)}{\left(1 + \frac{K_{eq}S_t}{1+2K_{eq}L_t - K_{eq}^2L_t^2}\right)} \tag{6.4}$$

For each concentration of L_t for which absorbance was measured, $[L]$ was determined by an initial guess of K_{eq} in Equation 6.4. Then, a Benesi-Hildebrand plot was constructed, and from the slope and intercept of the resulting linear fit, another value of K_{eq} was extracted. The initial guess in Equation 6.4 was modified until the K_{eq} determined from

the Benesi-Hildebrand plot was equivalent to the initial guess, which finally results in our reported value of K_{eq} for BCF binding to PFPT. See reference [107] for more details.

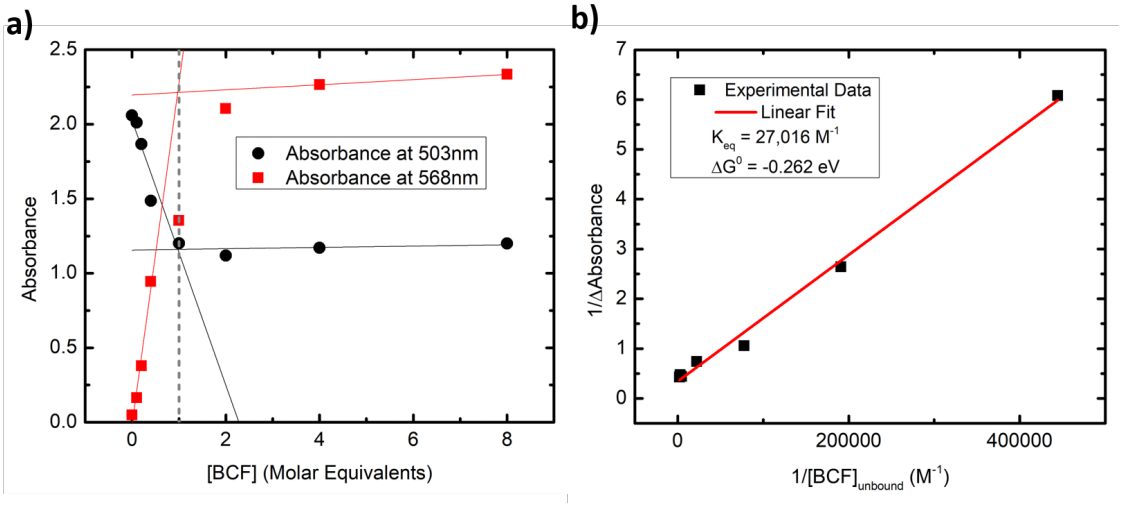

Figure 6.6: (a) Absorbance of the main PFPT optical transition (503 nm) and adduct optical transition (568 nm) as a function of BCF concentration. The dashed vertical line at 1.0 molar equivalents is a guide for the eye. Solid black and red lines are linear fits to regions of high and low BCF concentrations. (b) Benesi-Hildebrand plot.

The above procedure resulted in the determination of the equilibrium binding constant, K_{eq}, which we found to be 27,016 M^{-1} at room temperature, corresponding to a Gibbs free energy change, $\Delta G°$, of -0.262 eV ($\Delta G° = -k_B T ln(K_{eq})$, T = 298 K and k_B = Boltzmann constant). This binding constant is 2 orders of magnitude larger than what was reported for a planar oligomer bearing the PT unit, a difference which we attribute to the relative amount of backbone deformation in the Lewis basic molecule/polymer upon binding BCF, as mentioned above.[74] The procedure for determining these thermodynamic data from simple absorption measurements provides an alternative to NMR measurements, which can also be used to extract the same thermodynamic quantities.

These results suggest that (i) BCF can coordinate to every single PT unit of the polymer, and (ii) that there is only 1 binding site per repeat unit despite there being multiple Lewis basic sites. Previous studies of Lewis basic polymers suggest that BCF

is unable to coordinate to every single repeat unit.[73, 74] These studies also suggest that adduct formation results in a twisting of the otherwise planar polymer backbone. DFT calculations on a fluorene-PT-fluorene (F-PT-F) oligomer indicate that the PFPT backbone is already significantly twisted (Figure 6.7), and upon coordination, twists even further (Figure 6.8). Upon coordinating BCF at the pyridyl nitrogen, the F-PT dihedral angle, which is closest to the pyridyl nitrogen of PT, changes by 56° from −18° to −74°, and the other dihedral angle (PT-F, away from the pyridyl nitrogen) changes by 66° from −35° to +31°. However, the initially twisted state of the PFPT backbone may facilitate complete binding by minimizing steric interference, while also mitigating the energy penalty for breaking conjugation due to twisting of the backbone upon coordination, which may be a significant problem in polymers with planar backbone conformations. Thus, in order to maximize adduct formation, it may be advantageous to use conjugated polymers with non-planar backbones. Our Belgian collaborators are looking into these competing effects via additional DFT calculations.

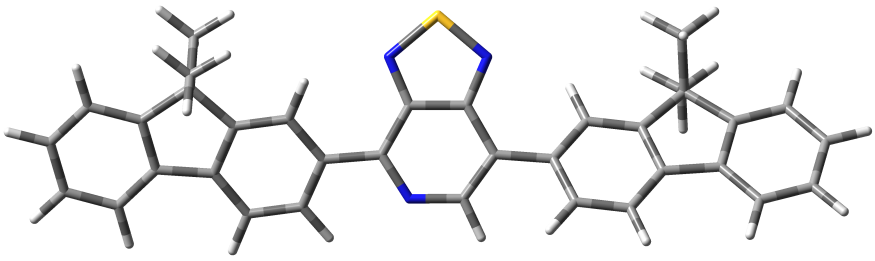

Figure 6.7: Optimized oligomer of PFPT. Dihedral angle of fluorene-PT on the right = −35°. Dihedral angle of fluorene-PT on the left (pyridyl side) = −18°.

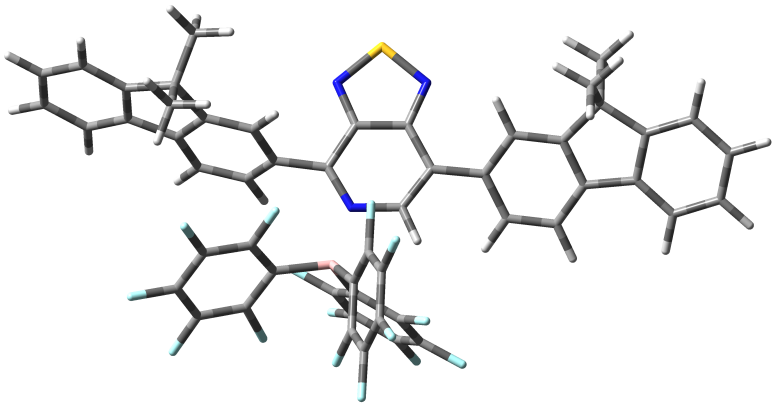

Figure 6.8: Optimized oligomer of PFPT with BCF coordinated to the pyridyl nitrogen. $\Delta U^{\circ} = -0.08$ eV. Dihedral angle of fluorene-PT on the right = 31°. Dihedral angle of fluorene-PT on the left (pyridyl side) = −74°. B-N distance is 1.69 Å.

With 0.5 equivalents of BCF in solution, photoluminescence (PL) is observed from both the adduct and the pure polymer (Figure 6.9a), with adduct emission red-shifted from PFPT emission by about 0.5 eV (173 nm). At 1.0 equivalents of BCF the PL is dominated by adduct emission even though many binding sites are not occupied by BCF, as confirmed by optical absorption. This is clearly a result of inter and intramolecular energy transfer processes. The Stokes shift (peak to peak energy difference) of the adduct (0.5 eV, 175 nm) is large relative to the Stokes shift of PFPT itself (0.3 eV, 67 nm), indicating that the adduct undergoes significant geometrical changes while in the excited state. We suspect that these geometrical changes are also responsible for the large decrease in the photoluminescence quantum yield (PLQY) upon adduct formation, as shown in Table 6.3. These observations are consistent with the 'loose bolt' or 'free rotor effect, which are known to enhance non-radiative decay pathways.[3] In fact, we observed the lifetime of the adduct at 0.5 and 1.0 molar equivalents to be shorter than

the lifetime of the polymer by itself (Figure 6.9b).

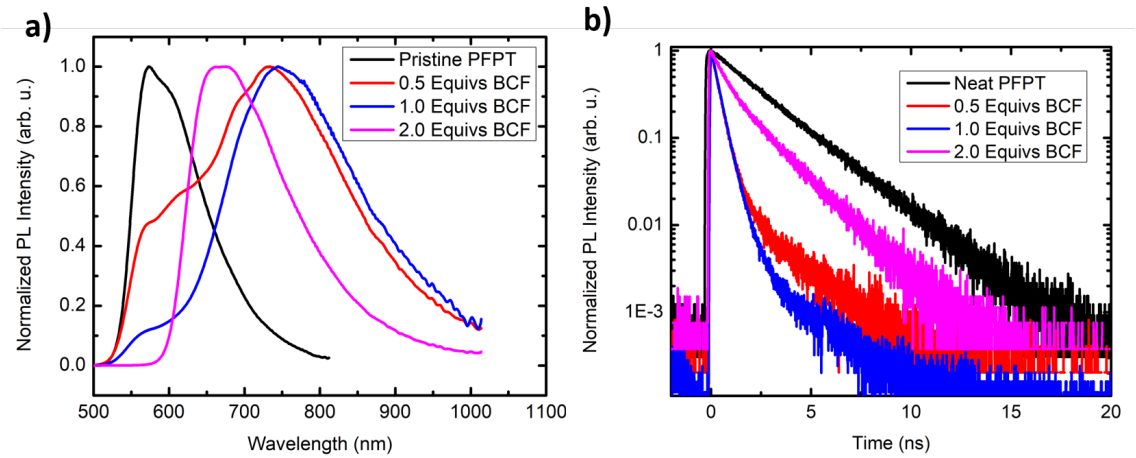

Figure 6.9: (a) Photoluminescence spectra of PFPT with various concentrations of BCF in chlorobenzene. (b) PL decays (710 nm detection wavelength) of PFPT in chlorobenzene with various amounts of BCF.

Interestingly, upon addition of 2.0 equivalents of BCF, the PL maximum blue-shifts relative to the lower BCF concentrations, and the lifetime increases slightly. We attribute this trend to a twisting of the PFPT backbone upon complete coordination of BCF, which then inhibits further geometric relaxation in the excited state. In polymers with only partial coordination of BCF, i.e. at concentrations of 0.5 and 1.0 equivalents, the unbound FPT moieties, together with adduct chain segments, are able to undergo a more favorable geometric relaxation in the excited state, resulting in the observed red-shifted emission. Because the adduct absorption peak wavelength does not significantly change with differing concentrations of BCF, the underlying cause of the blue shifting PL with increasing BCF concentration must be related to the polymer:Lewis acid excited state properties.

The PL of pure PFPT in the solid state (Figure 6.10a) is similar to its PL in solution, although the PLQY of thin films (11%) is lower than the PLQY in solution (75%). From PLQY and lifetime measurements we were able to calculate the radiative (k_r) and non-

radiative (k_{nr}) decay rates in film and solution for the pure polymer (Table 6.3). The relevant equation is as follows:

$$\Phi = \frac{k_r}{k_r + k_{nr}} = \tau \times k_r \tag{6.5}$$

where Φ is the measured PLQY and τ is the measured PL lifetime. (Note that in this interpretation, only decay pathways from the singlet state are considered. Another way of thinking about this is that the rate of intersystem crossing has been lumped into the rate of non-radiative decay, and that any excitons in the triplet state decay non-radiatively to the ground state. Only in extremely rare circumstances are conjugated polymers phosphorescent at room temperature.) The calculated rates of radiative decay were comparable in film and solution, but the rate of non-radiative decay in the solid state was one order of magnitude larger than in solution. Thus, it is likely that in the solid state, where intermolecular energy transfer processes are enhanced due to short intermolecular distances, rapid energy transfer to defect sites and impurities is responsible for the decrease in PLQY.[8]

Table 6.2: Calculated rates of radiative and non-radiative decay for pristine PFPT.

	Solution	Film
k_r (s^{-1})	3.3×10^8	2.2×10^8
k_{nr} (s^{-1})	1.1×10^8	1.8×10^9

The PL maximum of thin films with BCF is red-shifted from the PL maximum of pure PFPT films by about 0.4 eV, or 145 nm (Table 6.3). The Stokes shift of the adduct (0.5 eV, 151 nm) is greater than that of pure PFPT (0.3 eV, 74 nm), not unlike the results in solution. However, in contrast to what is observed in solution, the adduct PL lifetimes are longer than the PL lifetime of neat PFPT (Figure 6.10). From a theoretical standpoint (Einstein's coefficient of spontaneous emission and the Strickler-Berg

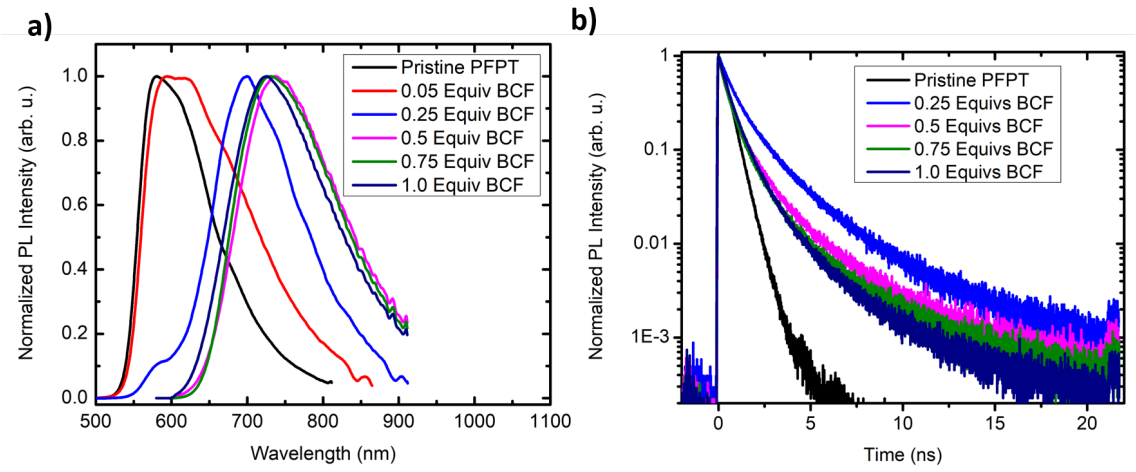

Figure 6.10: (a) Photoluminescence spectra of PFPT thin films with various concentrations of BCF. (b) PL decays of PFPT thin films with various amounts of BCF. A detection wavelength of 705 nm was used for films with BCF. A detection wavelength of 580 nm was used for the pristine PFPT film.

relationship), one would typically expect that a decrease in the optical transition energy would be concomitant with an increase in the natural lifetime (decrease in the rate of radiative decay).[3] In the solution phase an increase in lifetime is not observed due to significant non-radiative decay, as evidenced by the large decrease in PLQY. Furthermore, the PL maximum in the solid state red-shifts with increasing concentration of BCF up until about 0.75 equivalents, after which there is only a very slight blue-shift. These photoluminescence results are consistent with the restricted motion expected in solid-state films as compared to solution, which considerably weakens the impact of the free rotor and loose bolt effects, as well as excited-state geometric relaxation effects. Despite these differences, the PLQY of the PFPT:BCF 1:1 adduct in the solid state is still low, 6.6%, similar to the adduct PLQY in solution, 5.4%. Concerning adduct formation with polyfluorene-based polymers and BCF, Zalar et al. observed an increase in the PLQY of thin films, whereas Lin et al. observed a decrease in the PLQY of thin films.[78, 79]

6.4 Solution NMR

The formation of PFPT:BCF adduct in chloroform was investigated via ^{11}B NMR spectroscopy. In particular, ^{11}B chemical shifts are expected to be sensitive to changes in the chemical bonding environments such that tri- and tetracoordinated boron atoms can be identified and distinguished.[108, 109] As shown in Figure 6.11, a significant displacement in the isotropic ^{11}B chemical shift occurs upon adduct formation, as compared to the ^{11}B chemical shifts of neat BCF, which can be attributed to the change in the bonding environment of the central boron atom. This observation is exemplified by geometrical changes around the boron atom in the optimized DFT structures of bound and unbound BCF, as shown in Figure 6.11a,b, respectively.[110] Notably, the boron atom in unbound (3-coordinate sp^2) BCF adopts a trigonal planar geometry ($\delta \approx 56$ ppm). By comparison, the same boron atom in the adduct (4-coordinate sp^3) adopts a more tetrahedral-like geometry, which has a much different chemical shift ($\delta \approx -3$ ppm). By comparing the relative integrals of bound and unbound BCF in a solution of PFPT with 1.0 molar equivalents of BCF, we determined an equilibrium binding constant of 21,000 M^{-1} which is in excellent agreement with the optical absorbance results and analyses. For determining the equilibrium constant, the integrated peaks of interest and initial concentrations were used to determine the precise equilibrium concentrations of adduct, $[PFPT : BCF]$, free polymer $[PFPT]$, and unbound Lewis acid $[BCF]$. The concentration of the polymer [PFPT] is relative to the repeat unit of the polymer, i.e. F-PT. Then, the following equation was used to determine the equilibrium constant:

$$K_{eq} = \frac{[PFPT : BCF]}{[PFPT] \times [BCF]} \tag{6.6}$$

which is in accordance with the 1:1 reaction stoichiometry between the Lewis acid and polymer repeat unit. The relative integration also indicates that 95% of PT moieties on PFPT are bound to BCF. Moreover, the presence of only one peak near 0 ppm suggests that there is only a single preferred Lewis basic binding site in the polymer. When BCF was added to 4,7-dibromobenzo[*c*]-1,2,5-thiadiazole, no tetracoordinate boron was observed by ^{11}B NMR, suggesting that azole nitrogen atoms and sulfur atoms are either not sufficiently Lewis basic, or too sterically crowded, to result in adduct formation (Figure 6.12).

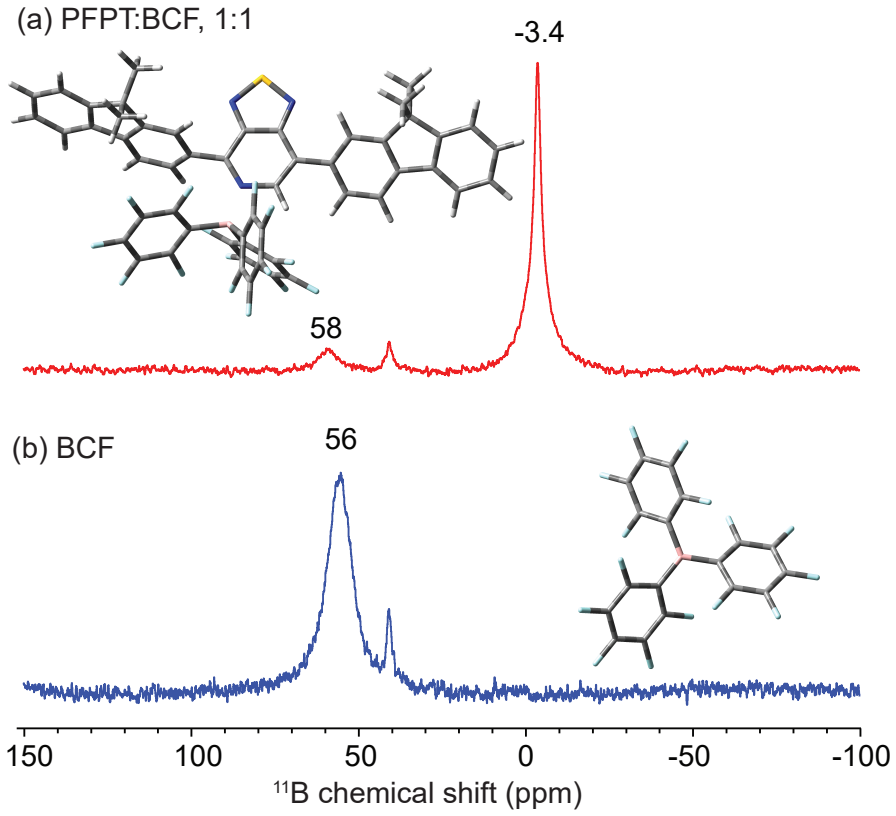

Figure 6.11: Solution-state ^{11}B NMR spectra acquired at 11.7 T and at room temperature of (a) PFPT with 1.0 molar equivalents of BCF and (b) neat BCF. The displacement of the ^{11}B signal is characteristic of the change in the local bonding environment of the boron atom. DFT optimized structures are also depicted.

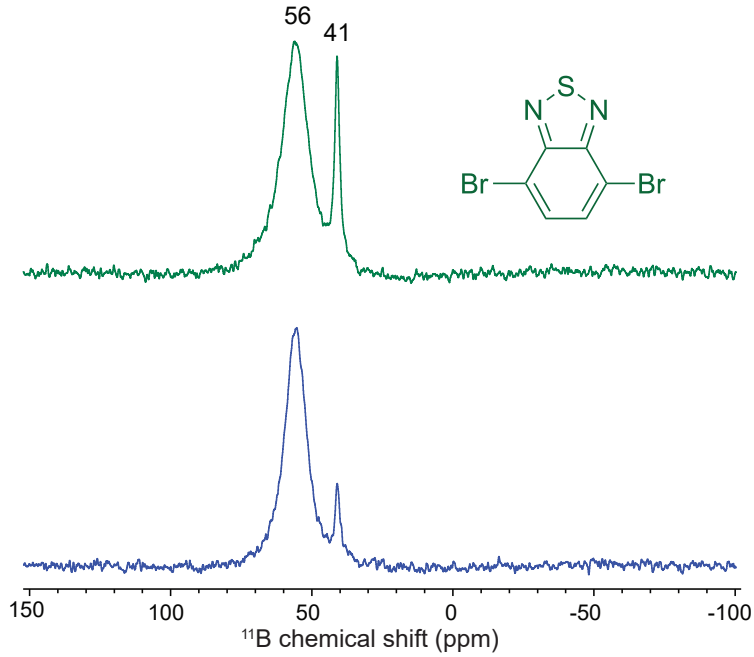

Figure 6.12: ^{11}B NMR spectra acquired at 11.7 T and at room temperature of 4,7-dibromobenzo[*c*]-1,2,5-thiadiazole (BT-Br_2) and 1 equivalent BCF in $CDCl_3$ (upper panel, green) and of neat BCF in $CDCl_3$ (lower panel, blue). The chemical structure of BT-Br_2 is also shown. Note the lack of any peaks near 0 ppm chemical shift, where a 4-coordinate boron atom is expected to exhibit resonance.

6.5 Determination of the Binding Site by DFT and XPS

DFT calculations were employed to probe the binding site of BCF on the PFPT backbone by assessing the relative change in internal energy (ΔU°) of a F-PT-F oligomer upon coordination to different Lewis basic sites, temperature effects excluded. For binding at the azole nitrogen atoms of the PT moiety, ΔU° is positive. In contrast, for binding at the pyridyl nitrogen atom of PT, ΔU° is -0.08 eV. Attempts to force BCF to bind at the sulfur atom were unsuccessful. Thus, our calculations suggested that the pyridyl nitrogen atom of PT is the most likely position for BCF binding.

Thin films of PFPT and a 1:1 complex with BCF were also investigated by XPS. Both

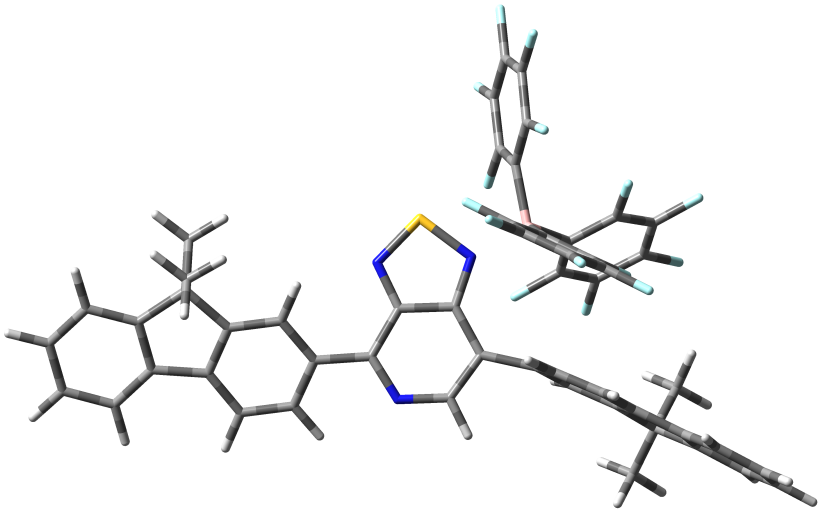

Figure 6.13: Optimized oligomer of PFPT with BCF coordinated to an azole nitrogen. $\Delta U^\circ = 0.22$ eV. B-N distance is 1.67 Å.

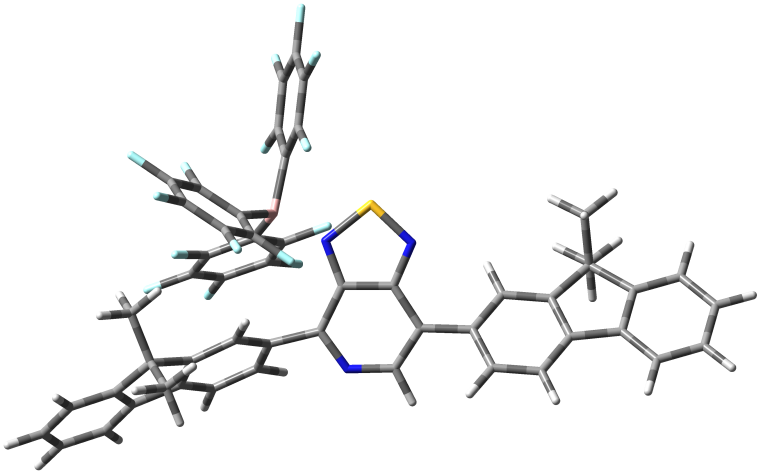

Figure 6.14: Optimized oligomer of PFPT with BCF coordinated to the other azole nitrogen. $\Delta U^\circ = 0.47$ eV. B-N distance is 1.68 Å.

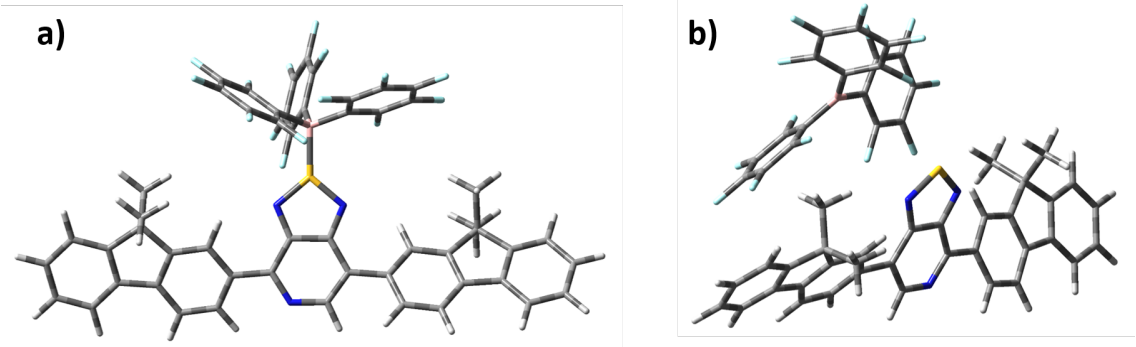

Figure 6.15: Attempted DFT geometry-optimization of PFPT with BCF coordinated to the sulfur atom. (a) Input geometry for DFT. (b) Optimized geometry of the converged structure that exhibits a B-S distance of 4.5 Å. The orientation of PFPT in (b) was chosen to more clearly show the distance of BCF relative to the oligomer and that BCF is in the trigonal planar geometry.

pristine PFPT and PFPT with 1.0 equivalents of BCF have identical sulfur 2p doublet peaks, indicating that there is no significant interaction of the Lewis acid with the sulfur atom on the PT moiety. Pristine PFPT exhibits two nitrogen 1s peaks, as shown in Figure 6.16, with peak areas corresponding to a ratio of approximately 2:1. This suggests that the larger peak at higher binding energy (400.1 eV) corresponds to the azole nitrogen atoms, whereas the smaller peak at lower binding energy (399.2 eV) corresponds to the pyridyl nitrogen atom.[111, 112] Upon addition of 1.0 equivalents of BCF, a new nitrogen 1s peak at higher binding energy (401.1 eV) is observed. Importantly, the relative area of the azole nitrogen peak, compared to the total area of the combined nitrogen peaks, does not change (Table 6.5). However, the peak corresponding to the pyridyl nitrogen atom is considerably reduced relative to the total area of nitrogen 1s peaks. These results indicate that BCF is interacting primarily with the pyridyl nitrogen atom of PT, and not the other Lewis basic sites. Because BCF is a Lewis acid, it withdraws electron density from the pyridyl nitrogen atom, making it overall more electron poor and, therefore, causing the new adduct peak to occur at higher binding energy, a shift of 1.9 eV.

Table 6.3: Peak percentages from Voigt fits to N 1s high-resolution XPS spectra of PFPT and PFPT:BCF (1:1) films.

Peak Center	PFPT	PFPT:BCF
399.2 eV	30%	22%
400.1 eV	70%	68%
401.1 eV	N/A	10%

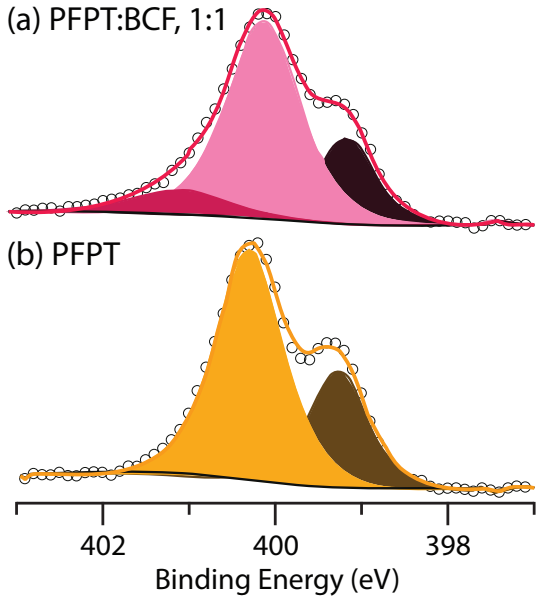

Figure 6.16: High-resolution XPS spectra of N 1s for thin films of (a) PFPT with 1.0 molar equivalents of BCF and (b) neat PFPT.

6.6 Bulk Morphology and Electrical Characteristics

The impact of BCF on the morphology of PFPT in the solid-state was probed by grazing-incidence wide-angle X-ray scattering (GIWAXS) and atomic force microscopy (AFM). The surface roughness of PFPT films do not change considerably upon addition of BCF. The root-mean-square surface roughness of pristine PFPT is 0.51 nm and increases only slightly to 0.56 nm upon addition of 0.10 molar equivalents BCF. GIWAXS data show that pristine PFPT is rather amorphous and that there are no discernable changes in the GIWAXS diffraction pattern with up to 0.10 molar equivalents BCF. We investigated

how the addition of BCF impacts the conductivity of PFPT films, but the conductivity of PFPT was found to be too low to make any conclusions. At room temperature, the conductivities of PFPT and PFPT with 0.10 molar equivalents BCF were below the limit of detection, precluding further electrical measurements.

6.7 Solid-State NMR

The data and analysis contained in this section were contributed by Dr. G. N. Manjunatha Reddy in the laboratory of Prof. Bradley Chmelka. The samples were prepared by myself.

To gain molecular-level insight into the local structures of the PFPT:BCF adducts in the solid state, multinuclear MAS-NMR spectra were acquired and analyzed. The analyses of isotropic ^{1}H, ^{13}C, ^{19}F and ^{11}B NMR chemical shifts are expected to provide information on local bonding environments in BCF and PFPT. For example, the one-dimensional (1D) solid-state ^{11}B MAS NMR spectrum of a 1:1 PFPT:BCF complex in Figure 6.17a exhibits a signal at -1.8 ppm, which is characteristic of tetrahedrally coordinated boron atoms and is consistent with the solution-state ^{11}B NMR spectrum of the PFPT:BCF complex. While this reflects bonding interactions between BCF and PFPT moieties, the ^{11}B MAS NMR spectrum provides little specific information concerning the intermolecular structure(s) or binding sites of PFPT:BCF complexes. Although ^{1}H MAS NMR spectroscopy benefits from the high sensitivity associated with ^{1}H nuclei (100% natural abundance) that can be used to characterize conjugated backbone moieties in PFPT and BCF, such spectra often suffer from considerably lower spectral resolution.

Complementary insights on the local bonding environments of ^{13}C moieties in PFPT:BCF adducts can be obtained by analyzing solid-state 1D ^{13}C$\{^{1}$H$\}$ and ^{13}C$\{^{19}$F$\}$ CP-MAS spectra. Such analyses exploit the enhancement of certain ^{13}C signal intensities that

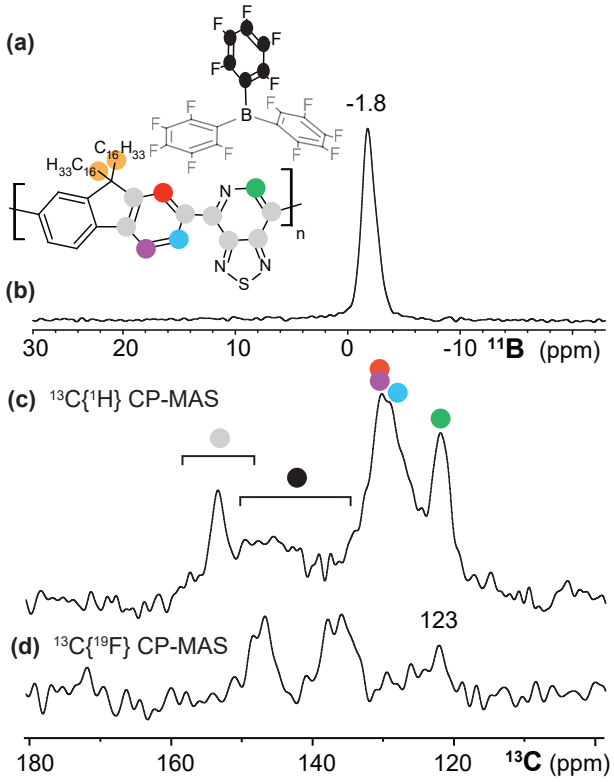

Figure 6.17: Solid-state 1D NMR spectra of PFPT:BCF complex acquired at 298 K, 9.4 T, and 15 kHz MAS. (a) Single-pulse ^{11}B MAS NMR spectrum with the signal at -1.8 ppm assigned to tetrahedrally coordinated boron atoms in PFPT:BCF. (b) ^{13}C{^{1}H} and (c) ^{13}C{^{19}F} CP-MAS NMR spectra acquired using 2 ms of CP contact time. The color code depicts assignments of ^{13}C atoms in the BCF and PFPT moieties according to the schematic structural diagram of the PFPT:BCF complex in (a).

are increased by transfer of ^{1}H or ^{19}F spin-polarization, according to the strengths of their ^{1}H-^{13}C or ^{19}F-^{13}C dipole-dipole couplings, from specific BCF and PFPT aromatic carbon moieties. This enables distinct local C-H and C-F environments to be resolved and identified. For example, a comparison of the 1D ^{13}C{1H} and ^{13}C{^{19}F} CP-MAS NMR spectra in Figure 6.17 shows ^{13}C signals with different intensities that are associated with different BCF and PFPT moieties of the complex. In particular, the analyses of the ^{13}C{^{1}H} and ^{13}C{^{19}F} CP signal enhancements associated with the ^{13}C site adjacent to the pyridyl nitrogen atom (shown in green in the schematic diagram in Figure 6.17a) enabled the intramolecular ^{13}C-^{1}H interactions in PFPT and the intermolecular

^{13}C-^{19}F interactions between PFPT and BCF moieties in the PFPT:BCF complex to be separately identified and distinguished. In the 1D ^{13}C{^{1}H} CP-MAS spectrum (Figure 6.17b), the partially-resolved signal at 123 ppm in the aromatic region is associated with the carbon atom (green) bearing a proton next to the pyridyl nitrogen atom of PFPT. The broad intensity distribution centered at 129 ppm corresponds to aromatic carbon atoms (red, cyan, and purple) that are directly bonded to protons in fluorene moieties. The relatively weak ^{13}C signals in the range 133-150 ppm are attributed to the overlapping contributions from carbon atoms (black) in the BCF moieties, which while not directly bonded to hydrogen atoms, are nevertheless within 1 nm. The relatively narrow ^{13}C signal at 153 ppm is assigned to the six carbon atoms (grey) of the FPT moieties. Further insights were obtained from the 1D ^{13}C{^{19}F} CP-MAS spectrum (Figure 6.17c), in which partially resolved ^{13}C signals in the ranges 145-150 and 132-138 ppm are enhanced by ^{19}F nuclei that are directly bonded to the carbon atoms (black) in the BCF moieties. Interestingly, the ^{13}C signal at 123 ppm associated with the carbon atom (green) adjacent to the pyridyl nitrogen in the FPT moiety is also relatively enhanced by ^{19}F spin-polarization, which indicates its nanoscale proximity to the fluorine atoms in C_6F_5 units. Together, the ^{13}C{^{1}H} and ^{13}C{^{19}F} analyses enable the intramolecular C-H and intermolecular C-F interactions to be distinguished in the PFPT:BCF complex, further supported by the analyses of 2D ^{1}H{^{1}H} and ^{1}H{^{19}F} NMR spectra discussed below.

Molecularly proximate and dipole-dipole-coupled spin pairs within approximately 1 nm can be probed by using solid-state two-dimensional (2D) NMR techniques, enabling intermolecular ^{19}F-^{1}H interactions between BCF and PFPT to be identified and elucidated.[93, 98, 113, 114, 115, 116] For example, a rotor-synchronized 2D dipolar-mediated ^{1}H{^{19}F} heteronuclear multiple-quantum correlation (HMQC) spectrum acquired using 0.32 ms of recoupling time is shown in Figure 6.18a, accompanied by 1D ^{1}H

MAS and 1D ^{19}F MAS spectra along the top horizontal axis and the left vertical axis, respectively. The relatively broad distribution of intensity centered at -133 ppm corresponds to ^{19}F moieties in the ortho position of the C_6F_5 moieties in BCF, while partially resolved ^{19}F signals in the range -158 to -163 ppm correspond to fluorine atoms in para and meta positions. These assignments are consistent with the isotropic ^{19}F chemical shifts of aromatic groups reported in the literature.[117] In the solid-state 2D $^{1}H\{^{19}F\}$ HMQC NMR spectrum of Figure 6.18a, intensity correlations are observed between ^{1}H signals at 8.2 ppm (aromatic groups of PFPT) and 1.1 ppm (branched alkyl sidechains of PFPT) with the ^{19}F signals at -163 and -158 ppm from the meta and para ^{19}F atoms in BCF, which establish the close spatial proximities of these PFPT and C_6F_5 moieties. In contrast, no such correlated intensity is observed between aromatic ^{1}H signals of PFPT and the ortho ^{19}F signal of C_6F_5 moieties (-133 ppm), reflecting weaker ^{19}F-^{1}H dipole-dipole interactions between the PFPT backbone and sidechain ^{1}H moieties. These 2D intensity correlations are consistent with the formation of a polymer:Lewis acid adduct in which BCF molecules bind near the pyridyl nitrogen atoms of PFPT.

Complementary insights on the inter- and intramolecular ^{1}H-^{1}H interactions of PFPT polymer chains in the presence of BCF are obtained from the 2D $^{1}H\{^{1}H\}$ DQ-SQ spectra. In Figure 6.18b, the left vertical dimension shows the ^{1}H double-quantum (DQ) chemical shifts at the sum of the respective single-quantum (SQ) chemical shifts for dipole-dipole-coupled ^{1}H spin pairs within a distance of approximately 0.5 nm. For example, intensity at a ^{1}H SQ chemical shift of 1.1 ppm and a ^{1}H DQ chemical shift of 1.1 + 1.1 = 2.2 ppm, originates from adjacent ^{1}H moieties in the methyl and methylene groups of the hexadecylalkyl chains. In addition, off-diagonal intensity correlations at ^{1}H SQ chemical shifts of 1.1 and 8.2 ppm and a ^{1}H DQ chemical shift of 1.1 + 8.2 = 9.3 ppm reflect the intramolecular proximities of the hexadecylalkyl chains and aromatic ^{1}H atoms in the fluorene moieties of PFPT. As expected, no such DQ-SQ intensity is observed for

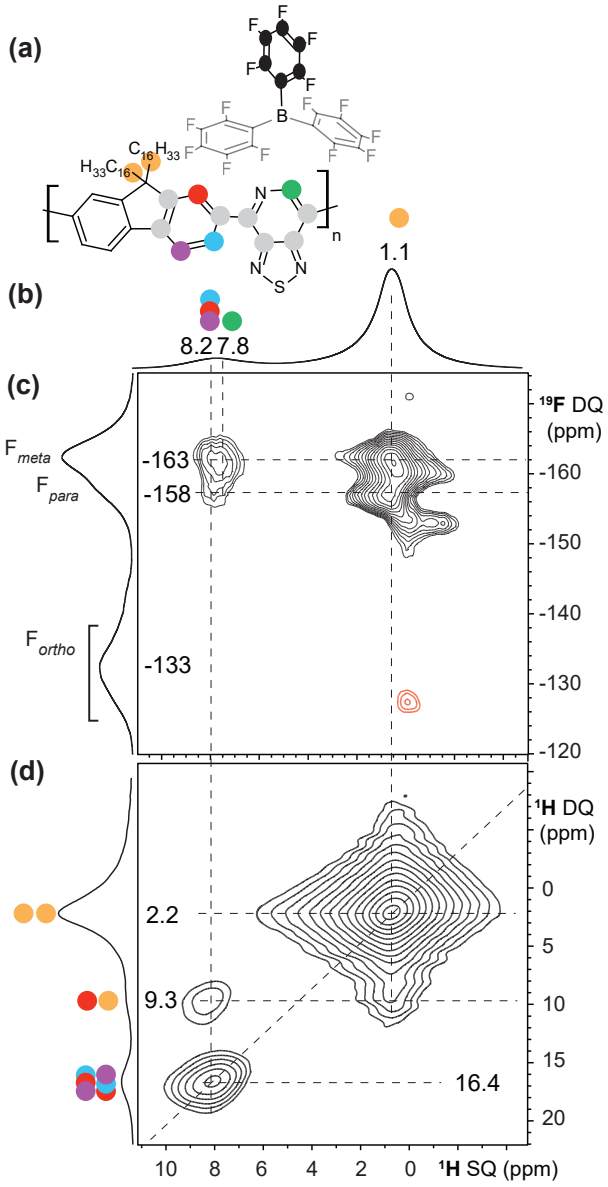

Figure 6.18: (a) A solid-state 2D ^{1}H{^{19}F} HMQC NMR spectrum of a 1:1 PFPT:BCF complex (schematic structure shown) with 1D ^{1}H and ^{19}F MAS NMR spectra along the horizontal and vertical axes, respectively, for comparison. (b) A solid-state 2D ^{1}H{^{1}H} DQ-SQ NMR spectrum plotted with a double-quantum projection on the vertical dimension. The color code depicts the assignment of ^{19}F and ^{1}H signals associated with the BCF and PFPT species, as depicted also in the schematic structural diagram.

^{1}H nuclei adjacent to the pyridyl nitrogen atoms and ^{1}H nuclei in the alkyl sidechains attached to the fluorene moieties. Additional self-correlated intensity at a ^{1}H SQ chem-

ical shift of 8.3 ppm and a ^{1}H DQ chemical shift, 8.2 + 8.2 = 16.4 ppm indicates the closer through-space proximity of ^{1}H moieties in the aromatic fluorene and PT moieties of PFPT. The combined 2D ^{1}H{^{19}F} and ^{1}H{^{1}H} NMR analyses thus provide direct evidence of the spatial proximities of BCF and PFPT, and indicate that the BCF molecules are preferentially located between the branched $C_{16}H_{33}$ sidechains and that the boron atoms of BCF interact with the pyridyl nitrogen atoms of PFPT.

6.8 Analysis of Frontier Molecular Orbitals via UPS and DFT

With a detailed physical description of the nature of Lewis acid binding, we next investigated the solid-state electronic properties via UPS. The ionization potential (IP) of PFPT, -6.05 eV, became slightly deeper when 1.0 equivalents of BCF was added, resulting in an ionization potential of -6.15 eV (Figure 6.19). Assuming that the exciton binding energy of the adduct is similar to that of pristine PFPT, the change in electron affinity (EA) is then given by the sum of changes in the IP and E_{opt}.[118, 119] From the IP dropping by 0.1 eV and the optical bandgap decreasing by 0.3 eV, we can thus infer that the EA of the adduct decreases by 0.4 eV relative to pristine PFPT. Samples were sent to Prof. Kenneth Graham at the University of Kentucky in order to measure the EA of PFPT films with BCF, but the inverse photoemission spectroscopy (IPES) measurements were not successful. As for the approximation I made above concerning the determination of the change in EA upon BCF binding, subsequent work in Chapter 7 shows this approximation to be quite accurate. The IP and EA of the polymer PCPDTPT with and without BCF was able to measured via UPS and IPES. The change in the optical gap upon BCF addition was also determined by UV-Vis-NIR absorption. Thus,

we were able to directly compare the change in the optical gap versus the change in the electrical gap upon BCF addition. The difference was negligible, indicating that adduct formation with BCF does not cause a change in the exciton binding energy. These measurements elucidate a detailed picture of how frontier molecular orbitals change upon adduct formation, which is depicted in Figure 6.20.

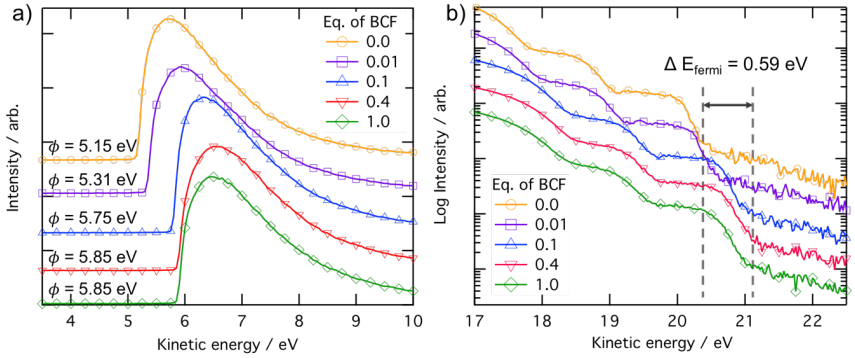

Figure 6.19: UPS spectra of (a) the photoemission onset, Φ, and (b) the position of the leading edge of the HOMO for thin films of PFPT with different equivalents of BCF.

Table 6.4: Summary of results from UPS measurements on thin films.

Molar Equivalents of BCF	Work Function (eV)	Ionization Potential (eV)
0.00	-5.15	-6.05
0.01	-5.31	-6.06
0.10	-5.75	-6.05
0.40	-5.85	-6.10
1.00	-5.85	-6.15

Time-dependent (TD) DFT calculations, carried out on an F-PT-F oligomer, provide further insight into why the LUMO energy is reduced significantly more than the HOMO energy upon coordination with BCF. The oligomer, by itself, has a HOMO wavefunction that is well delocalized on the conjugated backbone, but a LUMO that is localized on the PT acceptor moiety, demonstrating ICT character, as is expected for D-A molecules and polymers. Upon coordination of BCF to the pyridyl nitrogen, the HOMO is relatively

unaffected, although a very small portion of the wavefunction does extend onto aromatic rings of BCF. Thus, it is not surprising that by UPS we observed only a small reduction in IP upon adduct formation. However, the LUMO wavefunction, upon binding the Lewis acid, noticeably extends onto BCF, while simultaneously retracting from the neighboring fluorene moieties. This is clearly associated with the Lewis acid withdrawing electron density from the LUMO, which results in a significant stabilization (reduction) of the LUMO energy.

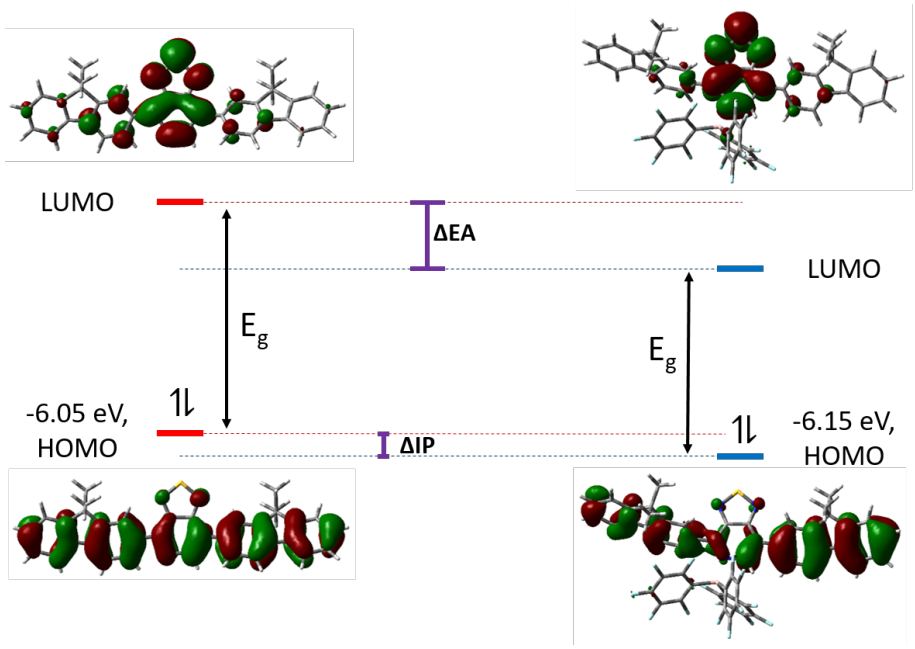

Figure 6.20: Energy diagram of how adduct formation changes the energy of molecular orbitals, accompanied by TD-DFT calculations which show the relevant wavefunctions. Experimental values of HOMO energies, as determined by UPS of thin films. The relative change in the LUMO energy, i.e. ΔEA, upon adduct formation is inferred by the experimentally determined change in HOMO energies, ΔIP, and reduction of the optical bandgap, E_{opt}, while assuming that the change in exciton binding energy upon adduct formation is negligible.

6.9 Conclusions for the Model System PFPT:BCF

To summarize, this in-depth study reveals how the Lewis acid $B(C_6F_5)_3$ can be used for post-synthesis bandgap engineering in a model Lewis basic polymer, PFPT. UPS measurements and TD-DFT calculations show that the reduction in the optical bandgap ($\Delta E_{opt} = 0.3$ eV) can be attributed primarily to $B(C_6F_5)_3$ withdrawing electron density from the LUMO of PFPT, resulting in a significant decrease of the LUMO energy of the PFPT:BCF adduct. A combination of XPS, solution- and solid-state multinuclear NMR, and DFT calculations show that, although PFPT has multiple Lewis basic sites which could potentially bind $B(C_6F_5)_3$, it is only the pyridyl nitrogen which forms the adduct. Importantly, solid-state 1D ^{11}B, ^{13}C$\{^1$H$\}$ CP-MAS and ^{13}C$\{^{19}$F$\}$ CP-MAS and 2D ^{1}H$\{^{19}$F$\}$ and ^{1}H$\{^1$H$\}$ correlation NMR analyses provide evidence that BCF molecules are intercalated between branched alkyl sidechains of PFPT and that the boron atoms of BCF interact with the pyridyl nitrogen atoms of PFPT. In particular, the relative ^{13}C$\{^1$H$\}$ and ^{13}C$\{^{19}$F$\}$ CP signal enhancements observed for the ^{13}C sites adjacent to the pyridyl nitrogen atoms of PFPT indicate the mutual nanoscale proximities of the BCF and PFPT moieties. These results are corroborated by the 2D ^{1}H$\{^{19}$F$\}$ correlation NMR measurements and analyses, which establish the ^{1}H and ^{19}F proximities in PFPT:BCF complex at sub-nm to nm distances. In addition, analysis of spectroscopic data reveals that adduct formation in solution is an equilibrium process, specifically, a 1:1 binding isotherm, with the equilibrium strongly favoring adduct formation ($\Delta G^\circ < -0.2$ eV). This detailed investigation also highlights the important role of the steric conformation of the polymer backbone, which in the case of PFPT, because of its non-planar structure, is able to bind one $B(C_6F_5)_3$ molecule for every repeat unit of PFPT.

Molecular-level and atomic-level insights into the structure and optical properties of Lewis acid adducts that form with Lewis basic polymers, as acquired in this study, are

expected to guide the development of new polymers which are compatible with bandgap engineering via Lewis acid adduct formation, which is of broad interest to the organic semiconductor community. This general strategy may be used not only for tailoring the optical properties of polymer light-emitting diodes (PLEDs) and organic photovoltaics (OPVs), but also for the fine-tuning of energy levels, post synthesis. In PLEDs and field-effect transistors, modifying the HOMO and LUMO energies may beneficially enhance (or inhibit) charge injection as well as tune the optical band gap, whereas in OPVs, energy level alignment between an electron acceptor material and electron donor material is critical for achieving efficient charge separation and high open-circuit voltage.[120, 121, 122, 123, 124, 125] Using BCF adduct formation to modify a solar cell's optical gap and energy levels has yet to be realized, although several reports exist of solar cell's that use BCF as an electrical dopant. A key difference in these two utilizations of BCF is the concentration of BCF used. For electrical doping, only small amounts of BCF are used (less than 1 mol %). For bandgap engineering, the concentration of BCF should be much higher, near 100 mol %.

Chapter 7

P-Type Doping of Conjugated Polymers via Lewis Acids

The contents of this chapter appear in [126].

The Lewis acid tris(pentafluorophenyl)borane, $B(C_6F_5)_3$, has recently garnered attention in the organic semiconductor community as a useful p-type dopant, rivaling, and even exceeding in some cases, the effectiveness of traditional p-type dopants such as 2,3,5,6-tetrafluoro-7,7,8,8-tetracyanoquinodimethane (F_4TCNQ). However, the precise mechanism by which the addition of $B(C_6F_5)_3$ increases the free charge carrier density (i.e. holes) of particular organic semiconductors remains elusive. In this chapter, I investigate the effect that Lewis acids of varying strength and size have on three different cyclopentadithiophene-containing polymers with varying degrees of Lewis basicity. Electrical measurements, optical absorption, and electron paramagnetic resonance (EPR) indicate that $B(C_6F_5)_3$ is a superior dopant to the other Lewis acids we investigated, including BF_3, BBr_3, and $AlCl_3$, despite the relatively weak Lewis acidity of $B(C_6F_5)_3$. In one case, $B(C_6F_5)_3$ is found to be superior even to F_4TCNQ. Furthermore, we find

that adduct formation with the polymers actually inhibits the process of doping. Finally, we use a combination of electron-nuclear double resonance (ENDOR) and nuclear magnetic resonance (NMR) techniques, in conjunction with density functional theory, to show that p-type doping occurs by (i) generation of a water:Lewis acid complex with significant Brønsted acidity, (ii) protonation of cyclopentadithiophene moieties, and (iii) subsequent electron transfer from a neutral chain segment to a positively charged, protonated one. A comparison with a prototypical strong Brønsted acid, trifluoroacetic acid, is made in order to corroborate the proposed doping mechanism of $B(C_6F_5)_3$. This study provides insight on the mechanism of protonic acid doping and shows how trace amounts of water can turn Lewis acids into powerful Brønsted acids

For this chapter specifically, I would like to thank Alexander Moreland. He was one of the only individuals who seriously entertained my theory about the doping mechanism and discussed with me how to go about proving it. He also introduced me to the ENDOR technique, which was a key piece of evidence in my work. I would also like to thank Dr. Viktor Brus and David Cao for their contributions to the project, as well as all of the other collaborators.

7.1 Background

The ability to precisely and controllably dope, i.e. modulate the free charge carrier concentration, inorganic semi-conductors is the underpinning of modern electronics. This importance provides much of the motivation behind the long-standing interest in doping organic semiconductors. In as early as 1977, it was shown that the conductivity of polyacetylene can be controlled over eleven orders of magnitude by vapor doping using volatile halogens, such as I_2, and other strong gaseous oxidizers, such as AsF_5.[127] However, this method of doping suffers from a practical viewpoint: reproducibility, bulk

homogeneity, and stability (over time these dopants tend to diffuse out of the films) present significant obstacles for commercial implementation. Not many years later, it was discovered that Brønsted acids, such as HF and trifluoroacetic acid (TFA), were able to effectively p-dope polyacetylene, as well as many other organic semiconducting polymers.[128, 129] It has been suggested that protonic acids result in p-type doping through a 2-step process: first, protonation of the conjugated backbone, and second, electron transfer from a neutral segment to a protonated one.[130, 131, 132, 133] However, identification and characterization of the protonated intermediates and resulting radical species have remained elusive. For a review on p-type doping mechansims, see Section 1.3.

Then, just before the turn of the century, controllable molecular p-doping of organic semiconductors was realized by co-sublimation of phthalocyanine derivatives with 2,3,5,6-tetrafluoro-7,7,8,8tetracyanoquinodimethane (F_4TCNQ).[134] Importantly, this molecular dopant is far less prone to diffusion in thin films, lending good stability to doped films over time. Since then, numerous studies have demonstrated that molecular p-doping is a viable strategy for modulating charge transport and charge injection in optoelectronic devices.[135, 136, 137, 138, 139] P-doping using molecular dopants such as F_4TCNQ proceeds when the lowest unoccupied molecular orbital (LUMO) level of the dopant is roughly equal to, or lower, in energy than the organic semiconductor's highest occupied molecular orbital (HOMO) level. If this criterion is met, then integer charge transfer (ICT) is expected to take place from the HOMO of the organic semiconductor into the LUMO of the dopant, creating a (mobile) hole and stationary dopant anion. Although p-type doping with F_4TCNQ can also occur through an alternative mechanism (charge-transfer complexation, CPX) in a few systems, ICT is the more commonly encountered mechanism and more efficient for doping.[140, 141] The success of F_4TCNQ as a molecular dopant has remained, for the most part, limited to processing by ther-

mal evaporation. Using F_4TCNQ in solution-processed organic semiconductors has been plagued with problems that typically derive from the drastically different solubilities of the organic semiconductor, neutral F_4TCNQ, and the F_4TCNQ anion.[139] Aggregation of F_4TCNQ in polymer films is a commonly encountered problem, where such aggregation severely disrupts the film's morphology, negatively impacting carrier transport pathways.[142, 143, 144, 145] Moreover, the ability to p-dope materials possessing a large HOMO energy necessitates the design of molecular dopants with an even greater electron accepting ability than F_4TCNQ, which is no simple task. Thus, the organic semiconductor community has continued to search for superior, solution-processable p-type dopants.

In 2014, it was shown that the addition of a Lewis acid, $B(C_6F_5)_3$, hereafter referred to as BCF, to a polymer with Lewis basic atoms increased the free charge carrier (hole) density, increased the hole mobility, and reduced the activation energy of charge transport - all indicators of p-type doping.[80] Since then, several research groups have used BCF to modulate the electronic properties of small molecular and polymeric semiconductors for use in organic field-effect transistors (OFETs), organic photovoltaics (OPVs), organic thermoelectrics, and organic light-emitting diodes (OLEDs).[85, 86, 83, 82, 79] BCF is advantageous compared to F_4TCNQ for p-type doping organic semiconductors for two primary reasons: (i) it has excellent solubility in common organic solvents (e.g. > 30 mg/mL in $CHCl_3$ compared to < 1 mg/mL for F_4TCNQ) and (ii) other work has suggested that it is capable of doping materials with relatively deep HOMO levels of ca. 5.8 eV.[84] It should also be noted that, in the case of poly(3-hexylthiophene-2,5-diyl) (P3HT), BCF has been shown to have an approximately equal doping efficiency to F_4TCNQ (free charge carrier increase relative to concentration of added dopant), but enables higher conductivity and hole mobility in doped semiconductors compared to F_4TCNQ.[81] Despite these studies on the enhanced electrical properties of organic

semiconductors upon the addition of BCF, little is understood about the mechanism of Lewis acid doping.

While I was researching this topic, there were generally 2 competing theories about the doping mechanism. One theory invoked adduct formation, followed by electron transfer from a pristine polymer chain segment to a segment with adduct formation, as depicted in Figure 7.1. The other theory was simply ICT from the organic semiconductor to BCF. This latter theory was particularly troublesome to disprove, so I will present here a more detailed argument against this mechanism.

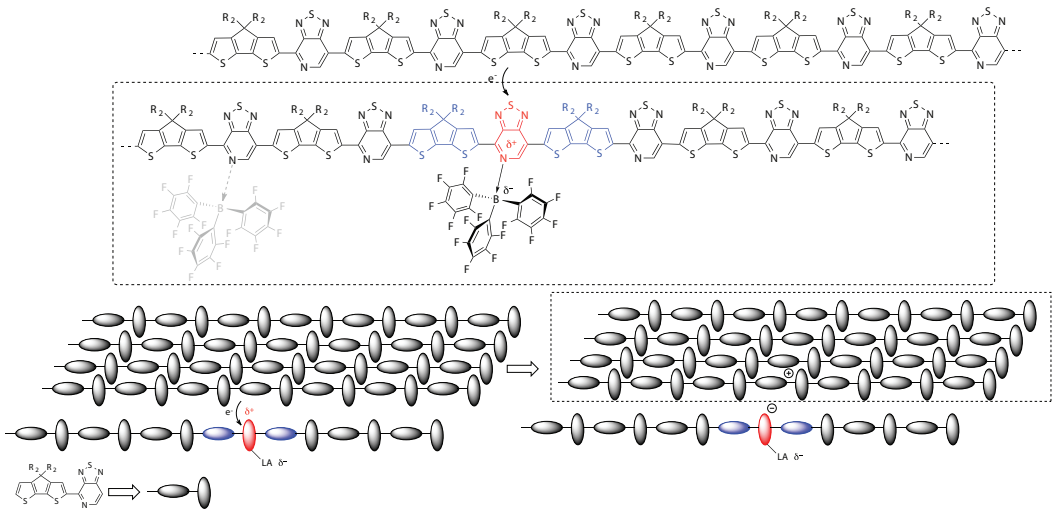

Figure 7.1: Schematic illustration of electron transfer from an uncomplexed chain to a more electron poor, Lewis acid-containing site. Later in the chapter I disprove this theory.

The possibility of ICT to BCF is unlikely for essentially 2 reasons: (i) the LUMO level of BCF, measured by cyclic voltammetry (CV) in dichloromethane, is 3.01 eV with respect to vacuum, a far cry from the HOMO level of most organic semiconductors (greater than 4 eV); (ii) not even metallic sodium or potassium are able to reduce BCF.[146, 147] In fact, various attempts to identify the one-electron reduction of BCF, i.e. the BCF radical anion, have proven unsuccessful.[89] As it turns out, the BCF radical anion isn't

stable above −50°C. This fact actually created significant doubt in my mind at times, because it demonstrates that ICT is a possiblity. There are some other reports in the organometallic literature that claim BCF can act as a one-electron reductant, but they were never able to prove the existance of a BCF radical anion intermediate. In light of this, an argument was posed by a colleague: "If the radical anion isn't stable at room temperature, then perhaps ICT occurs between BCF and the semiconductor, after which the BCF radical anion just decomposes into something else, eliminating the radical in the process." Although this could be possible, I think that the most likely reaction of the BCF radical anion would be to give the electron back to the semiconductor, rather than reacting with the solvent. More doubt was created in my mind because we primarily process with chlorinated solvents, and I know that chlorine is amenable to radical chemistry. In later NMR experiments, I would show that there are no products present after doping which would be consistent with the decomposition of the BCF radical anion.

There was still the question of BCF's energy levels, and whether or not they were compatible with the ICT mechanism. The LUMO level of BCF in dichloromethane was measured to be 3.01 eV, but one should be wary that energy levels can change considerably (hundreds of mV) when going from solution phase to the solid state. That CV measurement, by the way, was no simple task. After attempting some CV measurements myself on BCF and polymers with BCF, which were unsuccessful, I noted a paper in the literature whose sole thesis was on how to properly do CV of BCF. It turns out that very specific solvents and supporting electrolytes must be chosen, in order to avoid the BCF radical anion reacting with other species in solution (or the solvent itself). At any rate, we wanted to measure the electron affinity of BCF in the solid state by IPES. Those measurements proved to be unsuccessful, as described later in the chapter, but for a good amount of time certain people were convinced that the data could be interpreted such that BCF has an EA of around 5.2 eV, which would be sufficient to expect ICT from the

polymers in question. I had 2 main arguments against this: one was against the method of analysis used to determine the EA, and the other was a simple thought experiment which suggests that an EA of 5.2 eV for BCF is absurd. The argument against the method of analysis was straight-forward: it was obvious that the onset of emission from the BCF IPES data was not determined in the usual, accepted manner. The onset was chosen in an arbitrary manner.

UPS measurements of BCF appeared more robust (and the analysis done in the correct manner), suggesting an IP of 8.0 eV and WF of 6.0 eV, which are reasonable values to expect. Already an EA of 5.2 eV is warrant of suspicion, because this would suggest that the Fermi energy of BCF is well above the midpoint of it's electrical gap (the midpoint being where it should be for a non-doped semiconductor). The thought experiment goes like this: let's say that the electrical gap of BCF really is 2.8 eV (IP = 8.0 eV; EA = 5.2 eV). Now let's say that the exciton binding energy is small, around 0.3 eV. A review of the literature on exciton binding energies suggests this is a reasonable value. This means that the optical gap of BCF is about 2.5 eV, or 496 nm. First, this doesn't make sense since the optical gap of BCF, albeit in solution, is about 350 nm. A 100+ nm shift in absorption when going from solution to solid-state is very dramatic, especially for non-crystalline solids (BCF is a fluffy powder). Second, 496 nm corresponds to blue (cyan) light and is bordering green. If colored light were absorbed by BCF, it would not appear as a white solid! Third, even if the exciton binding energy is completely ignored, 2.8 eV corresponds to 442 nm - which is violet - so BCF would still not appear as a white solid! Only a negative exciton binding energy would justify the white appearance of BCF, which is obviously absurd. On the other hand, if the EA of BCF is around 4.0 eV, which seems much more reasonable in light of CV measurements, then its electrical gap is $8.0 - 4.0 = 4.0$ eV, or 310 nm. Let's give it a binding energy of 0.5 eV, which results in an optical gap of 3.5 eV, which is 354 nm. This would be consistent with a

white solid. This is also consistent with the optical gap observed in dichloromethane solution (≈350 nm). Furthermore, if the EA is around 4 eV, then one would expect the WF, or Fermi energy, to be 6.0 eV, which is the value we measured.

There is a publication in the literature, [82], which claims that BCF has an EA of 4.81 eV. However, this paper does not reveal how that number was determined! There is no evidence to support that value, and it should not be trusted. Unfortunately, some other scientists in the field have referenced that value in their own work without properly warning the reader that the 4.81 eV EA has no scientific basis. In order to avoid believing incorrect data, it is always good to ask oneself, "Does this value make sense?" This phrase was repeatedly mentioned in the many courses I taught at UCSB (by myself and various professors), and is good advice for anything in life that involves numbers.

It has been suggested that Lewis acid adduct formation with the organic semiconductor is critical to the doping process, although little has been done to correlate the binding of a Lewis acid with a Lewis basic site of the polymer/small molecule to evidence of doping. What is known (see Chapter 6), however, is that binding of a Lewis acid (e.g. BCF, BF_3, BBr_3, etc.) to a Lewis basic site of an organic semiconductor, i.e. adduct formation, results in the decrease of the bandgap of the semiconductor.[72, 74] In fact, this phenomenon has been used by various research groups to modulate the optical properties of organic semiconductors.[78, 75, 77, 76, 148, 149, 150] Unfortunately, many of these studies have not investigated whether or not the Lewis acid used for adduct formation also induces p-type doping. Thus, it remains to be shown (i) how addition of BCF results in p-type doping of organic semiconductors, (ii) which organic semiconductors are amenable to this type of doping, and (iii) which other Lewis acids are capable of p-type doping besides BCF.

In this work, I investigate the electronic and optical properties of thin films doped by the Lewis acids BCF and BF_3 using two model polymers, poly[2,6-(4,4-bis(2-hexadecyl)-

4*H*-cyclopenta[2,1-*b*;3,4-*b*]dithiophene)-*alt*-4,7(2,1,3benzothiadiazole)] (PCPDTBT) and poly[2,6-(4,4-bis(2-hexadecyl)-4*H*-cyclopenta[2,1-*b*;3,4-*b*]dithiophene)-*alt*-4,7-(4,4-dihexadecyl-4*H*-cyclopenta[2,1-*b*:3,4-*b*']-dithiophene-2,6-diyl)bis([1,2,5]thiadiazolo[3,4-*c*]pyridine)] (PCPDTPT), which have varying degrees of Lewis basicity. The chemical structure of these polymers are shown in Figure 7.2, along with the other dopants used in this study. The size and relative strength of the different Lewis acids are also indicated.[151] Our previous work has shown that for small molecules including either 2,1,3-benzothiadiazole (BT) or [1,2,5]-thiadiazolo[3,4-*c*]pyridine (PT), those with PT exhibit a greater propensity for binding Lewis acids due to the greater Lewis basicity of pyridyl nitrogen over azole nitrogen and its better steric accessibility.[74, 63] For reference, we also determine the electronic properties of the polymers doped by F_4TCNQ via the conventional ICT pathway. Conductivity measurements and impedance spectroscopy show that Lewis acid doping is more effective in the weaker of the Lewis basic polymers, and for this polymer, BCF is superior to both BF_3 and F_4TCNQ. Optical absorption, electron paramagnetic resonance (EPR), and X-ray photoelectron (XPS) measurements indicate that BCF binds to the more strongly Lewis basic polymer, which inhibits the doping process.

Further investigation into the doping mechanism of BCF in solution suggests that the underlying doping mechanism is, in fact, that of Brønsted acid doping. NMR spectroscopy reveals the presence of water in BCF despite precautions taken to exclude moisture (sample preparation being performed in a dry, inert atmosphere glovebox, using anhydrous solvents, and using custom-built, air-tight NMR tubes). Moreover, NMR spectroscopy reveals that the 4,4-dihexadecyl-4*H*-cyclopenta[1,2-*b*:5,4-*b*]dithiophene (CPDT) monomer becomes protonated in the presence of BCF, which we attribute to the Brønsted acidity of the BCF:H_2O complex. Spectroscopic comparisons are made with doping by the Brønsted acid trifluoroacetic acid (TFA), and support the hypothesis of the BCF:H_2O doping mechanism. Electron-nuclear double resonance (ENDOR) measurements, com-

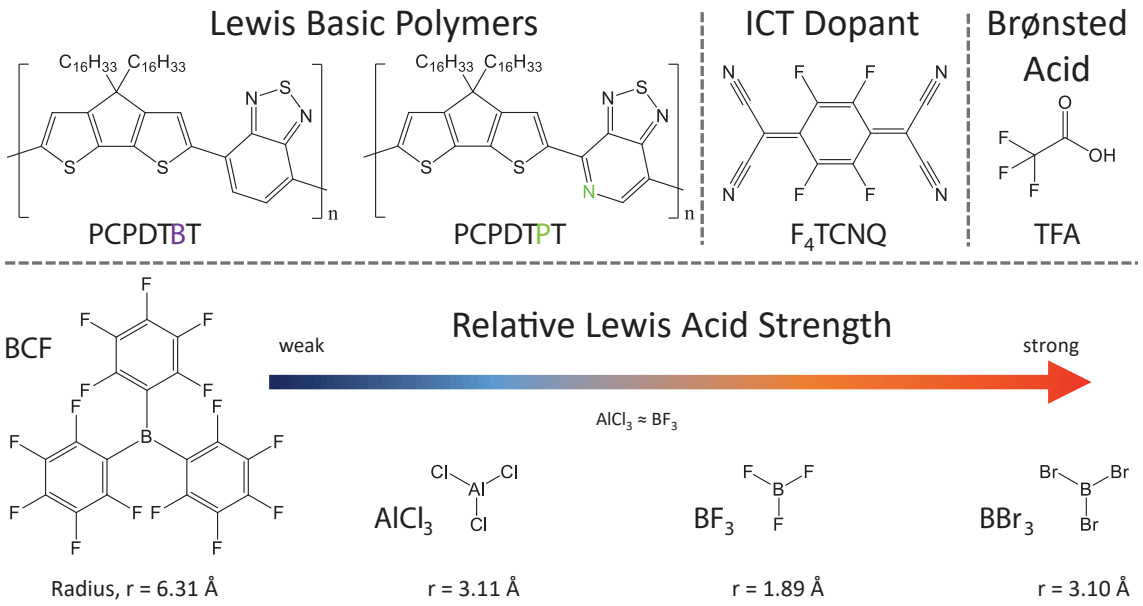

Figure 7.2: Chemical structures of the polymers studied, and the various molecules used to dope them. The relative Lewis acidity of the four Lewis acids is also conveyed, $AlCl_3$ being approximately equal to BF_3.[151] The relative sizes of the Lewis acids are also shown, as estimated from DFT optimized geometries. The regioregularity of PCPDTPT is not shown here for simplicity.

bined with density functional theory (DFT) simulations, further corroborate my hypothesis. Finally, a qualitative comparison of the doping efficiency of four different Lewis acids is made by examining the doping levels in solution for a polymer which lacks Lewis basic binding sites, but still bears a CPDT moiety. We find that BCF and BF_3 have similar efficiencies, whereas $AlCl_3$ and BBr_3 are found to be much less efficient. We suggest that the relative efficiencies can be explained by the stability of the different water:Lewis acid complexes and their subsequent Brønsted acidity.

7.2 Materials and Methods

BCF was purchased from Tokyo Chemical Industry Co., Ltd. and used as received. BF_3 (diethylether), BBr_3 (1.0 M in dichloromethane), $AlCl_3$, TFA, and the solvents

used herein were purchased from Sigma-Aldrich and used as received. PCPDTBT was purchased from 1-Material and used as received. PCPDTPT was synthesized in-house according to the literature procedure.[152] F_4TCNQ was purchased from Lumtec and used as received. All materials were stored in a dry, inert atmosphere (N_2) glovebox. Careful precautions were taken to exclude the presence of water and oxygen during all measurements and sample preparation, except where indicated. Thin films of the polymers with dopants were prepared by making a concentrated solution (≈20 mg/mL) in chloroform with the appropriate amount of dopant, allowing the solution to equilibrate for at least 12 hours, and then spin-casting onto the appropriate, clean substrate.

DC electrical conductivity of pristine and doped polymer films (0.002, 0.005, 0.01, 0.02 molar eq. of BCF and BF_3) was measured by using interdigitated gold contacts, photolithographically prepared on SiO_2. The width and length of the channel were 20 cm and 8 μm, respectively. The thickness of the gold contacts was 50 nm. The polymer films were spin-casted on pre-cleaned substrates with the interdigitated gold contacts from a chloroform solution (5 mg/ml) at the spin speed of 2000 rpm. I-V characteristics were measured by a semiconductor analyzer (Keithley 4200).

Impedance Spectroscopy measurements were obtained from a device structure of n^{++}-Si/SiO_2 (200 nm) / benzocyclobutene (30 nm) / active layer / Au to give the metal-insulator-semiconductor (MIS) architecture. Benzocyclobutene (BCB) was spuncast on top of the SiO_2 dielectric layer from a 1 mg/mL solution at 4000 rpm, and then annealed at 250°C for 1 hour. The active layer was spun-coat at 1200 rpm on top of BCB after cooling, followed by thermal evaporation of the gold contact. The n^{++}-Si was used as the working electrode. The stack of 200 nm SiO_2 and 20-30 nm BCB served as the insulator layer. Film thickness measurements were carried out using an Innova AFM. MIS devices were analyzed using a Solartron 1260 impedance analyzer. The impedance spectra were measured in a wide frequency range from 10 Hz to 3 MHz with a small AC amplitude

signal of 20 mV and different DC biases ranging from -15 V to 20 V.

UV-Vis-NIR absorption spectra were obtained using a Perkin-Elmer Lambda 750 UV-Vis-NIR spectrometer. Thin films were prepared on cleaned glass substrates and encapsulated inside a glovebox using epoxy around the film edges and another glass substrate. After curing, the samples were measured outside the glovebox. For solution absorption the concentration of PCPDTPT was always 0.025 mg/mL, whereas the concentration of PCPDTBT was always 0.05 mg/mL. The concentration of PhF2,5 for solution absorption was always 0.025 mg/mL.

EPR measurements were taken on a Bruker EMXplus Spectrometer System in continuous wave mode in the X-band frequency (9.3 GHz) using a Bruker ER 4119HS-LC high sensitivity resonator. The microwave cavity was tuned each time a new sample was loaded. 1.0 mm inner-diameter quartz capillaries were used to hold the samples. For each set of experiments which indicates the intensity of the EPR signal, the sample position was adjusted in the cavity to keep Q-values within 10% of each other. Error bars of 20% are included to account for variations in the Q-value, as well as potential fluctuations in the amount of solution loaded by capillary action into the quartz tubes, despite every precaution taken to keep sample preparation identical every time. Solid-state samples were prepared by drawing up a concentrated solution of the polymer (20 mg/mL in chloroform) with the appropriate amount of dopant, and letting the solvent evaporate in a glovebox over the course of 24 hours. Both ends were capped with Critoseal before bringing outside of the glovebox and measuring immediately. For solution-state measurements, the concentration of polymer was kept at a constant 0.125 mg/mL in chlorobenzene.

Experimental continuous-wave ENDOR was acquired on a Bruker EMXplus Spectrometer System fitted with an ENDOR probehead (Bruker EN 801 resonator). A solution of PCPDTBT (20 mM in chloroform with respect to the repeat unit) with 1.0 molar equivalents of BCF was prepared in a glovebox using an air-tight, quartz EPR

tube (outer diameter 5 mm). The sample was brought out of the glovebox, flash-frozen in liquid nitrogen, and kept at 100 K during the measurement. The microwave power was 6.3 mW, the microwave frequency was 9.5 GHz, and the magnetic field strength was 3390 G. The radio frequency power was attenuated by 10 dB. ENDOR spectra were simulated from DFT calculations using the EasySpin software.[153] A magnetic field strength of 3390 G and 0.8 MHz linewidth (full width at half maximum, Gaussian broadening) were used as parameters of the simulation. First-order perturbation theory was used to speed up the calculations. For the oligomeric structures of PCPDTBT (e.g. '4mer Cation'), the magnetic properties of alkyl protons and the two terminal aromatic protons were not considered. This was done in order to better reflect the physical nature of the polymer.

Gaussian09 was used for DFT geometry optimization at the B3LYP/6-31G(d,p) level of theory.[26, 102] Alkyl chains were replaced by methyl groups to expedite calculations. The conductor-like polarizable continuum model, CPCM, was used for considering the energetics of proton transfer and electron transfer (solvent = chlorobenzene). The coordinates of the optimized geometries were then used as a starting point for the DFT calculation of magnetic properties (g-tensors and hyperfine coupling constants) using the ORCA computational package.[154] The magnetic properties were calculated using the B3LYP functional and EPR-II basis set (except for sulfur atoms, which used the def2-TZVPP basis set) in vacuo.[155, 156] The anisotropic magnetic dipole and isotropic Fermi contact contributions to hyperfine coupling constants were calculated only for aromatic protons of the 4mer, excluding the two terminal protons (one on each end) of the oligomer. For BCF, only contributions from boron and fluorine were considered. This approach (neglecting the effect of solvent, replacing alkyl chains with methyl groups, choice of oligomeric length, etc.) for calculating magnetic properties via DFT methods is described and justified in more detail in reference [157].

Details on the other experimental methods (UPS, XPS, IPES, GIWAXS, AFM, etc.)

can be found in the relevant publication of this work.

7.3 Electrical Measurements and Bulk Morphology

As shown in Figure 7.3, the conductivity of PCPDTPT increases by over one order of magnitude upon the addition of 0.02 molar equivalents (with respect to the repeat unit of the polymer) of BCF and F_4TCNQ, from 1.9×10^{-5} S/cm up to a conductivity of 6.5×10^{-4} S/cm and 3.2×10^{-4} S/cm, respectively. Our initial electrical measurements and EPR experiments suggest that BF_3 does not significantly dope PCPDTPT; thus, we did not pursue a complete set of electrical measurements for this blend combination. In Figure 7.3b we see that just 0.02 molar equivalents of BCF is able to increase the conductivity of PCPDTBT by about 2 orders of magnitude, from 2.4×10^{-7} S/cm to 1.8×10^{-5} S/cm, whereas F_4TCNQ at the same concentration increases the conductivity by only one order of magnitude, up to 2.1×10^{-6} S/cm. Meanwhile, BF_3 induces a conductivity of only 7.4×10^{-7} S/cm at 0.02 molar equivalents, an increase of less than one order of magnitude.

There are many factors which could contribute to enhanced conductivity in an organic semiconductor, such as decreased contact resistance, improved morphology, trap-filling, changes in electronic structure, and others.[1] While F_4TCNQ has been rigorously studied and there is no question it is a p-type dopant, fewer studies have conclusively demonstrated that Lewis acids, such as BCF, are, in fact, p-type dopants. Therefore, we began by measuring the contact resistance for the pristine polymer films, and the polymer films with 0.05 molar equivalents of BCF. We found the contact resistance to be negligible in all cases. Next, we investigated how the ionization potential (IP) and work function (WF) of the polymers change with increasing amounts of BCF via ultraviolet photoelectron spectroscopy (UPS).

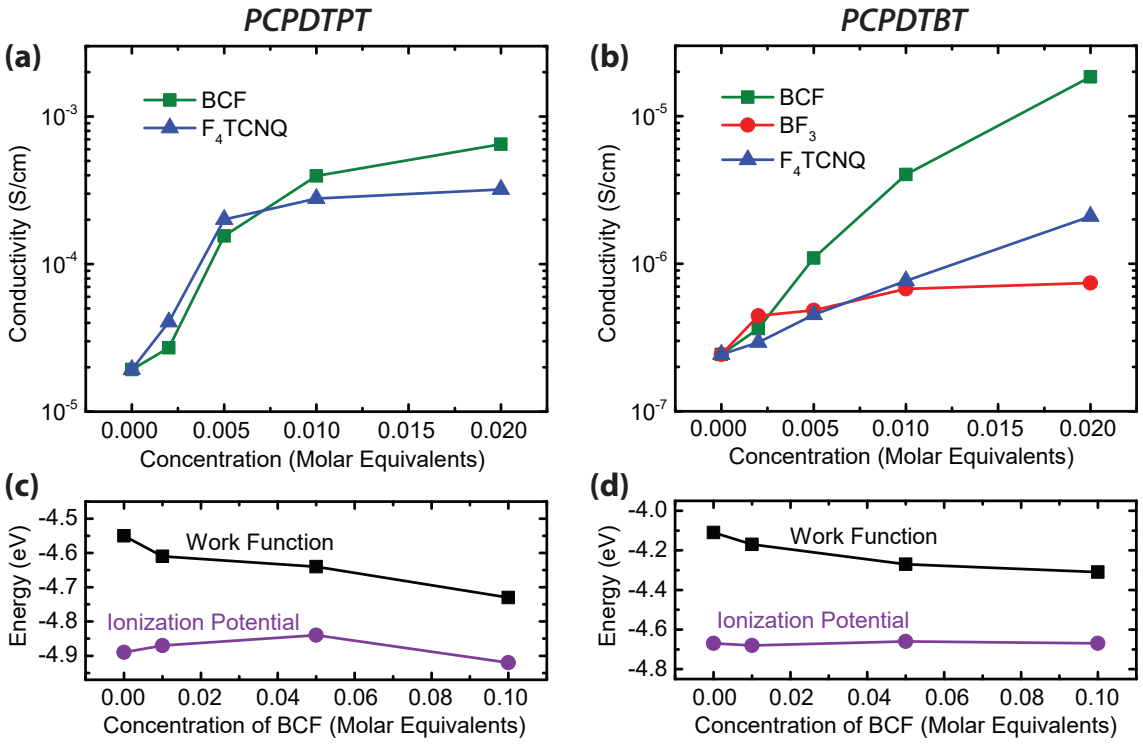

Figure 7.3: Conductivity of thin films of PCPDTPT (a) and PCPDTBT (b) with various amounts of the indicated dopant. Work function and ionization potential with respect to vacuum of PCPDTPT (c) and PCPDTBT (d), obtained by UPS, with increasing amounts of BCF.

Figure 7.3c,d show the results of UPS measurements for PCPDTPT and PCPDTBT, respectively. The marked increase in WF, while the IP remains essentially constant, is expected to be observed for p-type doping, wherein the creation of excess holes in the HOMO density of states induces a shift of the Fermi level toward the HOMO level.[158, 159, 160] These results are a good indicator that the observed increases in conductivity upon addition of BCF are, at least partially, attributable to p-type doping. Furthermore, the ionization potential of both pristine PCPDTPT (4.9 eV) and pristine PCPDTBT (4.7 eV) is low enough to expect ICT from F_4TCNQ, whose electron affinity is approximately 5.2 eV.[138] Thus, F_4TCNQ makes for a good comparison of ICT doping versus Lewis acid doping. While this manuscript was under review, a particular referee was sceptical that F_4TCNQ was doping our polymers through the ICT mechanism, so I spent some

time attempting to prove this by UV-Vis-NIR absorption and FTIR spectroscopy. The fruits of my labor are shown in Figure 7.4.

UV-Vis-NIR absorbance (Figure 7.4a) was performed on 0.05 mg/mL PCPDTBT with 1.0 molar equivalents of F_4TCNQ and 0.025 mg/mL PCPDTPT with 1.0 molar equivalents of F_4TCNQ. The solvent was chlorobenzene. The two distinct optical transitions of the F_4TCNQ^- anion (765 and 867 nm) are easily recognizable in PCPDTBT, but absent in the case of PCPDTPT.[161] Both polymers show increased NIR absorption, indicative of polaron absorption. From this data alone, we can conclude that F_4TCNQ dopes PCPDTBT by the integer charge transfer (ICT) mechanism. The data is inconclusive with respect to PCPDTPT. In Figure 7.4b the UV-Vis-NIR absorbance of thin-films of PCPDTBT with 0.07 molar equivalents of F_4TCNQ and PCPDTPT with 0.05 molar equivalents F_4TCNQ is shown. The concentration of PCPDTBT was 7.5 mg/mL and the concentration of PCPDTPT was 5 mg/mL. The concentration of F_4TCNQ in the solutions prepared for spin-casting (0.2 mg/mL in chloroform) were already approaching the solubility limit in chloroform, preventing us from doping the films to higher levels. This is precisely the reason why Lewis acid doping is so attractive: Lewis acid dopants typically have excellent solubility in common organic solvents and do not significantly disrupt film quality, enabling highly doped thick films from spin-casting methods. Comparing the spectrum of PCPDTBT with F_4TCNQ to the spectrum of PCPDTBT with BCF (Figures 7.7 and 7.18), we see essentially the same NIR absorption features. Although this corroborates our assignment of polaron absorption, it does not provide any mechanistic insight into the doping process, since we only see one of the products that result from doping, i.e. the positive polymer polaron. The key problem, then, in the case of Lewis acid doping, is determining how that polaron gets generated.

Figure 7.4c shows FTIR spectra of the solutions described in subfigure (b). The solutions were sandwiched in between two NaCl salt plates and the data collected in

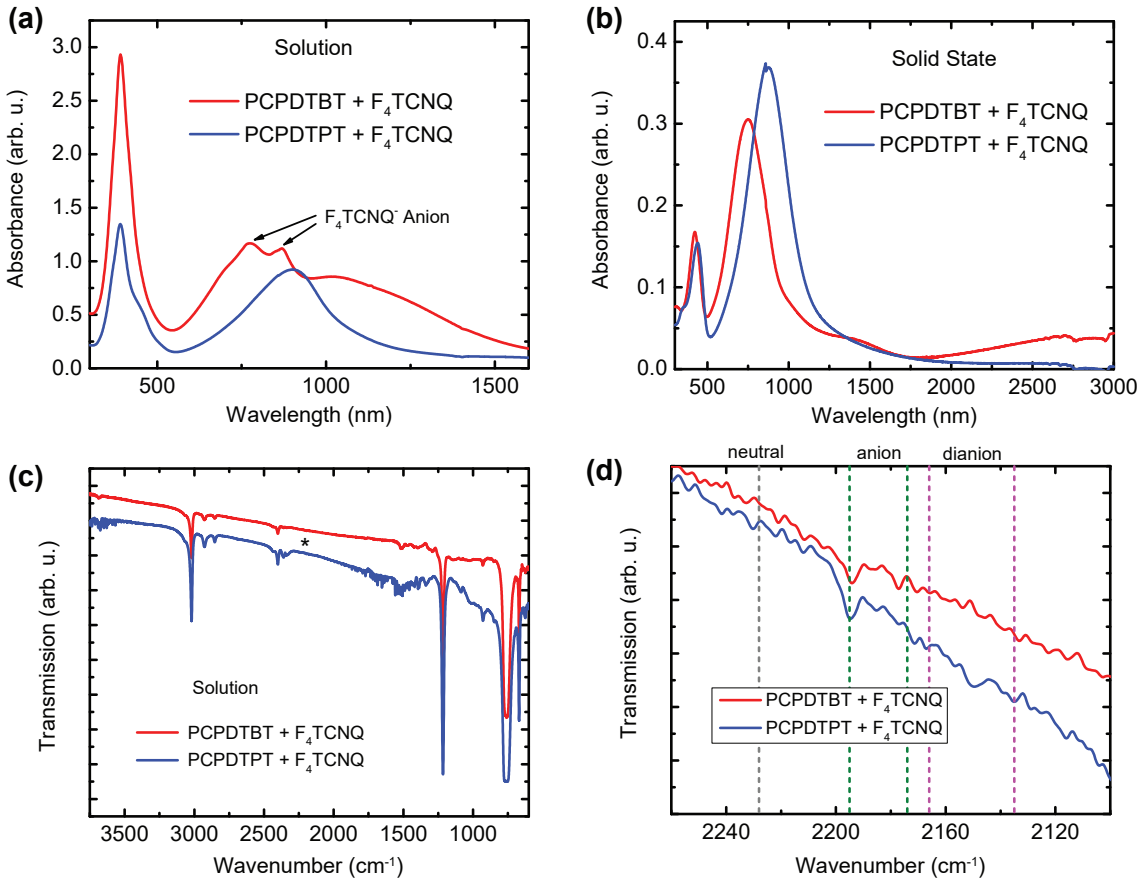

Figure 7.4: UV-Vis-NIR absorption and FTIR spectroscopy of PCPDTBT and PCPDTPT with F_4TCNQ. (a) Absorbance in chlorobenzene solution. (b) Absorbance of thin films. (c) FTIR transmission in chloroform solution. (d) Zoomed in region of (c) relevant to nitrile stretching.

transmission mode. I attempted spin-casting and drop-casting on a single salt plate and collecting transmission-mode FTIR, but the signal was too low to observe any features in the 2240 cm^{-1} region, which is where the resonant frequency of the nitrile stretch lies (indicated on the plot with an asterisk). The spectrum is dominated by features of chloroform. In Figure 7.4d I show a zoomed-in region of the spectra in (c) in order to identify the presence of the nitrile functional group. Because the signal was poor, we did not attempt to perform a background correction. As F_4TCNQ gains additional electron density from charge transfer, the nitrile stretch shifts to lower wavenumber.[162] The

neutral F_4TCNQ molecule absorbs IR radiation very weakly at 2,228 cm^{-1} (indicated on the plot by the gray dashed vertical line). Previous work also noted the apparent lack of any neutral F_4TCNQ IR absorption in doped solutions. The F_4TCNQ^- anion exhibits a strong absorption feature at 2,195 cm^{-1} and a weaker absorption at 2,174 cm^{-1} (indicated on the plot by green dashed vertical lines). For both PCPDBT and PCPDTPT we see clear evidence of the F_4TCNQ^- anion at approximately 2,195 cm^{-1}. This is strong evidence that both polymers are doped by F_4TCNQ through the ICT mechanism. The work referenced above suggests that F_4TCNQ is actually capable of accepting two electrons under particular circumstances, thereby forming a F_4TCNQ^{2-} dianion. The dianion exhibits IR absorption at 2,166 and 2,135 cm^{-1}, both with moderate oscillator strength (indicated on the plot by magenta dashed vertical lines). Interestingly, PCPDTPT doped by F_4TCNQ shows weak absorption features at these two locations. There is also a broad absorption feature centered at 2,150 cm^{-1}, which may also be related to nitrile stretching in the presence of increased electron density (greater than one additional electron). This could explain the apparent lack of F_4TCNQ^- anion absorption in the UV-Vis-NIR spectrum (doping with PCPDTPT in the solid state may favor the dianion over the singly charged anion).

Conductivity (σ) alone does not give much insight into the nature of the interaction between polymer and dopant, because, for the case of p-type materials, it is the product of the hole mobility (μ_p), the free (or mobile) charge carrier density (p), and the elementary charge q:

$$\sigma = qp\mu_p \tag{7.1}$$

To further investigate how the dopants affect the electrical properties of the two polymers, we fabricated metal-insulator-semiconductor (MIS) devices with various concentrations of dopant and studied the devices via impedance spectroscopy (Figure 7.5). From these

measurements the free charge carrier densities were determined, which then allowed for the determination of mobility, via Equation 7.1, as well as doping efficiency. Capacitance spectra of the MIS structures (Figure 7.5a) at different DC bias were calculated from the real and imaginary parts of measured impedance, corrected by the effect of the series resistance R_s and parasitic inductance of electrical cables L_i, that is important in the high-frequency region:

$$C_{cor} = -\frac{1}{\omega}\left[\frac{Z'' - \omega L_i}{(Z' - R_s)^2 + (Z'' - \omega L_i)^2}\right] \tag{7.2}$$

where Z' and Z'' are the real and imaginary parts of the measured impedance, respectively; ω is the angular frequency.[163]

In the accumulation regime (large negative bias) and at low frequencies, the total capacitance of the MIS structure should be equal to the insulator capacitance $C_{cor}(-15\,V) = C_i$.[164, 165] The larger capacitance, measured at low frequencies (< 50 kHz), originates from parasitic processes (a lateral spread of charge carriers, traps, leakage current, etc.), which can follow the low-frequency signal, and thereby contribute to the measured capacitance. At higher frequencies their effect is negligible. However, the capacitance effect of the neutral region of the active layer, connected in series, reduces the capacitance of the MIS structure with increasing frequency. The saturated high frequency (10 MHz) corrected capacitance C_{cor}(10 MHz) is equal to the geometric capacitance of the stack of the insulator and polymer layers: C_{cor} (10 MHz) $= C_g = \frac{C_p C_i}{C_p + C_i}$.

The capacitance-voltage (C-V) characteristics, determined at the medium frequency of 50 kHz when C_{cor}(-15 V) $= C_i$ clearly reveals two distinct operation regimes: accumulation and depletion (Figure 7.5b). The concentration of uncompensated acceptors

$(N_A - N_D)$ was determined from the slope of the Mott-Schottky plot (Figure 7.5c):

$$N_A - N_D = \frac{2}{q\epsilon\epsilon_0 \frac{d(\frac{A}{C})^2}{dV}} \tag{7.3}$$

where N_A is the concentration of ionized acceptors, N_D is the concentration of ionized donors, $\epsilon = 2.5$ is the dielectric constant, determined from the geometric capacitance (C_g), ϵ_0 is the permittivity of free space, and $A = 0.025$ cm^2 is the area of the MIS structure.[164, 166, 167, 168] Assuming that all uncompensated acceptors are ionized in the neutral region of the semiconductor layer, their concentration is equal to the concentration of free holes, i.e. $N_A - N_D = p$. The doping efficiency was determined by:

$$\textit{Doping Efficiency} = \frac{p - p_0}{N_{dop}} \tag{7.4}$$

where p_0 is the background concentration of free holes in the pristine polymer films (intrinsic charge carrier density plus unintentional doping) and N_{dop} is the concentration of doping molecules in the polymer film. This was determined by $N_{dop} = N_{mon} \times [dopant]$, where N_{mon} is the concentration of monomer units in the polymer film, and $[dopant]$ is the concentration of dopant in molar equivalents. The concentration of monomer units was calculated from $N_{mon} = \frac{N_A \rho}{M_W}$, where N_A is Avogadro's number, ρ is the film density, and M_W is the molar mass of the monomer unit. The density of the studied polymers was measured by means of X-ray reflectivity (PCPDTBT and PCPDTPT both have film densities of 1.06 g cm^{-3}).

The results from impedance spectroscopy are displayed in Figure 7.6, where the plots on the left-hand side are for PCPDTPT and the plots on the right-hand side are for PCPDTBT. In Figure 7.6a,b we see how the various dopants impact the hole mobility of the polymers. Overall, F_4TCNQ has a rather small impact on mobility, although it no-

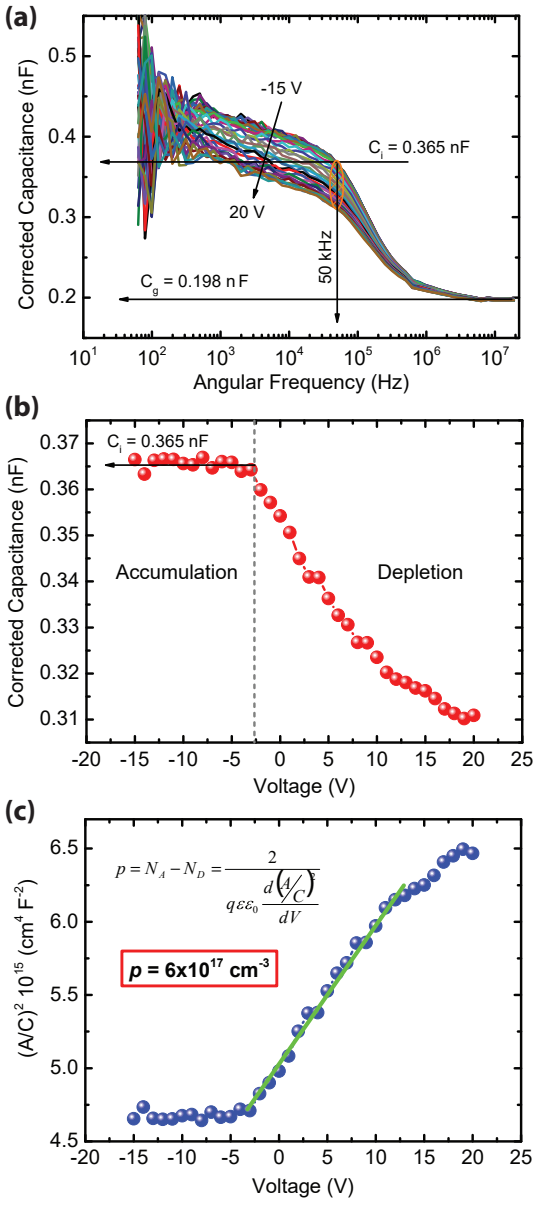

Figure 7.5: Impedance spectroscopy of PCPDTBT with 0.5% BCF in a MIS device architecture. (a) The corrected capacitance was measured as a function of AC frequency with various DC biases going from -15 V to 20 V in 1 V steps. (b) Corrected capacitance at 50 kHz plotted versus the DC bias. These values were extracted from plot (a) in the region indicated by an orange oval and black arrow at 50 kHz. (c) Mott-Schottky plot used to determine the concentration of free charge carriers, p.

ticeably decreases with PCPDTBT, an effect also seen for P3HT and F_4TCNQ.[169] For PCPDTPT, the addition of BCF results in a significant increase of mobility, from 0.002

cm^2/Vs to 0.02 cm^2/Vs. Notably, for PCPDTBT, BCF has a negative impact on mobility at the three lowest concentrations investigated, and only at 0.02 molar equivalents BCF do we finally see an improvement of the mobility compared to pristine PCPDTBT, from 2.7×10^{-5} cm^2/Vs to 5.1×10^{-5} cm^2/Vs. The effect of BF_3 is somewhat opposite, where there is an initial enhancement of the mobility at 0.002 molar equivalents, followed by a precipitous drop, resulting in a decrease of over one order of magnitude by 0.02 molar equivalents of BF_3 added, to a mobility of 3.3×10^{-6} cm^2/Vs.

In Figure 7.6c,d we see how the different dopants impact the free hole density (p) of the polymers. In the case of PCPDTPT, F_4TCNQ does a far superior job of generating free charge carriers compared to BCF. PCPDTPT with 0.02 molar equivalents of F_4TCNQ has 7.4×10^{17} holes/cm^3 compared to pristine PCPDTPT which has 5.2×10^{16} holes/cm^3, an increase of over one order of magnitude. With 0.02 molar equivalents of BCF, PCPDTPT has only 2.1×10^{17} holes/cm^3, increasing only by a factor of 4. Similar to its effect on PCPDTPT, F_4TCNQ increases the hole density of PCPDTBT by just over one order of magnitude, from 5.5×10^{16} holes/cm^3 in the neat film to 6.4×10^{17} holes/cm^3 with 0.02 molar equivalents of F_4TCNQ. The effect of the Lewis acids on PCPDTBT, however, are in stark contrast to their effect on PCPDTPT. With 0.02 molar equivalents of BCF the hole density of PCPDTBT increases by almost two orders of magnitude, up to 2.6×10^{18} holes/cm^3. With BF_3 the increase in hole density is just slightly less than with BCF, such that 0.02 molar equivalents of BF_3 is able to achieve a free charge carrier density of 1.4×10^{18} holes/cm^3.

Finally, these measurements are used to determine the doping efficiency (Figure 7.6e,f) of the various dopants as a function of their concentration in the polymer films. We define the doping efficiency to be the number of free charge carriers produced per molecule of dopant added. Thus, a doping efficiency of 10% means that for every 100 dopant molecules added, 10 free charge carriers are generated. In Figure 7.6e we see very clearly

that, for PCPDTPT, F_4TCNQ has a higher doping efficiency than BCF. At low concentration (0.002 molar equivalents), F_4TCNQ has a doping efficiency of 15.7% while that of BCF is a meager 0.5%, but by 0.02 molar equivalents of added dopant the efficiency of F_4TCNQ has dropped substantially to 4.4%, whereas the efficiency of BCF has increased slightly to 0.9%. Taking a look back at the conductivity measurements, a clear picture of how F_4TCNQ and BCF compare as dopants for PCPDTPT begins to emerge. At lower concentrations, the superior doping efficiency of F_4TCNQ is responsible for the higher conductivity measured in comparison to BCF. However, at higher concentrations, the conductivity with BCF is higher than that measured with F_4TCNQ, which can be attributed to (i) the decreased doping efficiency of F_4TCNQ and (ii) the significantly increased mobility of PCPDTPT films with BCF. That BCF significantly enhances the mobility of PCPDTPT is a notable improvement in dopant performance when compared to F_4TCNQ, which often disrupts film morphology, leading to a decrease of the hole mobility.[139, 142, 143, 144, 145]

We found BCF to have only a minor impact on PCPDTPT film morphology at the concentrations used in this study, based on atomic force microscopy (AFM) and grazing incidence wide-angle X-ray scattering (GIWAXS) measurements. 2D GIWAXS patterns of PCPDTPT films with increasing BCF content show that addition of BCF changes the preferred orientation of PCPDTPT crystallites from edge-on to face-on. This phenomenon has been previously observed for an oligomer of similar chemical structure, and may be due to kinetic trapping of the polymer crystallization during spin-coating, arising from the presence of BCF.[170] Despite the change in orientation of the polymer crystallites relative to the substrate, no change in π-π stacking distances ($q = 1.8\mathring{A}^{-1}$, $d = 3.5\mathring{A}$) is observed. The surface roughness of thin films of PCPDTPT does not change substantially with up to 0.10 molar equivalents BCF, as evidenced by AFM. These results are in agreement with other studies done on polymers doped by BCF, which do not

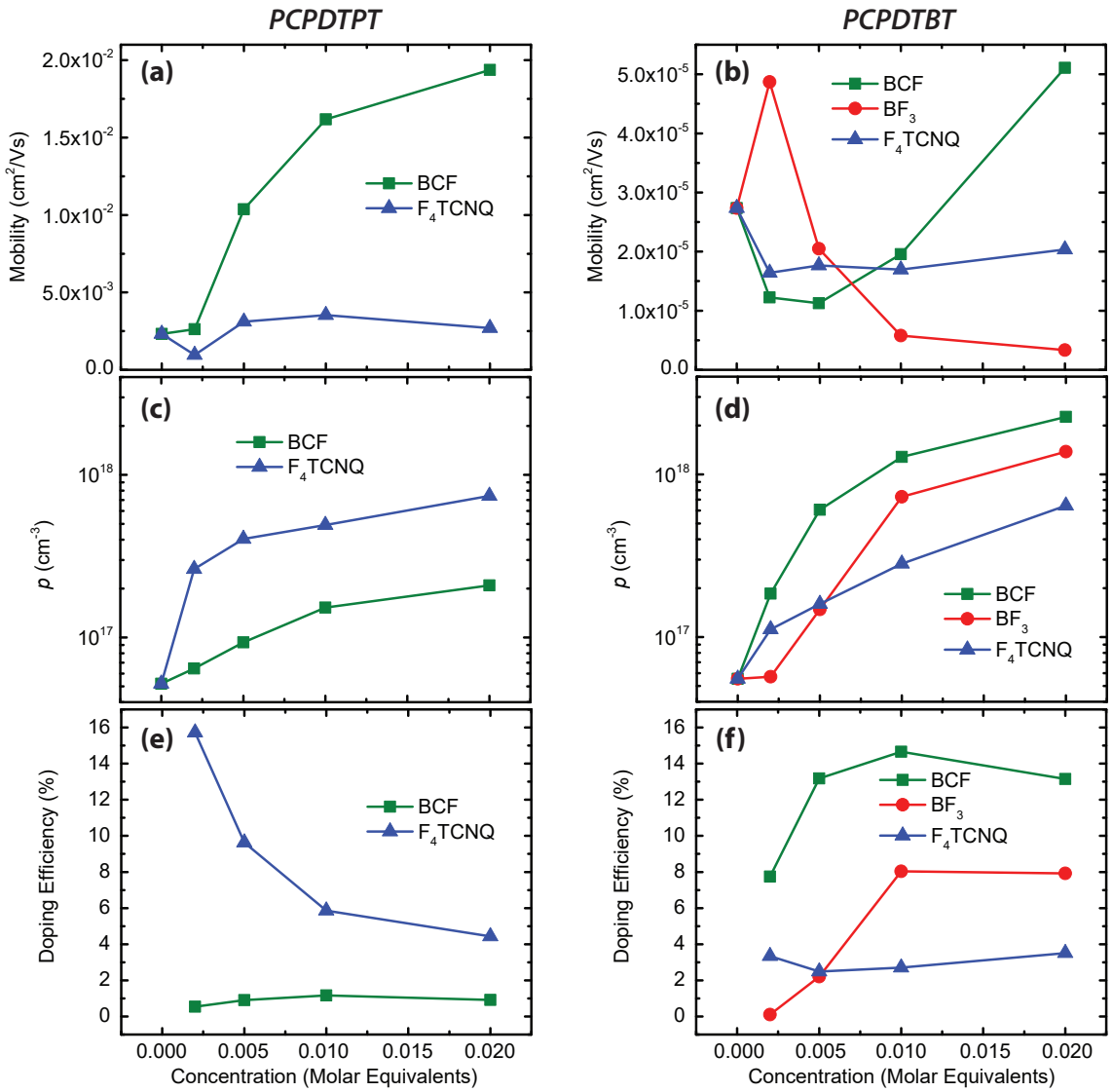

Figure 7.6: Results obtained from impedance spectroscopy for PCPDTPT (left) and PCPDTBT (right). (a,b) show hole mobility, (c,d) show the free charge carrier density, p, and (e,f) show the doping efficiency. The concentration of dopants is given in molar equivalents with respect to the polymer repeat unit.

indicate significant morphological changes at low doping concentrations.[83, 84]

In the case of PCPDTBT, BCF is clearly a better dopant than F_4TCNQ at all concentrations considered here. Although F_4TCNQ induces higher mobility than BCF at the two lowest concentrations, this difference is too small to outweigh the large difference in doping efficiency. At 0.002 molar equivalents in PCPDTBT, BCF has a doping effi-

ciency of 7.7%, whereas F_4TCNQ has an efficiency of 3.3%. By 0.02 molar equivalents, the doping efficiency of BCF has increased to 13.1% (with a maximum of 14.6% efficiency at 0.01 molar equivalents), while the doping efficiency of F_4TCNQ has stayed relatively constant. Increasing BCF concentration only results in a small increase in the isotropic distribution of PCPDTBT crystallite orientations, as seen in the 2D GIWAXS patterns, and no change in π-π stacking distances ($q = 1.8\mathring{A}^{-1}$, $d = 3.5\mathring{A}$). Similar to PCPDTPT, BCF seems to have an insignificant impact on film morphology as assessed by AFM. In terms of the effectiveness of BF_3 as a p-type dopant, its doping efficiency follows a similar trend to BCF but lower in magnitude. The doping efficiency of BF_3 at 0.002 molar equivalents is a poor 0.1%, but by 0.02 molar equivalents the efficiency has increased to 7.9% (with a maximum efficiency of 8.0% at 0.01 molar equivalents), which is about twice as efficient as F_4TCNQ at the same concentration. Thus, at low concentrations BF_3 performs better than F_4TCNQ, but at higher concentrations F_4TCNQ performs better, most likely attributable to the negative impact BF_3 has on PCPDTBT's mobility at high concentrations.

From here we decided to focus primarily on the Lewis acid BCF, since it is clearly the superior Lewis acid dopant in terms of electrical properties, and it can be easily handled as a pure solid (BF_3 must be added in the form of liquid borontrifluoride etherate). To this end we investigated how much BCF can increase the conductivity of PCPDTBT films. We found that a maximum conductivity of 8×10^{-3} S/cm is achieved with 0.2 molar equivalents of BCF, an increase of over four orders of magnitude in comparison to pristine PCPDTBT films. Next, we sought to investigate the relationship between doping and Lewis acid adduct formation via UV-Vis-NIR absorption spectroscopy, EPR spectroscopy, and XPS.

7.4 Adduct Formation vs. Doping

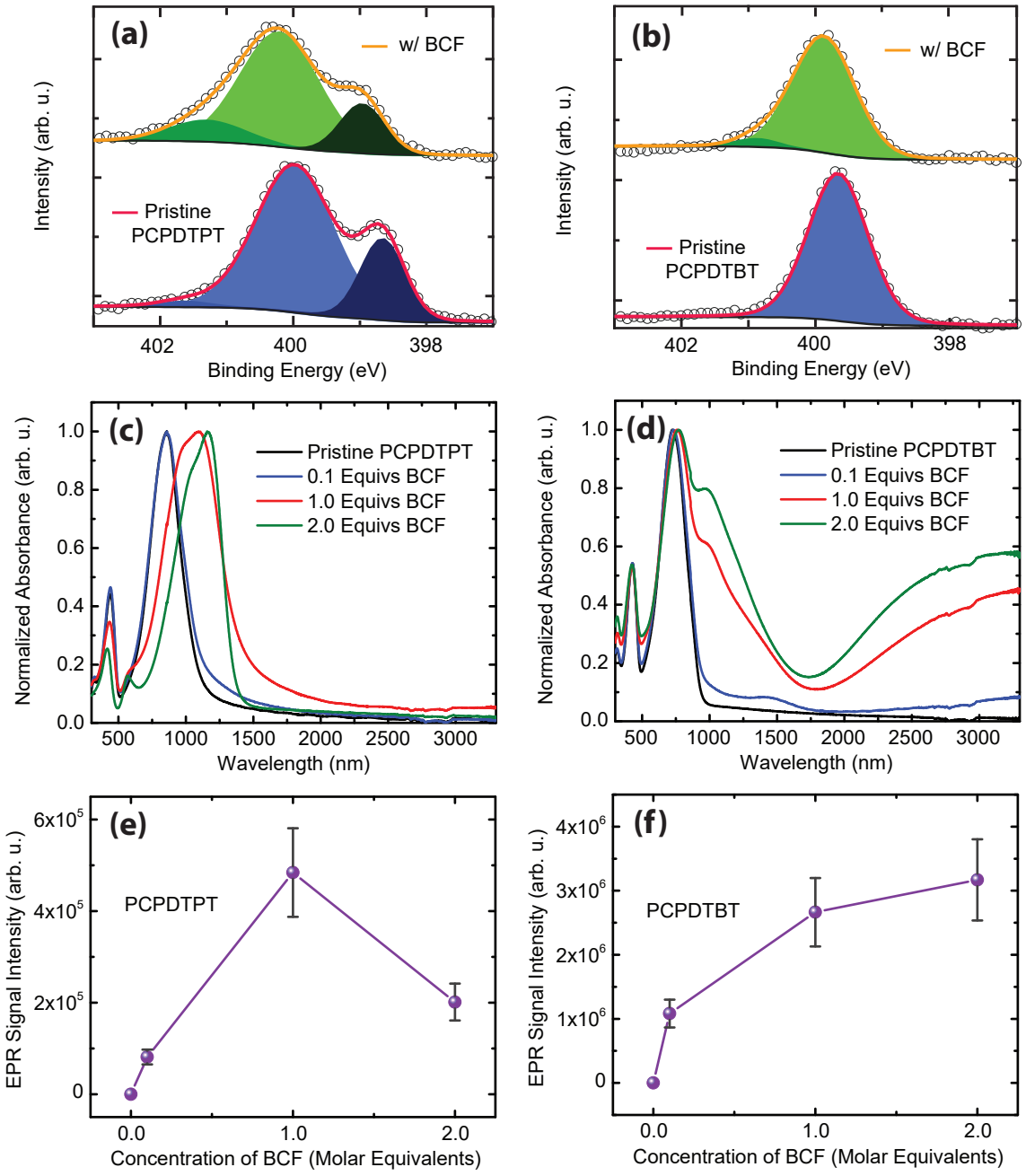

Figure 7.7: Thin-film properties of PCPDTPT (left panels) and PCPDTBT (right panels) with the Lewis acid BCF. XPS N 1s of PCPDTPT (a) and PCPDTBT (b) with 1.0 molar equivalents of BCF. Absorption of PCPDTPT (c) and PCPDTBT (d) with BCF. EPR signal intensity of PCPDTPT (e) and PCPDTBT (f) with BCF at the same microwave power (1.002 W).

Figure 7.7 shows data for thin films of PCPDTPT (top row) and PCPDTBT (bottom row) with BCF. In Figure 7.7a we show the nitrogen 1s binding energies obtained from XPS measurements. In pristine PCPDTPT we observe two peaks with a relative area ratio of 2:1, corresponding to the two chemically equivalent azole nitrogen atoms (peak center 400 eV) and one pyridyl nitrogen (peak center 399 eV) apparent from the chemical structure of PCPDTPT.[111, 112] In the presence of BCF, an additional peak at higher binding energy (401 eV) appears, a clear result of the boron atom of BCF interacting with the pyridyl nitrogen of PCPDTPT, i.e. adduct formation. High-resolution S 2p spectra with and without BCF are identical, suggesting that BCF does not interact with the sulfur atoms of CPDT (which are Lewis basic, but very weak compared to pyridyl nitrogen). In Figure 7.7c we see that the addition of BCF results in redshift of PCPDTPT's main absorption peak, from 859 nm (pristine) to 1158 nm (2.0 molar equivalents of BCF), a dramatic shift of 299 nm (0.37 eV). This is consistent with the redshift observed upon addition of BCF to small molecules and polymers with a strong Lewis basic binding site, e.g. pyridyl nitrogen.[74, 78] Notably, Figure 7.7e shows that the concentration of radicals in PCPDTPT decreases when going from 1.0 to 2.0 molar equivalents of BCF. Also, note how the absorption shoulder around 1500 nm changes with concentration of BCF. From 0.1 to 1.0 molar equivalents there is an increased amount of absorption of this spectral region, with a concomitant increase in EPR signal. However, from 1.0 to 2.0 molar equivalents the absorption in this region decreases significantly, returning to the level seen in pristine PCPDTPT. Similarly, the EPR intensity decreases when going from 1.0 to 2.0 molar equivalents. Thus, we attribute the weak absorption around 1500 nm to polaron absorption. At 1.0 molar equivalents there is also non-negligible absorption further in the NIR, around 3000 nm, which is most likely additional polaron absorption. Upon doping, conjugated polymers typically have two low-energy regions of increasing NIR absorption from polarons.[1]

As shown in Figure 7.8, similar absorption and EPR results were observed in solution for PCPDTPT. Note how the shape of the spectra change at high concentrations of BCF. Polaron absorption in the 1100 - 1600 nm range is evidenced at 1.0 molar equivalents of BCF by (i) the shoulder around 1350 nm and (ii) by the redshifted maximum absorption. By 8.0 molar equivalents of BCF, the shoulder has disappeared and the peak has blueshifted. No radicals were observed by EPR at 8.0 molar equivalents of BCF. These data strongly suggest that binding and doping are separate, independent events, such that binding outcompetes doping at high concentrations. To further verify that adduct formation is not responsible for doping, we added the stronger Lewis acid BBr_3 to PCPDTPT, for which we observed adduct formation but no doping (Figure 7.9).

For PCPDTBT and BCF, the XPS measurements of the nitrogen 1s binding energy (Figure 7.7b) show that there is an insignificant amount of BCF that binds to the Lewis basic azole nitrogens of PCPDTBT. In line with previous results, BCF is found to not interact strongly with azole nitrogen atoms due to steric constraint and the relatively poor Lewis basicity of these nitrogen atoms. Figure 7.7d shows the absorption of PCPDTBT films with BCF. The considerable NIR absorption around 3000 nm which increases with the concentration of BCF added is attributable to polaron absorption. The concomitant increase in absorption in the region of 1000 - 1500 nm suggests that this is also polaron absorption. Notice, also, how the main absorption band of PCPDTBT (peak of 727 nm) is still clearly present even with 2.0 molar equivalents of BCF. In Figure 7.7f we see that the EPR signal intensity increases with increasing concentration of BCF added, suggesting that the NIR features observed by absorbance spectroscopy are, indeed, attributable to polaron absorption. Just as for PCPDTPT, the results of PCPDTBT interacting with BCF indicate that binding, i.e. Lewis acid adduct formation with the polymer, is not responsible for the p-type doping of these polymers. Interestingly, I found that the absorption spectrum of PCPDTBT in chlorobenzene with BF_3 is substantially different

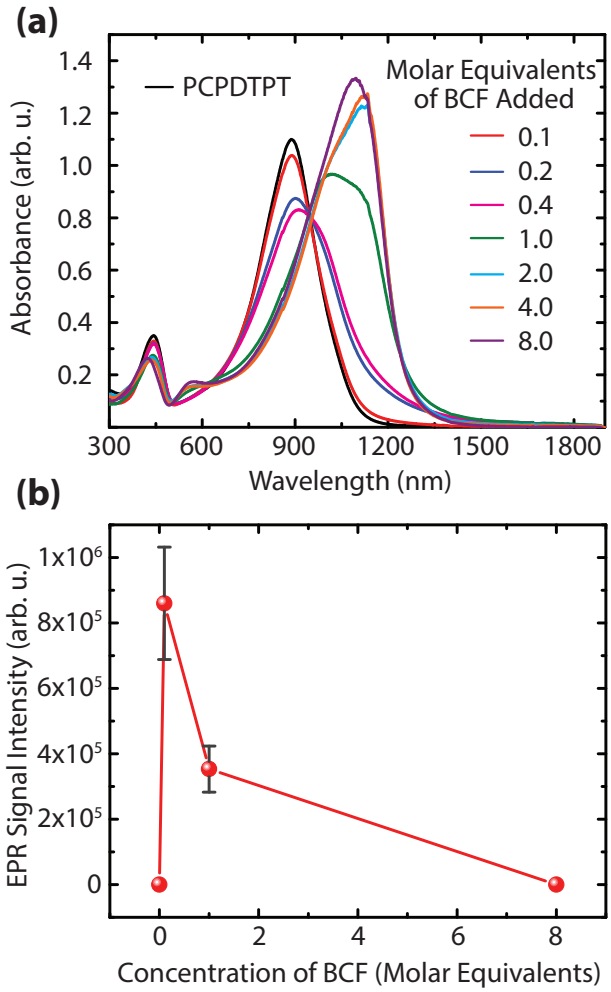

Figure 7.8: Absorption in chlorobenzene (a) of PCPDTPT with various amounts of BCF. The concentration of PCPDTPT was 0.025 mg/mL. EPR signal intensity (b) of PCPDTPT with various amounts of BCF. The concentration of PCPDTPT was 0.125 mg/mL. The microwave power was 10.02 mW.

from that with BCF. I hypothesize that this is the result of some adduct formation between the smaller and stronger Lewis acid (BF_3) with the azole nitrogens of the polymer.

Our final inquiry into the electronic structure of polymer films doped with BCF was performed through inverse photoemission spectroscopy (IPES). UPS and IPES results, obtained from our Kentucky collaborators Prof. Kenneth Graham and his graduate student, Tuo Liu, are shown in Figure 7.10, Table 7.4, and Table 7.4. Unfortunately, it was not possible to obtain IPES spectra of pristine BCF due to the difficulty in fabricating

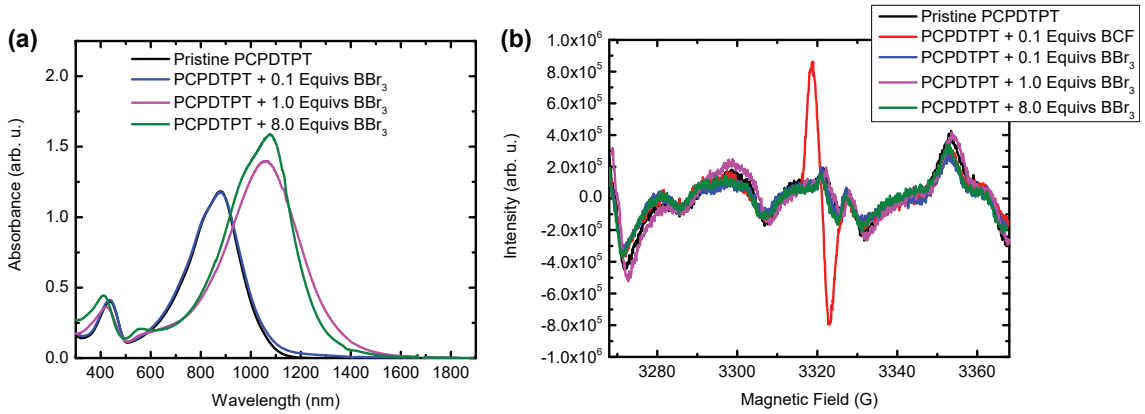

Figure 7.9: Absorption in chlorobenzene (a) of PCPDTPT with various amounts of the stronger Lewis acid BBr_3. The concentration of PCPDTPT was 0.025 mg/mL. EPR signal intensity (b) of PCPDTPT with various amounts of BBr_3. The concentration of PCPDTPT was 0.125 mg/mL. The microwave power was 10.02 mW. The EPR signal of PCPDTPT with 0.1 molar equivalents of BCF is included for comparison.

uniform films. As mentioned previously, the IPES attempts with BCF were a significant point of contention. Ultimately, the IPES data obtained from pristine BCF was determined to be unreliable. Because the effect of BCF on PCPDTBT is dominated by doping and not binding, we attribute this drastic change in the transport gap to the appearance of HOMO-derived unoccupied sub-levels (i.e. gap states) in the bandgap.[171, 172] The creation of holes in the HOMO of an organic semiconductor is accompanied by the appearance of unoccupied gap states just above the HOMO level of the material, as a result of Coulomb interactions. Thus, the increase in apparent electron affinity of PCPDTBT with increasing BCF concentration is not actually a measure of the blend's LUMO, i.e. transport level. Rather, this effect is observed due to the capture of electrons in the gap states. Additionally, the ionization potential of the material is expected to increase with increasing hole concentration, due to Coulomb effects. Because PCPDTPT is dominated by the effects of binding, and not doping, we attribute the changes in IP and EA to the emergence of the new electronically structured material, i.e. the Lewis acid-base adduct, and suggest that these energy levels reflect actual transport levels of the material. In-

deed, the change in PCPDTPT's transport gap upon adduct formation with BCF is in excellent agreement with the change in the optical gap as determined by UV-Vis-NIR absorption. This means that there is essentially no change in the exciton binding energy of the pristine polymer and polymer:BCF adduct (which I had assumed would be the case in Chapter 6). The shift in the Fermi energy toward the HOMO energy in PCPDTPT with increasing BCF concentration indicates that the material is doped with holes, but that the doping level is sufficiently low that we do not see the appearance of gap states in the IPES spectra, which are clearly observed for the highly doped PCPDTBT samples.

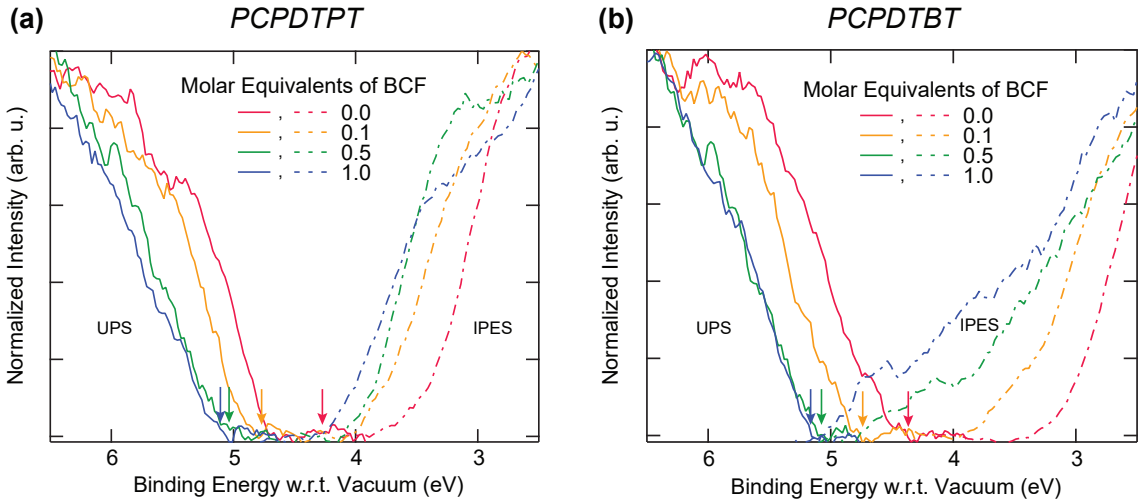

Figure 7.10: Ultraviolet photoelectron spectroscopy (UPS) and inverse photoemission spectroscopy (IPES) results for PCPDTPT (a) and PCPDTBT (b) with various amounts of BCF. The Fermi level position (and thus work function) for each sample is indicated with an arrow of the corresponding color.

Table 7.1: Properties of PCPDTPT films extracted from UPS and IPES measurements.

Molar Equivalents of BCF	Ionization Potential (eV)	Work Function (eV)	Electron Affinity (eV)
0.0	4.75	4.27	3.43
0.1	4.86	4.77	3.86
0.5	5.06	5.03	4.04
1.0	5.11	5.11	4.22

Table 7.2: Properties of PCPDTBT films extracted from UPS and IPES measurements.

Molar Equivalents of BCF	Ionization Potential (eV)	Work Function (eV)	Electron Affinity (eV)
0.0	4.53	4.37	3.08
0.1	4.86	4.74	3.87
0.5	5.00	5.06	4.84
1.0	5.21	5.18	5.09

From these measurements we were able to measure the effect that BCF has on the transport gap. The results are in excellent agreement with changes in the optical gap, indicating that (i) PCPDTBT is heavily doped by BCF, and (ii) that adduct formation with PCPDTPT results in a 0.4 eV increase in the IP and a 0.8 eV increase in the electron affinity (0.4 eV reduction in the transport gap). The marked increase in the IP of PCPDTPT with BCF may account for the loss of doping effects upon increasing adduct formation, since protonation becomes increasingly difficult for materials with larger IP. Alternatively, the added steric bulk of the adduct may preclude the doping process. At any rate, the change in Gibbs free energy is expected to be negative for adduct formation, whereas for protonation it is expected to be positive. Hence, adduct formation outcompetes doping at high concentrations of Lewis acid.

The observation that adduct formation inhibits the doping process can be used to explain the trends in doping efficiency for the two Lewis basic polymers. The doping efficiency of BCF is higher for PCPDTBT than for PCPDTPT, because the latter polymer has stronger Lewis basic sites, specifically the pyridyl nitrogen atoms, which are conducive to adduct formation. Similarly, the doping efficiency of BF_3 is higher for PCPDTBT than for PCPDTPT (for which there was an insignificant amount of doping). Because BF_3 is a stronger and smaller Lewis acid than BCF, it is expected to bind more easily with Lewis basic sites. Thus, it is not surprising that the doping efficiency of BF_3

is lower than that of BCF. The more Lewis acids that are occupied by adduct formation, the fewer that are available for doping.

7.5 The Proposed Doping Mechanism

Bearing all of the above results in mind, we formulate a hypothesis for the mechanism of p-type doping by BCF which does not involve adduct formation with the polymers, nor ICT to the Lewis acid. Because BCF does form an adduct with PCPDTPT, but does not form an adduct with PCPDTBT, our mechanistic studies focus on the latter, for simplicity's sake. The proposed doping mechanism is outlined in Figure 7.11. First, a highly acidic (i.e. Brønsted acidity) BCF:H_2O complex protonates the CPDT moiety of the backbone, generating a negatively charged $[BCF:OH]^-$ complex and a positively charged polymer backbone $[PCPDTBT\text{-}H]^+$. Second, a neutral chain segment transfers an electron to the positively charged segment, resulting in a neutral, protonated radical species $[PCPDTBT\text{-}H]^\bullet$ and a positively charged radical species $[PCPDTBT]^{\bullet+}$. Although we have indicated the electron transfer is an intermolecular process, it could very well be an intramolecular process. The negatively charged $[BCF:OH]^-$ complex acts as the counterion to the positively charged radical of the polymer backbone $[PCPDTBT]^{\bullet+}$, the species which we attribute to be the free charge carriers observed in our electrical measurements.

The propensity for the intial reaction between CPDT and BCF:H_2O can be conveniently visualized through their electrostatic potential (ESP) surfaces, as shown in Figure 7.12. Note how the BCF:H_2O complex has greater partial positive charge than either BCF or H_2O, indicating its powerful acidity. These calculations suggest that there will be a strong interaction between the blue regions of CPDT and red regions of BCF:H_2O.

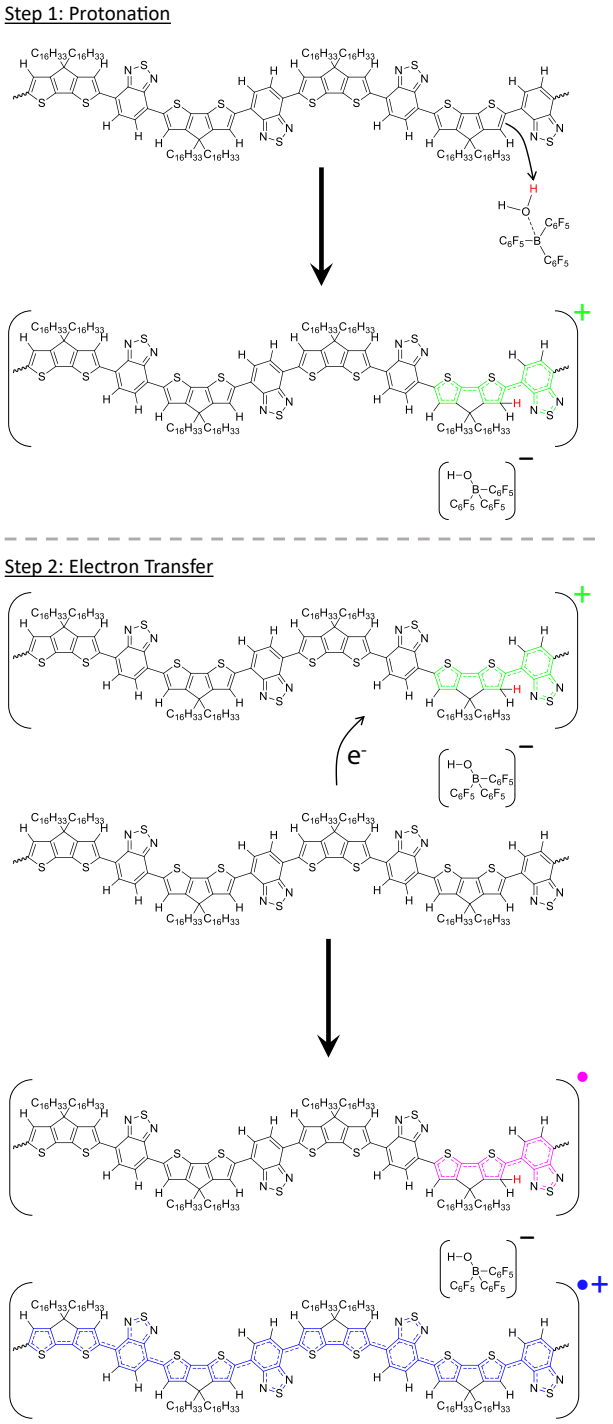

Figure 7.11: Proposed doping mechanism of PCPDTBT by BCF. The formation of the BCF:H_2O complex is assumed to have already taken place by Step 1.

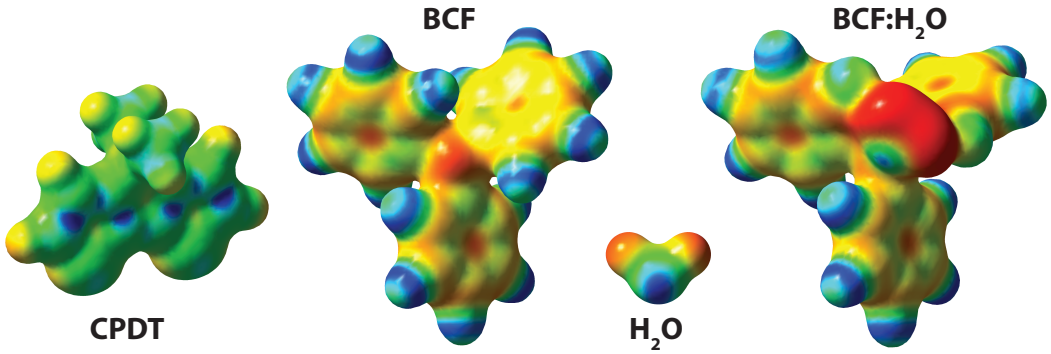

Figure 7.12: Electrostatic surface potentials of selected molecules. Areas of blue and red depict regions of negative and positive electrostatic potential, respectively. Recall that electrons will move from regions of low potential to regions of high potential, i.e. electrons want to move from blue to red. Essentially, blue regions have partial negative charge, and red regions have partial positive charge. The scale was kept constant between the different molecules, except for CPDT, which was changed in order to better emphasize its electron-rich areas.

7.6 Probing the Doping Mechanism by NMR

BCF is known to strongly complex water, and the resulting Brønsted acidity of the complex has been well documented in the literature.[173, 174, 175, 105, 92, 91] To demonstrate this Brønsted acidity, we investigated the protonation of the CPDT monomer, 4,4-dihexadecyl-4*H*-cyclopenta[1,2-*b*:5,4-*b*']dithiophene, by solution-state ^{1}H NMR in dry $CDCl_3$, shown in Figure 7.13. Despite using dried solvent, preparing samples in an inert atmosphere, dry glovebox, and using air-free NMR tubes, a proton resonance at around 6.5 ppm chemical shift was observed when neat BCF was added to $CDCl_3$, which is attributable to the protons in a BCF:H_2O complex and in good agreement with literature values.[105] In the trace below, the ^{1}H NMR spectrum of 20 mM CPDT is shown, with its characteristic set of two doublets in the aromatic region (6.9, 7.1 ppm). When 3.7 molar equivalents of BCF was added to 20 mM CPDT, 4 new resonances (5.3, 7.4, 7.6, 8.8 ppm) were detected in this region of interest, not including the resonances originating from neat CPDT (6.9, 7.1 ppm) and neat BCF (6.6 ppm), which suggest that the

majority of CPDT is not protonated at these concentrations.

Upon the addition of 100 molar equivalents of TFA, a strong Brønsted acid, to 20 mM CPDT, we see 4 resonances (5.4, 7.4, 7.7, 8.8 ppm) which align very well with those observed in CPDT + BCF, and the complete disappearance of the neat CPDT aromatic resonances indicates 100% conversion of CPDT to its protonated form. The integration and multiplicity of these 4 new peaks are consistent with the protonation of CPDT (Figure 7.14). When BCF was added to CPDT, the multiplicity of the peaks were discernable at room temperature. However, when TFA was added to CPDT the multiplicity of the protonated resonances could not be identified due to excessive peak broadening. I suspected that there was a fast equilibrium between the protonated and neutral forms of CPDT, so I retook the NMR at lower temperatures, to slow down the rate of reaction. Sure enough, at the lower temperatures the multiplicity was easily identifiable. This suggests that TFA is a significantly weaker Brønsted acid than the BCF:H_2O complex. When I added 11.0 molar equivalents of TFA to CPDT I didn't observe any protonation, as assessed by ^{1}H NMR. When comparing the protonated resonances caused by TFA versus BCF, the small difference in chemical shift for the resonances in the range of 7.5-7.7 ppm and 5.2-5.4 ppm is likely caused by the different nature of the counterion, since these protons are closest to the site of protonation. By contrast, the other two resonances of the protonated form (7.4, 8.8 ppm), which are on the opposite side of CPDT relative to the site of protonation, show almost no difference in chemical shift when comparing between BCF and TFA. These NMR data show unequivocally that BCF, in the presence of water, is capable of protonating CPDT. Figure 7.15 shows DFT calculations of the expected chemical shifts of a protonated CPDT, for which we find excellent agreement with the experimental results. Annotated spectra with integrations and J couplings can be found in the SI of the relevant publication.

The protonation of CPDT by TFA has been reported in the literature previously, al-

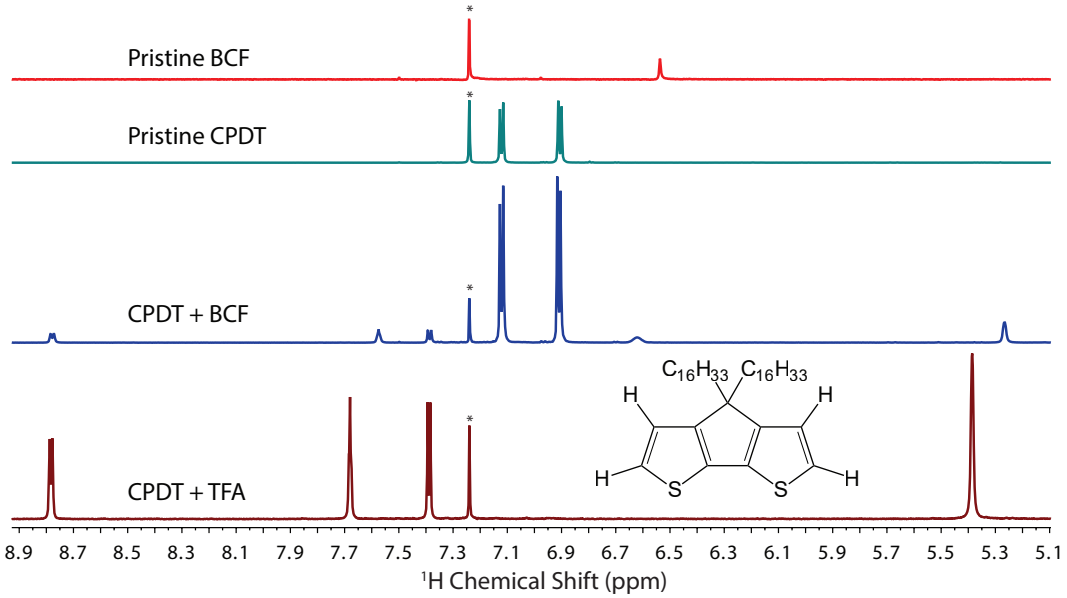

Figure 7.13: Solution phase ^{1}H NMR spectra in $CDCl_3$. The proton resonance of $CHCl_3$ is indicated with an asterisk. The molecular structure of CPDT is also shown.

though the authors did not directly observe the protonated form of CPDT experimentally as in our study.[176, 177] They also failed to see if protonation of their CPDT-containing molecules resulted in doping. In fact, they incorrectly attributed the proton resonance from TFA as the additional proton on [CPDT-H]$^+$. When I read through that paper, the proton NMR they took immediately stood out to me because the new resonance that appeared upon addition of TFA had a chemical shift which changed substantially with different concentrations of TFA. That didn't make sense to me. Also, they suggested that the protons opposite the side of protonation don't have a change in chemical shift compared to neutral CPDT, which seemed highly unlikely (and which DFT suggested was an incorrect analysis). So I looked at the ^{1}H NMR of TFA in $CHCl_3$ at various concentrations (Figure 7.16). Sure enough, the chemical shift of TFA changes with concentration. Because TFA is present in such large quantities, the change in chemical shift can be attributed to an effective change of the solvent properties - of which the amount/extent of hydrogen-bonding probably has the greatest effect (as opposed to a

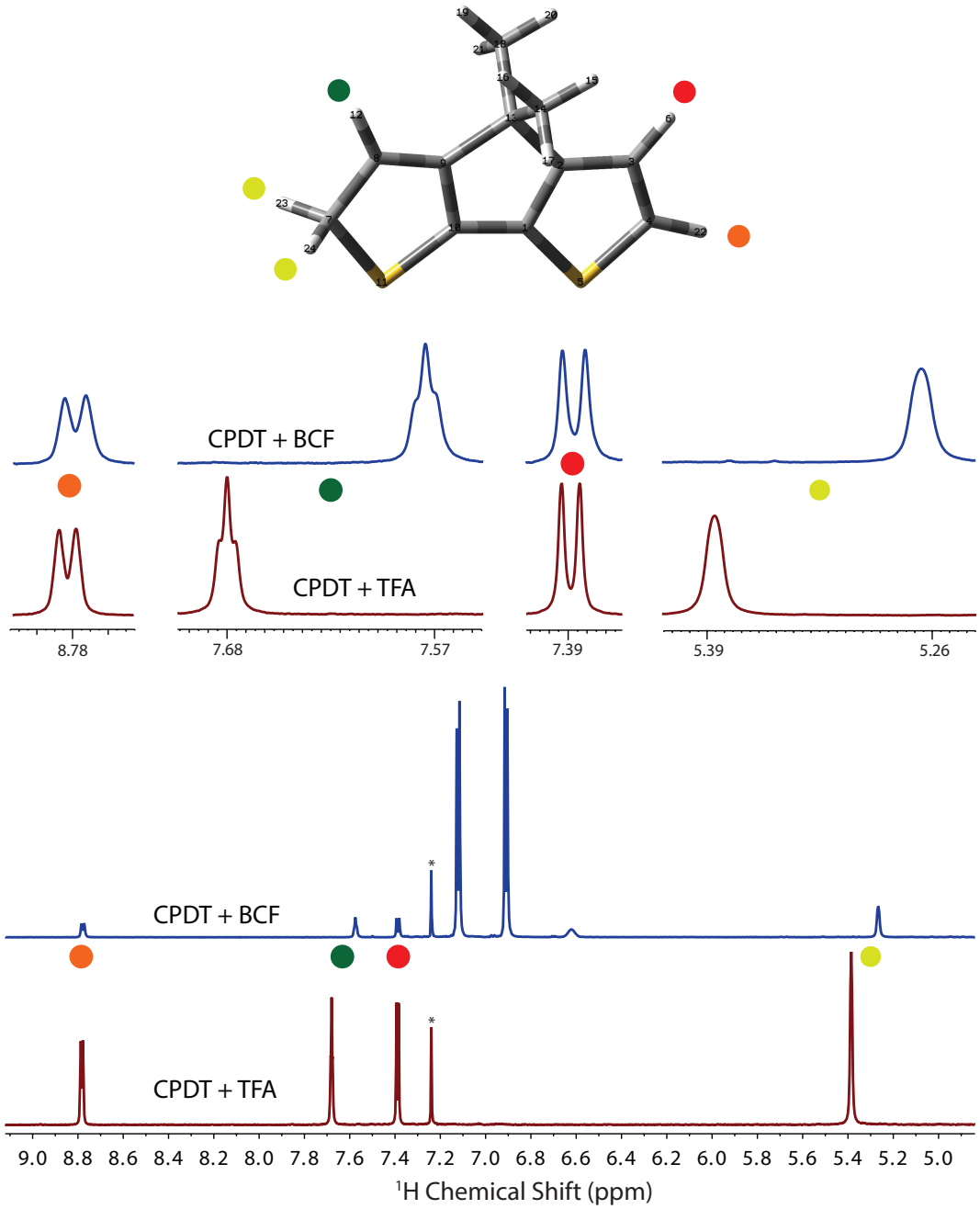

Figure 7.14: Highlighted regions of interest from the spectra in Figure 7.13. Peak assignments shown by the appropriately colored dots. The asterisk indicates the resonance originating from residual $CHCl_3$ ($\delta = 7.24$ ppm).

change in effective dielectric of the medium, for example). A higher concentration of TFA results in more hydrogen-bonding, meaning that protons become more deshielded,

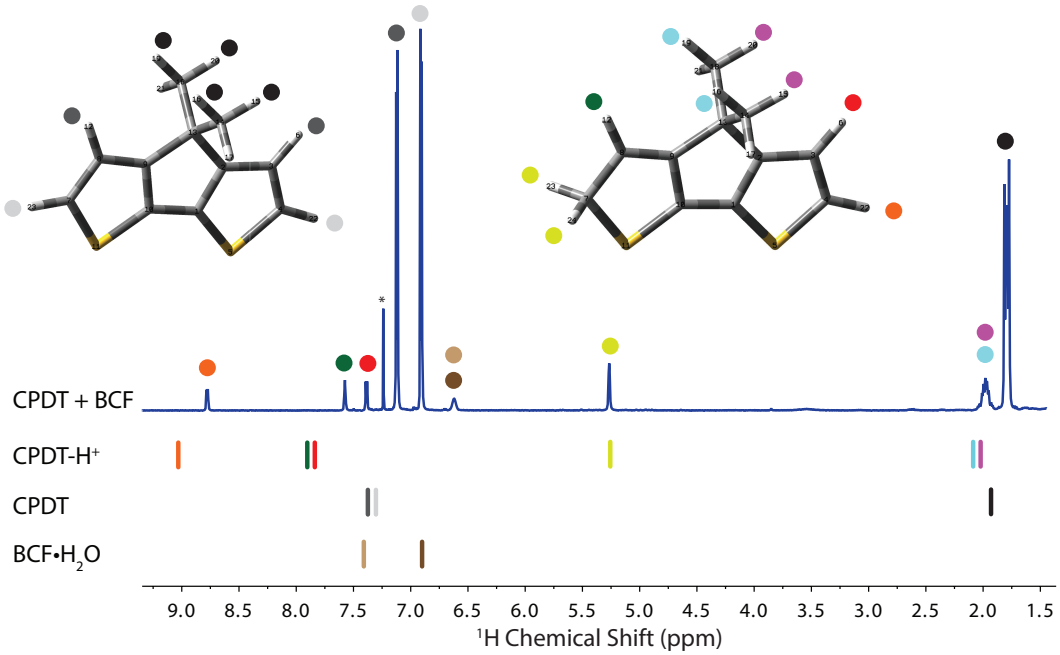

Figure 7.15: ^{1}H NMR spectrum of CPDT + BCF compared to DFT calculations. Optimized structures (shown) were calculated using the B3LYP functional and 6-31G(d,p) basis set using the CPCM solvent model (solvent = chloroform). The proton chemical shifts were calculated at the same level of theory and referenced to TMS. The asterisk indicates the resonance originating from residual $CHCl_3$ ($\delta = 7.24$ ppm).

increasing their chemical shift value.

Although the sharp resonances suggest that there are no paramagnetic centers present in the aforementioned solutions, we decided to pursue EPR measurements of these solutions anyhow. To our surprise, a small amount of radicals were detected by EPR (Figure 7.17a) for both CPDT with BCF and CPDT with TFA. UPS measurements (Figure 7.17b) also indicate that BCF is able to dope CPDT in the solid state, inferred from the increase of the work function of CPDT, while its ionization potential ($\approx$ 6.1 eV) stays essentially unchanged. Previous work has suggested that, for a given acid strength, materials with a smaller ionization potential are more doped by the acid.[130] Thus, considering the relatively large ionization potential of CPDT, it is not surprising that BCF results in a relatively small amount of doping for this molecule. It is quite incredible

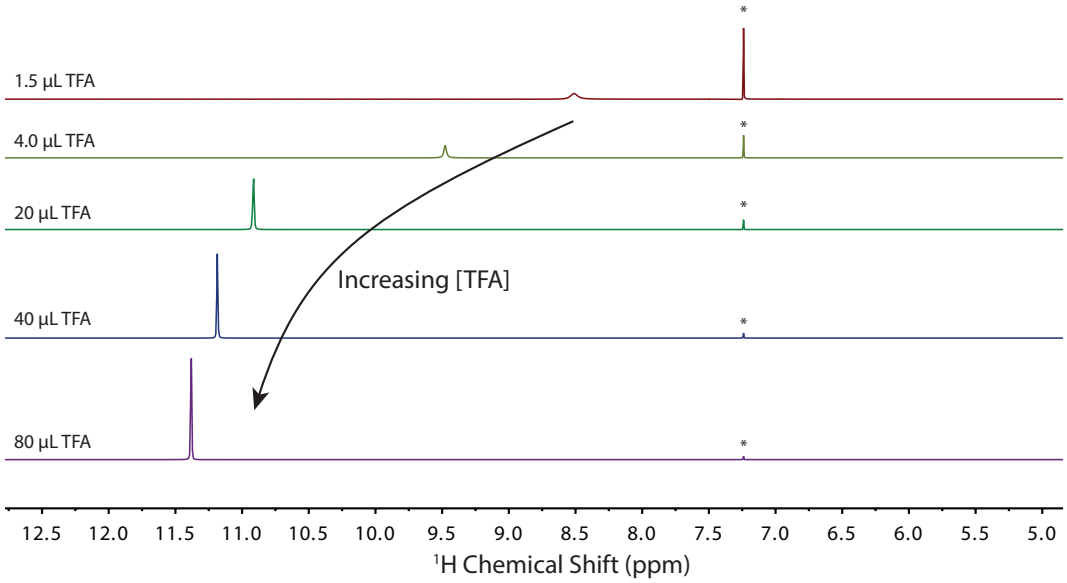

Figure 7.16: ^{1}H NMR of TFA in $CDCl_3$ acquired at 9.4 T (400 MHz) and room temperature. The total volume of each solution was approximately 700 μL. The asterisk indicates the resonance originating from residual $CHCl_3$ ($\delta = 7.24$ ppm).

that BCF can dope a material with such a large IP - yet another reason it is superior to F_4TCNQ.

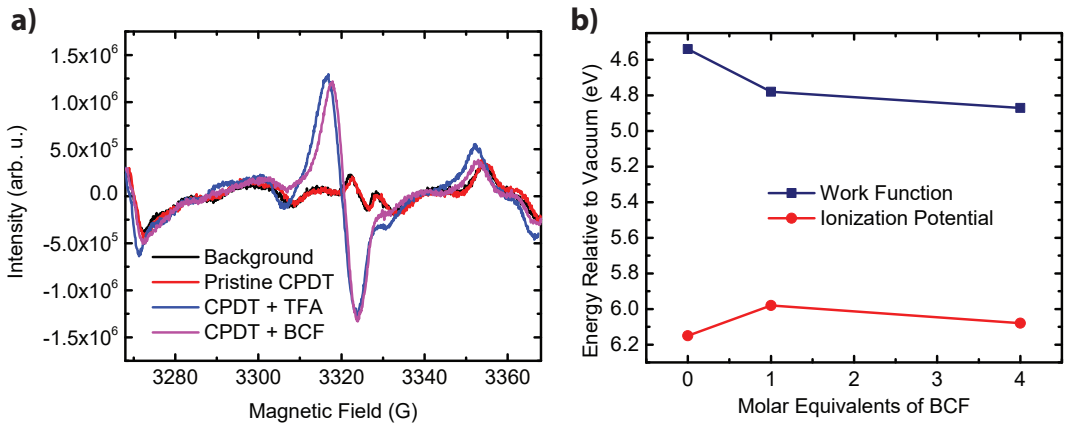

Figure 7.17: a) X-band EPR spectra of solutions in chloroform using a microwave power of 10.02 mW. The concentration of CPDT was always 20 mM. The amount of BCF and TFA added were 3.7 and 100 molar equivalents, respectively. The background scan consisted of an empty quartz capillary with Critoseal on each end. b) Results of UPS for CPDT films, neat and with BCF.

7.7 Evidence from UV-Vis-NIR Absorption

Next in our investigation, we compared the spectroscopic changes of PCPDTBT in chlorobenzene upon addition of various amounts of BCF and TFA, as shown in Figure 7.18. EPR measurements indicate that doping occurs in solution, not just in the solid-state. It is immediately apparent that BCF and TFA induce nearly identical spectroscopic changes in PCPDTBT, although one should note the relatively large amount of TFA (> 50 molar equivalents) required in order to effect these optical changes in comparison to BCF (< 1 molar equivalent), a testament to the strong Brønsted acidity of the BCF:H_2O complex. We attribute the increased absorption in the 1000 - 1600 nm range to polaron absorption, similar to the results observed in the solid-state. A comparison of PCPDTBT absorption in the solid-state and in solution, shown in Figure 7.19, suggests that the slight shoulder at around 850 nm can be attributed to aggregation. In the solid-state this shoulder is much more pronounced, even shifting the peak absorption from 712 nm (chlorobenzene) to 727 nm (thin film). Thus, it seems as though BCF induces some aggregation in PCPDTBT solution, while TFA does not. A slight redshift of the main absorption band of PCPDTBT upon addition of BCF is observed in the solid-state (Figure 7.7d), whereas there is no shift observed upon addition of TFA in solid-state (Figure 7.20a). Doping of PCPDTBT in the solid-state by TFA was also observed by EPR (Figure 7.20b). Impedance spectroscopy of PCPDTBT films with 0.02 molar equivalents of TFA reveal a doping efficiency of 0.1%. The poor doping efficiency of TFA relative to BCF is a manifestation of its Brønsted acidity, which is weaker than the BCF:H_2O complex, as inferred from the NMR and UV-Vis-NIR absorption data. For a given amount of acid, TFA will result in less protonation, which in turn results in fewer electron transfer events. Hence, a lower doping efficiency is observed. The relative acid strength of TFA compared to BCF:H_2O that is inferred herein is in agreement with other

work in the literature, which suggests that the pK_a of TFA is 12.65 in acetonitrile, while the pK_a of BCF:H_2O in acetonitrile is 8.4.[178, 179]

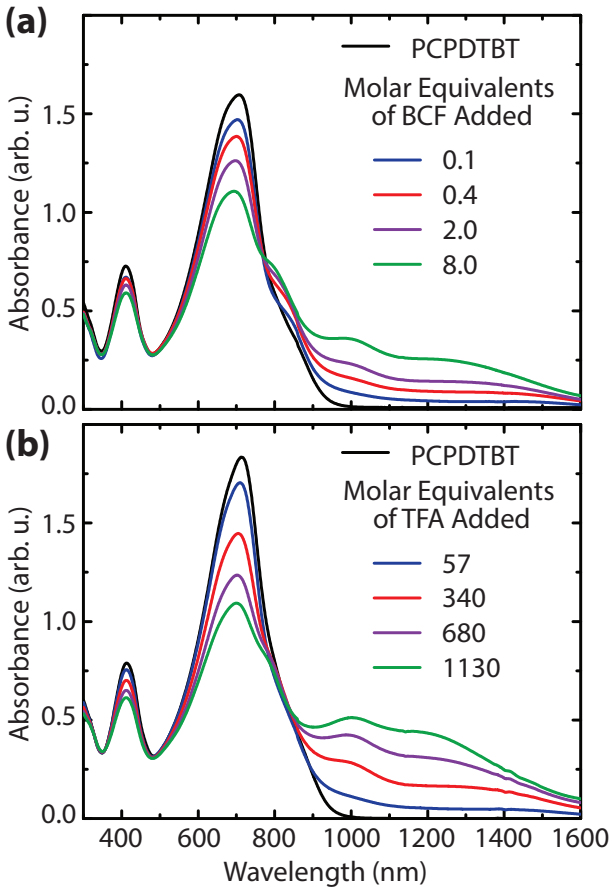

Figure 7.18: Absorption of PCPDTBT in chlorobenzene with various amounts of BCF (a) and TFA (b).

In Figure 7.21a we show that directly adding water to a solution of BCF and PCPDTBT increases the amount of absorption in the NIR region, in support of the proposed doping mechanism. The chlorobenzene solvent was initially dry, suggesting that water had been inadvertently introduced into the sample despite taking all precautions to exclude water (solutions prepared in an inert atmosphere glovebox with the concentration of water less than 1.0 ppm and using oven-dried glassware). When excess water (1,387 equivalents) was added to PCPDTBT in chlorobenzene and shaken vigorously, no spectroscopic

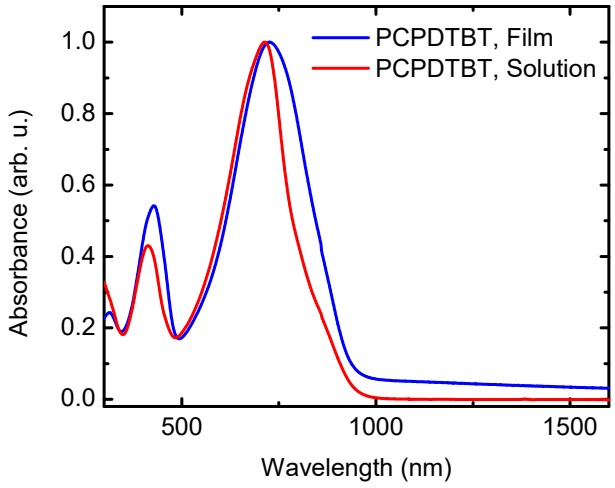

Figure 7.19: Normalized absorption of pristine PCPDTBT in solution (chlorobenzene) and as a thin film (spin-cast from $CHCl_3$).

changes were detected over the course of one day (Figure 7.21b). Clearly, it is the combined effect of BCF and H_2O that initiates doping in PCPDTBT. It is worth noting that the doping efficiencies reported from electrical measurements were calculated assuming that the dopant species is BCF, and not the BCF:H_2O complex. Because Figure 7.21a demonstrates that not all BCF molecules are initially complexed to water, we can conclude that the doping efficiencies of Lewis acids reported in this work are underestimated. In addition, the observed increase of mobility with BCF may be partially attributable to the capture of water molecules by BCF, which could otherwise act as traps in the material. On a side note, a paper was published in Nature Materials just a few weeks after this work was published, which explored how water molecules become traps in organic semiconductors.[180] And, several months before, another article in Nature Materials focusing on the same topic, i.e. water-induced traps.[181]

Completing the experiment that shows adding water increases the amount of doping led naturally to the question: "Will the doping go away entirely if water is completely excluded from the polymer:BCF mixture?" Because there were obvious signs of doping with PCPDTBT and BCF *without* intentionally introducing water and I had been work-

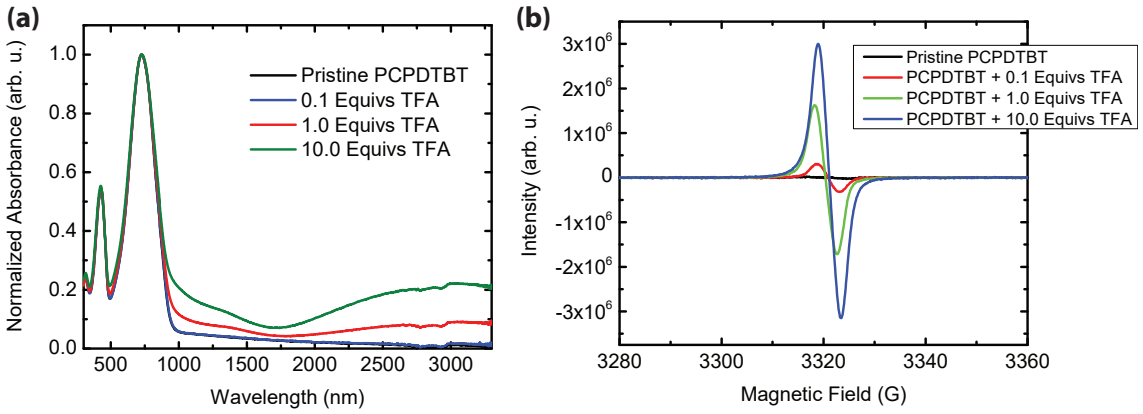

Figure 7.20: a) Solid-state absorption of PCPDTBT thin films with various amounts of TFA (spin-cast from $CHCl_3$). b) Solid-state EPR of PCPDTBT with various amounts of TFA.

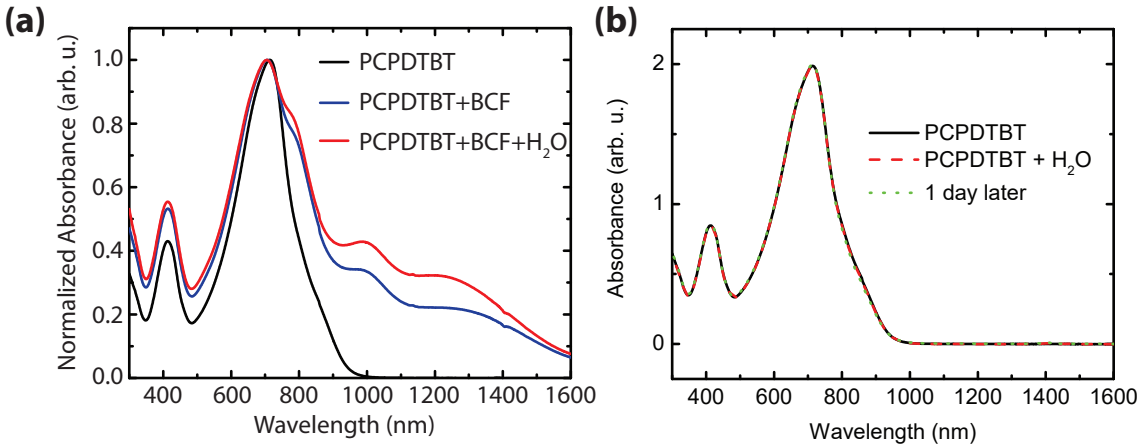

Figure 7.21: a) Normalized absorption of PCPDTBT after sequentially adding 2.0 molar equivalents of BCF, and then 2.0 molar equivalents of H_2O. b) A solution of PCPDTBT (0.06 mg/mL) was made in an inert atmosphere glovebox and transferred to an air-tight cuvette before measuring the absorbance (black line). Then, the cap was removed and 5 μL of DI H_2O (1,387 molar equivalents with respect to the repeat unit of the polymer) was added. The cap was replaced and the cuvette shaken vigorously for about a minute, then absorbance was measured again (red dashed line). The cuvette was shaken again, then set aside for 24 hours. The cuvette was vigorously shaken for about a minute before measuring the absorbance one more time (green dotted line).

ing in a controlled environment that was supposed to be devoid of water in the first place, I assumed that the complete removal of water would be extrememely difficult to achieve, if not impossible. This response was sufficient to deflect certain individuals, but when

my work was under review and 2 of the three referees asked the same question, I had no choice but to attempt to get rid of water entirely or show, at the very least, a reduction in the doping amount. As I had feared, this experiment was doomed to fail. I was, however, able to slightly reduce the amount of water present in the system by subliming BCF and being extra careful with sample preparation, which ended up reducing slightly the amount of doping by BCF for PCPDTBT, as shown in Figure 7.22.

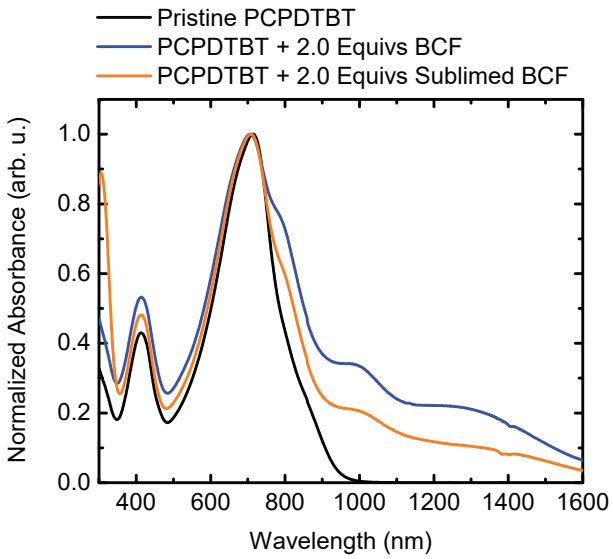

Figure 7.22: Absorption spectrum of PCPDTBT (0.025 mg/mL) in chlorobenzene with 2.0 molar equivalents of BCF after attempting to rigorously exclude the presence of water via sublimation of BCF.

I was unable to completely exclude water, as evidenced by the still-noticeable polaron absorption in Figure 7.22. The blue line in Figure 7.22 is the data taken from Figure 7.21. For the blue line, BCF was used as received from the supplier (TCI). In both cases, anhydrous chlorobenzene was further dried over excess molecular sieve before adding to polymer or BCF solids, oven-dried glassware was used, and the solutions were prepared in an inert atmosphere (N_2) glovebox with the concentration of water less than 1.0 ppm. The procedure for vacuum sublimation of BCF was as follows: approximately 200 mg of BCF was added to an oven-dried 25 mL round bottom flask fitted with a cold finger

in a N_2 glovebox. The apparatus was sealed, taken outside the glovebox, and put on an Argon gas Schlenk line. Room temperature water was circulated through the cold finger, and the round bottom flask was put under vacuum. The apparatus was lowered into an oil bath. The temperature was ramped to 50°C and allowed to sit for 45 minutes at this temperature. The temperature was then ramped to 62°C and allowed to sit at this temperature overnight. At this temperature, water should have evaporated and left the apparatus via the vacuum line. The temperature was slowly ramped to 80°C over the course of several hours, at which temperature sublimation of BCF was noted. Needle-like white crystals formed on the cold finger (compare to the white fluffy powder of BCF as received). Sublimation was complete after 3 hours. The apparatus was raised out of the oil bath, and back-filled with Argon. The apparatus was sealed and returned to the N_2 glovebox. The sublimed BCF was used immediately after its preparation. In addition to the rigorous drying of BCF, PCPDTBT solid was left under vacuum to dry for 24 hours before being brought directly into the glovebox for its use. Despite taking great effort to exclude water completely, our procedure was only marginally effective, as indicated by the polaron absorption still observed, albeit lower than before. Also note how the absorption around 300 nm has been significantly increased in the sample with sublimed BCF. Uncomplexed BCF is known to absorb in the 303-306 nm range and it is also known that upon binding a substrate, e.g. water, this optical transition is suppressed.[182] The re-emergence of the BCF absorption peak after sublimation is also an indicator that our procedure was at least partially effective.

Hoping to establish a more clear presentation of how water affects doping of PCPDTBT with BCF, I added water in a series of aliquots to PCPDTBT with BCF, as shown in Figure 7.23. The experiment was performed as follows: the spectrum of pristine PCPDTBT was acquired, after which 2.0 molar equivalents of sublimed BCF were added, the solution allowed to equilibrate (about an hour), and the spectrum re-acquired. Then, a specific

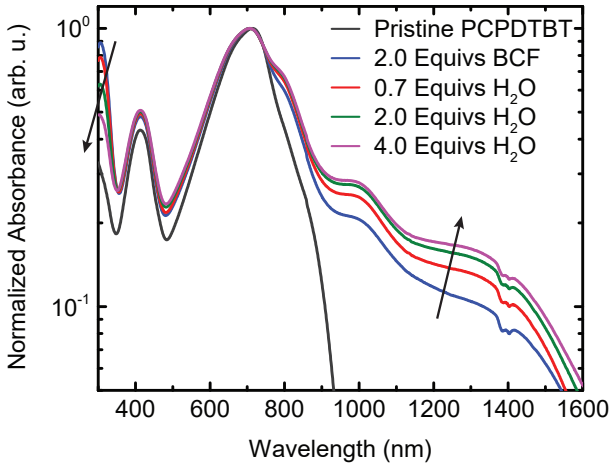

Figure 7.23: Absorption spectra of PCPDTBT (66 μM in chlorobenzene) with 2.0 molar equivalents of sublimed BCF and various amounts of water. The absorbance is presented on a logarithmic scale in order to emphasize the changes that occur upon addition of water.

amount of Milli-Q water was added to the solution and an absorption spectrum acquired after the solution was allowed to equilibrate again. Then, a larger amount of water was added, allowed to equilibrate, and a spectrum acquired. In order to add the water in experimentally reasonable quantities, the water was first diluted in dry chlorobenzene. The solutions were prepared in a nitrogen gas glovebox and never exposed to the atmosphere. The increase in polaron absorption with increasing concentration of water clearly demonstrates the profound role that water plays in the doping mechanism. In addition, the decrease of absorbance around 300 nm with increasing water concentration is consistent with previous work that found that the absorptivity of BCF around 300 nm is significantly reduced upon complexation with water.[182]

At this point, one may wonder: "How much water are we talking about here? What amount of water needs to be present in order to form enough BCF:H_2O complexes that a measurable amount of doping takes place?" The calculations that follow seek to address these questions. Table 7.7 shows some of the relevant parameters needed for these calculations.

Table 7.3: Values used for back-of-the-envelope calculations pertaining to water.

Volume of Single Length Glovebox (ft^3)	30
Concentration of Water in Glovebox (ppm)	0.1
Pressure in Glovebox (atm)	1.0
Temperature (K)	298
Gas Constant (L atm mol^{-1} K^{-1})	0.0826
Molar Mass of Water (g/mol)	18.0152
Density of Liquid Water (g/L)	1000.0

Using the glovebox volume and a concentration of water of 0.1 ppm, we find that the volume of gaseous water inside the glovebox is 8.50×10^{-5} liters. Using the ideal gas law, the molar mass of water, and its liquid density, we find that this volume of gaseous water corresponds to a liquid volume of 6.22×10^{-8} liters, which is equivalently 62.2 nanoliters. While this volume of water may not seem like much, one should consider that this is the water found in the vapor phase - it is likely that water may exist in significant quantities locally on surfaces (e.g. glassware, organic solids) to which it can adsorb. Now, let's consider the amount of water intentionally added in the solution UV-Vis-NIR absorbance experiments. Using the lowest concentration of water added (0.7 molar equivalents, or 44 μM), which also had the most dramatic effect on polaron absorption, we find that this is equivalent to a volume of liquid water that is approximately 2.58 nL. This corresponds to about 4% of the available gas-phase water molecules found in a typical glovebox, as calculated above.

Next, let's consider the amount of water that might have been present in the thin films produced for the electrical measurements. With 0.02 molar equivalents of BCF, PCPDTBT has a free charge carrier density (p) of 2.3×10^{18} cm^{-3}. Assuming that at least one molecule of water is responsible for each free charge carrier produced, we can estimate a lower bound of 2.3×10^{18} molecules of water per cm^3 of film. The volume of our films, spin-cast on substrates of 2.25 cm^2 and approximately 100 nm thick, corresponds to

about 2.25×10^{-5} cm^3. Thus, we can calculate the number of water molecules present in the film, and subsequently the volume of liquid water that it equates to. We find that the lower bound of water that must be present in the film doped with 0.02 molar equivalents of BCF is 1.5×10^{-12} liters, or equivalently 1.5 *picoliters*. These rough calculations demonstrate that just trace amounts of water are capable of resulting in the significant amount of doping that is observed upon addition of BCF. In light of these calculations, it is not surprising that we were unable to completely eliminate the presence of water in any of our experiments.

7.8 Evidence from ENDOR and DFT

To probe the nature of the radical species present in a mixture of PCPDTBT and BCF, we pursued DFT calculations in conjunction with continuous-wave (cw) electron-nuclear double resonance (ENDOR) spectroscopy. ENDOR spectroscopy is typically used to resolve the nuclear hyperfine structure of paramagnetic systems when it is not resolved by EPR due to inhomogeneous broadening.[183, 184, 185] Because hyperfine coupling results from the interaction of unpaired electrons with spin-bearing nuclides, ENDOR spectroscopy can provide a wealth of detail about the nature of radical species. In a cw-ENDOR experiment, the electron spin resonance (microwave frequency) transition is saturated, and then nuclear resonance frequencies (radio frequencies) are scanned while modulations in the EPR intensity are detected. ENDOR spectra are typically shown as the first derivative of absorption, because in practice this is how the data are acquired.

As shown in Figure 7.24, X-band (9 GHz) EPR did not resolve the hyperfine coupling of PCPDTBT with various dopants. Although the PCPDTBT polaron, $[\text{PCPDTBT}]^{\bullet+}$, should have a similar hyperfine coupling regardless of the dopant used, the opposing radicals, $[\text{F}_4\text{TCNQ}]^{\bullet-}$ and $[\text{PCPDTBT-H}]^{\bullet}$ should have drastically different hyperfine

coupling. In an attempt to resolve the hyperfine structure by EPR, I tried performing the experiments at much higher magnetic field strength and electromagnetic radiation frequency (240 GHz). Blake Wilson, a graduate student in the Physics Department, was kind enough to help me with the measurements which were performed on a home-built instrument. As shown in Figure 7.25, I was able to partially resolve the hyperfine coupling in PCPDTBT with BCF and TFA. These data suggest that the same radicals are present in the case of doping by TFA and BCF. Unfortunately, I was not able to obtain high-frequency EPR data with F_4TCNQ. I should note that I observed radicals in pristine F_4TCNQ solutions by X-band EPR. I would have liked to investigate the origin of those radicals in pristine F_4TCNQ, but time did not allow it. Also to my dismay, I was unable to get good agreement between the high-frequency EPR results and simulated spectra based on DFT-calculated hyperfine coupling constants. I pored over textbooks and journal articles trying to learn more about organic radicals and high-frequency EPR. I eventually realized that organic radicals in the solid-state, especially when mobile species, are notoriously difficult to study by EPR - both in terms of experiment and theory. The complexity of the theory behind high-frequency EPR of mobile radicals in the solid-state was a sufficient barrier to my continuing down this path so late in my PhD. However, I think that this could actually be a very fruitful avenue of research, should I stay in the field of organic semiconductors. After all, in this field we are chiefly concerned with the nature of mobile radicals, and no other technique is better suited to study such species. There is certainly a vast wealth of knowledge about organic semiconductors that could be revealed by high-frequency EPR studies, and there are currently very few research groups around the world who are doing this.

Based on the work of Niklas et al., we chose to simulate the structure of PCPDTBT by modeling an oligomer of 4 repeat units in length (‘4mer’), with the long alkyl chains replaced by methyl groups.[157] For the oligomeric structures of PCPDTBT (e.g. ‘4mer

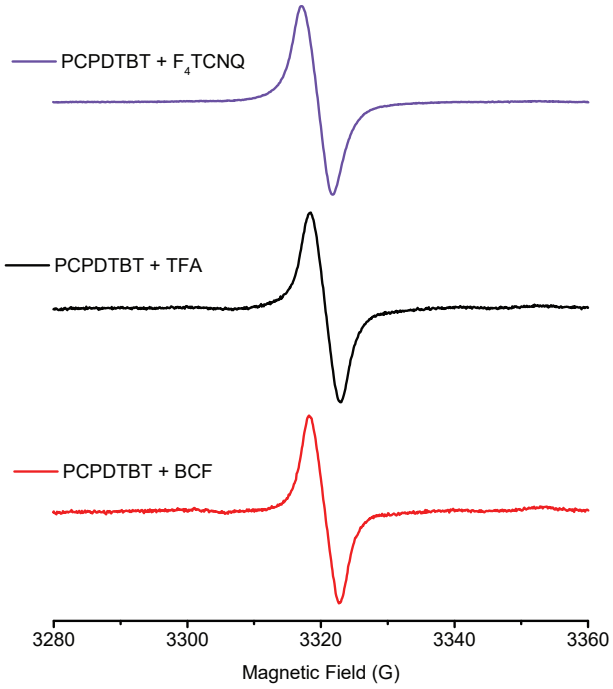

Figure 7.24: X-band EPR spectra of PCPDTBT (0.125 mg/mL in chlorobenzene) with various dopants. The concentrations of the dopants are as follows: 1.0 molar equivalents BCF, 1.0 molar equivalents F_4TCNQ, 1000 molar equivalents of TFA. The lack of hyperfine structure in these spectra make it impossible to identify the radical species present. Thus, X-band EPR is not suitable for differentiating between the various doping mechanisms.

Cation'), the magnetic properties of alkyl protons and the two terminal aromatic protons were not considered. This was done in order to better reflect the physical nature of the polymer. More details on the calculations can be found in Section 7.2. Figure 7.26 shows the calculated spin densities for the species of interest projected onto their optimized geometries. In the event that BCF and PCPDTBT undergo ICT, the resultant radical species are expected to be a $[BCF]^{\bullet-}$ radical anion and a $[PCPDTBT]^{\bullet+}$ radical cation, here simulated as the '4mer cation'. Note how the spin density for the 4mer cation is well delocalized along the backbone, as expected for a highly mobile polaron. The spin density of the BCF anion is also well delocalized throughout its three perfluoroaryl rings. If, however, our proposed doping mechanism is correct, then the resultant radical species

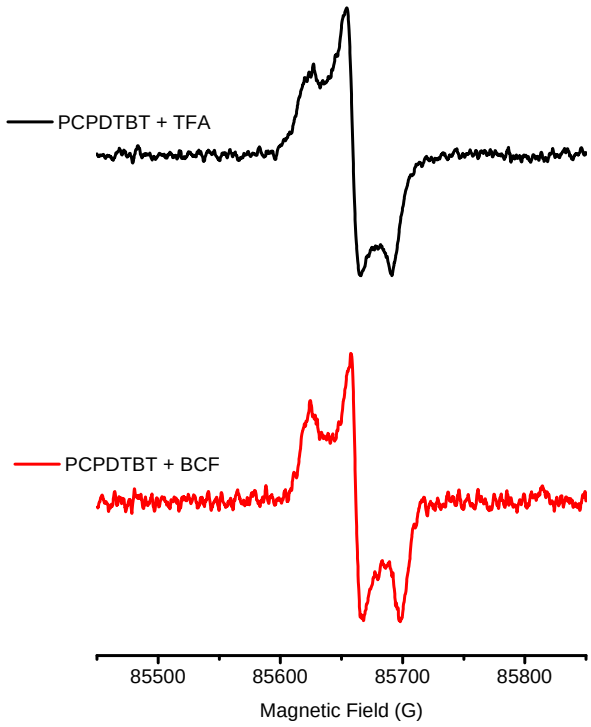

Figure 7.25: High frequency (240 GHz) EPR of solid-state samples. 1.0 molar equivalents of BCF was added, whereas 100 molar equivalents of TFA was used.

are expected to be the $[PCPDTBT]^{\bullet+}$ radical cation and the $[PCPDTBT\text{-}H]^{\bullet}$ protonated radical, here simulated as the '4mer protonated radical'. Note how the spin density of the 4mer protonated radical is not fully delocalized along the backbone. This suggests that the protonated radical is not a highly mobile species; most likely, it is somewhat confined to the region of protonation. Each of these three radical species has a unique ENDOR lineshape (Figure 7.27a) and intensity (Figure 7.27b), which were simulated based on the results of our DFT calculations and the experimental conditions used. In Figure 7.28a the experimental ENDOR signal of PCPDTBT with 1.0 molar equivalents of BCF is plotted against the results of the ENDOR simulations. The simulated results are the 1:1 addition of the ENDOR spectra simulated for the BCF anion and the 4mer cation. In Figure 7.28b the simulated results are the 1:1 addition of the ENDOR spectra

simulated for the 4mer cation and the 4mer protonated radical. These results clearly support my proposed doping mechanism, while also negating the likelihood of ICT.

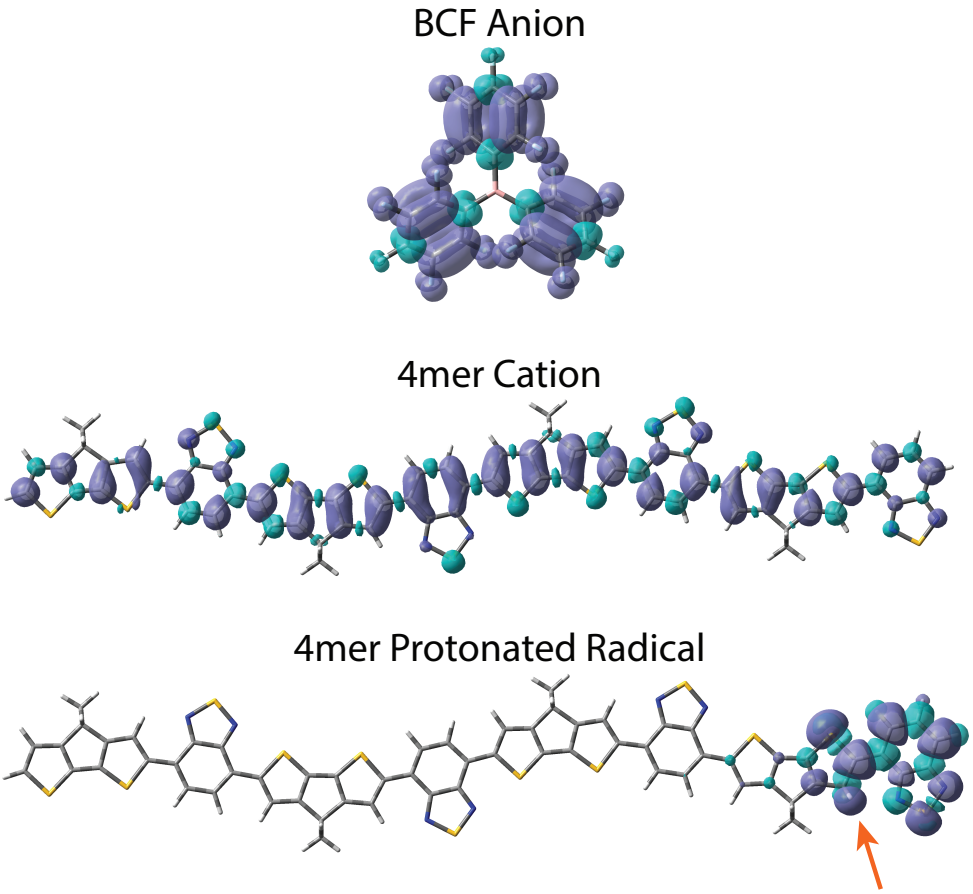

Figure 7.26: Spin density isosurface plots for the radical species of interest (contour level of 0.0004 electrons/bohr^3). The site of protonation is indicated by the orange arrow.

In retrospect, the excellent agreement I achieved between experiment and theory is probably attributable to the experimental conditions used. Or, perhaps, the ENDOR technique is just less sensitive to the conditions of the environment surrounding the radical. Consider that the ENDOR experiments were performed on liquid samples which were flash-frozen. This means that the polymer chains were probably encapsulated by a frozen solvent shell, confining the radicals and limiting electron-electron interactions. I suppose that the electron-electron interactions, which were not considered in my DFT

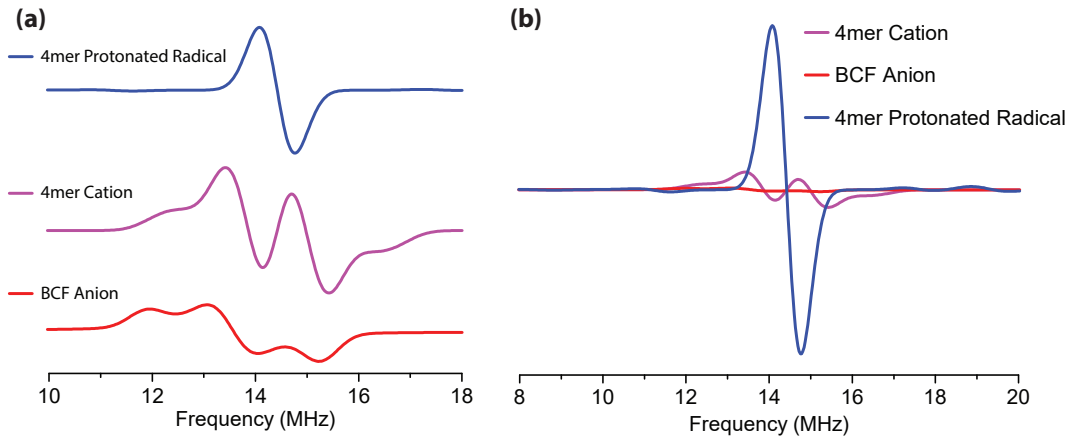

Figure 7.27: a) Simulated ENDOR spectra of the relevant radical species with arbitrary intensity in order to emphasize their different lineshapes. b) The same spectra as in (a), except that here the intensity of their transitions is considered.

calculations, had a significant effect on the high-frequency EPR experiments, which were all performed at room temperature and in the solid-state, i.e. in the absence of solvent.

DFT calculations were used to probe the energetics of protonation and electron transfer, as shown in Figure 7.29. From these calculations, it would seem that there is a significant energy barrier for the first step in the doping process, i.e. protonation. However, the second step in the doping process, electron transfer, is energetically favorable by about 0.2 eV. Therefore, protonation is most likely the rate limiting step in this doping mechanism. As such, it is unlikely that there is a significant amount of protonated, positively charged polymer at any time, as this species is unstable in light of the potential energy curve shown in Figure 7.29. The protonation step probably forms a rapid equilibrium where the non-protonated form of the polymer is favored over the protonated, positively charged form (which is exactly what was observed by NMR with CPDT and TFA). After many protonation attempts, the unstable intermediate is finally formed, followed quickly by electron transfer, since this is energetically favorable.

Intuitively, and from the consideration of the energies calculated above, we can infer that protonation results in the increase of the polymer's ionization potential, as well as an

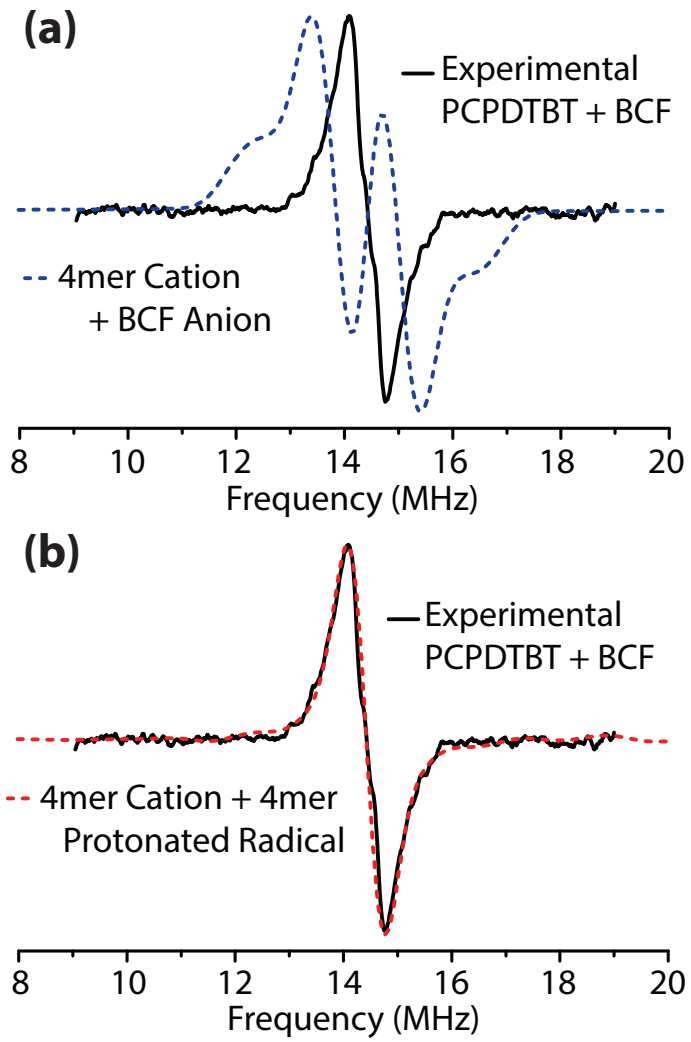

Figure 7.28: Experimental ENDOR spectrum of PCPDTBT with 1.0 molar equivalents of BCF compared to the simulated spectra. In (a) the simulated species are the hypothetical result of ICT. In (b) the simulated species are the hypothetical result of the doping mechanism proposed herein, i.e. protonation followed by electron transfer.

increase in electron affinity. In this sense, the protonated, positively charged species can be thought of as creating an electron trap within the bandgap of the pristine polymer. Given a favorable enough change in the electron affinity upon protonation, an electron will be donated from the HOMO of the pristine polymer into the protonated 'trap' site. The positively charged polaron is stabilized by its ability to delocalize over many repeat units, and is a relatively mobile species, assuming it can overcome the Coulombic

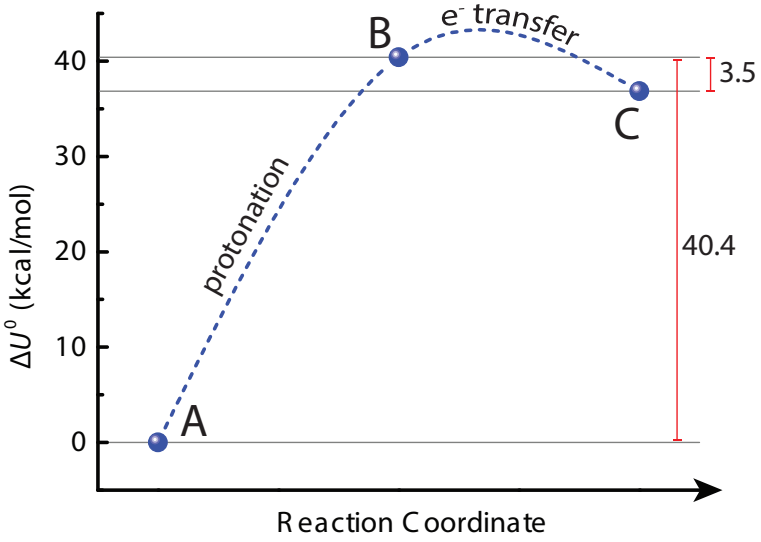

Figure 7.29: The change in internal energy (ΔU^0) for protonation and electron transfer in PCPDTBT were determined by comparing the total energy of relevant (isolated) structures calculated by DFT at the B3LYP/6-31G(d,p) level of theory (solvent model CPCM = chloroform). Site A represents the reactants, i.e. the 4mer and the BCF:H_2O complex. Site B represents the intermediates, i.e. a positively charged, protonated 4mer and a negatively charged $[BCF:OH]^-$ complex. Site C represents the products, i.e. a neutral, 4mer protonated radical and a positively charged 4mer. The reaction pathway is depicted in Figure 7.11. For reference, 40.4 kcal/mol is equivalent to 1.8 eV and 3.5 kcal/mol is equivalent to 0.2 eV.

attraction of the counterion, i.e. $[BCF:OH]^-$. Because the positive and negative charges are at least somewhat spatially separated (the charges are located on different molecules), overcoming this Coulomb attraction is reasonable at ambient thermal energies. However, consider the situation for the protonated radical, which is a neutral species. If the electron leaves the vicinity of the protonation site, it will leave behind a partial positive charge (the proton won't move synchronously with the electron, c.f. the Born-Oppenheimer approximation), while simultaneously creating partial negative charge wherever it goes. This spontaneous separation of charge is energetically unfavorable; hence, the radical electron on the protonated polymer is confined to the relative vicinity of the protonation site. This phenomenon is captured by the DFT calculations of spin density, shown in Figure 7.26. These considerations were also taken into consideration in Figure 7.11.

7.9 Lewis Acid Doping of a Polymer Lacking Lewis Basic Nitrogens

To extend the scope of the proposed doping mechanism, I sought to investigate how effective various Lewis acids are at doping a polymer that lacks Lewis basic nitrogen atoms altogether. This gives us the ability to assess the effectiveness of various Lewis acids without any convolution of adduct formation at Lewis basic sites on the polymer. XPS measurements of the CPDT monomer with BCF showed no changes in sulfur atom binding energies, indicating that these sulfur atoms are not sufficiently Lewis basic to coordinate BCF. For this study, I chose the polymer poly(4,4-dihexadecyl-4*H*-cyclopenta[1,2-*b*:5,4-*b*']dithiophene-2,6-diyl)-*alt*-(2,5-difluoro-1,4-phenylene) (PhF2,5), whose chemical structure is shown in Figure 7.30a.[71] This polymer was synthesized by Dr. Ming Wang for application in OFETs, and was just laying around in lab waiting to be used by the curious graduate student. I am very fortunate to have been in a laboratory where so many different organic semiconductors were available to me. In Figure 7.30b changes in the optical absorption of PhF2,5 in chlorobenzene are shown with 8.0 molar equivalents of various Lewis acids, as well as with 116 molar equivalents of TFA for reference. In Figure 7.30c, the EPR spectra of solutions with 8.0 molar equivalents of the Lewis acids (116 molar equivalents for TFA) are also shown, to demonstrate qualitatively which Lewis acids result in doping. As such, we attribute the increased absorption in the red and NIR region (700 - 1100 nm) to polaron absorption.

From the absorbance spectra, we can place the four Lewis acids into two categories: strongly doping and weakly doping. BCF and BF_3 fall into the strongly doping category, which is consistent with literature noting the Brønsted acidity of the water:Lewis acid complexes, and the stability of the negatively charged [OH:Lewis acid]$^-$ complexes.[186, 187, 188] BBr_3 and $AlCl_3$ fall into the weakly doping category. Because both of these

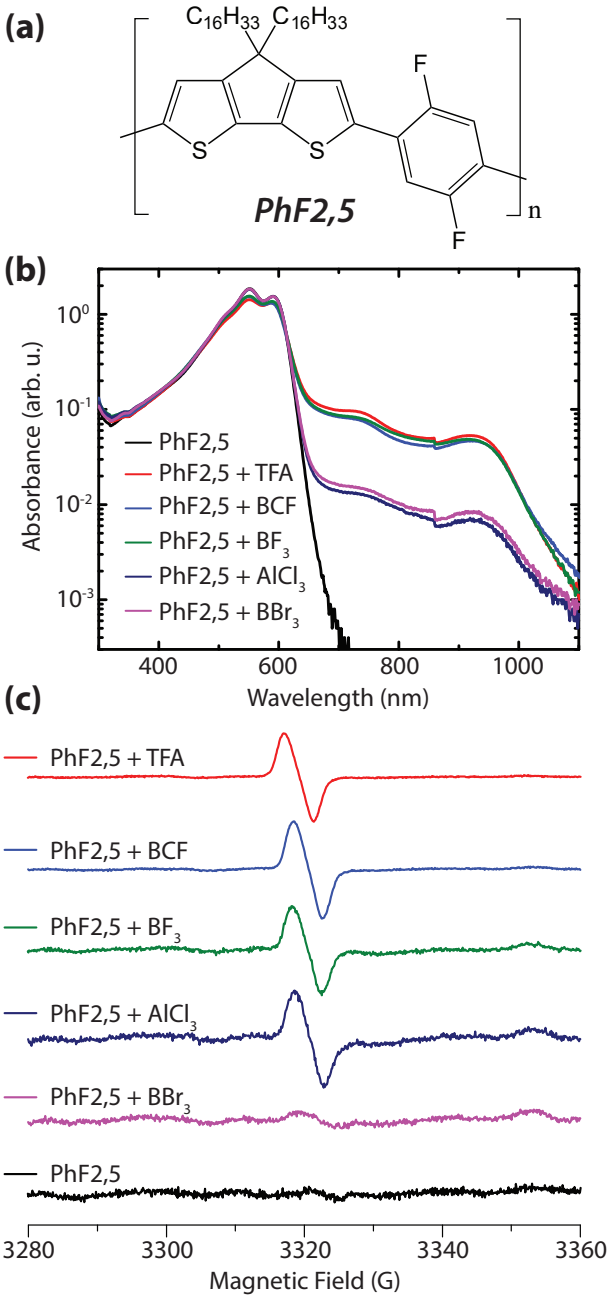

Figure 7.30: a) Molecular structure of PhF2,5. b) Absorption in chlorobenzene of PhF2,5 with 8.0 molar equivalents of various Lewis acids (116 molar equivalents for TFA), displayed on a semi-log plot for clarity. c) X-band EPR spectra of PhF2,5 in chlorobenzene with 8.0 molar equivalents of the various Lewis acids (116 molar equivalents for TFA).

Lewis acids are known to decompose in the presence of water (i.e. Al-Cl and B-Br bond cleavage), they may not be able to form a stable adduct with water and/or the corresponding stable conjugate base.[88, 189, 190, 191] However, it could be significant that the hydrolysis of $AlCl_3$ and BBr_3 produce acidic solutions, as indicated by the following chemical equations:

$$AlCl_3 + 3H_2O \rightarrow Al(OH)_3 + 3HCl \tag{7.5}$$

$$BBr_3 + 3H_2O \rightarrow B(OH)_3 + 3HBr \tag{7.6}$$

In fact, it has been suggested that $AlCl_3$, in the presence of small amounts of water, is acidic enough to be capable of protonating benzene moieties.[192] Thus, even if a Lewis acid does not form a stable complex with water that has high Brønsted acidity, the products of hydrolysis may have sufficient Brønsted acidity to initiate doping of an organic semiconductor, which could be the case encountered here. However, HCl and HBr are known to be weak acids in nonpolar solvents, with pK_a values above 40 in 1,2-dichloroethane, so it is unlikely that the acidic decomposition products are the agent of polymer protonation.[193, 194] Regardless, BCF and BF_3 are clearly superior dopants to $AlCl_3$ and BBr_3. We speculate that the strong proton-fluorine interactions of BCF and BF_3 in their complexes with water may contribute to the stability and acidity of the complexes, besides, of course, their known resistance to B-C and B-F bond cleavage, respectively.[88, 189, 87] Figure 7.31 shows how the proton-fluorine interactions of BCF and BF_3 are strong enough to tilt the complexed water molecule off-axis, resulting in a dipole moment for the complex that is not oriented parallel to the C_2 axis of water molecule, which it is for the case for $AlCl_3$ and BBr_3.

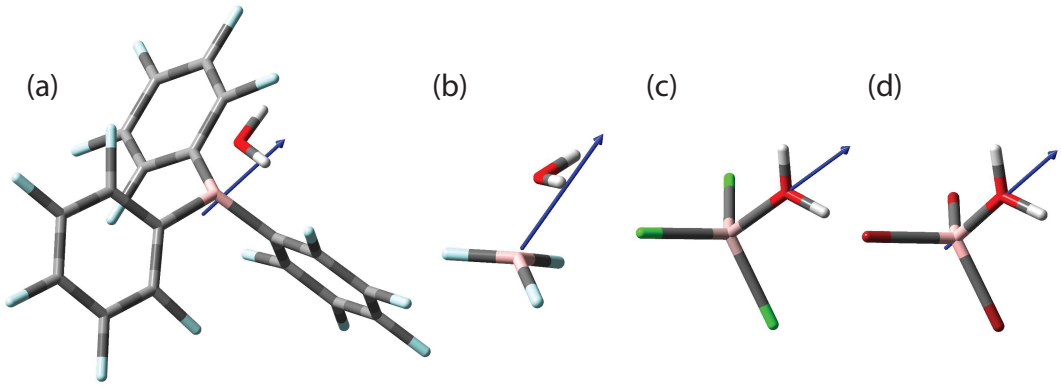

Figure 7.31: Optimized geometries of the Lewis acids BCF (a), BF_3 (b), $AlCl_3$ (c) and BBr_3 (d) when complexed to H_2O. The scale of each image is arbitrary (i.e. the relative size of BF_3 compared to BCF are not accurate). The blue arrows represent the vector of the dipole moment.

It is worth noting that the Lewis acids in the strongly doping category (BCF, BF_3) are weaker Lewis acids than those in the weakly doping category (BBr_3, $AlCl_3$).[151] If the Lewis acids doped by ICT, then one would expect the stronger Lewis acids, which have greater electron affinity, would be the more effective dopants. This is not the trend that we observe. Based on the absorption data, one would expect to observe a radical by EPR in the case of BBr_3, but this was not the case. For the EPR measurements, capillaries were loaded with the solution inside a dry, inert atmosphere glovebox and then capped with Critoseal on both ends. Samples were measured immediately after being brought out of the glovebox. Despite the precautions taken, air, and especially moisture, may have penetrated the Critoseal caps, accelerating the decomposition of BBr_3 (which is known to be extremely sensitive to moisture), thereby eliminating any radical species present. Absorption measurements were carried out using cuvettes with air-free Teflon seals, precluding exposure to further moisture upon measuring.

7.10 Conclusion

In this project we showed how the Lewis acids BCF and BF_3 affect the electrical properties of two CPDT-containing polymers with varying degrees of Lewis basicity. Investigation of the molecular properties with BCF reveal that adduct formation, i.e. binding to a Lewis basic nitrogen of the parent polymer, is detrimental to the doping efficiency. Thus, higher doping efficiencies are observed for the polymer with lesser Lewis basicity, PCPDTBT. In the case of PCPDTBT, we find that BCF outperforms F_4TCNQ in terms of p-type doping. A comprehensive investigation into the doping mechanism of BCF reveals that doping occurs in two steps: first, a BCF:H_2O complex protonates a CPDT moiety of the polymer backbone. Second, electron transfer takes place from a neutral chain segment to a protonated one, resulting in the creation of a mobile polaron, which increases the polymer's conductivity. This mechanism is corroborated by NMR and ENDOR experiments, in conjunction with DFT calculations. Doping by the Brønsted acid TFA is also shown for reference, and we find that the Brønsted acidity of the BCF:H_2O complex is greater than that of TFA.

Finally, we show that four different Lewis acids (BCF, BF_3, $AlCl_3$, and BBr_3) are capable of doping a CPDT-bearing polymer that lacks Lewis basic nitrogen. Absorption and EPR data suggest that $AlCl_3$ and BBr_3 are inferior to BCF and BF_3. Thus, Lewis acid strength does not correlate with the propensity for doping conjugated materials. A survey of the literature indicates that, for the materials which have shown to be doped by BCF, a structurally reoccurring theme is the presence of a thiophene-related moiety in the doped material.[80, 85, 86, 83, 84, 81, 73] In principle, however, any conjugated material with sufficient Brønsted basicity should be able to be doped by Lewis acids. Another limiting factor is expected to be the ionization potential of the conjugated material, for which there has already been shown to be an inverse relationship with the pK_a of acid

needed to initiate a significant amount of doping.[130]

This study provides clarity in the organic semiconductor community concerning the p-type doping mechanism of Lewis acids. The many structure-function relationships elucidated herein serve as a valuable guide to chemists who wish to pursue the design of new conjugated materials that are susceptible to doping by Lewis acids, as well as, on the other hand, the design of new p-type dopants. Moreover, there has been relatively little experimental evidence for the precise mechanism of protonic acid doping since its discovery in the early 1980s. My combined ENDOR measurements and DFT calculations are the first reported evidence of the precise nature of the radical species which are produced after protonation, a significant contribution toward understanding the mechanism of protonic acid doping itself.

Chapter 8

Outlook

8.1 TADF Materials

TADF materials are promising candidates for use in OLEDs owing to their ease of synthesis and lack of expensive heavy metal atoms. Indeed, they have just recently entered the commercial market. Perhaps their greatest weakness is their relatively short device lifetimes. Due to the high-energy excited-state byproducts of triplet-triplet annihilation and exciton-charge annihilation, OLEDs tend to degrade over time, becoming less and less bright as more unwanted byproducts degrade the organic semiconductors and accumulate in the device stack. The Hyperfluorescence strategy was able to increase device lifetimes through efficient FRET from TADF host molecules, reducing the overall exciton lifetime. Still, there is more progress to be made. Key to this progress will be the synthesis of new TADF materials with fast rates of reverse intersystem crossing. For those gains to be meaningful however, it must not come at the expense of simultaneously increasing the rate of forward intersystem crossing. If both rates are increased, then spin-cycling will become very significant, effectively extending exciton lifetime. Spin-cycling will also be reduced by a fast rate of radiative decay from the singlet state. Optimizing

these parameters in a single molecule with an ideal emission wavelength is no easy task and will require great effort to achieve. My preliminary studies show that the magnitudes of both directions of intersystem crossing are correlated with each other, so there may not be much room for optimization. However, my investigation also suggests that the rate of radiative decay is not inversely proportional to ΔE_{ST}. Thus, a way forward in the field is to increase the rate of radiative decay from the singlet without also increasing ΔE_{ST}, so that rates of reverse intersystem crossing are still reasonable. This will reduce the extent of spin cycling and the overall exciton lifetime, thereby increasing the longevity of OLED devices.

The discovery of TADF materials with high photoluminescence quantum yield may present opportunities for applications outside of OLEDs. Indeed, the discovery of TADF materials that undergo many spin cycles before decaying are an interesting new class of materials whose potential has yet to be realized. As I showed in my preliminary study of triplet-triplet annihilation photon upconversion (TTAUC), TADF materials can make for excellent triplet sensitizers (4). I look forward to learning about how their unique photophysical properties are leveraged in new technologies, and, as is already being done with OLEDs, used to improve old technologies.

8.2 Lewis Acids

The utility of adding Lewis acids to organic semiconductors must be understood in the context of their two separate effects: (i) modification of the bandgap and transport levels, and (ii) p-type doping. In the first case, Lewis acids will only be useful for OLED applications if adduct formation doesn't lower the PLQY substantially, which I did not find to be the case for PFPT and BCF. However, other work in the literature has demonstrated that adduct formation with BCF did not lower the PLQY. Thus, there is

still hope. A fruitful avenue of research, therefore, would be to investigate in detail how adduct formation impacts PLQY. This would involve studying not only how a particular Lewis acid affects the PLQY of different organic semiconductors, but also how different Lewis acids affect the PLQY of a common organic semiconductor. For application in solar cells (and perhaps OFETs), adduct formation will only be useful if the overall conductivity does not suffer too greatly. This has yet to be tested. Unfortunately, PFPT wasn't conductive enough to begin with for us to understand how adduct formation impacts conductivity. The obvious starting point for investigating this would be to measure the conductivity of PCPDTPT with 1 or 2 equivalents of Lewis acid. At these high concentations of Lewis acid, any change in electrical properties can be attributed to adduct formation and not p-type doping. I will also note that relatively little research has been done on adduct formation with Lewis basic sites other than the pyridyl nitrogen. For instance, Lewis acids might be able to form adducts with oxygen atoms incorporated into the backbone of an organic semiconductor. Perhaps adduct formation could also be achieved with carbazole or diketopyrrolopyrrole moieties.

Another lingering question is what the effect of adduct formation on the *donor* moiety of a donor-acceptor copolymer would be. This would be challenging, however, since acceptor moieties are, by definition, more Lewis basic than their donor counterparts. Nevertheless, a strongly Lewis basic site on the donor may be compatible with an acceptor moiety that has, overall, greater Lewis basicity than the donor moiety. Because increasing the relative electron donating strength of donor moieties results in narrowing the bandgap of donor-acceptor type molecules, adduct formation on the donor moiety may result in *increasing* the bandgap of the material: the Lewis acid would withdraw electron density from the donor substituent, making it less electron rich, and, hence, a weaker donor.

As for effect (ii), p-type doping, Lewis acids are probably a poor choice of dopant and do not warrant further investigation. This is primarily because of the difficulty in

controlling the precise amount of water that is coordinated with the Lewis acid. For a dopant to be commercially viable, you need to be able to control the precise concentration of the dopant. Furthermore, because the doping mechanism is attributable to the effects of protonation, Brønsted acidity ought to be the key measure of effectiveness, not Lewis acidity. Therefore, developing superior acid dopants ought to focus on more traditional strong acids, such as bis(trifluoromethanesulfonyl)imide, or perhaps even superacids. Another critical factor which will impact the effectiveness of the acid dopant is the stability of the counterion.

In my work I showed the profound role that water can have when mixed with Lewis acids and organic semiconductors. Interestingly, this is not the only role that water can play when in the midst of organic semiconductors. Two recent works in Nature Materials [180, 181] investigate how water-induced traps affect organic semiconductors. Clearly, if the field of organic semiconductors is going to progress, processing methods and synthetic routes need to be developed which exclude water entirely from devices made out of organic semiconductors.

Appendix A

A Personal Perspective on Lewis Acids and Organic Semiconductors

In this Appendix I would like to share my personal perspective on the history of adding Lewis acids to organic semiconductors and how I came to discover the p-type doping mechanism of Lewis acids. This story will also provide more insight into why adding Lewis acids to semiconductors has been split into two separate chapters of my thesis.

In 2009 a member of Guillermo Bazan's research group discovered that adding Lewis acids to a conjugated oligomer resulted in redshifting its absorbance to a degree consistent with the strength of the Lewis acid, a result of adduct formation. The Lewis acid was binding to a Lewis basic azole nitrogen of the organic semiconductor, withdrawing electron density from an already electron deficient moiety, resulting in a strong donor-acceptor interaction, in turn redshifting the absorbance. In 2011 a member of Bazan's lab did a more extensive and more thorough investigation of this phenomenon. In particular, oligomers and polymers where characterized that contained CPDT and either BT or PT. The binding characteristics of BCF with their series of synthesized oligomers and polymers was quite rigorously analyzed. They chose to focus more on the

PT-containing derivatives since it was found that pyridyl nitrogen atoms were more Lewis basic and more sterically accessible, and, therefore, better at binding Lewis acids. These initial studies, which demonstrated that Lewis acids could alter the optical properties of organic semiconductors, didn't generate much hype, but a handful of research groups around the world did begin to utilize this strategy in their own work.

Despite laying down some great intial groundwork, these first few investigations missed one key observation: radicals were being formed when BCF was added to PCPDTBT, and probably when added to other compounds they tested, too. One can even see from their absorption data the pronounced difference when BCF is added to PCPDTBT versus PCPDTPT. That's right, the interaction between BCF and those 2 polymers had been investigated well before I got involved. But it wasn't until 2014, when members of Thuc-Quyen Nguyen's research group measured the electrical properties of an organic semiconductor with the Lewis acid BCF and found that it increased mobility and background charge carrier concentration, that they realized BCF was capable of p-type doping. Since then, a handful of research groups have found that adding small quantities of the Lewis acid BCF improves the electrical properties of certain organic semiconductors. Despite these research groups using BCF as a p-type dopant, which it certainly appeared to be, nobody could prove exactly what made it a p-type dopant, i.e. how it was creating holes in the host organic semiconductor. When BCF was shown to work as good, or even better, than the archetypical p-type dopant F_4TCNQ, a significant amount of interest was generated. Thus, after flying relatively low on the radar since first added to organic semiconductors in 2009, there was now a lot of attention being paid to Lewis acids in the context of organic semiconductors.

When I became aware that nobody had been able to prove exactly how Lewis acid doping worked, and yet many people wanted to know and were actively trying to figure it out, I was instantly captivated. I must admit I was at least partially motivated by

my competitive nature, as I wanted to make the discovery myself. Besides, most of the research projects I had encountered up to this point were rather open-ended, and lacked a definitive end point. I wanted to prove to myself that I could solve a puzzling scientific problem with my own faculties. And so I endeavored to uncover the doping mechanism of Lewis acids.

There were already a few scientists in Quyen's lab who were trying to figure this out themselves, but with little success. Their *modus operandi* consisted of doing the usual measurements on a select few polymers and seeing what happened when BCF was added. These experiments measured the effect of BCF on Lewis basic polymers, but were really not designed to explore the mechanism of action between the Lewis acid and the polymers. Thus, it was not possible to draw significant conclusions from these preliminary experiments. After having some time to think about the specific nature of the problem at hand, I proposed some new experiments that were rationally designed to probe the nature of the polymer:Lewis acid interaction. These were chiefly NMR and EPR experiments. We already had some EPR results, but they were rather limited. All we knew from those measurements is whether or not a certain Lewis acid doped a certain polymer. Binary information which was helpful, but not particularly insightful. Moreover, I proposed that we study how the Lewis acids interact with the individual monomers of the polymers in question.

I began with simple experiments, measuring the UV-Vis absorbance, ^{1}H NMR, and ^{11}B NMR of the monomers with and without BCF. I quickly discovered, via ^{11}B NMR, that BCF would bind to PT-Br_2, but not BT-Br_2. In this case, the bromine atoms are located on the monomers in the position where they are eventually coupled to a donor moiety, e.g. CPDT. Previously, Welch and Bazan had shown that BCF binds to BT-Br, the key difference being that BT-Br lacks a bromine atom on *one* side of the monomer, which is the side where BCF was found to bind. With bromine atoms on both sides of

the BT monomer, no binding occurs, probably due to steric accessibility. I also found out that adding BCF to PT has essentially no effect on the absorption and fluorescence of the monomer (it actually enhances its fluorescence considerably, but there was no change in peak wavelength). Similarly, I found out that BCF had little impact on the absorption and fluorescence spectra of BT, although I did note that the BT:BCF mixture seemed to be sensitive to UV radiation. What really stood out, however, was what happened when I added BCF to the CPDT monomer. I didn't expect anything to happen, given CPDT lacks Lewis basic nitrogens altogether, and I figured the sulfur atoms weren't basic enough to induce any adduct formation. On the first sweep of absorption and fluorescence, the BCF:CPDT mixture appeared about the same as the pristine CPDT absorption and fluorescence. However, I noticed a tiny little hump in the fluorescence spectrum of CPDT:BCF, significantly redshifted from the main fluorescence peak of CPDT, which seemed odd. So I retook the fluorescence spectrum, and that little side peak got bigger! The peak continued to grow with subsequent scans. This experiment significantly reshaped how I thought about the Lewis acid doping problem and drove me to focus nearly all my effort on what was happening between CPDT and BCF.

Later on, I would find that CPDT is actually unstable to UV light, but it didn't matter. I was convinced that there was something going on between CPDT and BCF, and I believed that it was this interaction which might have something to do with the doping mechanism of BCF with polymers. I figured that ^{1}H NMR would reveal to me the nature of this reaction, which it eventually did. Initially, when I added BCF to CPDT, I noticed a slight color change by eye, but no changes were evident in the proton NMR spectrum. After exposing the mixture to UV radiation, I observed a forest of new peaks in the proton NMR spectrum, which was not very insightful, other than the fact that it put the notion in my mind that a significant chemical reaction was taking place. This didn't seem like just the effects of adduct formation. Around this time I was deep in the

organometallic catalysis literature, trying to figure out what types of substrates are known to react with BCF, and in what manner. I was scratching my heads for months - all I knew was that something was happening between BCF and CPDT, but I couldn't get a clean NMR, so I really had no idea what was going on. Eventually, I noticed that BCF had been reported to hydrogenate certain thiophene derivatives in the presence of hydrogen gas. I also noticed that BCF was known to form a Brønsted acid when complexed to water. Finally, I noticed two papers which investigated the effects of adding a strong Brønsted acid, TFA, to the CPDT monomer, as well as some conjugated oligomers that contained the CPDT moiety. They claimed that TFA could protonate CPDT, and observed that upon protonation the spectral properties of oligomers containing the protonated CPDT unit became *massively* redshifted. The redshift was so dramatic I instantly recognized that it could probably be attributed to polaron absorption. However, those scientists did not investigate whether or not any doping was also taking place upon protonation, and if doping might have been responsible for the spectral changes (i.e. polaron absorption).

At this point I knew that CPDT was capable of being protonated, and that BCF was capable of protonating certain molecules. To my dismay, I still couldn't get any definitive NMR evidence of a protonated CPDT species upon adding BCF. I was very frustrated, but hadn't quite lost hope. I was lying in bed at home one evening, with a pretty nasty cold. There was supposed to be a project update the next day and I felt poorly enough that I probably wasn't going to go, even though I had a presentation made. Then, out of nowhere, I realized that a convincing piece of evidence supporting the idea that BCF could be protonating CPDT lied in its interaction with the PCPDTBT polymer. NMR spectra and UV-Vis absorption spectra suggested that BCF was not interacting with the BT moieties, and yet adding BCF to the polymer was having a significant effect on its UV-Vis-NIR absorption. I asked myself, "What would happen if I added the strong Brønsted acid, TFA, to the PCPDTBT polymer?" In a rapture that completely

eradicated the symptoms of my cold, I went to lab (it was around 10pm), found some TFA, and added it to PCPDTBT. The absorption spectrum looked nearly identical to the spectrum of PCPDTBT with BCF! It now seemed highly probable that BCF was protonating the polymer, rather than forming an adduct with it. My enthusiasm for having acquired this little piece of evidence was enough to get me to make the project update meeting, despite my cold symptoms returning.

When I returned to lab a few days later, I knew I had to get NMR evidence that BCF was protonating CPDT. In a desperate attempt, I figured I would just add as much BCF as I possibly could to CPDT (well, just below its solubility limit), and see if something happened in the NMR spectrum. Sure enough, if was that simple. I just needed to add more BCF to see the protonated form of CPDT via ^{1}H NMR. With this knowledge in hand, now I just had to characterize the radical species that were formed when BCF was added to the polymers in question. This turned out to be extremely difficult, since X-band EPR revealed no hyperfine coupling, and NMR resonances were washed out by the radicals. My last resort in identifying the nature of the radical species was high-frequency EPR. That proved to not be very successful, as explained later. Thankfully, Alex Moreland mentioned the ENDOR technique to me around this time. After acquiring the ENDOR spectrum of PCPDTBT:BCF, and hundreds of DFT calculations later, I finally had solid evidence of the precise nature of the radical species. Most importantly, these results negated the likelihood of ICT (the prevailing theory at the time) and confirmed the existence of a protonated, neutral radical species on the polymer backbone, which my theory of protonation and electron transfer predicted should exist.

All that was left to do at this point was 'round-out' the study, i.e. get a complete set of measurements with various Lewis acids and the polymers in question, and analyze the data set in light of my discovery. At this point it was clear that PFPT, which lacked the CPDT unit, only formed adducts with the Lewis acids and wasn't doped by them.

So this polymer was set aside for its own story, the result of which is Chapter 6. The PCPDTBT:BCF interaction was rather easy to describe, since it wasn't convoluted by adduct formation. However, its interaction with PCPDTPT was much more complex since we had evidence it could both dope the polymer, as well as form adducts with its pyridyl nitrogen. Furthermore, it looked as if PCPDTBT could form adducts with smaller, stronger Lewis acids, limiting the scope of my proposed mechanism. Slightly avoiding this problem, I realized we had some polymer available which had no Lewis basic nitrogens on it, but did have the CPDT moiety. I was able to confirm that many Lewis acids were able to dope this polymer, which again strongly suggested that the doping mechanism had nothing to do with adduct formation.

As I was 'rounding-out' the UV-Vis-NIR absorption, which required adding various Lewis acids in a range of concentrations to the polymers in question, I decided that we should also retake the EPR data we already had up to this point, which was only done at one concentration of Lewis acid, and only for BCF and BF_3. I wanted to expand the concentration range, like we were already doing with absorption, and also include more Lewis acids. Upon doing these measurements I realized that at higher concentration of Lewis acids, PCPDTPT was no longer doped. Thus, I finally had a complete picture of how Lewis acids interact with Lewis basic organic semiconductors, which is summarized in Figure 5.4. An overview of how specific Lewis acids interact with specific polymers is given in Figure A.1. Organizing the data in this manner tremendously helped in understanding the big picture of what happens when a Lewis acid is added to a certain organic semiconductor, and why.

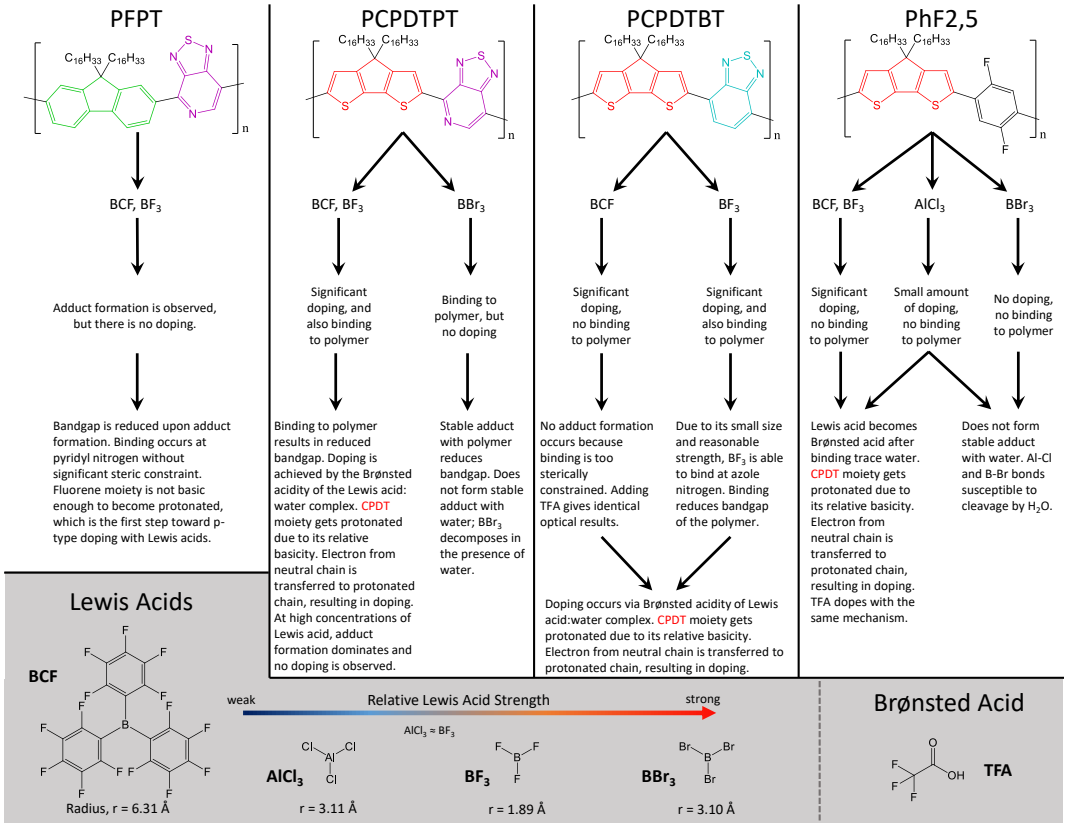

Figure A.1: Summary of results obtained by UV-Vis-NIR absorption and EPR experiments, which helped identify cases of adduct formation and doping, respectively.

Appendix B

Bandgap Engineering with Other Lewis Acids, Polymers

The contents of this appendix are unpublished.

Once the relationship between doping and bandgap reduction (i.e. adduct formation) became clear, it was possible to compare how various Lewis acids affect the bandgap of certain polymers. If an excess of Lewis acid were added to a polymer with pyridyl nitrogens, then the observed changes should be overwhelmingly dominated by adduct formation, and not doping. Thus, we explored how the Lewis acids BCF, BF_3, BBr_3, and $AlCl_3$ affect the absorption of PFPT and PCPDTPT in chlorobenzene solution. PCPDTPT was always at a concentration of 0.025 mg/mL, and PFPT at 0.05 mg/mL. In Figure B.1, the absorption of the polymers with 8.0 molar equivalents of Lewis acid are shown. Also included are the polymers with 5 μL of TFA. In the case of PCPDTPT + TFA, no doping was observed, corroborated by EPR experiments of films and in solution. Interestingly enough, the protons of TFA prefer binding to the pyridyl nitrogen of the PT moiety forming an adduct and redshifting the absorbance, as opposed to protonating

the CPDT moiety and doping the polymer. This is in stark contrast to the effect of TFA on PCPDTBT. At any rate, Lewis acid size and strength seem to scale proportionally with the bandgap reduction in PFPT. However, there is no clear trend with PCPDTPT. Strangely, $AlCl_3$ does not seem to form an adduct with PCPDTPT, although it does with PFPT. In fact, $AlCl_3$ seems to dope PCPDTPT, as evidenced by the slightly increased NIR absorption. I would point out, however, that $AlCl_3$ is a redox-active species. From all of these results a lingering question remains: what is the relationship between steric effects and electronic effects for bandgap reduction? Especially for the case of PCPDTPT, which has a planar backbone conformation, one wonders how adduct formation, which twists the backbone, competes with the energetic benefit of a planar backbone. Work is currently underway in order to disentangle these effects.

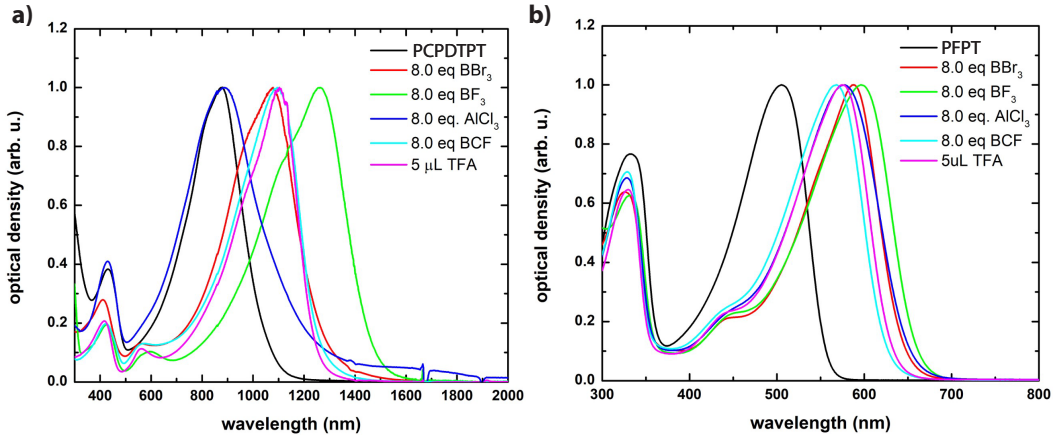

Figure B.1: Absorption spectra of the polymers PCPDTPT (a) and PFPT (b) with various Lewis acids, as well as the Brønsted acid, TFA.

Appendix C

TADF Materials in Different Molecular Environments

The contents of this appendix are unpublished.

Theoretical calculations have suggested that the surrounding medium of a TADF material can have a signficant impact on its ΔE_{ST}. [41] In fact, my Belgian collaborators found that when they included the effects of a polarizing medium when calculating ΔE_{ST} that 4CzIPN sometimes had a negative ΔE_{ST}, implying a triplet energy higher than the singlet energy. [22] Because ΔE_{ST} is inversely proportional to k_{RISC}, this phenomenon could potentially be exploited to further increase rates of k_{RISC}, which would be highly desirable for OLED applications. Given more time and funding, I would have liked to use PL quenching and my analytical model to accurately measure k_{RISC} for some TADF materials in a variety of host matrices. As an exploration into this area of research, I studied the properties of 4CzIPN-tBu and FSA-XT in a couple of different host matrices. Besides as neat films, I measured their properties using the Berberan-Santos method when diluted (2% by weight) in PMMA, poly(methyl methacrylate), and PVDF-HFP,

poly(vinylidene fluoride-co-hexafluoropropylene). The dielectric constant of PMMA and PVDF-HFP are about 3.0 and 10.0, respectively. The results are shown in Figures C.1 and C.2, and ΔE_{ST} values are given in Table C.

For both materials PMMA induces a large blueshift in the PL spectrum, whereas PVDF-HFP induces a slight redshift. This is consistent with the relative polarities of the environments (analogous to solvatochromic shifts in PL), where the highly polarizable PVDF-HFP is able to stabilize the S_1 energy of the TADF material, resulting in a redshift. PMMA being much less polarizable, S_1 energies are destabilized, resulting in the blueshift. The same trend was observed for ΔE_{ST}, where PMMA increased the splitting energy, whereas PVDF-HFP increased the splitting energy. These results are consistent with a picture of an S_1 state that has a larger degree of charge-transfer character than the T_1 state, which was predicted by the quantum chemical calculations performed in Chapter 3. Thus, a highly polar surrounding medium lowers the energy of S_1 more than it does for T_1, resulting in an overall reduction of ΔE_{ST}. Although ΔE_{ST} was reduced by PVDF-HFP, the rate of reverse intersystem crossing at room temperature was actually lowered. However, in solving for k_{RISC}, I had to approximate the k_{ISC}, which I did by just using the value obtained using my analytical model for neat films. Thus, the absolute magnitudes of k_{RISC} are probably inaccurate, and perhaps, too, their relative magnitudes. Indeed, the values of ΔE_{ST} are also likely to be inaccurate, although I suspect the trends I observe using the Berberan-Santos method are real, since they are consistent with the microscopic description give above, which is corroborated by the relative changes in PL maxima, which are definitively accurate.

With the right combination of host matrix and TADF material, perhaps a negative ΔE_{ST} is experimentally achievable. Time-permitting, I would have liked to properly characterize the effects of host matrix on TADF using my analytical model. Perhaps 4CzIPN-Br, with its very low ΔE_{ST}, would have a near-zero or negative ΔE_{ST} in PVDF-

HFP.

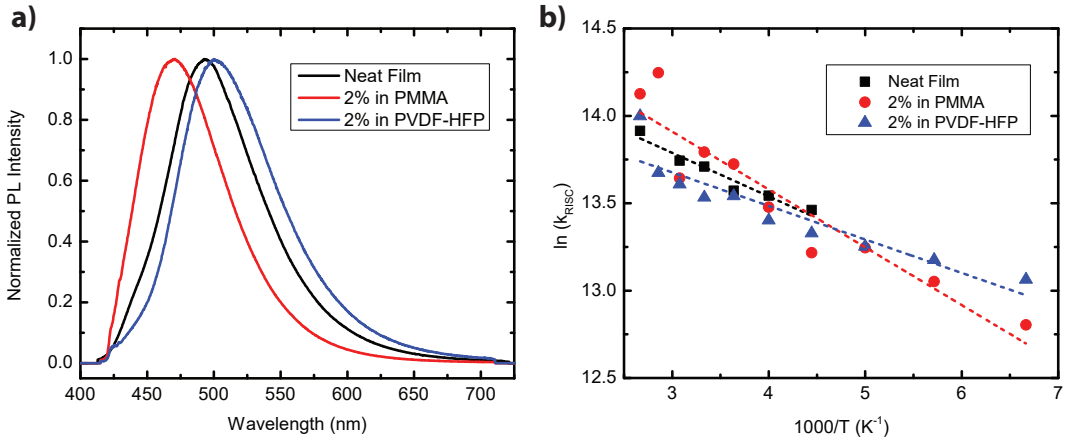

Figure C.1: a) PL spectra of FSA-XT in different molecular environments. b) Arrhenius plot of k_{RISC} for FSA-XT in different molecular environments as determined by the Berberan-Santos method. Dashed lines are linear fits whose slopes are proportional to ΔE_{ST}.

Table C.1: Singlet-triplet splitting energy determined for TADF materials using the Berberan-Santos method in various molecular environments.

Molecular Environment	FSA-XT ΔE_{ST} (meV)	4CzIPN-tBu ΔE_{ST} (meV)
Neat Film	21	55
PMMA	28	63
PVDF-HFP	14	32

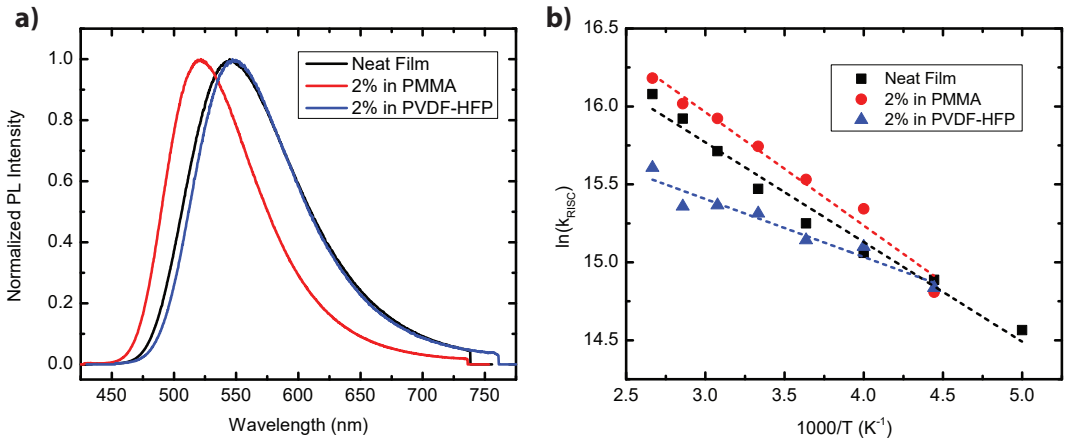

Figure C.2: a) PL spectra of 4CzIPN-tBu in different molecular environments. b) Arrhenius plot of k_{RISC} for 4CzIPN-tBu in different molecular environments as determined by the Berberan-Santos method. Dashed lines are linear fits whose slopes are proportional to ΔE_{ST}.

Appendix D

Lewis Acids and TADF Materials

The contents of this appendix are unpublished.

Having worked extensively with TADF materials and, subsequently, with Lewis acids, a natural question arose: "Can Lewis acids be used to modify the optical properties of TADF materials?" Thus, I investigated the effects of the Lewis acids BCF, BF_3, and BBr_3 on the TADF materials 2CzPN, 4CzIPN, and FSA-XT. In particular, I focused on the effects of adding BCF to 4CzIPN. The possibility of p-type doping by BCF is unlikely due to the relatively deep HOMO and LUMO energies of most TADF materials. In addition, I did not observe any NIR absorption when Lewis acids were added to the TADF materials. Furthermore, I found that not even TrTPFB could dope 4CzIPN.

In chloroform solution I found that adding 10 molar equivalents of BCF to 50 μM 4CzIPN resulted in the appearance of a new, redshifted absorption peak and a slightly redshifted fluorescence spectrum, as shown in Figure D.1a,b. In the solid-state, I found that 0.20 molar equivalents of BCF resulted in redshifting the absorbance, although the increased absorption was featureless, and redshifting the PL spectrum by 57 nm, as shown in Figure D.1c,d. Because of equilibrium binding dynamics in solution, the

effects of adduct formation are more prominent in the solid-state. The PL spectra of FSA-XT and 2CzPN were redshifted by 49 and 54 nm, respectively, in solid-state thin films. Interestingly, no effect was observed upon addition of BF_3 or BBr_3 to 4CzIPN. In the case of 2CzPN and 4CzIPN, I suspect that BCF is able to form an adduct with the nitrile groups of the dicyanobenzene acceptor core, thereby withdrawing electron density, and narrowing the bandgap in the usual way, as described in Chapter 6. If that is the case, however, it remains to be understood why no adduct formation was observed with either BF_3 or BBr_3.

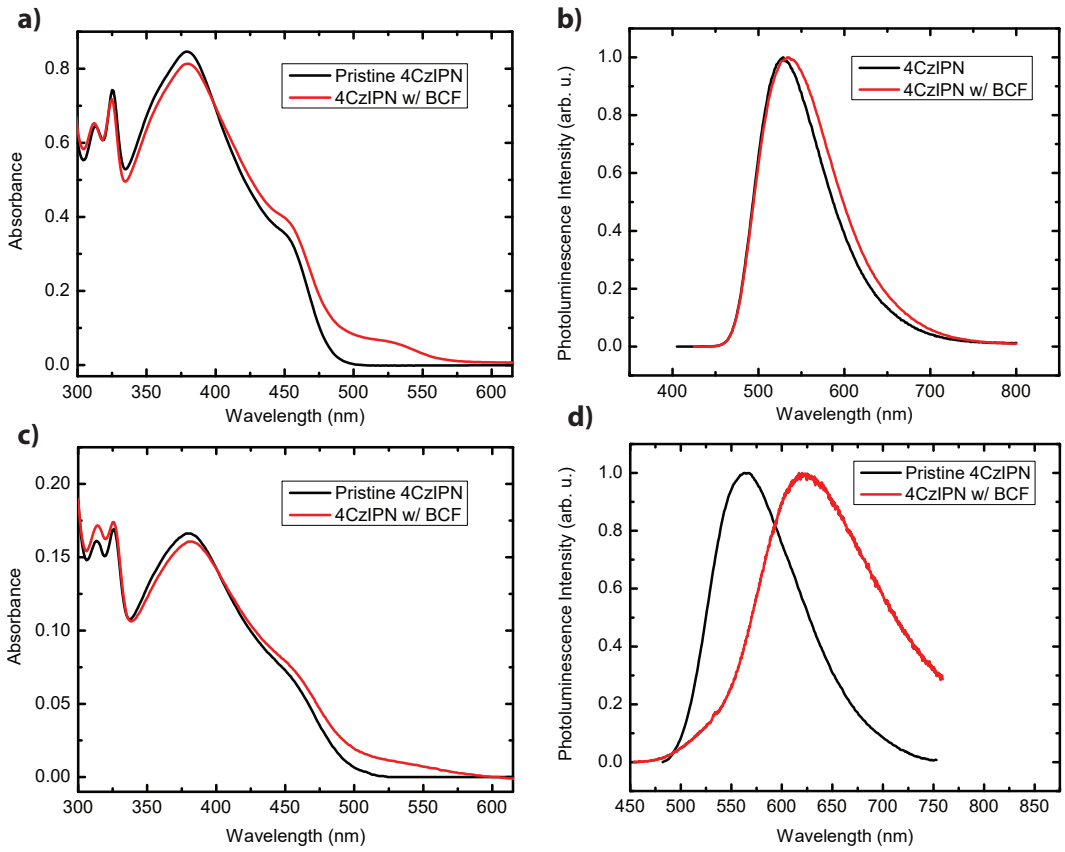

Figure D.1: Absorption of 4CzIPN with BCF in solution (a) and solid-state (b). Photoluminescence of 4CzIPN with BCF in solution (a) and solid-state (b).

The PLQY of 4CzIPN in solution was reduced by 50% upon addition of 10 molar equivalents of BCF. The PLQY of the other TADF materials with Lewis acids was not

investigated, nor was the PLQY of 4CzIPN solid-state films with BCF. However, I did observe a dramatic reduction in the relative amount of delayed fluorescence in 4CzIPN upon adding BCF. Although these observations do not bode well for the practical utility of using Lewis acids to modify the optical properties of TADF materials, the particular TADF materials I investigated are not inherently well-suited to form adducts with Lewis acids. In order to optimize adduct formation, the ideal TADF candidate should have a pyridyl nirogen on an acceptor moiety that is sterically accessible for adduct formation. It remains to be seen if adduct formation necessarily reduces the PLQY and amount of delayed fluorescence in TADF materials.

Bibliography

[1] A. Khler and H. Bssler, *Electronic Processes in Organic Semiconductors: An Introduction*. Wiley-VCH Verlag GmbH & Co. KGaA, Weinheim, Germany, 2015.

[2] B. G. Streetman and S. K. Banerjee, *Solid State Electronic Devices*. Pearson Education, Inc., 7 ed., 2015.

[3] N. Turro, V. Ramamurthy, and J. Scaiano, *Modern Molecular Photochemistry of Organic Molecules*. University Science Books, Sausalito, California, 2010.

[4] J. R. Lakowicz, *Principles of Fluorescence Spectroscopy*. Springer, 3rd ed., 2006.

[5] O. V. Mikhnenko, H. Azimi, M. Scharber, M. Morana, P. W. M. Blom, and M. A. Loi, *Exciton diffusion length in narrow bandgap polymers*, *Energy Environ. Sci.* **5** (Apr., 2012) 6960–6965.

[6] O. V. Mikhnenko, J. Lin, Y. Shu, J. E. Anthony, P. W. M. Blom, T.-Q. Nguyen, and M. A. Loi, *Effect of thermal annealing on exciton diffusion in a diketopyrrolopyrrole derivative*, *Phys. Chem. Chem. Phys.* **14** (Oct., 2012) 14196–14201.

[7] O. V. Mikhnenko, "eDiffusion."

[8] O. V. Mikhnenko, M. Kuik, J. Lin, N. van der Kaap, T.-Q. Nguyen, and P. W. M. Blom, *Trap-Limited Exciton Diffusion in Organic Semiconductors*, *Adv. Mater.* **26** (Mar., 2014) 1912–1917.

[9] B. Yurash, H. Nakanotani, Y. Olivier, D. Beljonne, C. Adachi, and T.-Q. Nguyen, *Photoluminescence Quenching Probes Spin Conversion and Exciton Dynamics in Thermally Activated Delayed Fluorescence Materials*, *Advanced Materials* **31** (2019), no. 21 1804490.

[10] A. Endo, M. Ogasawara, A. Takahashi, D. Yokoyama, Y. Kato, and C. Adachi, *Thermally Activated Delayed Fluorescence from Sn4+Porphyrin Complexes and Their Application to Organic Light Emitting Diodes A Novel Mechanism for Electroluminescence*, *Adv. Mater.* **21** (Dec., 2009) 4802–4806.

[11] Y. Tao, K. Yuan, T. Chen, P. Xu, H. Li, R. Chen, C. Zheng, L. Zhang, and W. Huang, *Thermally Activated Delayed Fluorescence Materials Towards the Breakthrough of Organoelectronics*, *Adv. Mater.* **26** (Dec., 2014) 7931–7958.

[12] Z. Yang, Z. Mao, Z. Xie, Y. Zhang, S. Liu, J. Zhao, J. Xu, Z. Chi, and M. P.Aldred, *Recent advances in organic thermally activated delayed fluorescence materials*, *Chemical Society Reviews* **46** (2017), no. 3 915–1016.

[13] C. Adachi, *Third-generation organic electroluminescence materials* , *Japanese Journal of Applied Physics* **53** (June, 2014) 060101.

[14] H. Uoyama, K. Goushi, K. Shizu, H. Nomura, and C. Adachi, *Highly efficient organic light-emitting diodes from delayed fluorescence*, *Nature* **492** (Dec., 2012) 234–238.

[15] H. Kaji, H. Suzuki, T. Fukushima, K. Shizu, K. Suzuki, S. Kubo, T. Komino, H. Oiwa, F. Suzuki, A. Wakamiya, Y. Murata, and C. Adachi, *Purely organic electroluminescent material realizing 100% conversion from electricity to light*, *Nat Commun* **6** (Oct., 2015).

[16] M. N. Berberan-Santos and J. M. M. Garcia, *Unusually Strong Delayed Fluorescence of C70*, *J. Am. Chem. Soc.* **118** (Jan., 1996) 9391–9394.

[17] E. G. Mik, J. Stap, M. Sinaasappel, J. F. Beek, J. A. Aten, T. G. van Leeuwen, and C. Ince, *Mitochondrial PO2 measured by delayed fluorescence of endogenous protoporphyrin IX*, *Nat Meth* **3** (Nov., 2006) 939–945.

[18] X. Wen, P. Yu, Y.-R. Toh, A.-C. Hsu, Y.-C. Lee, and J. Tang, *Fluorescence Dynamics in BSA-Protected Au25 Nanoclusters*, *J. Phys. Chem. C* **116** (Sept., 2012) 19032–19038.

[19] S. K. Lam and D. Lo, *Time-resolved spectroscopic study of phosphorescence and delayed fluorescence of dyes in silica-gel glasses*, *Chemical Physics Letters* **281** (Dec., 1997) 35–43.

[20] J. Gibson, A. P. Monkman, and T. J. Penfold, *The Importance of Vibronic Coupling for Efficient Reverse Intersystem Crossing in Thermally Activated Delayed Fluorescence Molecules*, *ChemPhysChem* **17** (Oct., 2016) 2956–2961.

[21] Y. Olivier, M. Moral, L. Muccioli, and J.-C. Sancho-Garca, *Dynamic nature of excited states of donoracceptor TADF materials for OLEDs: how theory can reveal structureproperty relationships*, *J. Mater. Chem. C* **5** (June, 2017) 5718–5729.

[22] Y. Olivier, B. Yurash, L. Muccioli, G. DAvino, O. Mikhnenko, J. C. Sancho-Garca, C. Adachi, T.-Q. Nguyen, and D. Beljonne, *Nature of the singlet and triplet excitations mediating thermally activated delayed fluorescence*, *Phys. Rev. Materials* **1** (Dec., 2017) 075602.

[23] C. Baleizo and M. N. Berberan-Santos, *Thermally activated delayed fluorescence as a cycling process between excited singlet and triplet states: Application to the fullerenes*, *The Journal of Chemical Physics* **126** (May, 2007) 204510.

[24] F. B. Dias, T. J. Penfold, and A. P. Monkman, *Photophysics of thermally activated delayed fluorescence molecules*, *Methods Appl. Fluoresc.* **5** (2017), no. 1 012001.

[25] X. Cai, X. Li, G. Xie, Z. He, K. Gao, K. Liu, D. Chen, Y. Cao, and S.-J. Su, *Rate-limited effect of reverse intersystem crossing process: the key for tuning thermally activated delayed fluorescence lifetime and efficiency roll-off of organic light emitting diodes*, *Chemical Science* **7** (2016), no. 7 4264–4275.

[26] M. J. Frisch, G. W. Trucks, H. B. Schlegel, G. E. Scuseria, M. A. Robb, J. R. Cheeseman, G. Scalmani, V. Barone, G. A. Petersson, H. Nakatsuji, X. Li, M. Caricato, A. Marenich, J. Bloino, B. G. Janesko, R. Gomperts, B. Mennucci, H. P. Hratchian, J. V. Ortiz, A. F. Izmaylov, J. L. Sonnenberg, D. Williams-Young, F. Ding, F. Lipparini, F. Egidi, J. Goings, B. Peng, A. Petrone, T. Henderson, D. Ranasinghe, V. G. Zakrzewski, J. Gao, N. Rega, G. Zheng, W. Liang, M. Hada, M. Ehara, K. Toyota, R. Fukuda, J. Hasegawa, M. Ishida, T. Nakajima, Y. Honda, O. Kitao, H. Nakai, T. Vreven, K. Throssell, J. A. Montgomery, Jr., J. E. Peralta, F. Ogliaro, M. Bearpark, J. J. Heyd, E. Brothers, K. N. Kudin, V. N. Staroverov, T. Keith, R. Kobayashi, J. Normand, K. Raghavachari, A. Rendell, J. C. Burant, S. S. Iyengar, J. Tomasi, M. Cossi, J. M. Millam, M. Klene, C. Adamo, R. Cammi, J. W. Ochterski, R. L. Martin, K. Morokuma, O. Farkas, J. B. Foresman, and D. J. Fox, *Gaussian 09*. Gaussian, Inc., Wallingford, CT, 2016.

[27] M. Moral, L. Muccioli, W.-J. Son, Y. Olivier, and J. C. Sancho-Garca, *Theoretical Rationalization of the SingletTriplet Gap in OLEDs Materials: Impact of Charge-Transfer Character*, *J. Chem. Theory Comput.* **11** (Jan., 2015) 168–177.

[28] T. Etienne, X. Assfeld, and A. Monari, *Toward a Quantitative Assessment of Electronic Transitions Charge-Transfer Character*, *J. Chem. Theory Comput.* **10** (Sept., 2014) 3896–3905.

[29] G. t. Velde, F. M. Bickelhaupt, E. J. Baerends, C. F. Guerra, S. J. A. v. Gisbergen, J. G. Snijders, and T. Ziegler, *Chemistry with ADF*, *Journal of Computational Chemistry* **22** (2001), no. 9 931–967.

[30] C. F. Guerra, J. G. Snijders, G. t. Velde, and E. J. Baerends, *Towards an order-N DFT method*, *Theor Chem Acc* **99** (Nov., 1998) 391–403.

[31] *ADF2016, SCM, Theoretical Chemistry*. The Netherlands.

[32] E. van Lenthe, E. J. Baerends, and J. G. Snijders, *Relativistic total energy using regular approximations*, *The Journal of Chemical Physics* **101** (Dec., 1994) 9783–9792.

[33] E. van Lenthe, A. Ehlers, and E.-J. Baerends, *Geometry optimizations in the zero order regular approximation for relativistic effects*, *The Journal of Chemical Physics* **110** (Apr., 1999) 8943–8953.

[34] M. T. Rispens, A. Meetsma, R. Rittberger, C. J. Brabec, N. S. Sariciftci, and J. C. Hummelen, *Influence of the solvent on the crystal structure of PCBM and the efficiency of MDMO-PPV:PCBM plastic solar cells*, *Chem. Commun.* (Aug., 2003) 2116–2118.

[35] Q. Peng, D. Fan, R. Duan, Y. Yi, Y. Niu, D. Wang, and Z. Shuai, *Theoretical Study of Conversion and Decay Processes of Excited Triplet and Singlet States in a Thermally Activated Delayed Fluorescence Molecule*, *J. Phys. Chem. C* **121** (June, 2017) 13448–13456.

[36] J. Lee, N. Aizawa, M. Numata, C. Adachi, and T. Yasuda, *Versatile Molecular Functionalization for Inhibiting Concentration Quenching of Thermally Activated Delayed Fluorescence*, *Adv. Mater.* **29** (Jan., 2017) n/a–n/a.

[37] N. C. Greenham, I. D. W. Samuel, G. R. Hayes, R. T. Phillips, Y. A. R. R. Kessener, S. C. Moratti, A. B. Holmes, and R. H. Friend, *Measurement of absolute photoluminescence quantum efficiencies in conjugated polymers*, *Chemical Physics Letters* **241** (July, 1995) 89–96.

[38] S. M. Menke and R. J. Holmes, *Exciton Transport in an Organic Semiconductor Exhibiting Thermally Activated Delayed Fluorescence*, *J. Phys. Chem. C* (Apr., 2016).

[39] V. H. C. Silva, V. Aquilanti, H. C. B. de Oliveira, and K. C. Mundim, *Uniform description of non-Arrhenius temperature dependence of reaction rates, and a heuristic criterion for quantum tunneling vs classical non-extensive distribution*, *Chemical Physics Letters* **590** (Dec., 2013) 201–207.

[40] R. Gmez-Bombarelli, J. Aguilera-Iparraguirre, T. D. Hirzel, D. Duvenaud, D. Maclaurin, M. A. Blood-Forsythe, H. S. Chae, M. Einzinger, D.-G. Ha, T. Wu, G. Markopoulos, S. Jeon, H. Kang, H. Miyazaki, M. Numata, S. Kim, W. Huang, S. I. Hong, M. Baldo, R. P. Adams, and A. Aspuru-Guzik, *Design of efficient molecular organic light-emitting diodes by a high-throughput virtual screening and experimental approach*, *Nature Materials* **15** (Oct., 2016) 1120–1127.

[41] H. Sun, Z. Hu, C. Zhong, X. Chen, Z. Sun, and J.-L. Brdas, *Impact of Dielectric Constant on the SingletTriplet Gap in Thermally Activated Delayed Fluorescence Materials*, *J. Phys. Chem. Lett.* **8** (June, 2017) 2393–2398.

[42] O. V. Mikhnenko, P. W. M. Blom, and T.-Q. Nguyen, *Exciton diffusion in organic semiconductors*, *Energy Environ. Sci.* **8** (July, 2015) 1867–1888.

[43] S. Arnold, J. L. Fave, and M. Schott, *Experimental study of triplet exciton diffusivity in crystalline pyrene at 300 K*, *Chemical Physics Letters* **28** (Oct., 1974) 412–417.

[44] M. A. Baldo and S. R. Forrest, *Transient analysis of organic electrophosphorescence: I.\quad{}Transient analysis of triplet energy transfer*, *Phys. Rev. B* **62** (Oct., 2000) 10958–10966.

[45] S. D. Oosterhout, V. Savikhin, J. Zhang, Y. Zhang, M. A. Burgers, S. R. Marder, G. C. Bazan, and M. F. Toney, *Mixing Behavior in Small Molecule:Fullerene Organic Photovoltaics*, *Chem. Mater.* **29** (Apr., 2017) 3062–3069.

[46] R. R. Lunt, N. C. Giebink, A. A. Belak, J. B. Benziger, and S. R. Forrest, *Exciton diffusion lengths of organic semiconductor thin films measured by spectrally resolved photoluminescence quenching*, *Journal of Applied Physics* **105** (Mar., 2009) 053711.

[47] O. V. Mikhnenko, F. Cordella, A. B. Sieval, J. C. Hummelen, P. W. M. Blom, and M. A. Loi, *Temperature Dependence of Exciton Diffusion in Conjugated Polymers*, *J. Phys. Chem. B* **112** (Sept., 2008) 11601–11604.

[48] J. D. A. Lin, O. V. Mikhnenko, T. S. van der Poll, G. C. Bazan, and T.-Q. Nguyen, *Temperature Dependence of Exciton Diffusion in a Small-Molecule Organic Semiconductor Processed With and Without Additive*, *Adv. Mater.* **27** (Apr., 2015) 2528–2532.

[49] S. M. Menke and R. J. Holmes, *Exciton diffusion in organic photovoltaic cells*, *Energy Environ. Sci.* **7** (Jan., 2014) 499–512.

[50] J. D. A. Lin, O. V. Mikhnenko, J. Chen, Z. Masri, A. Ruseckas, A. Mikhailovsky, R. P. Raab, J. Liu, P. W. M. Blom, M. A. Loi, C. J. Garca-Cervera, I. D. W. Samuel, and T.-Q. Nguyen, *Systematic study of exciton diffusion length in organic semiconductors by six experimental methods*, *Mater. Horiz.* **1** (Feb., 2014) 280–285.

[51] T. C. Wu, D. N. Congreve, and M. A. Baldo, *Solid state photon upconversion utilizing thermally activated delayed fluorescence molecules as triplet sensitizer*, *Appl. Phys. Lett.* **107** (July, 2015) 031103.

[52] N. Yanai, M. Kozue, S. Amemori, R. Kabe, C. Adachi, and N. Kimizuka, *Increased vis-to-UV upconversion performance by energy level matching between a TADF donor and high triplet energy acceptors*, *J. Mater. Chem. C* **4** (July, 2016) 6447–6451.

[53] H. Nakanotani, T. Higuchi, T. Furukawa, K. Masui, K. Morimoto, M. Numata, H. Tanaka, Y. Sagara, T. Yasuda, and C. Adachi, *High-efficiency organic light-emitting diodes with fluorescent emitters*, *Nature Communications* **5** (May, 2014) 4016.

[54] D. Zhang, L. Duan, C. Li, Y. Li, H. Li, D. Zhang, and Y. Qiu, *High-Efficiency Fluorescent Organic Light-Emitting Devices Using Sensitizing Hosts with a Small SingletTriplet Exchange Energy*, *Adv. Mater.* **26** (Aug., 2014) 5050–5055.

[55] T. N. Singh-Rachford and F. N. Castellano, *Photon upconversion based on sensitized triplettriplet annihilation*, *Coordination Chemistry Reviews* **254** (Nov., 2010) 2560–2573.

[56] S. B.Darling and F. You, *The case for organic photovoltaics*, *RSC Advances* **3** (2013), no. 39 17633–17648.

[57] J. A. Briggs, A. C. Atre, and J. A. Dionne, *Narrow-bandwidth solar upconversion: Case studies of existing systems and generalized fundamental limits*, *Journal of Applied Physics* **113** (Mar., 2013) 124509.

[58] Y. YapCheng, T. Khoury, R. G. C. R.Clady, M. J. Y.Tayebjee, N. J.Ekins-Daukes, M. J.Crossley, and T. W.Schmidt, *On the efficiency limit of triplettriplet annihilation for photochemical upconversion*, *Physical Chemistry Chemical Physics* **12** (2010), no. 1 66–71.

[59] C. Fan, L. Wei, T. Niu, M. Rao, G. Cheng, J. J. Chruma, W. Wu, and C. Yang, *Efficient TripletTriplet Annihilation Upconversion with an Anti-Stokes Shift of 1.08 eV Achieved by Chemically Tuning Sensitizers*, *J. Am. Chem. Soc.* **141** (Sept., 2019) 15070–15077.

[60] N. Yanai and N. Kimizuka, *New Triplet Sensitization Routes for Photon Upconversion: Thermally Activated Delayed Fluorescence Molecules, Inorganic Nanocrystals, and Singlet-to-Triplet Absorption*, *Acc. Chem. Res.* **50** (Oct., 2017) 2487–2495.

[61] I. B. Berlman, *Handbook of Fluorescence Spectra of Aromatic Molecules*. Academic Press, New York, 2 ed., 1971.

[62] T. Ogawa, M. Hosoyamada, B. Yurash, T.-Q. Nguyen, N. Yanai, and N. Kimizuka, *DonorAcceptorCollector Ternary Crystalline Films for Efficient Solid-State Photon Upconversion*, *J. Am. Chem. Soc.* **140** (July, 2018) 8788–8796.

[63] B. Yurash, D. Leifert, G. N. M. Reddy, D. X. Cao, S. Biberger, V. V. Brus, M. Seifrid, P. J. Santiago, A. Khler, B. F. Chmelka, G. C. Bazan, and T.-Q. Nguyen, *Atomic-Level Insight into the Postsynthesis Band Gap Engineering of a*

Lewis Base Polymer Using Lewis Acid Tris(pentafluorophenyl)borane, *Chem. Mater.* **31** (Sept., 2019) 6715–6725.

[64] S. R. Forrest and M. E. Thompson, *Introduction: Organic Electronics and Optoelectronics*, *Chem. Rev.* **107** (Apr., 2007) 923–925.

[65] H. Meier, *Conjugated Oligomers with Terminal DonorAcceptor Substitution*, *Angewandte Chemie International Edition* **44** (Apr., 2005) 2482–2506.

[66] F. S. Kim, X. Guo, M. D. Watson, and S. A. Jenekhe, *High-mobility Ambipolar Transistors and High-gain Inverters from a DonorAcceptor Copolymer Semiconductor*, *Advanced Materials* **22** (Jan., 2010) 478–482.

[67] G. Dennler, M. C. Scharber, and C. J. Brabec, *Polymer-Fullerene Bulk-Heterojunction Solar Cells*, *Advanced Materials* **21** (Apr., 2009) 1323–1338.

[68] A. P. Kulkarni, X. Kong, and S. A. Jenekhe, *High-Performance Organic Light-Emitting Diodes Based on Intramolecular Charge-Transfer Emission from DonorAcceptor Molecules: Significance of Electron- Donor Strength and Molecular Geometry*, *Advanced Functional Materials* **16** (May, 2006) 1057–1066.

[69] Y. Sun, G. C. Welch, W. L. Leong, C. J. Takacs, G. C. Bazan, and A. J. Heeger, *Solution-processed small-molecule solar cells with 6.7% efficiency*, *Nature Materials* **11** (Jan., 2012) 44–48.

[70] C. P. Yau, Z. Fei, R. S. Ashraf, M. Shahid, S. E. Watkins, P. Pattanasattayavong, T. D. Anthopoulos, V. G. Gregoriou, C. L. Chochos, and M. Heeney, *Influence of the Electron Deficient Co-Monomer on the Optoelectronic Properties and Photovoltaic Performance of Dithienogermole-based Co-Polymers*, *Advanced Functional Materials* **24** (Feb., 2014) 678–687.

[71] M. Wang, M. J. Ford, A. T. Lill, H. Phan, T.-Q. Nguyen, and G. C. Bazan, *Hole Mobility and Electron Injection Properties of D-A Conjugated Copolymers with Fluorinated Phenylene Acceptor Units*, *Advanced Materials* **29** (Feb., 2017) 1603830.

[72] G. C. Welch, R. Coffin, J. Peet, and G. C. Bazan, *Band Gap Control in Conjugated Oligomers via Lewis Acids*, *J. Am. Chem. Soc.* **131** (Aug., 2009) 10802–10803.

[73] E. Poverenov, N. Zamoshchik, A. Patra, Y. Ridelman, and M. Bendikov, *Unusual Doping of DonorAcceptor-Type Conjugated Polymers Using Lewis Acids*, *J. Am. Chem. Soc.* **136** (Apr., 2014) 5138–5149.

[74] G. C. Welch and G. C. Bazan, *Lewis Acid Adducts of Narrow Band Gap Conjugated Polymers*, *J. Am. Chem. Soc.* **133** (Mar., 2011) 4632–4644.

[75] M. M. Hansmann, A. LpezAndarias, E. Rettenmeier, C. EglerLucas, F. Rominger, A. S. K. Hashmi, and C. RomeroNieto, *B(C6f5)3: A Lewis Acid that Brings the Light to the Solid State*, *Angewandte Chemie International Edition* **55** (Jan., 2016) 1196–1199.

[76] K. Yamaguchi, T. Murai, J.-D. Guo, T. Sasamori, and N. Tokitoh, *Acid-Responsive Absorption and Emission of 5-N-Arylaminothiazoles: Emission of White Light from a Single Fluorescent Dye and a Lewis Acid*, *ChemistryOpen* **5** (Oct., 2016) 434–438.

[77] N. M. Randell, K. M. Fransishyn, and T. L. Kelly, *Lewis AcidBase Chemistry of 7-Azaisoindigo-Based Organic Semiconductors*, *ACS Appl. Mater. Interfaces* **9** (July, 2017) 24788–24796.

[78] P. Zalar, Z. B. Henson, G. C. Welch, G. C. Bazan, and T.-Q. Nguyen, *Color Tuning in Polymer Light-Emitting Diodes with Lewis Acids*, *Angew. Chem.* **124** (July, 2012) 7613–7616.

[79] J. Lin, B. Liu, M. Yu, L. Xie, W. Zhu, H. Ling, X. Zhang, X. Ding, X. Wang, P. N. Stavrinou, J. Wang, D. D. C. Bradley, and W. Huang, *Heteroatomic Conjugated Polymers and the Spectral Tuning of Electroluminescence via a Supramolecular Coordination Strategy*, *Macromolecular Rapid Communications* **37** (Nov., 2016) 1807–1813.

[80] P. Zalar, M. Kuik, Z. B. Henson, C. Woellner, Y. Zhang, A. Sharenko, G. C. Bazan, and T.-Q. Nguyen, *Increased Mobility Induced by Addition of a Lewis Acid to a Lewis Basic Conjugated Polymer*, *Adv. Mater.* **26** (Feb., 2014) 724–727.

[81] P. Pingel, M. Arvind, L. Klln, R. Steyrleuthner, F. Kraffert, J. Behrends, S. Janietz, and D. Neher, *pType Doping of Poly(3hexylthiophene) with the Strong Lewis Acid Tris(pentafluorophenyl)borane*, *Advanced Electronic Materials* **2** (Oct., 2016).

[82] T. Ye, J. Wang, W. Chen, Y. Yang, and D. He, *Improved Performance and Reproducibility of Perovskite Solar Cells by Well-Soluble Tris(pentafluorophenyl)borane as a p-Type Dopant*, *ACS Appl. Mater. Interfaces* **9** (May, 2017) 17923–17931.

[83] H. Yan, J. Chen, K. Zhou, Y. Tang, X. Meng, X. Xu, and W. Ma, *Lewis Acid Doping Induced Synergistic Effects on Electronic and Morphological Structure for Donor and Acceptor in Polymer Solar Cells*, *Advanced Energy Materials* **8** (July, 2018) 1703672.

[84] Y. Han, G. Barnes, Y.-H. Lin, J. Martin, M. Al-Hashimi, S. Y. AlQaradawi, T. D. Anthopoulos, and M. Heeney, *Doping of Large Ionization Potential*

Indenopyrazine Polymers via Lewis Acid Complexation with Tris(pentafluorophenyl)borane: A Simple Method for Improving the Performance of Organic Thin-Film Transistors, *Chem. Mater.* **28** (Nov., 2016) 8016–8024.

[85] Panidi Julianna, Paterson Alexandra F., Khim Dongyoon, Fei Zhuping, Han Yang, Tsetseris Leonidas, Vourlias George, Patsalas Panos A., Heeney Martin, and Anthopoulos Thomas D., *Remarkable Enhancement of the Hole Mobility in Several Organic SmallMolecules, Polymers, and SmallMolecule:Polymer Blend Transistors by Simple Admixing of the Lewis Acid pDopant B(C6f5)3*, *Advanced Science* **5** (Oct., 2017) 1700290.

[86] J. Lee, J. Kim, T. L. Nguyen, M. Kim, J. Park, Y. Lee, S. Hwang, Y.-W. Kwon, J. Kwak, and H. Y. Woo, *A Planar CyclopentadithiopheneBenzothiadiazole-Based Copolymer with sp2-Hybridized Bis(alkylsulfanyl)methylene Substituents for Organic Thermoelectric Devices*, *Macromolecules* **51** (May, 2018) 3360–3368.

[87] G. Erker, *Tris(pentafluorophenyl)borane: a special boron Lewis acid for special reactions*, *Dalton Transactions* **0** (2005), no. 11 1883–1890.

[88] W. E.Piers and T. Chivers, *Pentafluorophenylboranes: from obscurity to applications*, *Chemical Society Reviews* **26** (1997), no. 5 345–354.

[89] W. E. Piers, *The Chemistry of Perfluoraryl Boranes*, *Adv. Organomet. Chem.* **52** (2005) 1–76.

[90] J. M. Blackwell, W. E. Piers, M. Parvez, and R. McDonald, *Solution and Solid-State Characteristics of Imine Adducts with Tris(pentafluorophenyl)borane*, *Organometallics* **21** (Apr., 2002) 1400–1407.

[91] F. Focante, P. Mercandelli, A. Sironi, and L. Resconi, *Complexes of tris(pentafluorophenyl)boron with nitrogen-containing compounds: Synthesis, reactivity and metallocene activation*, *Coordination Chemistry Reviews* **250** (Jan., 2006) 170–188.

[92] S. Guidotti, I. Camurati, F. Focante, L. Angellini, G. Moscardi, L. Resconi, R. Leardini, D. Nanni, P. Mercandelli, A. Sironi, T. Beringhelli, and D. Maggioni, *Synthesis and Reactivity of (C6f5)3bN-Heterocycle Complexes. 1. Generation of Highly Acidic sp3 Carbons in Pyrroles and Indoles*, *J. Org. Chem.* **68** (July, 2003) 5445–5465.

[93] M. R. Hansen, R. Graf, and H. W. Spiess, *Interplay of Structure and Dynamics in Functional Macromolecular and Supramolecular Systems As Revealed by Magnetic Resonance Spectroscopy*, *Chem. Rev.* **116** (Feb., 2016) 1272–1308.

[94] D. Dudenko, A. Kiersnowski, J. Shu, W. Pisula, D. Sebastiani, H. W. Spiess, and M. R. Hansen, *A Strategy for Revealing the Packing in Semicrystalline -Conjugated Polymers: Crystal Structure of Bulk Poly-3-hexyl-thiophene (P3ht)*, *Angewandte Chemie International Edition* **51** (2012), no. 44 11068–11072.

[95] V. Percec, M. Peterca, T. Tadjiev, X. Zeng, G. Ungar, P. Leowanawat, E. Aqad, M. R. Imam, B. M. Rosen, U. Akbey, R. Graf, S. Sekharan, D. Sebastiani, H. W. Spiess, P. A. Heiney, and S. D. Hudson, *Self-Assembly of Dendronized Perylene Bisimides into Complex Helical Columns*, *J. Am. Chem. Soc.* **133** (Aug., 2011) 12197–12219.

[96] M. T. Seifrid, G. N. M. Reddy, C. Zhou, B. F. Chmelka, and G. C. Bazan, *Direct Observation of the Relationship between Molecular Topology and Bulk Morphology for a -Conjugated Material*, *J. Am. Chem. Soc.* **141** (Apr., 2019) 5078–5082.

[97] G. N. M. Reddy, A. Marsh, J. T. Davis, S. Masiero, and S. P. Brown, *Interplay of Noncovalent Interactions in Ribbon-like Guanosine Self-Assembly: An NMR Crystallography Study*, *Crystal Growth & Design* **15** (Dec., 2015) 5945–5954.

[98] S. R. Chaudhari, J. M. Griffin, K. Broch, A. Lesage, V. Lemaur, D. Dudenko, Y. Olivier, H. Sirringhaus, L. Emsley, and C. P. Grey, *Donoracceptor stacking arrangements in bulk and thin-film high-mobility conjugated polymers characterized using molecular modelling and MAS and surface-enhanced solid-state NMR spectroscopy*, *Chem. Sci.* **8** (Mar., 2017) 3126–3136.

[99] N. C. Miller, E. Cho, M. J. N. Junk, R. Gysel, C. Risko, D. Kim, S. Sweetnam, C. E. Miller, L. J. Richter, R. J. Kline, M. Heeney, I. McCulloch, A. Amassian, D. AcevedoFeliz, C. Knox, M. R. Hansen, D. Dudenko, B. F. Chmelka, M. F. Toney, J.-L. Brdas, and M. D. McGehee, *Use of X-Ray Diffraction, Molecular Simulations, and Spectroscopy to Determine the Molecular Packing in a Polymer-Fullerene Bimolecular Crystal*, *Advanced Materials* **24** (2012), no. 45 6071–6079.

[100] M. D. McGehee, K. R. Graham, C. Cabanetos, J. P. Jahnke, A. E. Labban, G. O. N. Ndjawa, M. Idso, B. F. Chmelka, P. Beaujuge, and A. Amassian, *Role of molecular conformation at the donor-acceptor interface in organic photovoltaics*, *Abstracts of Papers of the American Chemical Society* **247** (2014).

[101] F. Etzold, I. A. Howard, N. Forler, A. Melnyk, D. Andrienko, M. R. Hansen, and F. Laquai, *Sub-ns triplet state formation by non-geminate recombination in PSBTBT:PC70bm and PCPDTBT:PC60bm organic solar cells*, *Energy Environ. Sci.* **8** (May, 2015) 1511–1522.

[102] A. D. Becke, *Densityfunctional thermochemistry. III. The role of exact exchange*, *J. Chem. Phys.* **98** (Apr., 1993) 5648–5652.

[103] J.-D. Chai and M. Head-Gordon, *Long-range corrected hybrid density functionals with damped atomatom dispersion corrections*, *Physical Chemistry Chemical Physics* **10** (2008), no. 44 6615–6620.

[104] L. Kronik, T. Stein, S. Refaely-Abramson, and R. Baer, *Excitation Gaps of Finite-Sized Systems from Optimally Tuned Range-Separated Hybrid Functionals*, *J. Chem. Theory Comput.* **8** (May, 2012) 1515–1531.

[105] T. Beringhelli, D. Maggioni, and G. D'Alfonso, *1h and 19f NMR Investigation of the Reaction of B(C6f5)3 with Water in Toluene Solution*, *Organometallics* **20** (Nov., 2001) 4927–4938.

[106] D. Skoog, F. Holler, and S. Crouch, *Principles of Instrumental Analysis*. Brooks/Cole, Cengage Learning, 6 ed., 2007.

[107] K. Connors, *Binding Constants: The Measurement of Molecular Complex Stability*. John Wiley & Sons, New York, 1987.

[108] M. Huk, A. Jegorov, J. Rohlek, A. Fitch, J. Czernek, L. Kobera, and J. Brus, *Determining the Crystal Structures of Peptide Analogs of Boronic Acid in the Absence of Single Crystals: Intricate Motifs of Ixazomib Citrate Revealed by XRPD Guided by ss-NMR*, *Crystal Growth & Design* **18** (June, 2018) 3616–3625.

[109] G. M. Peters, L. P. Skala, T. N. Plank, H. Oh, G. N. Manjunatha Reddy, A. Marsh, S. P. Brown, S. R. Raghavan, and J. T. Davis, *G4-QuartetM+ Borate Hydrogels*, *J. Am. Chem. Soc.* **137** (May, 2015) 5819–5827.

[110] J. Nelson, *Nuclear Magnetic Resonance Spectroscopy*. Pearson Education, Inc., Upper Saddle River, New Jersey, 2003.

[111] B. H. Lee, G. C. Bazan, and A. J. Heeger, *Doping-Induced Carrier Density Modulation in Polymer Field-Effect Transistors*, *Advanced Materials* **28** (Jan., 2016) 57–62.

[112] A. Garcia, G. C. Welch, E. L. Ratcliff, D. S. Ginley, G. C. Bazan, and D. C. Olson, *Improvement of Interfacial Contacts for New Small-Molecule Bulk-Heterojunction Organic Photovoltaics*, *Advanced Materials* **24** (Oct., 2012) 5368–5373.

[113] G. N. M. Reddy, A. Huqi, D. Iuga, S. Sakurai, A. Marsh, J. T. Davis, S. Masiero, and S. P. Brown, *Co-existence of Distinct Supramolecular Assemblies in Solution and in the Solid State*, *Chemistry A European Journal* **23** (Feb., 2017) 2315–2322.

[114] A. Melnyk, M. J. N. Junk, M. D. McGehee, B. F. Chmelka, M. R. Hansen, and D. Andrienko, *Macroscopic Structural Compositions of -Conjugated Polymers: Combined Insights from Solid-State NMR and Molecular Dynamics Simulations*, *J. Phys. Chem. Lett.* **8** (Sept., 2017) 4155–4160.

[115] C. K. Lo, B. R. Gautam, P. Selter, Z. Zheng, S. D. Oosterhout, I. Constantinou, R. Knitsch, R. M. W. Wolfe, X. Yi, J.-L. Brdas, F. So, M. F. Toney, V. Coropceanu, M. R. Hansen, K. Gundogdu, and J. R. Reynolds, *Every Atom Counts: Elucidating the Fundamental Impact of Structural Change in Conjugated Polymers for Organic Photovoltaics*, *Chem. Mater.* **30** (May, 2018) 2995–3009.

[116] J. E. Cochran, M. J. N. Junk, A. M. Glaudell, P. L. Miller, J. S. Cowart, M. F. Toney, C. J. Hawker, B. F. Chmelka, and M. L. Chabinyc, *Molecular Interactions and Ordering in Electrically Doped Polymers: Blends of PBTTT and F4tcnq*, *Macromolecules* **47** (Oct., 2014) 6836–6846.

[117] G. N. M. Reddy, M. V. V. Kumar, T. N. G. Row, and N. Suryaprakash, *NHF hydrogen bonds in fluorinated benzanilides: NMR and DFT study*, *Physical Chemistry Chemical Physics* **12** (2010), no. 40 13232–13237.

[118] J.-L. Brdas, J. Cornil, and A. J. Heeger, *The exciton binding energy in luminescent conjugated polymers*, *Advanced Materials* **8** (May, 1996) 447–452.

[119] M. Knupfer, *Exciton binding energies in organic semiconductors*, *Appl. Phys. A* **77** (Oct., 2003) 623–626.

[120] N. A. Ran, J. A. Love, C. J. Takacs, A. Sadhanala, J. K. Beavers, S. D. Collins, Y. Huang, M. Wang, R. H. Friend, G. C. Bazan, and T.-Q. Nguyen, *Harvesting the Full Potential of Photons with Organic Solar Cells*, *Advanced Materials* **28** (Feb., 2016) 1482–1488.

[121] Y. Zhao, Y. Guo, and Y. Liu, *25th Anniversary Article: Recent Advances in n-Type and Ambipolar Organic Field-Effect Transistors*, *Advanced Materials* **25** (Oct., 2013) 5372–5391.

[122] J. Zaumseil and H. Sirringhaus, *Electron and Ambipolar Transport in Organic Field-Effect Transistors*, *Chem. Rev.* **107** (Apr., 2007) 1296–1323.

[123] N. C. Greenham, S. C. Moratti, D. D. C. Bradley, R. H. Friend, and A. B. Holmes, *Efficient light-emitting diodes based on polymers with high electron affinities*, *Nature* **365** (Oct., 1993) 628–630.

[124] T. M. Brown, R. H. Friend, I. S. Millard, D. J. Lacey, J. H. Burroughes, and F. Cacialli, *Efficient electron injection in blue-emitting polymer light-emitting diodes with LiF/Ca/Al cathodes*, *Appl. Phys. Lett.* **79** (July, 2001) 174–176.

[125] B. P. Rand, D. P. Burk, and S. R. Forrest, *Offset energies at organic semiconductor heterojunctions and their influence on the open-circuit voltage of thin-film solar cells*, *Phys. Rev. B* **75** (Mar., 2007) 115327.

[126] B. Yurash, D. X. Cao, V. V. Brus, D. Leifert, M. Wang, A. Dixon, M. Seifrid, A. E. Mansour, D. Lungwitz, T. Liu, P. J. Santiago, K. R. Graham, N. Koch, G. C. Bazan, and T.-Q. Nguyen, *Towards understanding the doping mechanism of organic semiconductors by Lewis acids*, *Nat. Mater.* (Sept., 2019) 1–8.

[127] C. K. Chiang, C. R. Fincher, Y. W. Park, A. J. Heeger, H. Shirakawa, E. J. Louis, S. C. Gau, and A. G. MacDiarmid, *Electrical Conductivity in Doped Polyacetylene*, *Phys. Rev. Lett.* **39** (Oct., 1977) 1098–1101.

[128] A. G. MacDiarmid and A. J. Heeger, *Organic metals and semiconductors: The chemistry of polyacetylene, (CH)x, and its derivatives*, *Synthetic Metals* **1** (Mar., 1980) 101–118.

[129] B. McQuillan, G. B. Street, and T. C. Clarke, *The reaction of hf with polyacetylene*, *JEM* **11** (May, 1982) 471–490.

[130] C. C. Han and R. L. Elsenbaumer, *Protonic acids: Generally applicable dopants for conducting polymers*, *Synthetic Metals* **30** (Apr., 1989) 123–131.

[131] F. L. Lu, F. Wudl, M. Nowak, and A. J. Heeger, *Phenyl-capped octaaniline (COA): an excellent model for polyaniline*, *J. Am. Chem. Soc.* **108** (Dec., 1986) 8311–8313.

[132] C.-K. Mai, H. Zhou, Y. Zhang, Z. B. Henson, T.-Q. Nguyen, A. J. Heeger, and G. C. Bazan, *Facile Doping of Anionic Narrow-Band-Gap Conjugated Polyelectrolytes During Dialysis*, *Angewandte Chemie International Edition* **52** (2013), no. 49 12874–12878.

[133] A. Abate, D. J. Hollman, J. Teuscher, S. Pathak, R. Avolio, G. DErrico, G. Vitiello, S. Fantacci, and H. J. Snaith, *Protic Ionic Liquids as p-Dopant for Organic Hole Transporting Materials and Their Application in High Efficiency Hybrid Solar Cells*, *J. Am. Chem. Soc.* **135** (Sept., 2013) 13538–13548.

[134] J. Blochwitz, M. Pfeiffer, T. Fritz, and K. Leo, *Low voltage organic light emitting diodes featuring doped phthalocyanine as hole transport material*, *Appl. Phys. Lett.* **73** (Aug., 1998) 729–731.

[135] K. Walzer, B. Maennig, M. Pfeiffer, and K. Leo, *Highly Efficient Organic Devices Based on Electrically Doped Transport Layers*, *Chem. Rev.* **107** (Apr., 2007) 1233–1271.

[136] K.-H. Yim, G. L. Whiting, C. E. Murphy, J. J. M. Halls, J. H. Burroughes, R. H. Friend, and J.-S. Kim, *Controlling Electrical Properties of Conjugated Polymers via a Solution-Based p-Type Doping*, *Advanced Materials* **20** (2008), no. 17 3319–3324.

[137] S. Sivaramakrishnan, M. Zhou, A. C. Kumar, Z.-L. Chen, R.-Q. Png, L.-L. Chua, and P. K. H. Ho, *Solution-processed conjugated polymer organic p-i-n light-emitting diodes with high built-in potential by solution- and solid-state doping*, *Appl. Phys. Lett.* **95** (Nov., 2009) 213303.

[138] W. Gao and A. Kahn, *Controlled p-doping of zinc phthalocyanine by coevaporation with tetrafluorotetracyanoquinodimethane: A direct and inverse photoemission study*, *Appl. Phys. Lett.* **79** (Dec., 2001) 4040–4042.

[139] Y. Zhang, B. de Boer, and P. W. M. Blom, *Controllable Molecular Doping and Charge Transport in Solution-Processed Polymer Semiconducting Layers*, *Adv. Funct. Mater.* **19** (June, 2009) 1901–1905.

[140] A. Y. Sosorev and D. Y. Paraschuk, *Charge-Transfer Complexes of Conjugated Polymers*, *Isr. J. Chem.* **54** (June, 2014) 650–673.

[141] I. Salzmann, G. Heimel, M. Oehzelt, S. Winkler, and N. Koch, *Molecular Electrical Doping of Organic Semiconductors: Fundamental Mechanisms and Emerging Dopant Design Rules*, *Acc. Chem. Res.* **49** (Mar., 2016) 370–378.

[142] J. Gao, J. D.Roehling, Y. Li, H. Guo, A. J.Moul, and J. K.Grey, *The effect of 2,3,5,6-tetrafluoro-7,7,8,8-tetracyanoquinodimethane charge transfer dopants on the conformation and aggregation of poly(3-hexylthiophene)*, *Journal of Materials Chemistry C* **1** (2013), no. 36 5638–5646.

[143] I. E.Jacobs, E. W.Aasen, J. L.Oliveira, T. N.Fonseca, J. D.Roehling, J. Li, G. Zhang, M. P.Augustine, M. Mascal, and A. J.Moul, *Comparison of solution-mixed and sequentially processed P3ht:F4tcnq films: effect of doping-induced aggregation on film morphology*, *Journal of Materials Chemistry C* **4** (2016), no. 16 3454–3466.

[144] D. T. Scholes, S. A. Hawks, P. Y. Yee, H. Wu, J. R. Lindemuth, S. H. Tolbert, and B. J. Schwartz, *Overcoming Film Quality Issues for Conjugated Polymers Doped with F4tcnq by Solution Sequential Processing: Hall Effect, Structural, and Optical Measurements*, *J. Phys. Chem. Lett.* **6** (Dec., 2015) 4786–4793.

[145] D. T. Duong, H. Phan, D. Hanifi, P. S. Jo, T.-Q. Nguyen, and A. Salleo, *Direct Observation of Doping Sites in Temperature-Controlled, p-Doped P3ht Thin Films by Conducting Atomic Force Microscopy*, *Advanced Materials* **26** (Sept., 2014) 6069–6073.

[146] E. J.Lawrence, V. S.Oganesyan, G. G.Wildgoose, and A. E.Ashley, *Exploring the fate of the tris(pentafluorophenyl)borane radical anion in weakly coordinating solvents*, *Dalton Transactions* **42** (2013), no. 3 782–789.

[147] R. J. Kwaan, C. J. Harlan, and J. R. Norton, *Generation and Characterization of the Tris(pentafluorophenyl)borane Radical Anion*, *Organometallics* **20** (Aug., 2001) 3818–3820.

[148] B. Y.-W. Wong, H.-L. Wong, Y.-C. Wong, M.-Y. Chan, and V. W.-W. Yam, *Air-Stable Spirofluorene-Containing Ladder-Type Bis(alkynyl)borane Compounds with Readily Tunable Full Color Emission Properties*, *Chemistry A European Journal* **22** (Oct., 2016) 15095–15106.

[149] K. Wang, S. Huang, Y. Zhang, S. Zhao, H. Zhang, and Y. Wang, *Multicolor fluorescence and electroluminescence of an ICT-type organic solid tuned by modulating the accepting nature of the central core*, *Chemical Science* **4** (2013), no. 8 3288–3293.

[150] T. Ono and Y. Hisaeda, *Flexible-color tuning and white-light emission in three-, four-, and five-component host/guest co-crystals by charge-transfer emissions as well as effective energy transfers*, *J. Mater. Chem. C* **7** (Mar., 2019) 2829–2842.

[151] M. A. Beckett, D. S. Brassington, S. J. Coles, and M. B. Hursthouse, *Lewis acidity of tris(pentafluorophenyl)borane: crystal and molecular structure of B(C6f5)3OPEt3*, *Inorganic Chemistry Communications* **3** (Oct., 2000) 530–533.

[152] L. Ying, B. B. Y. Hsu, H. Zhan, G. C. Welch, P. Zalar, L. A. Perez, E. J. Kramer, T.-Q. Nguyen, A. J. Heeger, W.-Y. Wong, and G. C. Bazan, *Regioregular Pyridal[2,1,3]thiadiazole -Conjugated Copolymers*, *J. Am. Chem. Soc.* **133** (Nov., 2011) 18538–18541.

[153] S. Stoll and A. Schweiger, *EasySpin, a comprehensive software package for spectral simulation and analysis in EPR*, *Journal of Magnetic Resonance* **178** (Jan., 2006) 42–55.

[154] F. Neese, *The ORCA program system*, *Wiley Interdisciplinary Reviews: Computational Molecular Science* **2** (2012), no. 1 73–78.

[155] F. Weigend, *Accurate Coulomb-fitting basis sets for H to Rn*, *Phys. Chem. Chem. Phys.* **8** (Feb., 2006) 1057–1065.

[156] V. Barone, *Recent Advances in Density Functional Methods, Part I*, World Scientific Publ. Co., Singapore, 1996.

[157] J. Niklas, K. L. Mardis, B. P. Banks, G. M. Grooms, A. Sperlich, V. Dyakonov, S. Beaupr, M. Leclerc, T. Xu, L. Yu, and O. G. Poluektov, *Highly-efficient charge separation and polaron delocalization in polymerfullerene bulk-heterojunctions: a comparative multi-frequency EPR and DFT study*, *Phys. Chem. Chem. Phys.* **15** (May, 2013) 9562–9574.

[158] Z. Liang, M. J. Boland, K. Butrouna, D. R. Strachan, and K. R. Graham, *Increased power factors of organicinorganic nanocomposite thermoelectric materials and the role of energy filtering*, *J. Mater. Chem. A* **5** (Aug., 2017) 15891–15900.

[159] A. Dai, Y. Zhou, A. L. Shu, S. K. Mohapatra, H. Wang, C. FuentesHernandez, Y. Zhang, S. Barlow, Y.-L. Loo, S. R. Marder, B. Kippelen, and A. Kahn, *Enhanced Charge-Carrier Injection and Collection Via Lamination of Doped Polymer Layers p-Doped with a Solution-Processible Molybdenum Complex*, *Advanced Functional Materials* **24** (2014), no. 15 2197–2204.

[160] E. L. Ratcliff, P. A. Lee, and N. R. Armstrong, *Work function control of hole-selective polymer/ITO anode contacts: an electrochemical doping study*, *J. Mater. Chem.* **20** (Mar., 2010) 2672–2679.

[161] P. Pingel and D. Neher, *Comprehensive picture of p-type doping of P3ht with the molecular acceptor F$\{\}_{4}$TCNQ*, *Phys. Rev. B* **87** (Mar., 2013) 115209.

[162] D. Kiefer, R. Kroon, A. I. Hofmann, H. Sun, X. Liu, A. Giovannitti, D. Stegerer, A. Cano, J. Hynynen, L. Yu, Y. Zhang, D. Nai, T. F. Harrelson, M. Sommer, A. J. Moul, M. Kemerink, S. R. Marder, I. McCulloch, M. Fahlman, S. Fabiano, and C. Mller, *Double doping of conjugated polymers with monomer molecular dopants*, *Nature Materials* **18** (Feb., 2019) 149.

[163] V. V. Brus, C. M. Proctor, N. A. Ran, and T.-Q. Nguyen, *Capacitance Spectroscopy for Quantifying Recombination Losses in Nonfullerene Small-Molecule Bulk Heterojunction Solar Cells*, *Advanced Energy Materials* **6** (2016), no. 11 1502250.

[164] S. M. Sze and K. K. Ng, *Physics of Semiconductor Devices*. John Wiley & Sons, Inc., Hoboken, New Jersey, 3 ed., 2007.

[165] E. H. Nicollian and A. Goetzberger, *The si-sio, interface electrical properties as determined by the metal-insulator-silicon conductance technique*, *The Bell System Technical Journal* **46** (July, 1967) 1055–1033.

[166] E. J. Meijer, A. V. G. Mangnus, C. M. Hart, D. M. de Leeuw, and T. M. Klapwijk, *Frequency behavior and the MottSchottky analysis in poly(3-hexyl thiophene) metalinsulatorsemiconductor diodes*, *Appl. Phys. Lett.* **78** (June, 2001) 3902–3904.

[167] M. L. Tietze, L. Burtone, M. Riede, B. Lssem, and K. Leo, *Fermi level shift and doping efficiency in p-doped small molecule organic semiconductors: A photoelectron spectroscopy and theoretical study*, *Phys. Rev. B* **86** (July, 2012) 035320.

[168] M. L. Tietze, J. Benduhn, P. Pahner, B. Nell, M. Schwarze, H. Kleemann, M. Krammer, K. Zojer, K. Vandewal, and K. Leo, *Elementary steps in electrical doping of organic semiconductors*, *Nature Communications* **9** (Mar., 2018) 1182.

[169] P. Pingel, R. Schwarzl, and D. Neher, *Effect of molecular p-doping on hole density and mobility in poly(3-hexylthiophene)*, *Appl. Phys. Lett.* **100** (Apr., 2012) 143303.

[170] M. T. Seifrid, S. D. Oosterhout, M. F. Toney, and G. C. Bazan, *Kinetic Versus Thermodynamic Orientational Preferences for a Series of Isomorphic Molecular Semiconductors*, *ACS Omega* **3** (Aug., 2018) 10198–10204.

[171] R.-Q. Png, M. C. Y. Ang, M.-H. Teo, K.-K. Choo, C. G. Tang, D. Belaineh, L.-L. Chua, and P. K. H. Ho, *Madelung and Hubbard interactions in polaron band model of doped organic semiconductors*, *Nature Communications* **7** (Sept., 2016) 11948.

[172] S. Winkler, P. Amsalem, J. Frisch, M. Oehzelt, G. Heimel, and N. Koch, *Probing the energy levels in hole-doped molecular semiconductors*, *Mater. Horiz.* **2** (June, 2015) 427–433.

[173] A. R. Siedle, R. A. Newmark, W. M. Lamanna, and J. C. Huffman, *Structure of a zirconoxyborane having a zirconium-fluorine-carbon bridge*, *Organometallics* **12** (May, 1993) 1491–1492.

[174] A. A. Danopoulos, J. R. Galsworthy, M. L. H. Green, L. H. Doerrer, S. Cafferkey, and M. B. Hursthouse, *Equilibria in the B(C6f5)3H2o system: synthesis and crystal structures of H2oB(C6f5)3 and the anions [HOB(C6f5)3] and [(F5c6)3b(-OH)B(C6f5)3]*, *Chem. Commun.* **0** (Jan., 1998) 2529–2560.

[175] H. A. Kalamarides, S. Iyer, J. Lipian, L. F. Rhodes, and C. Day, *Pentafluoroaryl Transfer from Tris(pentafluorophenyl)boron Hydrate to Nickel. Synthesis and X-ray Crystal Structure of (PPh2ch2c(O)Ph)Ni(C6f5)2*, *Organometallics* **19** (Sept., 2000) 3983–3990.

[176] T. Tang, T. Lin, F. Wang, and C. He, *A new aspect of cyclopentadithiophene based polymers: narrow band gap polymers upon protonation*, *Chemical Communications* **51** (2015), no. 67 13229–13232.

[177] T. Tang, T. Lin, F. Wang, and C. He, *Regiospecific protonation of organic chromophores*, *Physical Chemistry Chemical Physics* **18** (2016), no. 28 18758–18766.

[178] F. Eckert, I. Leito, I. Kaljurand, A. Ktt, A. Klamt, and M. Diedenhofen, *Prediction of acidity in acetonitrile solution with COSMO-RS*, *Journal of Computational Chemistry* **30** (2009), no. 5 799–810.

[179] C. Bergquist, B. M. Bridgewater, C. J. Harlan, J. R. Norton, R. A. Friesner, and G. Parkin, *Aqua, Alcohol, and Acetonitrile Adducts of Tris(perfluorophenyl)borane: Evaluation of Brnsted Acidity and Ligand Lability with Experimental and Computational Methods*, *J. Am. Chem. Soc.* **122** (Nov., 2000) 10581–10590.

[180] N. B. Kotadiya, A. Mondal, P. W. M. Blom, D. Andrienko, and G.-J. A. H. Wetzelaer, *A window to trap-free charge transport in organic semiconducting thin films*, *Nat. Mater.* (Sept., 2019) 1–5.

[181] G. Zuo, M. Linares, T. Upreti, and M. Kemerink, *General rule for the energy of water-induced traps in organic semiconductors*, *Nat. Mater.* **18** (June, 2019) 588–593.

[182] J. Chojnowski, S. Rubinsztajn, J. A. Cella, W. Fortuniak, M. Cypryk, J. Kurjata, and K. Kamierski, *Mechanism of the B(C6f5)3-Catalyzed Reaction of Silyl Hydrides with Alkoxysilanes. Kinetic and Spectroscopic Studies*, *Organometallics* **24** (Dec., 2005) 6077–6084.

[183] M. Bersohn and J. C. Baird, *Double Resonance*, in *An Introduction to Electron Paramagnetic Resonance*, pp. 151–163. W. A. Benjamin, Inc., New York, 1966.

[184] J. A. Weil, J. R. Bolton, and J. E. Wertz, *Double-Resonance Techniques*, in *Electron Paramagnetic Resonance: Elementary Theory and Practical Applications*, pp. 366–392. John Wiley & Sons, Inc., New York, 1994.

[185] L. Piekara-Sady and L. D. Kispert, *ENDOR Spectroscopy*, in *Handbook of Electron Spin Resonance: Data Sources, Computer Technology, Relaxation, and ENDOR* (Charles P. Poole, Jr. and H. A. Farach, eds.), pp. 311–357. American Institute of Physics, New York, 1994.

[186] C. A. Wamser, *Equilibria in the System Boron TrifluorideWater at 25*, *J. Am. Chem. Soc.* **73** (Jan., 1951) 409–416.

[187] T. Higashimura, T. Miki, and S. Okamura, *Kinetic Studies of the Solution Polymerization of Trioxane Catalyzed by BF3O(C2h5)2. I. The Effect of the Catalyst and the Water Concentration on the Rate of Polymerization*, *BCSJ* **38** (Dec., 1965) 2067–2073.

[188] D. D. Eley, *Chemistry of Cationic Polymerization.* Macmillan, New York, 1963.

[189] H. A. Skinner and N. B. Smith, *The heat of hydrolysis of boron tribromide*, *Trans. Faraday Soc.* **51** (Jan., 1955) 19–22.

[190] C. R. Frink and M. Peech, *Hydrolysis of the Aluminum Ion in Dilute Aqueous Solutions*, *Inorg. Chem.* **2** (June, 1963) 473–478.

[191] J. Y. Bottero, J. M. Cases, F. Fiessinger, and J. E. Poirier, *Studies of hydrolyzed aluminum chloride solutions. 1. Nature of aluminum species and composition of aqueous solutions*, *J. Phys. Chem.* **84** (Oct., 1980) 2933–2939.

[192] P. Kovacic and J. Oziomek, *p-Polyphenyl from BenzeneLewis Acid CatalystOxidant. Reaction Scope and Investigation of the BenzeneAluminum ChlorideCupric Chloride System1*, *J. Org. Chem.* **29** (Jan., 1964) 100–104.

[193] A. Ktt, S. Selberg, I. Kaljurand, S. Tshepelevitsh, A. Heering, A. Darnell, K. Kaupmees, M. Piirsalu, and I. Leito, *pKa values in organic chemistry Making maximum use of the available data*, *Tetrahedron Letters* **59** (Oct., 2018) 3738–3748.

[194] E. Paenurk, K. Kaupmees, D. Himmel, A. Ktt, I. Kaljurand, I. A. Koppel, I. Krossing, and I. Leito, *A unified view to Brnsted acidity scales: do we need solvated protons?*, *Chem. Sci.* **8** (Sept., 2017) 6964–6973.